

DISS. ETH NO. 27519

Causal effects of acute cell-specific neuromodulation on resting-state functional connectivity and brain dynamics

A thesis submitted to attain the degree of
DOCTOR OF SCIENCES of ETH ZURICH
(Dr. sc. ETH Zurich)

presented by

Marija Markićević

MSc. Bioengineering, Trinity College Dublin

born on 02.04.1990
citizen of Serbia

accepted on the recommendation of

Prof. Dr. Nicole Wenderoth
Dr. Valerio Zerbi
Prof. Dr. Fritjof Helmchen
Prof. Dr. Johannes Bohacek

2021

Table of Contents

Acknowledgements iii

Summary v

Zusammenfassung vii

List of Figures ix

List of Tables x

List of Boxes x

Introduction 1

- 1.1. Motivation 1
- 1.2. Resting-state functional magnetic resonance imaging (rsfMRI) 2
- 1.3. Chemogenetic brain neuromodulation 8
- 1.4. Chemogenetic neuromodulation combined with resting-state fMRI in mouse 11
- 1.5. Cortical excitation - inhibition (E:I) balance 13
- 1.6. The basal ganglia 14
- 1.7. Specific aims of the thesis and chapter overviews 14

Emerging imaging methods to study whole-brain function in rodent models 17

- 2.1. Abstract 17
- 2.2. Introduction 18
- 2.3. Functional MRI 20
- 2.4. Ultrasound imaging 25
- 2.5. Fluorescence imaging 26
- 2.6. Intrinsic Optical Imaging 31
- 2.7. Photoacoustic imaging 35
- 2.8. Conclusions 38

Cortical excitation:inhibition imbalance causes abnormal brain network dynamics as observed in neurodevelopmental disorders 39

- 3.1. Abstract 39
- 3.2. Introduction 40
- 3.3. Materials and Methods 41
- 3.4. Results 49
- 3.5. Discussion 63
- 3.6. Supplementary Figures and Discussion 66

Cell specific neuromodulation in the striatum shapes BOLD fluctuations in multiple thalamic and cortical regions of an anatomically connected circuit 81

- 4.1. Abstract 81

- 4.2. Introduction 82**
- 4.3. Materials and Methods 83**
- 4.4. Results 89**
- 4.5. Discussion 98**
- 4.6. Conclusions 102**
- 4.7. Supplementary Figures and Tables 103**

General discussion and outlook 106

- 5.1. Hypoconnectivity following cell-specific DREADD-induced neuromodulation 106**
- 5.2. Using machine learning to assess DREADD-induced alterations in brain dynamics 108**
- 5.3. DREADD-rsfMRI approach; potential benefits for computational models 111**
- 5.4. Limitations 112**
- 5.5. Chemogenetic neuromodulation combined with resting-state fMRI 114**

References 116

Curriculum Vitae 141

Acknowledgements

My PhD journey has not only been an enriching scientific experience but also one of continuous personal self-growth. This would not have been possible without a number of people whom I would like to express my gratitude to.

My deepest gratitude goes to my supervisor, Prof. Nicole Wenderoth, for invaluable guidance, truthful and inspiring discussions, which have continuously encouraged me to give my best. Thanks to Nici's support, I have crossed out two important items from my "wish list": I have not only visited but lived in Australia ☺ and I had an honor to represent ETH at the Global Young Scientists Summit. I am truly grateful for these opportunities, that have immensely expanded my scientific and life horizons.

A big thank you to my concurrent supervisor, Dr. Valerio Zerbi, for his indispensable guidance throughout my PhD. His open-door policy has been crucial in shaping my early knowledge of rodent fMRI and meant that I always had someone to share with all the peculiarities of setting up new experiments (which I actively utilized ☺).

I am very grateful to Prof. Johannes Bohacek. Firstly, for agreeing to co-supervise this PhD thesis. Secondly, for allowing me to utilize and have full access to the equipment in his lab. Thanks to this access all my immunohistochemistry work and short-term genotyping have been possible.

I am also thankful to Prof. Fritjof Helmchen for agreeing to co-supervise this thesis and for collaboration and support of electrophysiology experiments presented in chapter 3 of this thesis.

My sincere thank you to Dr. Ben Fulcher. Primarily, for an inspiring collaboration visible in chapter 3 of this thesis. Secondly and most importantly, for hosting me in Sydney and selflessly sharing his knowledge about machine learning. Knowledge acquired during my short stay in Sydney has significantly contributed to a paper covered in chapter 4 of this thesis.

During my PhD I have had the luck to work alongside a number of talented people from a number of different labs, whom I have learnt a great deal from and would like to acknowledge.

Chris Lewis for performing electrophysiology experiments, during which I have learnt lots about electrophysiology data acquisition.

Past members of the AIC, for providing a memorable scanning environment. Special thanks to Giovanna Ielacqua, Aileen Schröter and David Bühlmann for teaching me mouse cannulation, intubation and perfusion and Mark Augath for reliable MRI scanner support.

Bohacek lab crew for creating a lab environment I always looked forward to returning. Special thank you goes to Amalia Floriou Servou and Mattia Privitera for introducing me to

immunohistochemistry and Oliver Sturman for helping with open field experimental setup and videos.

All the members of the NCM lab in the last five years, for stimulating working environment and numerous happy and cake hours. Michel Wälti, who I had enjoyed sharing teaching responsibilities with and who has taught me the importance of “start with the positive feedback first 😊”. Marc Bächinger, for numerous conversations about Switzerland, life and science. The RSA crew i.e., Sanne Kikkert, Finn Rabe, Ernest Mihelj, Ingrid Odermatt and Caroline Heimhofer, for reminding me how enjoyable team work really is. The mouse crew i.e., Christina Grimm and Iurri Savvateev for fun scanning sessions and fruitful science discussions of pre-pandemic times. The administrative team i.e., Maria Willecke, Xue “Snow” Zhang and Nicole Hintermeinter for help whenever needed. To all other (ex)members of the lab for multiple laughs, talks and fruitful discussions: Sarah Meissner, Miriam Schrafl-Alttermatt, Charlie Lambelet, Rea Lehner, Andreea Cretu, Onno van der Groen, Felix Thomas, Weronika Potok and Gabrielle Zbären.

I also thank Marc Bächinger, Dan Woolley, Michel Wälti and Iurri Savvateev for their time to provide me with critical feedback on my thesis introduction and discussion. Lastly, I am grateful to Marc Bächinger (again 😊) and Christina Grimm for tremendously improving the first draft of the German version of my thesis summary.

Finally, my highest gratitude goes to my mama Vesna, for her unlimited love, encouragement and trust in me. She is the wind at my back and someone I can always count on, regardless of the time zone difference 😊.

Last but not least my warmest gratitude goes to Rob, for his continuous support and unconditional love. A big thank you for bringing a much-needed balance and joy into my everyday life.

Summary

The brain is a complex network of anatomically connected and perpetually interacting neural populations. To comprehensively understand complex brain function, it is necessary to investigate the brain across different scales – from cellular and (micro)circuit levels to distinct brain networks – and to define relationships among these levels. Noninvasive resting-state functional magnetic resonance imaging (rsfMRI) is a common approach used to understand intrinsic brain network organization in healthy humans. RsfMRI is also widely utilized to investigate altered brain network organization in numerous psychiatric and neurodevelopmental disorders. However, the neural basis of brain network organization in healthy and diseased brains remains elusive, making it difficult to associate functional macroscopic observations with underlying cellular level alterations. The aim of this PhD thesis was to bridge this gap. To do so required invasive interventional approaches and controlled experimental conditions achievable with animal models. We provide causal insights into how altered neuronal signaling of specific cell populations map onto alterations of rsfMRI brain network organization, by combining rsfMRI with cell-specific neuromodulation of Designer Receptors Exclusively Activated by Designer Drugs (DREADDs) in mice. DREADDs are modified G protein coupled receptors insensitive to endogenous ligands but activated by an otherwise inert low dose pharmacological agent, allowing targeted control of neuronal signaling. This PhD thesis starts with a review of emerging methods to study neuronal activity of the rodent brain at the system and network levels and continues with two projects designed to bridge the gap between the cellular and network levels.

In the first project we investigated the effects of perturbing the excitation-inhibition (E:I) ratio, the putative mechanism in a number of neurodevelopmental disorders, on whole-brain functional connectivity (FC) and dynamics. Using DREADDs we increased the E:I ratio either by i) overexciting excitatory neurons, or ii) inhibiting inhibitory Parvalbumin (PV) interneurons within cortical microcircuits. Conventional FC analyses revealed significant reductions in long-range functional connectivity within anatomically connected areas, regardless of the E:I perturbation approach. Moreover, using an advanced machine learning approach, a trained classifier was able to correctly identify regions with perturbed E:I ratio elicited by our DREADD manipulation. We further validated the same classifier on an independent cohort of *Fmr1*^{-/-} knockout mice, a mouse model for autism with well-documented loss of PV neurons and chronic alterations in E:I. Our findings demonstrate a novel approach towards inferring microcircuit abnormalities from macroscopic fMRI measurements.

In the second project we explored the effects of excitation or inhibition of D1 medium spiny neurons (MSNs) of the right dorsomedial striatum on brain FC and dynamics. Dynamics of each region constituting a striato-thalamic-cortical circuit were assessed using an advanced machine learning approach and FC analyses. We showed that modulation of D1 MSNs in the striatum propagates through anatomically connected networks, thereby shaping the

dynamics of multiple thalamic and cortical regions within an anatomically defined circuit, while only perturbing cortico-striatal functional connectivity. Our findings demonstrate a complementary approach to FC analyses, which provides rich region-specific information in the context of altered brain dynamics.

Finally, some general implications of the major findings are discussed followed by an outlook of possible future directions to address open questions. Taken together, our results indicate that local cell-specific neuromodulation, whether of cortical or subcortical origin, shapes the brain dynamics and functional connectivity of anatomically connected regions, revealing distinct patterns of cell-specific neuromodulation across scales.

Zusammenfassung

Das Gehirn ist ein komplexes Netzwerk aus anatomisch verbundenen und ständig interagierenden neuronalen Populationen. Um komplexe Hirnfunktionen umfassend zu verstehen, ist es notwendig, das Gehirn auf verschiedene Skalen zu untersuchen - von der zellulären (Mikro-)Schaltkreisebene bis hin zu verschiedenen Hirnnetzwerken auf makroskopischer Ebene - und deren Beziehungen untereinander zu definieren. Die nicht-invasive funktionelle Magnetresonanztomographie im Ruhezustand (rsfMRI) ist ein gängiger Ansatz, um die intrinsische Netzwerkorganisation des Gehirns bei gesunden Menschen zu verstehen. RsfMRI wird auch häufig zur Untersuchung der veränderten Netzwerkorganisation des Gehirns bei zahlreichen psychiatrischen und neurologischen Erkrankungen eingesetzt. Allerdings ist die neuronale Basis dieser Netzwerkorganisation nach wie vor unbekannt. Es ist daher schwierig, funktionelle makroskopische Beobachtungen mit den ihnen zugrundeliegenden zellulären Prozessen zu assoziieren. Ziel der vorliegenden Dissertation war es, diese Verständnislücke zu schließen. Dies erforderte invasive, interventionelle Ansätze und kontrollierte experimentelle Bedingungen, welche so nur im Tiermodell realisiert werden können. Durch die Kombination von rsfMRI mit der zellspezifischen Neuromodulation von „*Designer Receptors Exclusively Activated by Designer Drugs*“ (DREADDs) in Mäusen konnten kausale Erkenntnisse darüber gewonnen werden, wie eine veränderte neuronale Signalübertragung spezifischer Zellpopulationen die Organisation von Gehirnnetzwerken auf makroskopischer Ebene beeinflusst. DREADDs sind modifizierte G-Protein-gekoppelte Rezeptoren, die unempfindlich gegenüber endogenen Liganden sind, jedoch durch einen pharmakologisch inerten, niedrig dosierten Wirkstoff aktiviert werden können. Dadurch wird eine gezielte Kontrolle der neuronalen Signalübertragung ermöglicht. Diese Doktorarbeit beginnt mit einem Überblick über neue Methoden zur Untersuchung der neuronalen Aktivität des Nagetiergehirns auf der System- und Netzwerkebene und präsentiert im Folgenden zwei Projekte, welche die Verständnislücke zwischen zellulärer und Netzwerkebene schließen sollen.

Im ersten Projekt untersuchten wir die Auswirkungen einer Störung der Exzitation-Inhibition Balance (E:I), welche vermutlich einer Reihe von neurologischen Entwicklungsstörungen zugrunde liegt, auf die funktionelle Konnektivität (FC) und Dynamik des gesamten Gehirns. Mit Hilfe von DREADDs erhöhten wir das E:I-Verhältnis entweder durch i) Übererregung von exzitatorischen Neuronen oder ii) Hemmung von inhibitorischen Parvalbumin (PV)-Interneuronen innerhalb kortikaler Mikroschaltkreise. Konventionelle FC-Analysen zeigten signifikante Reduktionen der funktionellen Fernkonnektivität innerhalb anatomisch verbundener Areale, unabhängig vom angewendeten E:I-Störungsansatz. Desweiteren war ein auf maschinellem Lernen basierender (ML-Ansatz) Klassifikator in der Lage, Regionen mit gestörtem E:I-Verhältnis aufgrund unserer DREADD-Manipulation korrekt zu identifizieren. Wir validierten diesen Klassifikator an einer unabhängigen Kohorte von *Fmr1y/-* Knockout-Mäusen, welche als ein murines Autismus-Modell mit gut dokumentiertem Verlust von PV-

Neuronen und chronischen Veränderungen der E:I gelten. Unsere Ergebnisse zeigen einen neuartigen Ansatz, um aus makroskopischen fMRI-Messungen auf Anomalien der Mikroschaltkreise zu schließen.

Im zweiten Projekt untersuchten wir die Auswirkungen der Erregung oder Hemmung von mittelgrossen dornentragenden Projektionsneuronen des Typs D1 (MSNs) des rechten dorsomedialen Striatums auf die funktionelle Konnektivität und Dynamik des Gehirns. Die Dynamik jeder Region, die einen striato-thalamisch-kortikalen Schaltkreis bildet, wurde hierbei mit Hilfe eines ML-Ansatzes und FC-Analysen bewertet. Wir konnten zeigen, dass sich die Modulation von D1 MSNs im Striatum durch anatomisch verbundene Netzwerke ausbreitet und dadurch die Dynamik mehrerer thalamischer und kortikaler Regionen innerhalb eines anatomisch klar definierten Schaltkreises beeinflusst, während sie nur die kortiko-striatale funktionelle Konnektivität stört. Unsere Ergebnisse zeigen einen komplementären Ansatz zu FC-Analysen auf, der wertvolle, regionsspezifische Informationen im Kontext der veränderten Hirndynamik liefern kann.

Abschließend diskutiere ich einige allgemeine Implikationen der wichtigsten Ergebnisse, gefolgt von einem Ausblick auf mögliche zukünftige Forschungsschwerpunkte, um offene Fragen zu klären. Zusammengefasst deuten unsere Ergebnisse darauf hin, dass lokale zellspezifische Neuromodulation, unabhängig davon ob sie kortikalen oder subkortikalen Ursprungs ist, die Hirndynamik und funktionelle Konnektivität anatomisch verbundener Regionen prägt und dabei über die verschiedenen Skalen hinweg unterschiedliche Muster zellspezifischer Neuromodulation aufzeigt.

List of Figures

- 1.1. The resting-state networks commonly found in humans. 5
- 1.2. The resting-state networks commonly found in mice. 7
- 1.3. Schematic illustration of the steps leading to neuronal activation/inhibition using hM3Dq/hM4Di DREADDs. 10
- 1.4. Schematic illustration of the potential benefit of causal perturbations. 12
- 2.1. The spatiotemporal overview of imaging techniques used for studying rodent whole-brain function. 19
- 2.2. Microscopy Designs. 30
- 3.1. Local changes in neural activity induced by activating hSyn-hM3Dq. 47
- 3.2. Long-range connectivity changes induced by activating hSyn-hM3Dq. 50
- 3.3. Changes induced by activating CAMK-hM3Dq in wildtype mice. 52
- 3.4. Changes induced by activating hSyn-hM4Di in PVCre mice. 53
- 3.5. DREADD manipulations lead to characteristic changes in univariate BOLD dynamics. 56
- 3.6. $Fmr1^{Y/-}$ exhibit similar local BOLD dynamics as DREADD-manipulated mice. 58
- S3.1. Schematic of the experimental pipeline. 62
- S3.2. Low doses of clozapine have no effect on neuronal activity. 63
- S3.3. Short- and long-range connectivity changes induced by activating hSyn-hM3Dq. 64
- S3.4. Long-range connectivity changes induced by activating hM3Dq. 65
- S3.5. hM3Dq activated by CNO causes inter-hemispheric connectivity reduction. 66
- S3.6. Changes induced by activating hM4Di in PVCre mice. 67
- S3.7. Viral expressions in the SSp of wt-hSyn-hM3Dq, PVCre-hSyn-hM4Di and wt-CAMKII-hM3Dq mice. 68
- S3.8. Statistical comparison between different doses of clozapine in wt-hSyn-hM3Dq and control mice. 69
- S3.9. Univariate BOLD dynamics are weakly distinguishable at the left SSp and VIS among the three groups. 70
- S3.10. Univariate BOLD dynamics change in similar ways in wt-hSyn-hM3Dq and PVCre-hSyn-hM4Di. 71
- 4.1. Chemogenetic targeting of D1 MSNs induces behavioral effects. 86
- 4.2. Simplified illustration of the procedure for striato-thalamic-cortical region selection. 88
- 4.3. Altered dynamics in thalamic regions forming anatomically closed loops with dorsomedial caudate putamen. 90
- 4.4. Characteristic changes observed in BOLD dynamics of region part of the striato-thalamic-cortical circuit. 92
- 4.5. Functional connectivity changes induced by chemogenetic neuromodulation. 93
- S4.1. Illustration on steps used to create three main CP subregions. 99

List of Tables

- S3.1. Demographics of mice used in the experiment. 72
- S4.1. Balanced Accuracies for 29 subregions of CP obtained from Mouse-Striatum Projectome. 100
- S4.2. List of thalamic ROIs and their anatomical projections from/to dorsomedial CP with references to the literature where the information was obtained. 101

List of Boxes

- 1.1. Summary of BOLD signal generation. 3
- 1.2. Common methods to analyze rsfMRI data. 4
- 2.1. Operational details of Widefield, Confocal, Multiphoton and Light-Sheet microscopes. 31

CHAPTER 1

Introduction

1.1. Motivation

The mammalian brain is a complex network of anatomically connected, perpetually interacting neuronal populations and supporting cells, which together form a structural foundation underlying neuronal function and complex behavior (Seung, 2012). With current advances in experimental tools and techniques, it is possible to study behavioral function at the level of anatomically distinct cell populations. However, it is rarely the case that complex behavior is solely regulated by a single brain region but rather through the interplay of a number of anatomically connected brain regions that form specialized circuits. Consequently, neuroscience is shifting away from only identifying the function of single brain regions, towards deciphering brain function within the context of complex dynamic brain networks (Sporns, 2011). A comprehensive understanding of the complex function of brain networks involves investigating the brain from the microscale (single neuron connections) to the mesoscale (neural populations forming local functional circuits) and macroscale (anatomically distinct brain regions) levels and defining relationships among them.

Measuring neural activity and relating it to complex network dynamics and ultimately behavior remains one of the central challenges in contemporary neuroscience. In humans, resting-state functional magnetic resonance imaging (rsfMRI) is the method of choice for estimating activity interdependences between brain networks. Since its onset in the mid 1990s, human rsfMRI has been an indispensable tool in understanding the workings of the healthy and pathological brain (Rosen and Savoy, 2012). RsfMRI examines temporal correlations of slow (<0.1Hz) fluctuations intrinsically generated by the brain at rest. While indirectly capturing the neuronal activity of the brain, these fluctuations form spatial patterns of correlated network activity, that reveal the brain's intrinsic functional architecture (Fox and Raichle, 2007). Resting-state networks exhibit high functional connectivity, are anatomically specific and have been shown to be sensitive to a variety of neurodevelopmental and psychiatric diseases, by displaying altered brain connectivity. In order to understand the pathobiology of diseases in humans, emphasis has been placed on finding rsfMRI biomarkers which could help quantify altered brain connectivity linked to an individual's disease state (Hohenfeld et al., 2018, Jack, 2018). While an increasing number of studies describe rsfMRI biomarkers at the pathological level (Gomez-Ramirez and Wu, 2014, Wager and Woo, 2017), mechanistic insights into how altered neuronal signaling of specific cell populations map onto alterations of rsfMRI connectivity are limited. In this PhD thesis, we bridge this gap by combining rsfMRI with chemogenetic neuromodulation in mouse.

Chemogenetics such as Designer Receptors Exclusively Activated by Designer Drugs (DREADDs), enable selective and controlled pharmacological neuromodulation of specific cells or circuits of the mouse brain. They are a powerful tool for targeted control of neuronal

signaling that can be leveraged towards more translational applications (English and Roth, 2015). rsfMRI as a translational noninvasive tool has found broad applications within the animal neuroimaging community (Mandino et al., 2020). Mouse rsfMRI studies have revealed resting-state networks with similar properties as those in the human brain, making it a promising translational model for studying physiological networks. In this thesis, we combine these two modalities to investigate the effects of cell-specific neuromodulation on whole-brain network dynamics. The goal of this thesis is to establish a causal link between cellular perturbations at the microscale and brain network dynamics at the macroscale, and potentially provide new insights for advancing neuroimaging as a tool, in the context of future clinical applications.

The remainder of this chapter provides an overview of rsfMRI with a focus on resting-state functional connectivity followed by a description of chemogenetic neuromodulation, before outlining the benefits of combining rodent rsfMRI with chemogenetics. Finally, excitation:inhibition (E:I) balance and basal ganglia are briefly introduced before the specific aims of this thesis and chapter overviews are provided.

1.2. Resting-state functional magnetic resonance imaging (rsfMRI)

In 1990, Ogawa and colleagues investigated responses to a physiological stimulus in rodent brains and reported that functional brain mapping was possible using venous blood oxygenation level-dependent (BOLD) magnetic resonance imaging (MRI) contrast (Ogawa et al., 1990a, Ogawa et al., 1990b). This BOLD contrast is the basis of functional MRI and relies on the magnetic properties of the hemoglobin, which is based on alterations in levels of deoxygenated and oxygenated blood resulting from neural activity (Buxton, 2013).

Neural activity propagates via synaptic transmission of action potentials, mediated by the release of neurotransmitters from the presynaptic terminals across the synaptic gap. Released neurotransmitters bind to postsynaptic receptors of the neighboring neuron resulting in the generation of postsynaptic potentials which travel further down the axon of that neuron. Propagation of neural activity is an energy-consuming process which requires a constant supply of nutrients through the dense vasculature of the brain. An increase in neural activity leads to an increased demand of oxygen and glucose, resulting in a local up-regulation of glucose metabolism, cerebral metabolic rate of oxygen consumption (CMRO₂) and cerebral blood flow (CBF). While CBF changes and glucose metabolism are closely coupled, the CBF increase upon neural activation surpasses the increase in CMRO₂ (Fox and Raichle, 1986), leading to a net increase of oxygenated hemoglobin present in the blood. This hemodynamic effect which arises from a mismatch between CBF increase and CMRO₂ change is the basis of the BOLD signal (Buxton, 2013). A summary of the BOLD signal generation can be found in Box 1.1.

The first researchers to show that brain activity is related to fluctuations of the BOLD signal applied visual and motor stimulus paradigms. To visualize areas responsive to those stimuli, the BOLD signal was measured relative to a baseline condition (Kwong et al., 1992). This seminal work led to a development and widespread use of task-based fMRI to study the human brain (Barch et al., 2013). However, in 1995 Biswal and colleagues (Biswal et al., 1995) illustrated that the slow (<0.1 Hz) spontaneous BOLD fluctuations in the right and left motor areas are temporally correlated, without performing any tasks. This is the first report of task-free BOLD-fMRI, denoted by many as resting-state fMRI (rsfMRI).

Box 1.1. Summary of BOLD signal generation

Intrinsic magnetic properties of the blood are used for BOLD signal generation. Local neural activation triggers an increase in the ratio of oxygenated vs deoxygenated hemoglobin, whose distinct magnetic properties give rise to the BOLD signal. Oxygenated hemoglobin is diamagnetic i.e., it does not affect the MR magnetic field leading to no signal intensity loss. It is the paramagnetic properties of the deoxyhemoglobin that cause magnetic susceptibility inside blood vessels and surrounding tissue, thus affecting the magnetic field and increasing T2* relaxation times. T2* relaxation time is a time constant used to measure the decay of the MRI signal that arises within the tissue of interest. Local increase in neural activity leads to an over-compensatory increase of regional CBF, which decreases the relative amount of deoxygenated hemoglobin leading to a slower T2* relaxation time and local increase in signal intensity. MRI sequences that enhance the T2* contrast and enable fast image acquisition, such as gradient-echo echo planar imaging (GRE-EPI) are often used for studying hemodynamic responses to neuronal activation (Chavhan et al., 2009). The GRE-EPI sequence has been applied in all the rsfMRI studies covered in this thesis.

Resting-state fMRI is a common noninvasive imaging modality capable of measuring human brain activity at a spatial resolution typically around 3mm and a temporal resolution of around 1s. Resting-state BOLD signals fluctuate in the slow frequency range (<0.1 Hz). They indirectly reflect spontaneous neuronal activity, which is intrinsically generated by the brain in the absence of any specific task or stimulus, i.e. during rest (Fox and Raichle, 2007).

With the expansion of resting-state fMRI came the need to study the origins of spontaneous BOLD signal fluctuations. Human resting-state networks were validated using magnetoencephalography (MEG), a modality that bypasses the hemodynamic response and measures magnetic fields induced by synchronized current flow in neuronal assemblies. This method displayed spatially similar resting-state networks compared to networks derived from rsfMRI, thus confirming their neuronal basis (Brookes et al., 2011). Several research groups independently focused on combining rodent rsfMRI with a direct measurement of neuronal and astrocytic activity via optical fluorescent calcium imaging. These studies reveal strong coupling of the neuronal and astrocytic calcium signals with rsfMRI BOLD responses (Schlegel et al., 2018, Tong et al., 2019). Recent work also in mice illustrated that ultra-slow oscillations of neuronal activity entrain fluctuations in arteriole diameter which are further

reflected in the resting-state BOLD signal (Mateo et al., 2017), thus, indicating its neuronal basis.

Resting-state BOLD signals are usually examined by investigating their temporally correlated patterns across the brain using functional connectivity analysis (Chen et al., 2020a). Functional connectivity (FC) describes the relationship between spontaneous BOLD fluctuations of distinct brain regions and reflects the level of functional communication between them. It is routinely calculated by using the Pearson correlation coefficient to assess the statistical interdependences between pairs of regions (van den Heuvel and Hulshoff Pol, 2010). A brief summary of the most common methods used to analyze the rsfMRI data can be found in Box 1.2.

Box 1.2. Common methods to analyze rsfMRI data

Prior to analyzing rsfMRI data a number of preprocessing steps are performed. There is usually more than one way (i.e., more than one algorithm) for performing each of the steps, thus preprocessing rsfMRI steps are not standardized and the individual details frequently vary across research groups. However, the most common steps include: **1)** Motion correction which accounts for any slight movements during the scan, usually lower than 1-2 voxels (if the motion is larger, it is recommended to reject the entire dataset). **2)** Filtering the data with a high pass filter in order to remove low frequency fluctuations arising from the system hardware. **3)** Spatial smoothening to improve signal to noise ratio. **4)** Co-registration to an anatomical reference template to allow group-level analyses.

Common methods to analyze rsfMRI data can be divided into data-driven and hypothesis-driven methods. The most widely used data-driven method is **independent component analysis (ICA)**.

ICA is a multivariate method aimed at reducing the data into a set of maps displaying regions that exhibit similar spatiotemporal patterns. This is followed by sorting the components into known brain networks, or artefacts arising from cardiovascular effects, respiration or motion.

The oldest and most commonly applied hypothesis-driven method to analyze rsfMRI data is referred to as **seed-based analysis**. A region-of-interest (ROI; i.e., seed) is chosen, which is based on an a priori hypothesis. Time-series extracted from the ROI are linearly correlated with the rest of the ROIs or voxels of the brain. The result is a map of the brain, where stronger correlations between the seed region with the rest of the brain imply higher functional connectivity.

1.2.1 Resting-state functional connectivity in humans

The human brain is a complex network of structurally interconnected regions that continuously communicate with one another. This functional communication has resulted in the identification of a number of robust resting-state networks. Perhaps the most widely studied one is the default mode network (DMN), consisting of distinct regions distributed across the cortex (from ventromedial and lateral prefrontal, posteromedial and inferior parietal to lateral and medial temporal regions) (Greicius et al., 2003) and subcortical regions such as basal forebrain and thalamus (Alves et al., 2019). The DMN is considered the backbone of cortical integration (Kernbach et al., 2018). Its regions display decreased activation during attention-demanding tasks and are strongly negatively correlated with task-

positive (regions activated during a task) networks, such as visual and somatosensory networks (Heine et al., 2012). By examining the temporal correlations between brain voxels at rest, a number of other robust resting-state networks were identified, including, auditory, visual, motor, and others (Chen et al., 2020a). Generally, these resting-state networks are defined by anatomically relevant structures that maintain, in their resting state, a significant degree of temporal coherence in their spontaneous activity (Fox and Raichle, 2007, Corbetta et al., 2008, van den Heuvel and Hulshoff Pol, 2010). Resting-state networks exhibit high functional connectivity and have been shown to be remarkably reproducible within and across healthy individuals (Fox and Raichle, 2007, Chen et al., 2020a). A representative list of human brain networks detectable by resting-state fMRI is shown in Figure 1.1.

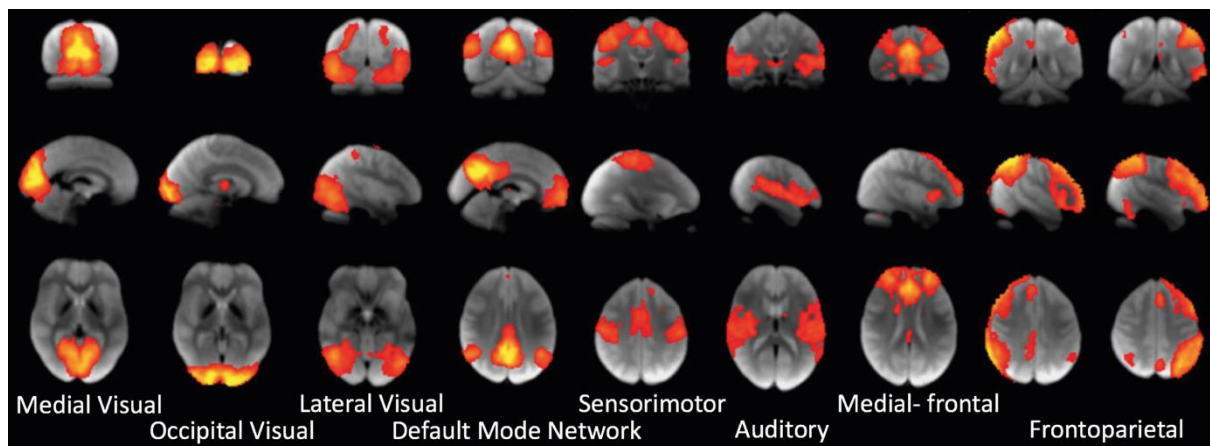


Figure 1.1. The resting-state networks commonly found in humans. Cortical resting-state networks modified from (Smith et al., 2009). Default mode network includes medial parietal cingulate, inferior-lateral-parietal and ventromedial frontal cortex. Sensorimotor network includes supplementary motor area, sensorimotor cortex and secondary somatosensory cortex. Auditory network includes the superior temporal gyrus, Heschl's gyrus and posterior insular. Medial-frontal network includes anterior cingulate and paracingulate. Frontoparietal network includes several frontoparietal areas including Broca's and Wernicke's areas. Resting-state networks were obtained using independent component analysis.

Perhaps more important than the functional organization of the healthy human brain is the fact that resting-state networks are sensitive to a variety of neurodevelopmental and psychiatric diseases, such as Autism Spectrum Disorder (ASD) (Hull et al., 2016), depression (Karim et al., 2017), and schizophrenia (Kraguljac et al., 2016), to name a few, rendering rsfMRI a potentially valuable tool for diagnostic purposes (Gomez-Ramirez and Wu, 2014, Wager and Woo, 2017). Interestingly, since its discovery in the mid 90s till 2010, over 20 disease states have been investigated using rsfMRI, including all major neurological and psychiatric diseases (e.g. ASD, Alzheimer's, Parkinson's, etc.) (Fox and Greicius, 2010) and this trend continues until today (Jack, 2018, Wolters et al., 2019, Jalilianhasanpour et al., 2019, Hohenfeld et al., 2018). Earlier studies focused mostly on FC comparisons between the healthy and unhealthy groups, revealing some type of aberrant connectivity in the unhealthy group (Hohenfeld et al., 2018). Recent studies are more diverse in the types of analyses chosen to assess rsfMRI and in addition to the conventional FC, include graph theory analyses,

machine learning classification, etc., (Jack, 2018, Kazeminejad and Sotero, 2019). Because rsfMRI is noninvasive, painless and requires minimal patient compliance, its use in clinical applications is directed towards finding reproducible biomarkers for obtaining diagnostic and prognostic information linked with the disease (Fox and Greicius, 2010). Machine learning is one of the analyses deployed to investigate the diagnostic value of rsfMRI to find neuroimaging-based biomarkers of distinct brain disorders. This has resulted in rsfMRI becoming one of the prevalent methods used to study the function of the human brain in health and disease. An example that demonstrates the importance of the rsfMRI signal is the existence of a number of research projects aimed at collecting large amounts of rsfMRI data across different institutions (Smith and Nichols, 2018), such as Human Connectome Project (Van Essen et al., 2013), UK Biobank (Miller et al., 2016) and many more (Horien et al., 2021).

1.2.2 Resting-state functional connectivity in mice

The noninvasive and task-free nature of rsfMRI allows a cross species comparison of neuronal activity of the brain, rendering rsfMRI a potentially suitable translational tool. The mouse brain is roughly three orders of magnitude smaller than the human brain, which constitutes a challenge in terms of achievable signal-to-noise (SNR) ratio in the scanner. SNR can be increased either by increasing the signal or decreasing the noise. Ultrahigh-field MR systems improve the signal achievable but introduce image artefacts due to magnetic field inhomogeneities. This can be overcome with the use of cryogenic coils, which are cooled to 30°K to reduce thermal noise from the electronic equipment, thus increasing the SNR in the order of 2.5 (Baltes et al., 2009). These technical advances have notably contributed to increasing the accuracy of the rsfMRI measurements in mice, a critical factor for conducting functional connectivity studies.

One common practice in mouse rsfMRI experiments is to use low-dose anesthetics in order to reduce animal distress and help restrain animals. This has prompted thorough research into evaluating various doses of different anesthetics on the FC of the mouse brain (Grandjean et al., 2014a, Nasrallah et al., 2014, Bukhari et al., 2017, Reimann and Niendorf, 2020). Medetomidine (Nasrallah et al., 2014, Grandjean et al., 2014a), isoflurane (Grandjean et al., 2014a), halothane (Sforzini et al., 2014, Liska et al., 2015), or a combination of medetomidine/isoflurane (Grandjean et al., 2014a, Zerbi et al., 2019a) are among the most common anesthetics used for rsfMRI studies in mice (Reimann and Niendorf, 2020). While the effects of these anesthetics on FC may differ, recent work from Grandjean and colleagues showed that regardless of the anesthetic protocols applied during scanning (referring to the four mentioned above), the resting-state networks were shown to be comparable in a multi-center comparison approach. Specifically, they analyzed 17 mouse rsfMRI datasets (consisting of 15 scans each) obtained from different institutions with various anesthesia protocols and illustrated the presence of network-specific functional connectivity in all datasets (Grandjean et al., 2020). This indicates to some extent that network properties are retained between

different conditions and illustrates the importance of proper sedation protocols for obtaining reliable functional connectivity results.

With ultrahigh MR systems, optimal anesthesia protocols and identical analytical methods as used in human rsfMRI work, researchers have identified a number of mouse resting-state brain networks. These networks display identical properties to the networks reported in humans, indicating an evolutionary preservation (Chuang and Nasrallah, 2017, Gozzi and Schwarz, 2016, Zerbi et al., 2015, Sforazzini et al., 2014, Nasrallah et al., 2014, Jonckers et al., 2011). A plausible default mode network homologue of the human DMN was also identified (Sforazzini et al., 2014, Stafford et al., 2014, Zerbi et al., 2015). Stafford and colleagues (2014) used seed-based analysis independently in humans, macaques, and mice to identify the DMN. In each species, the seed was placed in the identical region identified as part of the DMN in humans (RSP – retrosplenial area). Results indicate overlapping regions of mouse DMN with human and macaque DMN (anterior cingulate, orbitofrontal and parietal areas), followed also by a presence of primary visual and somatosensory areas not identified in the primate brain (Stafford et al., 2014). While some areas of DMN are conserved across species, others such as posterior cingulate cortex do not have a clear correlate in the mouse. By applying identical analytical methods as for human rsfMRI network analysis, additional mouse resting-state networks identified include visual, somatosensory, motor, basal ganglia, and hippocampus (Zerbi et al., 2015, Grandjean et al., 2017b, Liska et al., 2015). A representative list of mouse brain networks is illustrated in Figure 1.2.

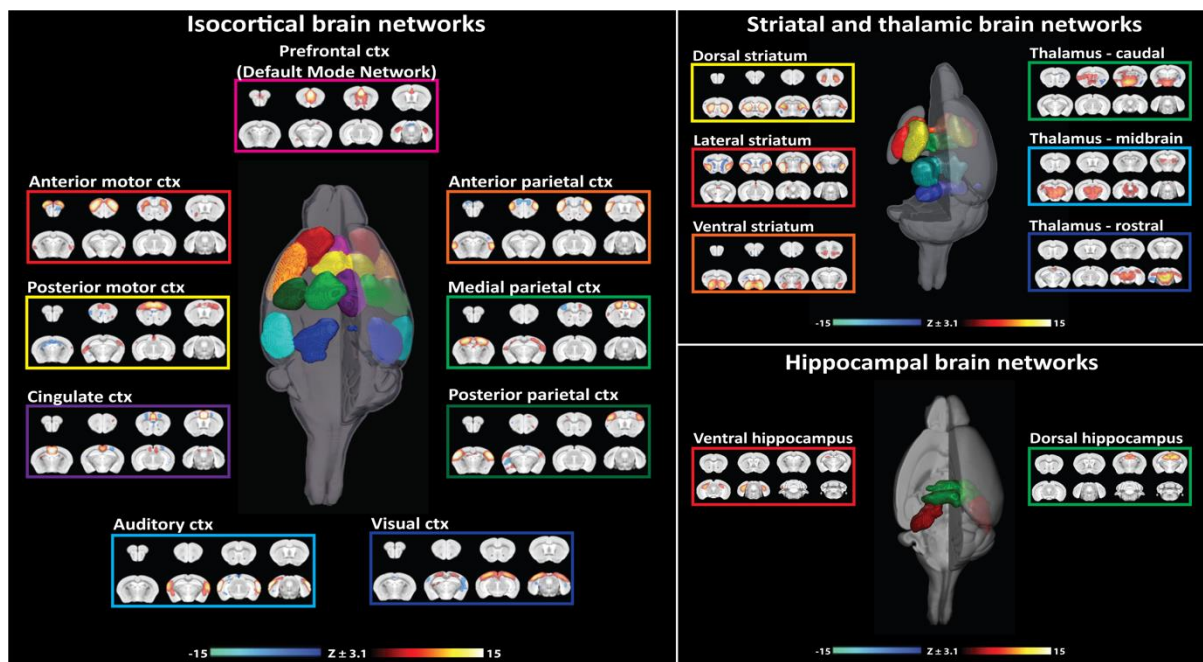


Figure 1.2. *The resting-state networks commonly found in mice. Mouse resting-state networks modified from (Grandjean et al., 2017b). Resting-state networks were obtained using independent component analysis.*

Hence, with the availability of analogous measurement methods, the presence of evolutionary-conserved and mutually interconnected functional networks, the mouse is a

promising translational model to understand the neural basis of brain structures and functions in health and disease. The availability of genetically modified (transgenic) mouse animal models of human diseases, such as *fmr1*^{-/-} knockout mice, associated with the Fragile X Syndrome (FXS) (Kazdoba et al., 2014), or mice lacking CNTNAP2 gene shown to be implicated in ASD (Penagarikano et al., 2011), also adds to their translational potential. Transgenic animal models allow studying the underlying repercussions of functional loss of genes on brain FC and allow assessing the efficiency of pharmacological compounds in ameliorating molecular and functional phenotypes of the disease (Zerbi et al., 2019b). A brief overview of rodent rsfMRI in shaping our understudying of the brain has recently been reviewed (as a part of an invited review paper) and can be found in chapter 2, section 2.2.

1.3. Chemogenetic brain neuromodulation

Brain neuromodulation allows insight into the architecture of the cellular organization that enables neuronal function and ultimately complex behavior. The first attempts to ‘remotely control’ neuronal signaling date back to the 1980s. However, most of the chemicals produced were found to be unstable *in vivo*. Only recently has research overcome this obstacle and enabled the control of neuronal activity *in vivo* (Rogan and Roth, 2011). Namely, the two most widely applied techniques that allow *in vivo* neuromodulation of brain neurons in type- and region-specific ways are optogenetics and chemogenetics, which have been around since 2005 and 2007, respectively (Boyden et al., 2005, Armbruster et al., 2007).

The developments of optogenetics and chemogenetics have revolutionized systems neuroscience by allowing targeted inhibition and excitation of specific neuronal subpopulations in distinct brain regions (Vlasov et al., 2018). For optogenetics, a light-sensitive ion channel is expressed in a targeted neuron and a permanent intracranial implant is used to deliver light pulses, which allow either neuronal depolarization or hyperpolarization of targeted neurons. Optogenetics allow precise temporal resolution at the millisecond timescale, by a regulated delivery of light pulses (Boyden et al., 2005). For chemogenetics, the most widely applied are DREADDs i.e., Designer Receptors Exclusively Activated by Designer Drugs. As DREADDs were chosen to modulate neuronal activity in this PhD thesis, the rest of this section focuses on them.

DREADDs are “engineered” muscarinic G protein coupled receptors, who lost the ability to respond to their native ligand acetylcholine and gained the ability to respond to an inert compound with nanomolar potencies. G protein coupled receptors (GPCRs) represent the largest family of membranous signaling molecules, they recognize an incredible variety of ligands (i.e., hormones, neurotransmitters, lipids, etc.) and play an essential role in modulating cellular transmembrane signaling (Allen and Roth, 2011, Zhu and Roth, 2015). Using directed molecular evolution in yeast, a synthetic process that mimics the process of natural selection to evolve molecules to have desired properties, muscarinic receptors eventually evolved to be insensitive to acetylcholine and activated by nanomolar

concentrations of pharmacologically inert clozapine metabolite - clozapine-N-oxide (CNO) (Rogan and Roth, 2011). These “engineered” receptors, termed as DREADDs, had minimal constitutive (basal) activity *in vitro* and *in vivo*, even when expressed at high levels in neurons (Alexander et al., 2009, Armbruster et al., 2007).

In the neurosciences, since the first description of the technology, two (out of four) DREADDs are most commonly used, and each can precisely control one of the two major GPCR signaling pathways: i) hM3Dq, modified M3 muscarinic receptor which couples to Gq signaling leading to PLC (enzyme phospholipase C) stimulation followed by consequent release of intracellular calcium and neuronal activation (Fig. 1.3, left); ii) hM4Di, modified M4 muscarinic receptor which couples to Gi signaling leading to inhibition of voltage-gated calcium channels, which hyperpolarizes the neuronal membrane (Fig. 1.3, right) (Urban and Roth, 2015, Roth, 2016). The third major GPCR signaling pathway (Gs) can be modulated by another rM3Ds or GsD DREADD evolved from a rat M3 muscarinic receptor (Roth, 2016). Finally, a fourth type of DREADD actively used *in vivo* is a κ -opioid receptor (KORD) activated through binding the ligand Salvinorin B, which results in the inhibition of neuronal activity via Gi signaling (Vardy et al., 2015). The benefit of using KORD is that it can be combined with hM3Dq in the same animal, for bidirectional control of neuronal activity (Vardy et al., 2015).

Spatiotemporal control of DREADD expression can be achieved either with the use of transgenic animals or via local infusions of a viral vector carrying the DREADD transgene. Specifically, generated transgenic mice expressing GsD DREADD under the direct control of the adenosine 2A receptor gene (*Adora2a*) were used to mimic the activation of Gs signaling in *Adora2a*-expressing neurons in a noninvasive manner (Farrell et al., 2013). Giorgi and colleagues also generated a transgenic mouse, who expressed hM3Dq in the serotonin-producing neurons (Giorgi et al., 2017). The advantage of transgenic mouse lines over viral vectors is that in viral vectors only a subset of cells is transfected while, in transgenic animals virtually all cells of interest will express the DREADD. However, the approach of generating transgenic animals is rather tedious and can lead to problems if the DREADD is expressed outside the region of interest (ROI) (Cassataro et al., 2014).

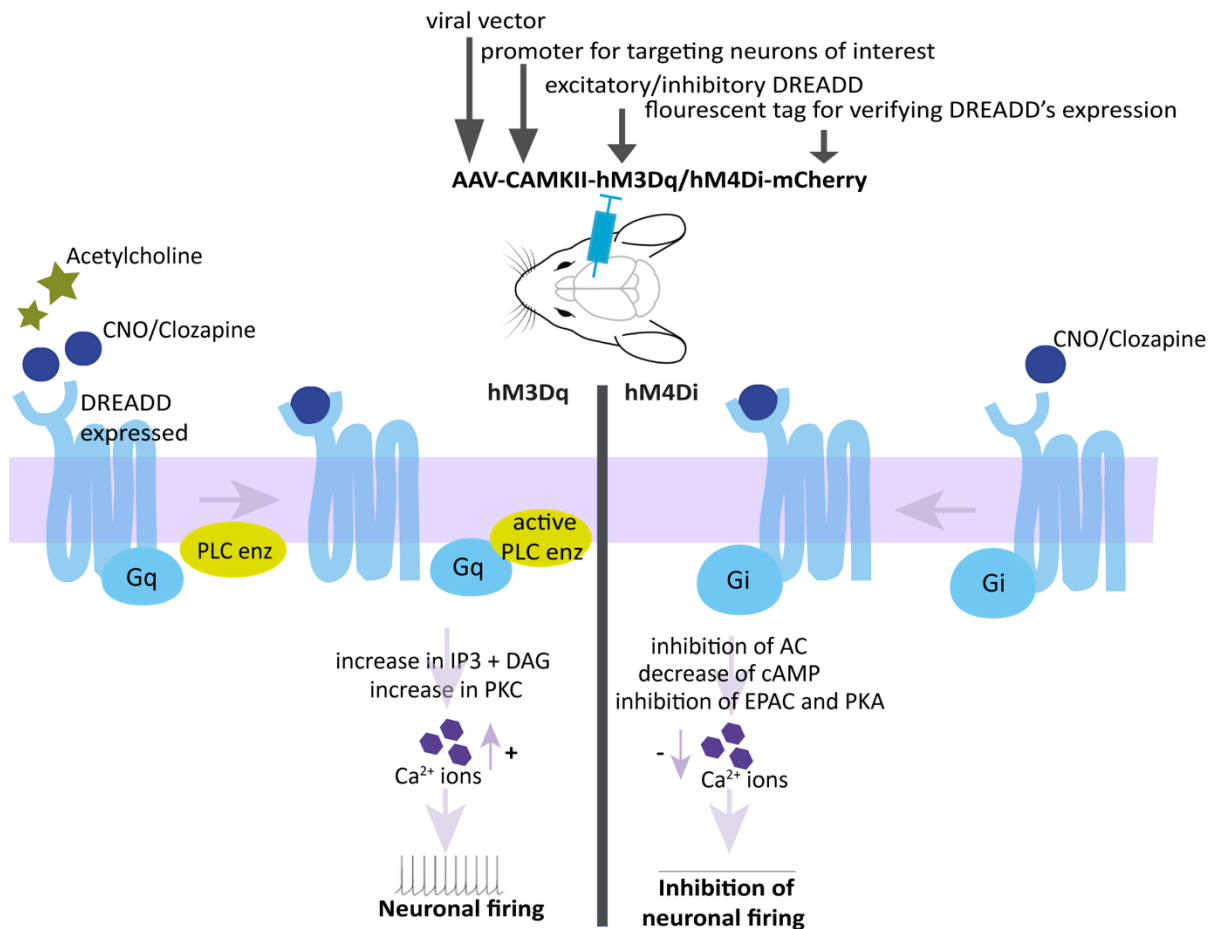


Figure 1.3. Schematic illustration of the steps leading to neuronal activation/inhibition using hM3Dq/hM4Di DREADDs. Top of the image displays a viral construct injected into the ROI followed below by events that trigger activation of hM3Dq (left) and hM4Di (right). Briefly, hM3Dq is activated by binding CNO/clozapine, which causes activation of Gq signaling pathway leading to stimulation of phospholipase C (PLC), which catalyzes the conversion of phosphatidylinositol 4,5-bisphosphate (PIP₂) to 1,2-diacylglycerol (DAG) and inositol 1,4,5-trisphosphate (IP₃). Both DAG and IP₃ possess second messenger functions: the former stimulates various forms of protein kinase C (PKC) whereas the latter binds to its receptors to trigger the release of Ca²⁺ from intracellular stores leading to neuronal firing. HM4Di is activated by binding CNO/clozapine leading to activation of the Gi signaling pathway, which causes inhibition of adenylyl cyclase (AC), resulting in decreased intracellular cAMP levels. Since both EPAC and protein kinase A (PKA) are activated by cAMP, the ligand's action at hM4Dq inhibits EPAC and PKA downstream signaling (Rogan and Roth, 2011, Vlasov et al., 2018, Atasoy and Sternson, 2018).

Infusions of the viral vectors in the ROI are a more common approach and can be achieved either by directly injecting a viral vector into the ROI or by cre-lox recombination system, as most widely applied. Cre-lox system involves a virus initially containing a Cre-dependent 'FLEX' or 'DIO' cassettes with the transgene of interest in a reverse (i.e., inactive) orientation. Using this approach, it is possible to target cells based on their projection patterns, in a circuit-specific way, by injecting a Cre-dependent virus near the somata of the cells of interest and a retrograde Cre vector near the axon terminals. However, a more common method is to use transgenic mouse lines that express Cre in a subset of cells of interest (Cassataro and Sjulson, 2015, Michaelides and Hurd, 2016, Roth, 2016). A commonly used vector is the adeno-associated viral (AAV) vector because of its low toxicity, high transduction efficiency, high

availability, low cost, and existence of various serotypes which differ in their tropism (Zhu and Roth, 2015).

To remotely activate DREADDs, CNO is administered either by an intraperitoneal or intravenous injection or in water/food pellets for longitudinal DREADD activation. It passes the blood-brain barrier, takes minutes to act, and lasts up to 2 hours (Wess et al., 2013). However, recent studies have shown that CNO has low *in vivo* affinity for DREADDs and back metabolizes to clozapine, which then readily passes the blood brain barrier to activate the DREADDs (Gomez et al., 2017, Manvich et al., 2018). Clozapine is an approved drug for schizophrenia in humans with high affinity for a number of serotonin, dopamine, muscarinic and adrenergic receptors (Allen and Roth, 2011). Nonetheless, Gomez and colleagues have demonstrated that clozapine has a high affinity and potency for DREADD receptors showing that doses below 0.1 mg/kg only activate the DREADDs and no other native receptors (Gomez et al., 2017). While this can be regarded as a potential limitation for using the DREADD technology, it also emphasizes the need for appropriate control groups, preferably ones that receive CNO/clozapine but not the DREADDs (Manvich et al., 2018). As of recently, new ligands have been suggested as an alternative to CNO, however their comprehensive reproducible characterisation *in vivo* is still ongoing (Thompson et al., 2018, Goutaudier et al., 2019, Bonaventura et al., 2019).

Overall, DREADD technology has provided neuroscientists with powerful novel tools to map neuronal circuits underlying brain function. DREADDs provide noninvasive, multiplexed, and reversible spatiotemporal control of specific neurons/brain circuits without any specialized equipment. Consequently, they have been extensively used to deconstruct behaviour, such as pain, mood, learning, memory, feeding, addiction and reward-guided behaviours (Wess et al., 2013, Smith et al., 2016, Whissell et al., 2016). Studies have also focused on using DREADDs to dissect the circuitry within animal models of human diseases, such as ASD, schizophrenia and Alzheimer's disease (Whissell et al., 2016). As an example, DREADD specific activation of oxytocin-expressing neurons of the hypothalamus successfully ameliorated impaired social behaviour in an ASD transgenic mouse model lacking CNTNAP2 gene (gene linked with impaired social behavior) (Peñagarikano et al., 2015). As DREADDs have begun to illuminate the underlying neuronal circuitry of numerous behaviours and disorders, there is growing interest in developing chemogenetic systems suitable for therapeutic applications in humans (English and Roth, 2015).

1.4. Chemogenetic neuromodulation combined with resting-state fMRI in mouse

Combining chemogenetic neuromodulation with rsfMRI provides unique benefits (Fig. 1.4) in studying functional brain network dynamics, as it allows the combination of translational aspects of rsfMRI with the versatility of neuromodulation at the cellular level. The benefit of such an approach lies in its potential to mechanistically link macroscale patterns with their underlying neuronal activity, by identifying how neuromodulated cellular activity maps onto

specific alterations of large-scale network activity. Understanding this mechanistic link between scales could benefit human resting-state fMRI studies which focus on finding unique and reproducible biomarkers of psychological and neurodevelopmental diseases.

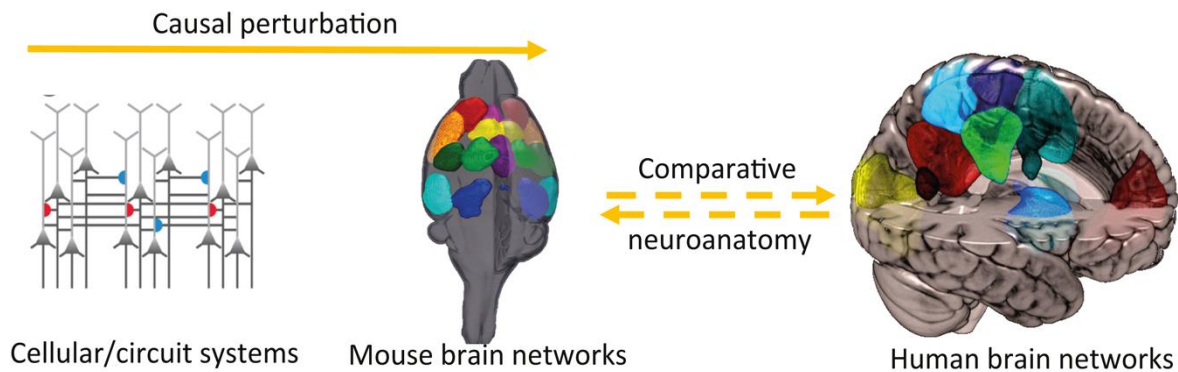


Figure 1.4. Schematic illustration of the potential benefit of causal perturbations. Neuromodulation of mouse cellular or circuit systems leads to causal perturbations of brain networks, thus bridging the micro- and macroscales within the mouse brain. Causal perturbations within mouse brain networks can potentially provide insight into perturbed neuroanatomically comparable human networks.

Resting-state fMRI research provides insights into the intrinsic functional organisation of the human brain and its dysfunctions caused by various disorders. Aberrant brain connectivity has also been characterized in mouse models of human disease, with a goal of establishing causal pathological contributions between specific disease-associated genetic variants and macroscopic connectivity. For example, we and others have demonstrated that genetically modified mouse models of Autism Spectrum Disorder (ASD) display aberrant whole-brain functional connectivity (Chelini et al., 2019, Liska et al., 2018, Pagani et al., 2018, Zerbi et al., 2018). A number of comparative studies across the two species have also been performed. The effects on brain connectivity were assessed in autism-associated single gene disorder (NF1) in children and transgenic mice. Similar alterations in cortical and cortico-striatal functional connectivity were observed across both species (Shofty et al., 2019). Furthermore, another autism-associated gene deletion (16p11.2) led to impaired long-range prefrontal connectivity in both humans and transgenic mouse models (Bertero et al., 2018). Homogeneous whole-brain functional network changes inferred from such comparative studies across the two species yield an understanding of macroscopic changes in brain connectivity. However, a deeper understanding of the origins and the significance of these macroscopic changes are greatly complicated by our limited understanding of the neurobiological foundations of macroscale functional connectivity. As long as the neural basis underlying the functions and dysfunctions of networks remain unclear, it will be difficult to associate macroscopic observations with underlying neurophysiological changes. Bridging this gap requires interventional approaches and controlled experimental conditions only achievable with animal models. Hence, mouse models hold considerable promise in this regard, because of the possibilities to i) measure mouse brain function at the macroscale with a method available to human research, ii) neuromodulate cell or circuit function at the

microscale and iii) establish a causal link between i) and ii). The work presented in this thesis investigates this causal link by probing the effects of controlled cell-specific neuromodulation induced by DREADDs on whole-brain connectivity and dynamics measured by rsfMRI. The ultimate goal of this work is to understand the biological underpinnings of neural network dynamics and potentially provide new insights for advancing neuroimaging as a tool, in the context of future clinical applications.

1.5. Cortical excitation - inhibition (E:I) balance

Glutamatergic pyramidal neurons are the principal type of excitatory cells in cortex and comprise approximately 70 - 90 % of all the neurons in cortex. GABAergic (inhibitory) interneurons are highly diverse but comprise of only about 12% of all neurons in cortex (Feldmeyer et al., 2018) and are divided into three different subtypes, i) fast spiking cells that target the cell bodies of excitatory neurons and coexpress the calcium-binding protein parvalbumin (PV), ii) low-threshold spiking cells that coexpress the peptide somatostatin (SST), and iii) sparse dendrite targeting cells that coexpress vasoactive intestinal peptide (VIP) (Cardin, 2018). GABAergic activity is crucial for entrainment of oscillatory activity across a neuronal population by regulating precise temporal patterns in the local circuit. PV cells are the most abundant type of interneuron and converging evidence suggests that they are important for promoting synchronized firing within pyramidal cell populations (Bartos et al., 2007, Cardin et al., 2009, Sohal and Rubenstein, 2019, Roux and Buzsaki, 2015). Synchronized firing is maintained through multiple cellular mechanisms which bring about temporally coordinated (balanced) activity of excitatory and inhibitory neurons. This balance of excitation and inhibition (E:I) is fundamental for *in vivo* network activity and its stability (Dehghani et al., 2016, He et al., 2018). The importance of balanced E:I was first suggested theoretically (van Vreeswijk and Sompolinsky, 1996) and later confirmed experimentally *in vivo* (Haider et al., 2006).

In 2003 Rubenstein and Merzenich hypothesized that some forms of ASD might be caused by changing circuit's E:I balance (Rubenstein and Merzenich, 2003). Since then, it has been shown that E:I imbalance is implicated in multiple brain disorders, including ASD and Schizophrenia (Selten et al., 2018). Numerous autism mouse models have been used to investigate candidate mechanisms in causing this E:I imbalances (Lee et al., 2017). Couple of those mechanisms suggest that increased E:I ratio can be attributed to depletion of GABAergic interneurons as well as increased intrinsic neuronal excitability (Lee et al., 2017). Since E:I imbalance has a significant role in multiple brain disorders, the first project of this thesis focused on acutely increasing E:I ratio to investigate its effects on macroscopic BOLD fluctuations.

1.6. The basal ganglia

The basal ganglia are a set of deep forebrain nuclei consisting of striatum, the external and internal globus pallidus (GPe/i), the subthalamic nucleus (STN) and the substantia nigra pars compacta and pars reticulata (SNc/r). The striatum is a main input structure of the basal ganglia, and receives glutamatergic inputs from cortical, thalamic and limbic regions combined with dopaminergic input from the midbrain, thus acting as an integrative hub that assists in the selection of optimal behaviors (Reig and Silberberg, 2014, Nelson and Kreitzer, 2014). The classical models of basal ganglia circuitry (Albin et al., 1989) propose that this optimal behavior results from the interplay of two sub circuits, the direct and indirect pathways, which originate from two different subpopulations of GABAergic medium spiny neurons (MSNs): i) dopamine D1 receptor-expressing MSNs that constitute the striatonigral or direct pathway, and ii) dopamine D2 receptor-expressing MSNs that constitute the striatopallidal or indirect pathway. In the context of movement, the direct pathway promotes movements by actively inhibiting two GABAergic output nuclei - GPi and SNr - which in turn project to thalamocortical and brainstem motor circuits. This reduction in inhibitory signals results in disinhibition of these circuits allowing the execution of necessary movements. In contrast, the indirect pathway increases the activity of two output nuclei - GPe and STN - which in turn leads to suppression of thalamocortical circuitry and ultimately inhibition of movements (Calabresi et al., 2014). Basal ganglia research has been guided by this classical model since it has been proposed, although recent work has shown that balanced activity in both MSN projection pathways is crucial for generation of movements (Tecuapetla et al., 2014) and other optimal behaviours (Vicente et al., 2016). This emphasized that the functional organisation of basal ganglia is more complex than classically proposed (Calabresi et al., 2014).

The basal ganglia have been shown to be implicated in multiple functions, including motor learning, planning, execution, decision making and reward (Bonnavion et al., 2019). This made striatum and its direct and indirect pathways one of the most extensively researched brain structures at the micro- and mesoscales. Taking advantage of this vast amount of knowledge available, our second project focused on selectively perturbing MSNs of the direct pathway. We sought to understand their perturbation effects on the BOLD fluctuations of anatomically connected regions of striato-thalamic-cortical network.

1.7. Specific aims of the thesis and chapter overviews

The aim of this PhD thesis was to combine macroscopic measurements of rsfMRI together with microscopic perturbations of DREADDs to establish a causal link between cell-specific perturbations and whole-brain network connectivity. Taking into account the lack of publications on the combined DREADD-rsfMRI approach at the start of my PhD, three major goals were set:

1. To develop and establish optimal protocols for a DREADD-rsfMRI approach.

2. To link perturbations of cortical excitation - inhibition balance (E:I) at the circuit level with alterations of BOLD connectivity.
3. To investigate how perturbation of dopaminergic signalling within the striato-thalamic-cortical network affects spontaneous BOLD fluctuations.

In **Chapter 2** a review paper is presented, currently under review, focusing on emerging methods for measuring spontaneous or evoked activity of a rodent brain and its functional implications at the systems and network level. Methods reviewed are ultrasound, photoacoustic, fluorescence, intrinsic optical imaging, and, relevant for this thesis, functional magnetic resonance imaging (fMRI). This review provides an overview of the unique features of each technique, their use, limitations and potential for future expansion.

Chapter 3 entails a peer-reviewed paper tackling the first two goals of my PhD. Increased E:I ratio is the putative mechanism in neurodevelopmental disorders such as ASD. Thus, we explored the effects of E:I perturbation on brain connectivity and BOLD fluctuations using conventional FC analysis and machine learning. E:I ratio is chemogenetically increased either by i) overexciting excitatory neurons or ii) inhibiting inhibitory Parvalbumin (PV) interneurons within cortical microcircuits. Regardless of the E:I perturbation approach, we identified significant reduction in long-range functional connectivity within anatomically connected areas. Using an advanced machine learning approach, we showed that a classifier can be trained to use only rsfMRI time-series data to correctly identify areas with perturbed E:I ratio due to our DREADD manipulation. We verified this on an independent cohort of *Fmr1*^{-/-} knockout mice, a mouse model for autism with a well-documented loss of PV neurons and chronic alterations in E:I.

The pilot data of this study were used to establish an optimal protocol for DREADD-rsfMRI, including volume of the DREADD virus and DREADD activator, approach to activate the DREADDs (intraperitoneal or intravenous), type (continuous or sequential) and length of the rsfMRI scan, etc.

In **Chapter 4**, we explored the effects of cell-specific perturbations of D1 medium spiny neurons (MSNs) of dorsomedial striatum on BOLD signal dynamics of remote, yet anatomically connected, regions. We used publicly available atlases of the mouse mesoscale structural connectome to objectively map regions that constitute the striato-thalamic-cortical circuit. An advanced machine learning approach was applied to assess changes in the BOLD dynamics within each region of the circuit. Perturbations of D1 MSNs caused altered BOLD dynamics in a number of cortical and thalamic regions, while conventional FC analyses revealed perturbed cortico-striatal connectivity.

In **Chapter 5**, the main findings from chapters 3 & 4 are summarized and some implications raised by the individual studies are discussed, followed by suggestions for future experiments or analyses aimed at tackling open questions of this PhD thesis.

CHAPTER 2

Emerging imaging methods to study whole-brain function in rodent models

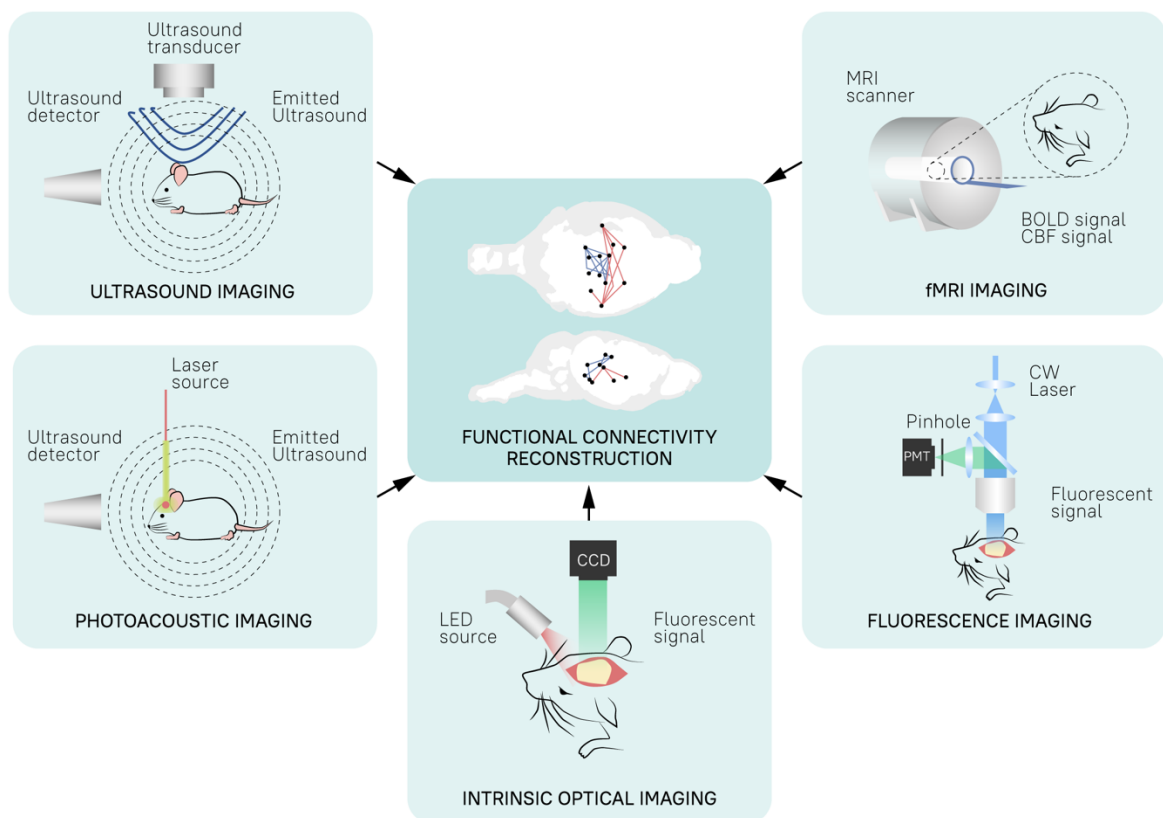
Marija Markicevic, Iurii Savateev, Christina Grimm, Valerio Zerbi

Manuscript under review

First author contributions

Preparatory literature reading and writing of functional MRI section of the article, including Figure 2.1 and first draft of the abstract. Rereading of the manuscript with all co-authors.

Graphical abstract



Graphical abstract by Iurii Savateev

2.1. Abstract

In the past decade, the idea that single populations of neurons support cognition and behavior has gradually given way to the realization that connectivity matters, and that complex behavior results from interactions between remote yet anatomically connected

areas that form specialized networks. In parallel, innovation in brain imaging techniques has led to the availability of a broad set of imaging tools to characterize the functional organization of complex networks. However, each of these tools poses significant technical challenges and faces limitations, which require careful consideration of their underlying anatomical, physiological and physical specificity. In this review, we focus on emerging methods for measuring spontaneous or evoked activity in the brain. We discuss methods that can measure large-scale brain activity (directly or indirectly) with relatively high temporal resolution, from milliseconds to seconds. We further focus on methods designed for studying the mammalian brain in preclinical models, specifically in mice and rats. This field has seen a great deal of innovation in recent years, facilitated by concomitant innovation in gene editing techniques and the possibility of more invasive recordings. This review aims to give an overview of currently available preclinical imaging methods and an outlook on future developments. This information is suitable for educational purposes and for assisting scientists in choosing the appropriate method for their own research question.

2.2. Introduction

Galaxies of thought, cognition and movement. The observation of natural phenomena is the basis of modern scientific thought, and a common approach to all scientific disciplines, from astronomy to neuroscience. Through observations we can generate, confirm, extend or challenge theories and models of how nature works. And just as telescopes are the means of unlocking the secrets of outer space, our understanding of the brain depends on the methods we use to observe its constituent elements and study how they interact with each other, creating galaxies of thought, cognition and movement. While there is no single technique (yet) capable of observing all these phenomena, there are many technologies at our disposal to study brain activity across multiple temporal and spatial dimensions (Figure 2.1).

The basic substrate used by the brain to transmit information is represented by electrical events called neuronal spikes and the release of chemical neurotransmitters in the synaptic terminals. Decades of (electro)physiological research facilitated by *in-vitro* preparations, neuronal cell cultures or organoids, and *in-vivo* recordings have advanced our understanding of the mechanisms that drive neurons to fire and transmit their signals through the network. While neuronal rhythmicity plays an essential role in facilitating information processing across spatial and temporal hierarchies in the brain (Lakatos et al., 2019), individual neural spikes per se are too weak to influence complex behavior (with notable exceptions) (Houweling and Brecht, 2008). If our cognition really depended on individual spikes, we would deal with a poorly defined, high-dimensional system, not suitable for life. According to this view, correlates between the activity of a single neuron and a specific cognitive process provide a limited description of the causal relationship between brain activity and behavior (Elsayed and Cunningham, 2017). Thus, it seems increasingly likely that the brain does not use actual spike coding but population - or neural ensembles - coding that unfold on a limited, low-dimensional portion of the full neural space (Gao and Ganguli, 2015, Gallego et al., 2018). As

information flows through the brain, population activity is further integrated into large-scale networks via the *connectome* (Sporns et al., 2005). The result is that large numbers of brain regions are active during every aspect of cognition and behavior.

Since one of the more tractable goals of quantitative neuroscience is to develop predictive models that relate brain activity to behavior, observing activity and dynamics in neural networks – possibly in multiple brain areas – can get us closer to this goal. To do that, scientists and engineers have developed an array of methods capable of looking at whole-brain activity from a zoomed-out perspective. In this review, we aim to provide the reader with an overview of the emerging methods for observing system and network-level brain function in rodents. While this article is not designed to provide a full review of the literature, history and physics behind each method, we distil the nature and the unique features of each technique, and comment on their use and potential for future expansion and of course, their limitations. We wrote this article for scientists who want to expand their view on preclinical imaging methods, are looking for the appropriate method to address their research question, and for didactical purposes.

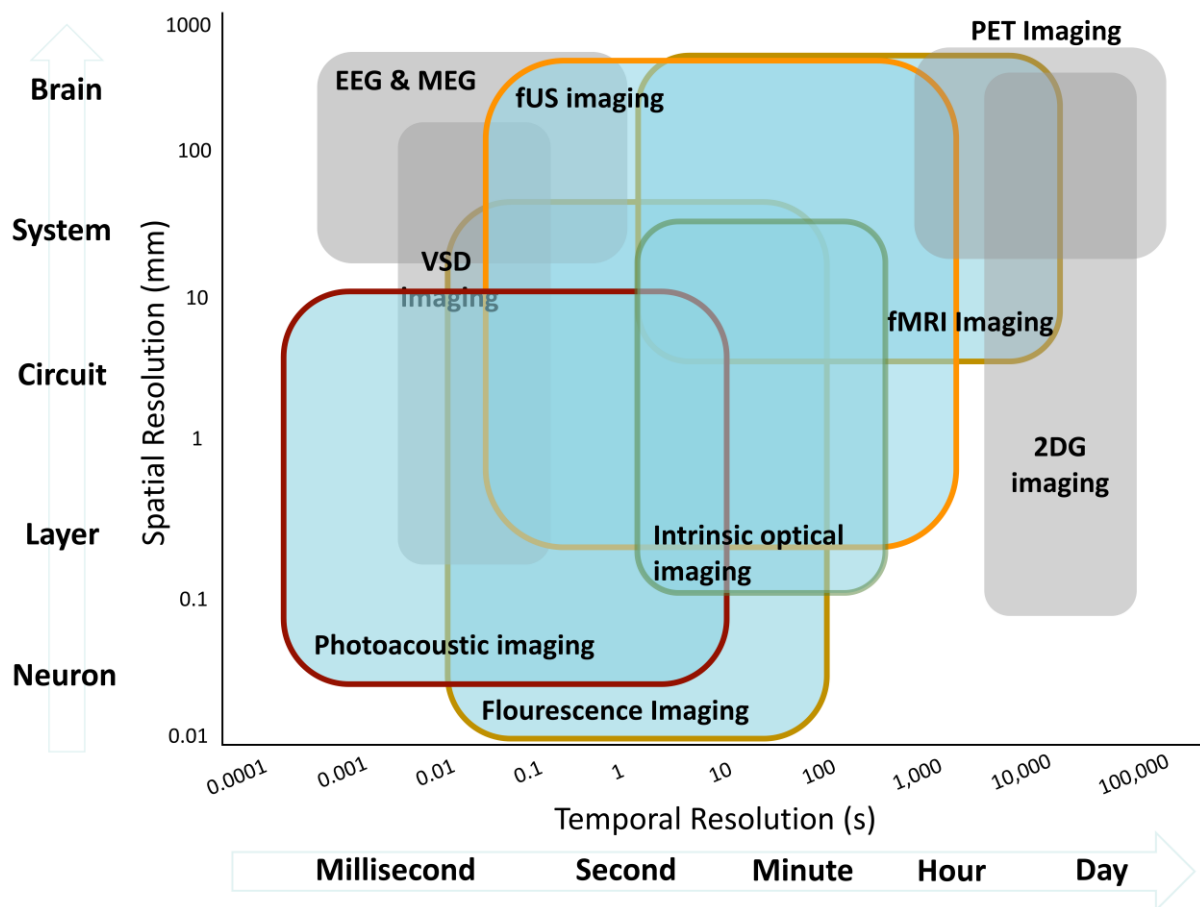


Figure 2.1. The spatiotemporal overview of imaging techniques used for studying rodent whole-brain function. Each colored box represents approximate spatiotemporal scope of the labelled technique. Light blue colored boxes represent techniques covered in this review, while grey boxes techniques not covered. EEG, electroencephalography; MEG, magnetoencephalography; PET, positron emission tomography; 2-DG, 2-

deoxyglucose; fUS, functional ultrasound; fMRI, functional magnetic resonance imaging; VSD, voltage-sensitive dye imaging.

2.3. Functional MRI

Functional Magnetic Resonance Imaging (fMRI) is one of the leading techniques to study whole-brain function in humans. Its first description dates back to the early 1990s, when Ogawa and colleagues (Ogawa et al., 1990b) described the principles of blood oxygen level-dependent (BOLD) magnetic resonance imaging (MRI): local changes in neuronal activity require a dynamic supply of oxygen and glucose, provided by a highly dense vascular system. More specifically, the process of neurovascular coupling, which entails the acute regulation of cerebral blood flow (CBF) via vasoactive molecules and neural messengers, ensures that this change in energetic demand is met (extensively reviewed in (Raichle and Mintun, 2006, Cauli and Hamel, 2010, Buxton et al., 2014, Kleinfeld et al., 2011)). To this day, much research effort is directed to the identification of cellular and molecular messengers that communicate neuronal activity to the vasculature, helping us understand cerebrovascular regulation and more accurately interpret observed fMRI signals (Desjardins et al., 2019, Anenberg et al., 2015, Devor and Boas, 2012, Uhlirva et al., 2016, Devor et al., 2007). Ultimately, regional alterations in CBF influence the ratio of oxygenated vs deoxygenated haemoglobin, whose distinct magnetic properties give rise to the BOLD signal. It is the paramagnetic properties of the deoxyhaemoglobin that cause magnetic susceptibility inside blood vessels and surrounding tissue, thus affecting the magnetic field and the spin-spin relaxation time (T_2 / T_2^*).

MRI sequences that are sensitive to the T_2^* , such as gradient-echo (GRE) echo planar imaging (EPI), are often used for studying the fast dynamics of hemodynamic responses with a spatial resolution of ~ 1 to 3mm and with a temporal resolution of ~ 1 to 3 seconds (Kim and Ogawa, 2012, Gore, 2003). In 1995 Biswal et al. (Biswal et al., 1995) showed that also slow (< 0.1 Hz), spontaneous fluctuations of the BOLD signal measured during rest periods (i.e. without the overt perceptual input or motor output typically present in traditional task-based fMRI studies) could be measured with a GRE-EPI sequence. These fluctuations form spatial patterns of correlated activity (i.e. networks) that unfold along the long-range axonal connections of the brain, revealing its intrinsic functional architecture (Fox and Raichle, 2007). Since then, resting-state fMRI (rsfMRI) has become the method of choice to map regional interactions that occur in a resting or task-negative state across the whole brain in humans (with $\sim 16,000$ rsfMRI papers published in the past two decades; source: Pubmed, Jan 2021). To this day, GRE-EPI sequences with intrinsically high T_2^* sensitivity, high temporal resolution and signal stability, are the most common choice for BOLD fMRI. It should be noted, though, that few technical caveats of the T_2^* contrast remain (Markl and Leupold, 2012). In fact, GRE sequences are more frequently troubled by susceptibility and chemical shift artifacts given their high sensitivity to large vessels, potentially leading to overestimations of activated regions (Markl and Leupold, 2012). However, there are other types of MRI sequences that

can work around these problems. The most common are T2-weighted techniques such as EPI spin-echo (SE) sequences, which filter signals associated with larger veins and enhance contrast from small capillaries that are more likely to be closer to the site of neuronal activity (Boxerman et al., 1995). This advantage comes at the expense of lower BOLD sensitivity and longer acquisition times (Zhao et al., 2004, Keilholz et al., 2006). Given that different techniques of contrast weighting are likely to involve different trade-offs between sensitivity and spatial specificity of the observed fMRI responses, making an informed decision regarding the choice of MRI pulse sequence to best fit one's research question and study design is advisable.

Rodent functional MRI

While the evidence provided by fMRI imaging in humans continues to teach us a lot about brain-behaviour relationships, studying the biological underpinnings which underlie large-scale networks and dynamics requires interventional and controlled experimental conditions only achievable in animal models. The past 10 years have seen a rapid increase in studies applying rsfMRI in rodent models. Early work mapped the spatial extent of resting-state networks in rats (Zhao et al., 2008, Pawela et al., 2008, Zhang et al., 2010, Hutchison et al., 2010) and mice (Jonckers et al., 2011). These findings have led to the realization that the rodent brain is organized in large-scale networks, the properties of which are similar to those reported in humans. This laid the foundation for studying the rodent brain using multiple approaches adapted from the human literature, such as independent component analysis (Sforazzini et al., 2014, Zerbi et al., 2015, Lu et al., 2012, Jonckers et al., 2014), seed-based correlation (Liang et al., 2015, Nasrallah et al., 2014, Zerbi et al., 2015, Paasonen et al., 2018, Grandjean et al., 2020), dynamic functional connectivity analysis (Grandjean et al., 2017a, Sethi et al., 2017, Belloy et al., 2018) and tools from graph theory (Liska et al., 2015, Bertero et al., 2018). Other work focused on the relationship between network function and neuronal axonal connectivity, for example by comparing rsfMRI data with the underlying anatomical connectivity from tracer injection experiments by the Allen Institute (Oh et al., 2014). Thanks to this work, we have learned that high functional connectivity emerges predominantly between monosynaptically connected regions in the cortex, albeit this relation is not always present in subcortical regions like the thalamus (Grandjean et al., 2017b). In another study, Mills and colleagues showed that, in addition to neuro-anatomical wiring, the genetic profiles of individual brain regions strongly contribute to functional connectivity, and that the variance of fMRI signals is best explained by a linear combination of axonal and gene expression data (Mills et al., 2018).

Rodent fMRI has also been used to better elucidate the mechanism of BOLD, for example by combining it with direct measurement of neural and astrocytic activity (Schlegel et al., 2018, Wang et al., 2018a, Tong et al., 2019, Lake et al., 2020, Schulz et al., 2012). Schlegel and colleagues (Schlegel et al., 2018) performed sensory-evoked (hind-paw stimulation) astrocytic and neuron specific calcium recordings with simultaneous BOLD-fMRI, and showed strong correlations between BOLD and calcium signals (both neuronal and astrocytic). Similarly, Tong

and colleagues (Tong et al., 2019) revealed a strong coupling between the neuronal calcium signal and task-based and task-free BOLD responses.

Given that rodent and human fMRI share the same sequences for signal generation and use the same (pre)processing techniques, the technique holds great promise to understand the biological basis of human pathologies and link those with clinical outcomes in patients. Genetically modified (transgenic) animal models provide a crucial advantage in this undertaking. An extensive list of transgenic models has been investigated using rsfMRI to study numerous neuropsychological conditions, including Alzheimer's disease (Zerbi et al., 2014b, Grandjean et al., 2014b, Grandjean et al., 2016), schizophrenia (Errico et al., 2015b), pain (Buehlmann et al., 2018) and autism (Sforzini et al., 2016, Liska et al., 2018, Zerbi et al., 2018) (Zerbi et al., 2019b). For example, a recent study mapped the connectivity changes in subjects with autism-associated 16p11.2 deletion and in the mouse model with the same genetic mutation. Both groups displayed diminished functional connectivity in allegedly homologous brain networks (Bertero et al., 2018). In this context, fMRI represents a valuable tool for addressing the growing need to formally identify common brain circuits between rodents and humans to determine the scope and limits of rodent translational models (Stafford et al., 2014) (Balsters et al., 2020). One caveat is that rodent fMRI is usually carried out in the anesthetized state to minimise head-motion during scanning, and only a handful of labs are acquiring fMRI data in awake animals (Stenroos et al., 2018, Desjardins et al., 2019, Liu et al., 2020b). The choice of anaesthetic introduces confounds in fMRI measurements and is certainly a limitation for translating findings to humans (Grandjean et al., 2020, Paasonen et al., 2018).

New Avenues

New acquisition sequences to assess brain function with MRI are emerging at an ever-increasing rate. A family of MRI methods assess brain activity in rodents (other than BOLD) by measuring cerebral blood volume (CBV) and CBF, usually referred to as *perfusion MRI*. CBV and / or CBF are often measured by injecting a paramagnetic contrast agent (CA) into the bloodstream (Kim et al., 2013). The CA's passage causes transient magnetic field inhomogeneities and introduces phase distortion of the water proton spins resulting in changes in T1, T2 or T2* relaxation times, which can be captured with different MRI sequences. Commonly used CAs are paramagnetic gadolinium chelates, which increase T1, and superparamagnetic iron oxide nanoparticles, which decrease T2/T2* (for a thorough review of techniques of perfusion MRI and comparison of CA see (Kim et al., 2013, Barbier et al., 2001, Wirestam, 2012)). CBV-weighted fMRI in small animals has some advantages over BOLD measurements, including higher signal-to-noise ratio (SNR) and reduced susceptibility artefact. Furthermore, CBV represents a direct and easily interpretable component of the neurovascular cascade compared to the BOLD signal (Kim et al., 2013). CBV-fMRI in combination with chemogenetic or optogenetic neuromodulation has been used to study the influence of serotonergic transmission on brain function. Giorgi and colleagues (Giorgi et al., 2017) measured the effects of pharmacological and chemogenetic serotonin modulation on

whole-brain CBV. Their results indicate that serotonin modulation change the CBV in multiple primary target regions of serotonin encompassing corticohippocampal and ventrostriatal areas. A similar study from Grandjean and colleagues (Grandjean et al., 2019) showed that optogenetic activation of the dorsal raphe nucleus resulted in a CBV decrease in primary target regions of serotonin. Additionally, inducing acute stress by forced immobilization prior to the MRI also decreased the CBV in the same dorsal raphe's primary target regions.

Other MRI sequences have been developed to achieve faster recordings, artifact-free images or increase the specificity of MRI responses in relation to the underlying neural signals. Compared to conventional fMRI sequences, ultrafast fMRI sequences aim to shorten the repetition time (TR), which is the time from the application of a radiofrequency excitation pulse to the application of the next pulse. This can be achieved in a number of ways. One approach is to use simultaneous multi-slice imaging. Recently, Lee and colleagues (Lee et al., 2019) developed a sequence for rodent fMRI that can encode multiple slices simultaneously by using slice-select gradient blips. Blips impose different amounts of linear phase for different slices; thanks to an extended field of view (FOV), each slice is shifted towards a different and non-overlapping portion of the FOV, thus speeding up the acquisition by a factor of 4, while keeping a similar signal-to-noise ratio to conventional EPI sequences.

Being able to use high spatio-temporal resolution is also critical to discern the direction of information flow using the onset times of fMRI responses. For example, Jung and colleagues (Jung et al., 2021) applied a GRE-EPI sequence at ultra-high magnetic field (15.2 T) with a temporal resolution of 250ms and spatial resolution of $156 \times 156 \times 500 \mu\text{m}^3$ during either electrical paw stimulation or optogenetics stimulation of the motor cortex. Their results showed that the order of onset times varies between regions and active layers and coincides with their known sequence of neural activation. This work provided further evidence that ultra-high resolution BOLD MRI can be useful to identify bottom-up and top-down processes between cortico-cortical and cortico-thalamic regions and to assess the direction of information flow.

Images generated by conventional fMRI sequences in rodents suffer from a high sensitivity to magnetic susceptibility artifacts due to the high field of scanners and the relatively long echo time required to generate the BOLD contrast. To solve this problem, MacKinnon and colleagues combined a zero-time echo (ZTE) pulse sequence with iron oxide nanoparticles to acquire CBV. The ZTE sequence is characterized by a very short echo time, which means that signal acquisition occurs immediately after the radio frequency pulse, preventing signal decay. At the same time, iron oxide nanoparticles shorten the T1 relaxation time, resulting in the detection of CBV-weighted functional activations in the brain even with a low echo time. This allows for a three-fold increase in the magnitude of the signal-to-noise ratio, along with a reduction in susceptibility artifacts and acoustic noise (MacKinnon, 2020).

New MRI sequences have also been developed to measure brain activity differently from the hemodynamic response. One example is given by diffusion functional imaging (dfMRI). In dfMRI, a spin-echo echo planar (SE-EPI) sequence is combined with an isotropic diffusion encoding (IDE) gradient, to impart isotropic diffusion-weighting contrast in the acquired

signal. This makes dfMRI sensitive to rapid changes in three-dimensional tissue boundaries induced by neuronal activation (Le Bihan et al., 2006, Abe et al., 2017a). Evidence from intrinsic optical signals (IOS) studies suggests a strong coupling between neural activity and microscopic (sub)cellular morphological changes (Andrew et al., 1999). Therefore, dfMRI was developed to detect changes in water diffusion properties related to "cell swelling" and coupled to neuronal activity rather than hemodynamic responses (Le Bihan et al., 2006, Abe et al., 2017b). Nunes et al., (Nunes et al., 2021) were the first to investigate in greater depth the mechanism underlying neuromorphological coupling by developing an ultrafast line-scanning dfMRI SE-EPI sequence with a time resolution of 100 ms, which enabled the detection of rapid diffusion dynamics. Upon forepaw stimulation, they detected in the rat somatosensory cortex that the dfMRI signal contains two different components: a fast-onset component that is insensitive to vascular change, followed by a slower component sensitive to vascular change. Independent IOS of optogenetically stimulated brain slices confirmed the close similarity between fast IOS and the fast-onset dfMRI component, thus suggesting further evidence of neuromorphological coupling. Moreover, in human studies, dfMRI showed higher spatial accuracy at activation mapping compared to classic functional MRI approaches (Aso et al., 2013) (De Luca et al., 2019). Nunes and colleagues applied dfMRI in rodent fMRI, and tested the specificity of dfMRI by mapping whole-brain responses upon hind-paw stimulation with voxel resolution (Nunes et al., 2019). Their results indicated that the dfMRI signal exhibits layer specificity and is spatially overlapping with the underlying neural activity within the thalamocortical pathway.

Another family of methods that has recently been developed to evaluate neural activity is called molecular fMRI. Molecular fMRI monitors brain activity through the use of chemical or genetically-encoded probes i.e., MRI molecular imaging agents, which are designed to bind to specific molecular and cellular targets in the brain, analogous to fluorescent dyes for optical imaging (Jasanoff, 2007, Bartelle et al., 2016, Ghosh et al., 2018). These MRI molecular imaging agents work by interacting with water molecules to alter T1 and T2 relaxation times, or in some cases by incorporating nuclei that can be probed using radio frequencies distinct from those used to measure water protons (Bartelle et al., 2016, Hsieh and Jasanoff, 2012). Thus, molecular fMRI readout reflects distinct molecular hallmark of neural activity, rather than hemodynamic coupling that underlies BOLD fMRI. The first molecular fMRI study to combine molecular specificity and spatial coverage using a neurotransmitter sensor detectable by MRI assessed dopamine signalling. They injected MRI contrast agent sensitive to dopamine into the rat nucleus accumbens (NAc) and measured changes in dopamine concentration in NAc and caudate putamen (CPu) upon electrical stimulation of the medial forebrain bundle in lateral hypothalamus (Lee et al., 2014). Recently, this approach was combined with BOLD fMRI (Li and Jasanoff, 2020), where simultaneous functional BOLD and molecular imaging responses were recorded throughout the rat brain using multi-gradient echo MRI pulse sequence, during electrical stimulation of hypothalamus. Results indicated that phasic dopamine release in the NAc and medial CPu alters the duration, but not the magnitude, of the stimulus responses across the striatum via postsynaptic effects that vary

across subregions, and that dopamine causally modulates BOLD fMRI responses in the distal cortical regions.

Another method that allows quantitative and noninvasive assessment of cerebral metabolism during brain activity is functional magnetic resonance spectroscopy (fMRS). The goal of fMRS is to obtain precise quantitative *in vivo* measurements of various metabolic concentration changes during brain activity. While broadly used in human brain studies, its application in rodents is still limited mainly due to low signal-to-noise ratio, low (~4sec) temporal resolution and anaesthesia confounds (Just, 2021, Rhodes, 2017). A recent review gives a detailed overview of the methodological aspects and translational prospects of fMRS in rodents (Just, 2021).

2.4. Ultrasound imaging

Ultrasound imaging is a widely used diagnostic technique in medicine that is based on the principle of the emission of ultrasonic waves (from 20KHz to about 15MHz) and the transmission of echoes. Using the speed of sound and the time of each echo's return, an ultrasound system calculates the distance from the transducer to the tissue boundary and then uses this information to generate images of tissues and organs (Mace et al., 2013). Ultrasound systems can also be tuned to assess blood flow using the Doppler effect. The principle of Doppler ultrasound consists of detecting the movement of red blood cells by repeating pulsed emissions and studying the temporal variations of subsequent backscattered signals (Evans and McDicken, 2000). In clinics, Doppler ultrasound is the most commonly used technique to study blood circulation in the heart, arteries, limbs, kidney, and liver. However, for the brain, the application of transcranial Doppler (TCD) ultrasound is limited due to strong attenuation of the ultrasound beam by the skull, and its only clinical use is to diagnose cerebrovascular pathologies in newborns through the fontanel (for a review of TCD applications see (LaRovere, 2015)).

Functional ultrasound imaging in rodents

Until recently, little work has been done in preclinical rodent neuroscience using TCD. While partial skull removal could resolve scattering problems, conventional ultrasound still suffers from low sensitivity, which limits its application to image blood volume or flow in major cerebral arteries. However, the development of new concepts and technologies, such as ultrafast ultrasound and the use of plane-wave illumination as opposed to focused beam scanning, have enabled the use of ultrasound in basic neuroscience research (Deffieux et al., 2018). Thanks to new scanners capable of acquiring images at a very high frame rate (~20 kHz), ultra-fast ultrasound can boost the power Doppler signal-to-noise ratio over 50-fold, without the need of contrast agents (Mace et al., 2013). This increased sensitivity allows mapping of blood flow changes in small arterioles (up to 1 mm/s) that are related to small and transient changes in neuronal activity, laying the foundation for functional ultrasound (fUS) imaging (for a review on the techniques and physics of this technology see (Mace et al., 2013) and (Deffieux et al., 2018)).

The first application of fUS imaging in translational neuroscience appeared in 2011, when Macé and colleagues showed the activation of the barrel cortex following whisker stimulation in anesthetized rats with high spatiotemporal detail (Macé et al., 2011). Furthermore, the authors measured the spatiotemporal dynamics of epileptiform seizures, showing cortical spreading depression propagating throughout the entire brain. Since then, more groups have started to use fUS as a tool to record whole-brain activity in many behavioral and cognitive tasks, such as forepaw electrical stimulation in rats (Urban et al., 2014), or at rest (Rideau et al., 2016, Osmanski et al., 2014). In most cases, large cranial windows or skull thinning procedures were used for stable chronic imaging of deep brain structures. However, in 2017 Tiran and colleagues showed that the whole brain vasculature could be imaged through the skull and skin in awake and freely moving mice, whereas young rats can be imaged up to 35 days of age without prominent reductions in image quality (Tiran et al., 2017). A year later, Macé et al used fUS to map the brain areas activated during optokinetic reflex in awake mice and functionally dissect the regions whose activity depended on the reflex's motor output (Macé et al., 2018). To date, new strategies can further increase the resolution of acquired images while maintaining rapid acquisition, for example using microbubble contrast agents and time tracking of microbubble positions (Errico et al., 2015a).

In general, brain imaging in awake and behaving animals confers an advantage to fUS over fMRI. Furthermore, fUS combines whole brain reading with relatively high spatial resolution (100 x 100 x 300 μm) but with higher temporal resolution and low operating and maintenance costs. Although the skull remains an obstacle in fUS imaging for ultrasound wave propagation, the use of contrast agents (Errico et al., 2016) or a surgical procedure to produce a craniotomy or thinned skull window can solve this problem. Thanks to recent developments in injectable ultrasound contrast media or ultrafast high SNR sequences, an expansion of preclinical fUS applications in neuroscience is expected in the near future.

2.5. Fluorescence imaging

There are several optical imaging techniques that measure the activity of single neurons or neural groups, based on voltage or calcium dyes or genetically encoded probes. More recently the field has seen strong development of methods that increase the visual field and allow large-scale measurements of neural activity. The basic principle common to these techniques lies in the light emission of specific chemical compounds named fluorophores. The fluorophore absorbs light of a specific wavelength that brings it from a ground state to an excited state. When the fluorophore relaxes back to the ground state, in a process named luminescence, it emits light at a specific wavelength and energy. The light emitted during the luminescence – the fluorescence signal – is then captured by the adjacent optical system. The two key factors defining a fluorescent imaging technique are (i) the type of a fluorophore used (Dana et al., 2019, Chen et al., 2013) and (ii) the design of the optical system . In the following

sections, we will address both factors with respect to *in-vivo* functional brain imaging in rodents.

Fluorophores

Fluorophores can change their fluorescent properties, such as the wavelength or the intensity of the fluorescent signal, when involved in a specific physiological process, e.g., the firing of an action potential. The two most popular families of fluorophores used for *in-vivo* brain imaging are (i) calcium and (ii) voltage indicators. Calcium indicators measure changes in intracellular calcium ion concentration, whereas voltage indicators assess alterations in the membrane potential.

Both calcium and voltage indicators can be further divided into two main groups: organic (e.g. chemical) (Paredes et al., 2008, Grinvald et al., 1986, Bando et al., 2019) and genetically encoded (Oh et al., 2019, Bando et al., 2019). Organic calcium (e.g. fluo-4) or voltage (e.g. ANINNE-6) indicators are synthesized organic molecules that are delivered into a target cell via bulk loading or cell microinjections (Paredes et al., 2008, Russell, 2011, Kuhn and Roome, 2019, Bando et al., 2019). In contrast, genetically encoded calcium (e.g., GCaMPs) or voltage (e.g., ASAPs) indicators are expressed directly by the target cell. The incorporation of the indicator genes is achieved by using transgenic animals and/or virus vectors designed to express the genetic material under the control of a tissue specific promoter (Russell, 2011, Oh et al., 2019, Miyawaki et al., 1997, Bando et al., 2019). The cell type specific expression ensured by a tissue specific promoter makes genetically encoded calcium indicators (e.g., GCaMPs) the most popular choice for *in-vivo* brain fluorescent imaging in rodents.

Voltage indicators are sensitive to subthreshold membrane voltage dynamics and have a higher temporal resolution in comparison to the calcium indicators (Piatkevich et al., 2019, Bando et al., 2019). Nevertheless, their use for wide field *in-vivo* brain imaging in rodents is hampered by the intrinsic low SNR (Russell, 2011) and by the technical challenge of achieving a precise localization of the voltage indicators in the cell membrane (Piatkevich et al., 2019, Bando et al., 2019). Therefore, while recognizing recent developments (Piatkevich et al., 2019, Bando et al., 2019) and the potential of multi-area voltage imaging (Piatkevich et al., 2019), we will focus our review on calcium indicators.

Optical designs

There are several optical systems currently available for detecting the fluorescent signal emitted by a fluorophore. Each of these can be used to maximize certain image parameters such as: acquisition speed, spatial resolution, FOV and dimensionality (e.g. 2D slice or 3D image) (Choi et al., 2015). In the next sections, we focus on the most common fluorescence imaging procedures used for *in-vivo* brain imaging in rodents. For each method, we explain the basic principles of the optical design and review work that demonstrates its application in studying brain function with a large FOV.

Wide-field fluorescence imaging

Wide-field fluorescence imaging (WF) refers to a procedure in which a whole specimen (e.g., the targeted brain regions or the entire cortex) is illuminated and the emitted fluorescence is recorded by a joined optical system (Figure 2.2/Box 2.1). In WF, it is essential to guarantee the passage of light with minimal dispersion and absorption; for this reason, WF is often combined with a procedure to replace the skull with a glass cranial window (Rossi et al., 2017, Kim et al., 2016). For example, Kim and colleagues measured GCaMP fluorescent signals with single neuron resolution throughout the entire dorsal cortex in awake, head-fixed mice (Kim et al., 2016). However, WF can also be conducted through the skull by removing only the scalp. This severely limits the precision and resolution of the images but also minimizes invasiveness. Using WF imaging of GCaMP through the intact skull, Peters and colleagues functionally mapped activity across the entire dorsal cortex in awake head-fixed mice, with a spatial resolution of 20 μm (Peters et al., 2021).

Animal experiments with head restraints impose a fundamental technical limit on the behavior that can be studied. To overcome this limitation, WF micro-endoscopes and optical fibers have been designed to visualize cortical and subcortical activity in awake and freely moving animals (Malvaut et al., 2020, Hamel et al., 2015, Gonzalez et al., 2019, de Groot et al., 2020, Ziv and Ghosh, 2015). De Groot and colleagues (de Groot et al., 2020) integrated two micro-endoscopes for simultaneous recording from distant brain regions, an inertial measurement unit for movement monitoring and an LED driver for optogenetic stimulation in a single device named the “NINscope”. In one of their demonstrations, NINscopes were used to record the fluorescence of GCaMPs from the cortex and cerebellum and study the generation of movement upon cerebellar optogenetic stimulation in freely moving mice.

Despite the great potential of WF for *in vivo* brain imaging, its optical design suffers from a strong susceptibility to background fluorescence caused by the signal coming out of the focal plane. This places some fundamental constraints on WF applications. First, the background fluorescence decreases the SNR, which limits the spatial resolution and does not allow scanning subcellular structures (e.g., synaptic boutons). Second, since the depth of focus is determined by fixed parameters of the optics, there is greater blur in the image when targeting deeper structures due to the background signal from the regions above. This currently limits the depth of WF imaging to the superficial layers of cortex. Finally, the continuous excitation of fluorophores from outside the focal plane can lead to an increase in phototoxicity and the production of reactive oxygen species (ROS), and photobleaching, which results in the inactivation of the fluorophore.

Confocal fluorescence imaging

Confocal microscopes use the same optical scheme as WF but with two additional features in order to increase the SNR. First, confocal microscopes utilize a tiny diaphragm, named a “pinhole”, to remove the signal coming out of the focal plane. Second, confocal microscopes

use lasers as a light source instead of LEDs or arc-lamps. This increases the focus of the illumination beam on the targeted region, while minimizing out of focus illumination. To achieve a large FOV, a complete 2D or 3D image of a sample is usually acquired by moving the illumination spot across the sample (Russell, 2011, Webb et al., 1987, Choi et al., 2015). Confocal fluorescence imaging was used by Yoshida and colleagues (Yoshida et al., 2018) to measure GCaMP6 fluorescence from individual axonal boutons in behaving head-restrained mice. By using a multispot confocal design, they could image for the first time a relatively large FOV of 1mm². This allowed the study of long-range projecting axons from the thalamus to the primary motor cortex (M1) in layer 1. In order to circumvent the need for a head-fixation constraint, Dussaux and colleagues developed a fibrescope adaptation of the confocal design, which allows a FOV of 230µm with single cell spatial resolution. This design was used to study changes in the velocity of red blood cells in cortical micro vessels in freely behaving mice compared to anaesthetized animals (Dussaux et al., 2018). Nevertheless, in the confocal design the photons out of the focal plane still contribute to phototoxicity and photobleaching (Yang and Yuste, 2017). Another drawback is related to tissue scattering, which limits the depth of focus to a maximum of 100-200µm (Dussaux et al., 2018, Yoshida et al., 2018).

Multiphoton fluorescence imaging

Multiphoton microscopes use two or three photons to provide the energy needed to excite a fluorophore. The use of multiple photons means that the individual energy of each photon will be lower than that of a single excitation photon. Therefore, the corresponding wavelengths are shifted in the red / infrared part of the light spectrum, which is less scattered by brain tissues than other wavelengths. This gives multiphoton fluorescence imaging a greater depth of penetration than one-photon modes (e.g., WF, confocal). Also, due to the greater focus of the laser beam, the fluorophores outside the focal plane do not absorb two photons (or three by three photons) simultaneously and are not excited. Therefore, the use of multiple photons ensures that the fluorophores are activated only in the focal plane, thus reducing background fluorescence and phototoxicity (Denk et al., 1990, Yang and Yuste, 2017).

Sofroniew et al. (Sofroniew et al., 2016) used the two-photon design to simultaneously record GCaMPs signals from a circular FOV with 5mm radius, reaching depths of up to 1mm. This was used to simultaneously monitor the activity from somatosensory, parietal and motor cortical areas in head-fixed, behaving mice. At the same time, the high spatial resolution permitted the visualization of calcium signals from individual spines. In order to further increase the FOV, Yang et al. (Yang et al., 2019) introduced the “MATRIEX” design for multiarea two-photon imaging. MATRIEX uses multiple water-immersed miniature objectives, each having its own focal plane. Importantly, the images from these objectives can be simultaneously observed through one low-magnification dry objective. The use of several miniature objectives permitted not only simultaneous imaging from distant brain areas, but also the ability to adjust the imaging depth of each region independently. This was used to

simultaneously record GCaMP fluorescence from multiple brain regions distributed across an area up to 12mm² and located at different depths: primary visual cortex (V1), primary motor cortex (M1) and CA1 region of hippocampus. Wagner and colleagues used two independent two-photon systems to image calcium activity from L5 of premotor cortex and cerebellum granule cells (GrCs) with single cell spatial resolution (Wagner et al., 2019). The experiment was conducted on awake head-restrained mice and allowed the researchers to examine the activity patterns in L5 and GrCs during a motor learning task. In order to use multiphoton imaging in freely moving animals, miniature versions of two-photon microscopes were recently developed (Helmchen et al., 2013, Helmchen et al., 2001, Zong et al., 2017). Zong et al. (Zong et al., 2017) used mini two-photon microscopes for calcium imaging in V1 in freely moving mice while keeping the spatial resolution at the level of individual spines, which is comparable to the conventional design. More recently, Klioutchnikov et al. adopted a three-photon design for a head-mounted version and performed cortical imaging to a depth of 1.1 mm in freely moving rats with a spatial resolution of a few micrometers, enabling imaging of calcium signals from single soma and dendrites (Klioutchnikov et al., 2020).

Despite these technical advances, both conventional multiphoton and confocal methods are point-scanning techniques. Therefore, they have a speed acquisition limit which is set by the fluorescence lifetime of the fluorophore and the pulse of the laser. In other words, one can proceed with the next scanning point of the specimen only after the signal from the previous point is fully acquired. This limitation could be overcome by performing multiple scans in parallel, therefore, performing multispot multiphoton imaging (see Figure 2.2/Box 2.1 for details) (Katona et al., 2012, Cheng et al., 2012). However, the parallel scanning of multiple spots requires spreading the laser beam to excite multiple spots in parallel, which reduces the excitation intensity at each individual spot, potentially compromising the fluorophore excitation. This constraint cannot be simply overcome by increasing the laser power due to excessive heating of the tissue. An increase in the excitation intensity in the multispot two-photon design can be achieved by combining two-photon imaging with light sheet microscopy (Hillman et al., 2019, Truong et al., 2011). The light sheet microscopy approach uses a side illumination that increases the chance of a photon being absorbed by the fluorophore in the desired plane (e.g., increased photon yield) while reducing photobleaching and phototoxicity, since it uses less laser power in comparison to confocal and multiphoton approaches. Photon light sheet fluorescent calcium imaging has been used for *in-vivo* functional imaging in awake head-restrained mice. However, it still has limited FOV (340x650µm) and depth (135µm), which restricted the analysis to only the motor cortex (Bouchard et al., 2015). *In-vivo* two-photon light sheet imaging (Hillman et al., 2019, Maioli et al., 2020, Schrödel et al., 2013, Truong et al., 2011) has not yet been applied for wide field imaging in mice or rats. However, taking into account the rapid technical advances in multiphoton imaging, we anticipate that the combination of a two-photon setup and light sheet microscopy will soon be implemented to further increase the FOV of functional fluorescent imaging.

2.6. Intrinsic Optical Imaging

Despite being one of the most widely used methods for *in-vivo* wide field fluorescent brain imaging, the use of artificial fluorophores (e.g., GCaMPs) is inevitably linked with either invasive interventions such as microinjections or with genetically modified organisms (Russell, 2011). This impedes the application of these methods to other experimental animals (e.g., non-human primates) and humans. Intrinsic Optical Imaging (IOI) (Grinvald et al., 1986, Hillman, 2007) relies on the difference in light absorption between oxygenated and deoxygenated hemoglobin and provides a non-invasive alternative to fluorescent imaging. In brief, oxygenated hemoglobin (HbO₂) has lower absorption at 630nm in comparison to deoxygenated hemoglobin (HbR). This decreased absorption leads to higher reflectance, which can be detected by an optical system. The opposite effect occurs at 480nm, where HbO₂ has higher absorption in comparison to HbR. The absorption at 530nm or 590nm is insensitive to the oxygenated state of hemoglobin and is used to assess changes in hemoglobin concentration (HbT) (Ma et al., 2016). State-of-the art IOI use standard charged coupled device (CCD) cameras to collect the reflected light, while the illumination source at a specific wavelength can be achieved with LEDs or filters applied to a white light source (Ma et al., 2016).

The first application of IOI in neuroscience was by Grinvald and colleagues in 1986 (Grinvald et al., 1986). In their work, IOI with light at a wavelength of 665 to 750 nm was used to map the activation of the exposed barrel cortex in anesthetized rats during mechanical stimulation of whiskers. In the same study, IOI was used to map orientational columns in the visual cortex of cats and monkeys, highlighting a potential implementation of IOS in cross-species research. Over the years, IOI has been adapted for imaging in the entire cortex in rodents (White et al., 2011, Kura et al., 2018). White et al. used IOI to study resting state functional connectivity in the dorsal cortex in anesthetized mice with a FOV of 1 cm² across the exposed intact skull (White et al., 2011). Specifically, they used multiple LEDs (478 nm, 588 nm, 610 nm and 625 nm) to simultaneously acquire signals of both HbO₂ and HbR and used these patterns for functional parcellation of the mouse cortex. Kura and colleagues later compared the resting state cortical connectivity maps based on IOS from multiple wavelengths versus those obtained from a single wavelength. The results revealed that connectivity maps based on IOS from HbO₂ and HbR are quantitatively comparable with the maps based on HbT changes (Kura et al., 2018).

However, conventional IOI has some fundamental constraints. Since IOI is based on the hemodynamic response, it lacks cell-type specificity and has limited temporal resolution compared to other optical methods. Furthermore, like all optical imaging methods, it suffers from limitations in spatial resolution due to signal scattering by the skull. In experiments where non-invasiveness is not a necessary parameter, IOI can be combined with other imaging techniques (e.g., calcium imaging), bypassing these limitations. For example, researchers from Hillman's lab measured the IOS and GCaMP fluorescent signal from bilaterally exposed dorsal cortex in awake, head-fixed mice (Ma et al., 2016). The

simultaneous assessment of IOS and fluorescent signals, named Wide Field Optical Mapping (WFOM), allowed an increase in spatial resolution after correcting for the cross-talk between the excitation and emission spectra of GCaMP and the absorption of oxygenated and deoxygenated hemoglobin. Ultimately, it was possible to achieve single-cell resolution, with cell type-specificity ensured by the GCaMP expression.

2.7. Light scattering imaging

In the Fluorescence Imaging section, we have focused on practical approaches that rely on measurements of absorbed light. However, the interaction of light with the sample (i.e., the brain) is not limited to absorption and is also affected by scattering. In the following section we will briefly discuss light scattered imaging. We limit our focus to two areas: (1) light scattering mechanisms and their influence on IOS and (2) Laser Speckle Imaging.

Mechanisms of light scattering and its influence on IOS.

As summarized by Villringer and Chance (Villringer and Chance, 1997), there are two types of light scattering associated with neural activity: *fast* and *slow*. In 1980 Tasaki, Iwasa and Gibbons (Tasaki et al., 1980) described the physiological basis of *fast scattering*. They used a photon sensor located on the surface of a claw nerve to detect motion of the nerve surface upon travelling of an action potential *in-vitro*. As shown later (Villringer and Chance, 1997), this movement of the cell membrane leads to changes in the refractive index of the membrane, which ultimately affect the scattering of light. In the early 1990s MacVicar and Hochman studied the mechanism of *slow scattering* by measuring light transmission in the dendritic area of the CA1 region in slices of rat brain. Synaptic activity has been found to result in increased light transmission. This effect was related to the potential glial swelling triggered by the increased extracellular concentration of K⁺, which occurred during the generation of an action potential. The swelling of the cells causes less light scattering, therefore, increasing light transmission (MacVicar and Hochman, 1991). This could not be explained by changes in HbO₂ absorbance (MacVicar and Hochman, 1991, Andrew and MacVicar, 1994), thus exposing a mainly different factor that affects IOS.

The “fast” and “slow” scatterings were further confirmed by *in-vivo* rodent experiments. Rector and colleagues (Rector et al., 2005) recorded IOS from the barrel cortex of anaesthetized rats. Using a specifically designed fiber optic probe (Rector et al., 1999) that was placed on top of the dura matter, they measured fluctuations in scattered light intensity on a millisecond time scale upon twitching of the whisker. The data from “fast scattered” light was further used to map the individual columns in the barrel cortex. Subsequently, Pan et al. (Pan et al., 2018) were able to simultaneously measure two effects that drive IOS upon spontaneous neuronal activation: (1) the increased absorption driven by increased HbO₂ concentration (2) the reduction of overall neural tissue scattering caused by neural tissue swelling. In Brief, Pan and colleagues used two implantable optodes (i.e. a fibre pair): the light source and the detector, to measure the light transmission through the neural tissue of anaesthetized rats. The pair of fibres was used to measure from either primary somatosensory

area or caudate putamen. Importantly, both effects: absorption by HbO₂ and scattering by swelled tissue, were on the same timescale – seconds, emphasizing the interference between *slow scattering* and IOS. This interference can lead to a potential misinterpretation of the imaging results. One of the possible solutions to circumvent this pitfall is the one suggested by Pan et al. simultaneous measurement of light absorption and scattering. Finally, the underlying physiology of *slow scattering* and *fast scattering* is independent from neurovascular coupling suggesting scattering as a separate imaging contrast (Rector et al., 2005, Pan et al., 2018). Despite the current limitation to a single area of the brain, the potential use of, for example, different pairs of fibers may allow for in vivo "imaging" from multiple brain areas.

Laser Speckle Imaging

In addition to the *static scattering*, in which particle motion is ignored, light scattering is also used for CBF quantification in Laser Speckle Contrast Imaging (LSCI). In short, if coherent light -such as from a laser- is scattered on moving particles -such as red blood cells- the resulting interference patterns, or speckles, will cause a dynamic change in the backscattered light.

In 1981, Ferchner and Briers (Fercher and Briers, 1981) suggested making a short exposure (in the 10 millisecond interval (Dunn et al., 2001)) of the speckle temporal fluctuations, thus converting the unknown distribution of the velocities to the variations of the speckle contrast. These contrast changes were then converted into intensity distributions, which reflect the velocity distribution of the moving particles. This approach established a basis for LSCI's CBF visualization. In the early 2000s Dunn and colleagues (Dunn et al., 2001) were the first to use LSCI to measure CBF in anesthetized rats. The researchers used a CCD camera through the 6x6 mm FOV of the cortex of rats suffering from diffuse cortical depression or cerebral ischemia. The spatio-temporal resolution was 10 μm and 1 ms, respectively. In 2020 Postnov and colleagues (Postnov et al., 2020) monitored CBF after stroke induction in mice with an exposure time of approximately 30μs and a spatial temporal resolution of 10 μm and 10 μs. Importantly, LSCI is currently used for clinical research in several fields of medicine, including neurology (Richards et al., 2017). This increases the translational potential of this technique, which could in the near future lead to a general acceptance of LSCI as the standard for CBF monitoring in neurosurgery.

Microscopy Designs

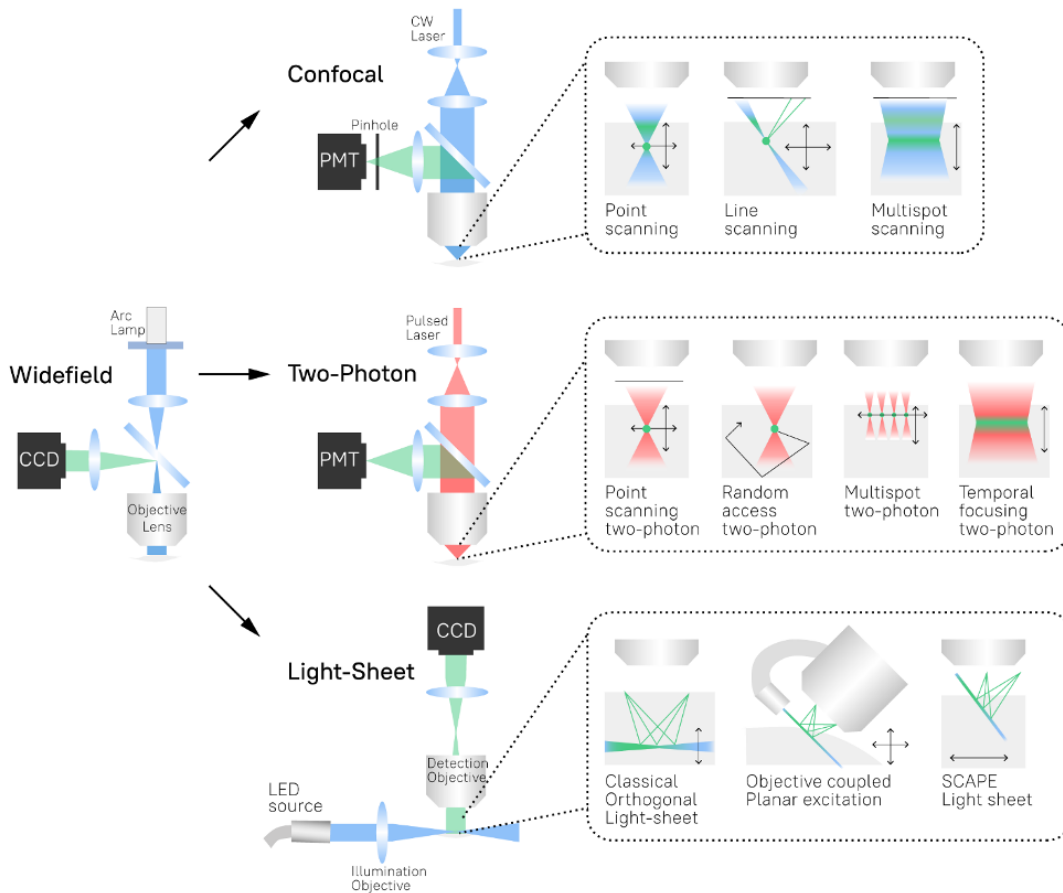


Figure 2.2. Microscopy Designs. The main engineering components and operational modes of Widefield, Confocal, Two-Photon and Light-Sheet microscopes. Abbreviations: Light Emitting Diode -LED, Charge-Coupled Device-CCD. Operational details are outlined in Box 2.1.

Box 2.1. Operational details of Widefield, Confocal, Multiphoton and Light-Sheet microscopes

Widefield microscopes use Arc Lamps or LEDs (not shown) to produce a beam of light at a specific wavelength. In the case of Arc Lamps filters (horizontal blue bulk) are used to select a specific wavelength from a continuous spectrum. The illumination light irradiates the entire specimen through the objective lens causing the excitation of fluorophores. The fluorescent signal emitted during the luminescence process is collected by the same objective lens and reflected by the dichroic mirror (deflected blue bulk) toward the CCD camera. **Confocal microscopes** use the same optical system as a widefield microscope, with a few differences: (i) lasers are used as a light source, (ii) a “pinhole” is used to cut off the light outside of the focal plane and (iii) a Photo-Multiplier Tube (PMT) is used for image acquisition. Continuous Wave Lasers (CW Laser) are typically used in confocal designs ensuring the stable amplitude and wavelength of the illumination light. Depending on the operational mode the illumination is focused on the specific point (point-scanning), line (line-scanning) or multiple points (multispot scanning) inside a specimen. The black arrows feature possible scanning directions. The emitted fluorescent light is passed through the pinhole and ultimately collected by the PMT, which enhances the amplitude of the impingement light. Note that scanning mechanisms (XY) are not shown

in Fig.2.2 and that the confocal pinhole would need to be placed in the descanned pathway. When featured, XY scanner (e.g., galvo mirror scanner) is located on the detection pathway between the objective and dichroic mirror. Z-steppers or Tunable Acoustic Gradient (TAG) lens for z-scanning are also not shown. When depicted, they are located at the back focal aperture of the objective. **Multiphoton microscopes** are represented by the example of the two-photon design. It utilizes the same components as the confocal, but with two principal differences: (i) a pulsed laser is used, (ii) a “pinhole” is not required. Two-photon microscopy is based on the two-photon excitation process: a fluorophore simultaneously absorbs two photons that together bring sufficient energy to cause the fluorophore excitation. Subsequent relaxation of the excited fluorophore back to the ground state is accompanied by the fluorescence emission. For the practical realization of the simultaneous absorption of two photons, a pulsed laser produces a beam of photons with the energy tuned for the two-photon excitation process of the targeted fluorophore: $\frac{1}{2}$ of the excitation energy per photon. Since only the fluorophores at the focal plane can simultaneously absorb two photons, a pinhole is not used. Two-photon microscopes can be used in various scanning modes. Point scanning mode refers to an illumination of a single point per scanning session. Random access is the point scanning mode which is used for a set of predefined locations in the sample. Therefore, the random-access technique does not image the whole specimen, but rather the part sufficient for the analysis. During a multispot session multiple points are illuminated in parallel during the same scanning session. Finally, during the temporal focusing the laser beam impinges on the diffraction grid, producing several beams that are further guided by the optical system to constructively interfere in the focal plane located at the specimen. Thus, the two-photon temporal focusing mode leads to the activation of a single plane. **Light sheet microscopes** typically use an LED (or several) to illuminate the specimen from the side. Such illumination process is called “Oblique Illumination”. Emitted fluorescent signal is captured by the objective lens and further transmitted to the CCD camera. Classical Orthogonal Light-Sheet Microscopy uses two orthogonal objectives: the first is for illumination and the second is for detection. This design requires a highly constrained sample geometry and either physical sample translation for 3D imaging or complex synchronization of illumination and detection planes. Both constraints limit the acquisition speed of Classical Orthogonal Light-Sheet Microscopy. In the Objective Coupled Planar Excitation (OCPE) design the position of the illumination and detection objectives are mechanically coupled. Despite the ensured alignment of the illumination and detection planes, OCPE still requires mechanical movement of the coupled objectives to perform scanning. Finally, SCAPE microscopy acquires images using an angled, swept light sheet in a single objective. SCAPE permits completely translationless three-dimensional imaging of intact samples at rates exceeding 20 volumes per second.

2.8. Photoacoustic imaging

Despite recent methodological breakthroughs, non-invasive *in vivo* optical microscopy still faces inherent optical limitations that restrict it to mostly cortical investigations (Ntziachristos, 2010). To this end, photoacoustic (optoacoustic) imaging (PAI) offers high resolution in tissue depths far beyond current microscopy standards while maintaining rich optical contrast (Wang and Yao, 2016, Zackrisson et al., 2014). In PAI, signal generation relies on the absorption of pulsed laser light at specific optical wavelengths by endogenous chromophores like oxy-/deoxy-hemoglobin or exogenous contrast agents. Tissue heating due

to the process of photon absorption produces broadband acoustic waves at megahertz frequencies (photoacoustic effect) which can be detected at the tissue surface by ultrasound transducers and reconstructed based on the distribution of absorbed optical energy (Wang and Yao, 2016). While PAI's prevailing application is in cancer research (Laufer et al., 2012, Levi et al., 2013), its non-invasive nature and ability to directly monitor biological processes make it an appealing tool for *in vivo* neuroimaging. The following part will review the most recent applications of PAI in wide-field functional imaging in rodents.

Photoacoustic visualization of *in vivo* neural dynamics

Given that PAI combines both optical excitation and acoustic detection, a variety of imaging techniques are available, with photoacoustic microscopy (PAM) and tomography (PAT) being the most promising ones for pre-clinical *in vivo* functional neuroimaging (see (Deán-Ben et al., 2017) for a comprehensive overview of PAI methods).

Photoacoustic microscopy

PAM operates by scanning a tightly focused laser beam point-by-point across the tissue surface and detecting the thermoelastically evoked acoustic waves (Maslov et al., 2008). It provides a comprehensive and quantitative characterization of cerebral hemodynamics with excellent spatial resolution of a few microns (Ovsepian et al., 2017). An early application of PAM verified the 'initial dip' of the BOLD-fMRI hemodynamic response to an electric stimulus as rapid changes in arteriolar oxy-/deoxy-hemoglobin ratios (Liao et al., 2012). PAM systems have since been further developed and used for many applications in neuroscience (Chen et al., 2020b, Ntziachristos, 2010, Liu et al., 2019). Using acoustic-resolution PAM (AR-PAM), Stein et al. (Stein et al., 2009) non-invasively imaged blood-oxygenation dynamics of several cortical vessels in rodents during controlled hypoxia and hyperoxia challenges. Follow-up systems, capable of three-dimensional high-speed imaging, were introduced a few years after to non-invasively map cortical blood-oxygenation at the capillary level (Yao et al., 2015, Hu et al., 2009, Maslov et al., 2008). Modern PAM systems now enable the investigation of spontaneous cerebral hemodynamic fluctuations and their associated functional connections in rodent research (Chen et al., 2020b, Hariri et al., 2016). With contrast enhancing agents like genetically-encoded chromophores and voltage sensitive dyes (VSD), the repertoire of PAI was extended to not only include the detection of hemodynamic processes but also direct detection and quantification of neuronal activity (Giepmans et al., 2006, Chudakov et al., 2010). For example, Shemetov et al. (Shemetov et al., 2020) engineered a genetically encoded calcium indicator with an increase up to 600% in the fluorescence response to calcium. The probe was validated *in vivo* using hybrid photoacoustic and light sheet microscopy, where both neuronal and hemodynamic activity could be captured with high resolution through the intact mouse skull. Despite constant technical advances, though, PAM's high resolution and imaging speed are yet to be applicable to tissue penetration depths beyond 1 mm. In such cases, photoacoustic tomographic systems based on ring-shaped transducer arrays can

provide deep brain volumetric visualization of hemodynamics and stimulus-evoked brain activity (Deán-Ben et al., 2017, Ntziachristos, 2010, Ku and Wang, 2005).

Photoacoustic tomography

PAT uses several wavelength lasers to evoke photoacoustic waves, making it possible to non-invasively and volumetrically measure varying concentrations of endogenous chromophores and exogenous contrast agents in deep brain tissue (Wang and Gao, 2014, Li et al., 2016, Yao et al., 2013). In fact, the first *in vivo* photoacoustic images of small animals were reconstructed based on PAT system scans from a rat's head: Wang et al. (Wang et al., 2003) accurately mapped brain structures with and without lesions, as well as functional cerebral hemodynamic changes in cortical blood vessels around the barrel cortex in response to whisker stimulation. PAT has also been successfully applied to study whole-brain hemodynamics (Yao et al., 2013) and even resting-state functional connectivity in rodents (Nasiriavanaki et al., 2014). In 2016, Tang et al. (Tang et al., 2016a, Tang et al., 2016b) described a similar but wearable cap-like PAT system for awake and behaving rats, with a high in-plane spatial resolution of 200 μ m at depths of up to 11 mm. In a mouse model of epilepsy, an oxy-/deoxy-hemoglobin based photoacoustic computed tomography (PACT) scanning system captured the superficial epileptic wave spreading around the epileptic focus and a corresponding wave propagating in the opposite hemisphere (Zhang et al., 2018). Going beyond superficial cortical measurements, a newly devised system combining PACT and electrophysiological recordings enabled the first non-invasive visualization of real-time thalamo-cortical activity during an epileptic seizure in the whole mouse brain. Furthermore, endogenous contrast based PACT successfully mapped brain-wide activation during electrical fore- and hindpaw stimulation in mice to their somatosensory cortex forelimb and hindlimb areas, respectively (Avanaki et al., 2013). Using contrast enhancement, Gottschalk et al. (Gottschalk et al., 2017) recently measured real-time *in vivo* calcium transients across the mouse brain by devising a functional PA neuro-tomography setup. They reached sufficient sensitivity to directly detect fast neural responses to electrical hindpaw stimulation. Using a near infrared VSD, Kang et al. (Kang et al., 2019) monitored *in vivo* chemically evoked seizures in rats at sub-mm spatial resolution, without the need for invasive craniotomy of skull thinning.

Although still in its infancy, whole-brain functional PAI has rapidly evolved in recent years to meet the standards of the mainstay neuroimaging methods. With its multiscale imaging capabilities comprising rich optical contrast, high spatial resolution and imaging rate, PAI sits at a unique position to directly visualize key parameters of brain function. While PAI does come with its own set of limitations, much like any other neuroimaging technique, it nevertheless shows great potential to bridge the gap between micro- and macroscopic functional neuroimaging.

2.9. Conclusions

Until recently, the inability to measure brain activity in its entirety and simultaneously link it to physiologically relevant processes has limited our understanding of the relationship between neuronal activity and complex cognitive processes. This has changed dramatically with new large-scale functional imaging methods, which allow us to study previously invisible processes both in real time and longitudinally, and to associate these processes with healthy or impaired neural function.

In this review, we have seen how the development of these approaches has allowed for higher spatial resolution, a wider field of view, and greater temporal resolution. However, there are still many limitations of these techniques that prevent a full understanding of local and global brain dynamics and their impact on behavior and cognition. We have outlined some of these gaps in each section of this review to guide current and future investigators.

Besides precise measurement of neural activity, the field of functional imaging also requires integration with computational models capable of using this data in order to make predictions about behavioral functions, which can then be tested experimentally. However, this has not been addressed here to give greater emphasis to the technical / experimental aspect of the methods discussed. The challenge for the future is therefore not only to design and engineer systems capable of detecting brain functions with the highest possible precision and accuracy, but also to integrate and analyze this data within theoretical models to develop a complete picture that can guide our understanding of the human brain. This review aims to attract new researchers to help unravel the mysteries of large-scale neural activity.

CHAPTER 3

Cortical excitation:inhibition imbalance causes abnormal brain network dynamics as observed in neurodevelopmental disorders

Marija Markicevic, Ben D. Fulcher, Christopher Lewis, Fritjof Helmchen, Markus Rudin, Valerio Zerbi* and Nicole Wenderoth*

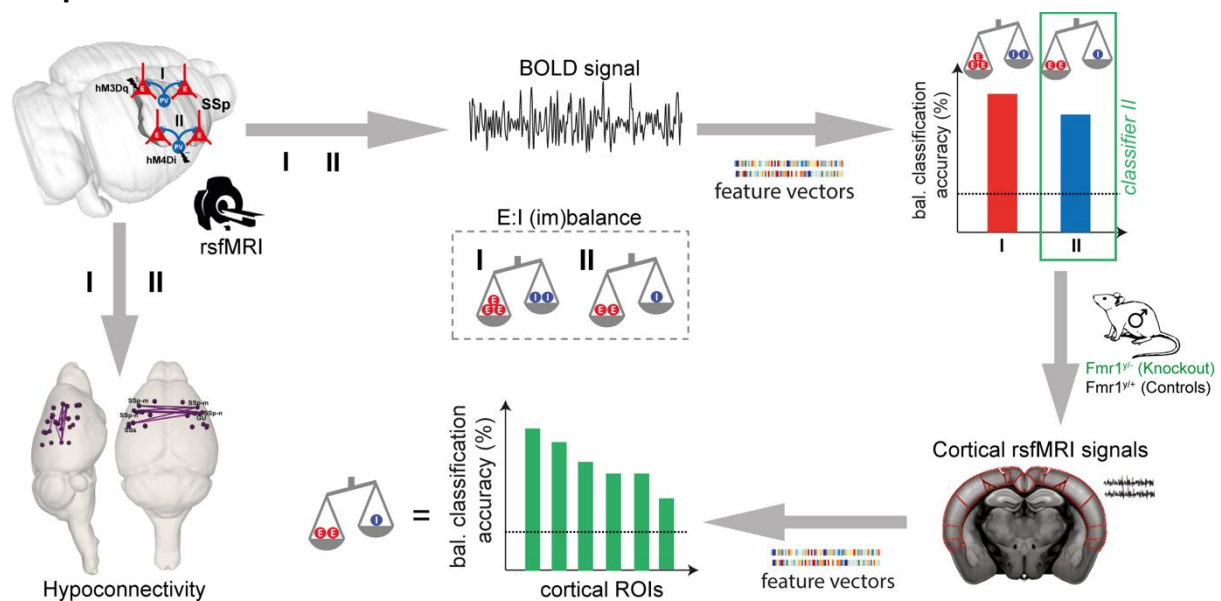
(*shared last authorship)

Manuscript published in *Cerebral Cortex* (2020)

First author contributions

Experimental design, performed viral injections, conducted the fMRI experiments, performed immunohistochemistry, conducted electrophysiology experiments together with C.L., performed the data analysis except the electrophysiology and machine-learning analyses and wrote the manuscript.

Graphical abstract



Graphical abstract not part of the published manuscript

3.1. Abstract

Abnormal brain development manifests itself at different spatial scales. However, whether abnormalities at the cellular level can be diagnosed from network activity measured with functional magnetic resonance imaging (fMRI) is largely unknown, yet of high clinical relevance. Here a putative mechanism reported in neurodevelopmental disorders, i.e.

excitation-to-inhibition ratio (E:I), was chemogenetically increased within cortical microcircuits of the mouse brain and measured via fMRI. Increased E:I caused a significant reduction of long-range connectivity, irrespective of whether excitatory neurons were facilitated or inhibitory Parvalbumin interneurons were suppressed. Training a classifier on fMRI signals, we were able to accurately classify cortical areas exhibiting increased E:I. This classifier was validated in an independent cohort of *Fmr1*^{0/0} knockout mice, a model for autism with well-documented loss of Parvalbumin neurons and chronic alterations of E:I. Our findings demonstrate a promising novel approach towards inferring microcircuit abnormalities from macroscopic fMRI measurements.

3.2. Introduction

Complex behavior results from the interplay of distributed yet anatomically connected neuronal populations which form brain-wide networks. Abnormal brain development as in Autism Spectrum Disorders (ASD) often affects the structural and functional connectivity within these networks at different spatial scales: at the cellular and (micro)circuit levels, neurodevelopmental disorders are associated with dysregulated synaptogenesis, cell excitability, synaptic transmission, and plasticity (Bulow et al., 2019, Penagarikano et al., 2011), as well as aberrant axonal migration and abnormal functioning of cortical (micro)circuits (Contractor et al., 2015); at the network level, long-range functional connectivity and macroscopic neuronal dynamics are altered (Zerbi et al., 2018, Haberl M. G. et al., 2015). Mechanistically linking disease mechanisms across scales is an important goal for neuropsychiatry, particularly, to identify whether certain cellular disease pathways map onto specific alterations of large-scale network activity, which are accessible in human patients and might thus allow to infer the underlying pathobiology of an individual patient. An abnormal increase of the excitation-to-inhibition (E:I) ratio within specific cortical circuits (Rubenstein and Merzenich, 2003) has been hypothesized as a putative disease mechanism underlying ASD pathology and its core behavioral symptoms (Kazdoba et al., 2014, Silverman et al., 2010). In transgenic mouse models of ASD, elevated E:I has been observed either because excitatory transmission is increased (Gibson et al., 2008), or because inhibitory transmission is reduced, for example, due to the loss of fast-spiking parvalbumin (PV) GABAergic interneurons (Penagarikano et al., 2011, Vogt et al., 2017, Wöhr et al., 2015). However, it is unknown whether such an imbalance at the microcircuit level propagates across scales, and whether macroscopic markers of brain activity signal these abnormalities with anatomical specificity.

Here we acutely increase microcircuit E:I within one brain region and test whether this well-controlled manipulation causes an anatomically specific change of neuronal dynamics and macroscopic connectivity of the mouse brain. We used chemogenetics (Michaelides and Hurd, 2016, Rogan and Roth, 2011) to manipulate cell activity of somatosensory cortex (SSp)

while simultaneously imaging brain activity using resting-state functional magnetic resonance imaging (rsfMRI). rsfMRI is a non-invasive method used to measure spontaneous low-frequency fluctuations of the blood oxygen level-dependent (BOLD) signal (an indirect estimate of neuronal activity) in the absence of a task and across the entire brain (Fox and Raichle, 2007). A growing body of evidence suggests that rsfMRI has great potential for translation, as it detects abnormalities in long-range network correlations in human patients as well as homologous networks in mouse models expressing similar transgenic mutations (Strand et al., 2007, Smucny et al., 2014, Shofty et al., 2019). Here, we show that experimentally increasing E:I in primary somatosensory cortex (SSp) by either (i) facilitating excitatory neurons, or (ii) suppressing inhibitory PV interneurons, both caused a *reduction* of long-range functional connectivity between SSp and anatomically connected areas. Increasing E:I changed the dynamics of BOLD fluctuations, an effect that was most pronounced in the targeted SSp. We used the BOLD timeseries measured during experimentally controlled chemogenetic suppression of PV interneurons to train a classifier to detect acutely over-excited brain areas. We applied this classifier to an independent cohort of *Fmr1^{Y/-}* knockout mice, a well-characterized model for ASD (Haberl M. G. et al., 2015, Zerbi et al., 2018) which suffers from PV interneuron depletion and exhibits increased cortical E:I due to the loss of inhibitory inputs (Antoine et al., 2019). Importantly, the classifier identified specific brain regions in somatosensory and prefrontal cortices which exhibited an over-excitation phenotype based on their BOLD dynamics. This new finding indicates that chemogenetically perturbing microcircuit abnormalities in wildtype mice allows us to build “computational sensors” for detecting E:I imbalances from non-invasive macroscopic rsfMRI measurements in a disease model. Our results demonstrate a promising novel approach towards inferring microcircuit abnormalities from macroscopic measurements which potentially opens new opportunities for investigating disease mechanisms across species.

3.3. Materials and Methods

All experiments and procedures were conducted following the Swiss federal Ordinance for animal experimentation and approved by Zurich cantonal Veterinary Office (ZH238/15). C57BL/6J mice were obtained from Charles River Laboratories (Germany), while *Pvalb^{tm1(cre)Arbr}* (PVCre) mice were derived from in-house breeding (first generation obtained from the Jackson Laboratory). All mice were kept in standard housing under 12h light/dark cycle with food and water provided *ad libitum* throughout the whole experiment. A total of 29 male C57BL/6J mice were used in the experiment, aged 9 ± 1 weeks and weighing 25.1 ± 1.8 gr (mean \pm SD) at the day of the surgery. A total of 19 PVCre mice were utilized in this experiment, aged 11 ± 1.6 weeks and weighing 26.1 ± 3.8 gr at the day of the surgery.

Procedures for wildtype (hM3Dq) mice study

Transfection procedures for wt-hSyn-hM3Dq and wt-CAMK-hM3Dq mice

Each mouse was initially anesthetized using a mixture of midazolam (5mg/ml; Sintetica, Switzerland), fentanyl (50mcg/ml; Actavis AG, Switzerland) and medetomidine (1mg/ml; Orion Pharma, Finland). Upon anesthesia induction, mice were placed on a heating pad and the temperature was kept at 35°C (Harvard Apparatus, USA). Following shaving and cleaning, an incision along the midline of scalp was made. The right primary somatosensory cortex was targeted at the coordinates of +0.5 mm AP (anterior-posterior), -3.0 mm ML (medio-lateral) and -2.25 mm DV (dorso-ventral) relative to Bregma using a drill and microinjection robot (Neurostar, Germany) with a 10 ul NanoFil syringe and 34Ga bevelled needle (World Precision Instruments, Germany). 950 nl of ssAAV8-hSyn-hM3Dq-mCherry (n=13) of a physical titer $\geq 5.4 \times 10^{12}$ vg/ml (*vector genomes; fluorometric quantification) was injected at the rate of 0.06 ul/min. The virus was provided by Viral Vector Core Facility of the Neuroscience Centre Zurich (<http://www.vvf.uzh.ch/en.html>). Upon the injection, the needle was left in place for 10 min and then slowly withdrawn. C57BL/6J control mice (n=9) underwent the same surgical procedures, where the needle was kept in place for 5min but without any viral injections. Subsequently, mice were given an anesthesia antidote consisting of tegmestic (0.3mg/ml; Reckitt Benckiser AG, Switzerland), annexate (0.1mg/ml; Swissmedic, Switzerland) and antisedan (0.1mg/ml; Orion Pharma, Finland) and left to fully recover. Following the surgery, ketoprofen (10mg/kg; Richter Pharma AG, Austria) was subcutaneously injected daily for at least 3 days to reduce any post-operative pain. Animals were given 3-4 weeks to fully recover from the surgery and to allow for expression of the transgene prior to the scanning session. Another cohort of 13 C57BL/6J mice was injected with 950nl of ssAAV8-mCAMKII α -hM3D-mCherry of a physical titer $\geq 1.8 \times 10^{12}$ vg/ml following identical procedures as outlined above, Figure S7 illustrates the extension of viral expression at the targeted region.

Electrophysiological recordings

The electrophysiological data used for verification of neuronal activity were acquired in 4 wt-hSyn-hM3Dq animals and 2 wildtype animals that have not received a viral DREADD injection i.e., controls. Briefly, animals were anesthetized with isoflurane to match conditions used in imaging studies (2-4% for induction, 0.5% for data collection), and their body temperature was maintained using a heating pad. A small craniotomy was performed over the right and left somatosensory cortex and the brain was covered with silicone oil. A small trepanation was performed over the cerebellum and a silver wire was placed in contact with the CSF to serve as reference electrode. For hM3Dq validation, one silicon probe (Atlas Neurotechnologies, E16-100-S1-L6NT, 16 sites, 100 μ m spacing, iridium oxide contacts) was implanted in each hemisphere. After implantation, we waited 20-30 minutes in order to allow the recording to stabilize. After stabilization, the broadband voltage was amplified and digitally sampled at a rate of 30 kHz or 48 kHz using one of two commercial extracellular recording systems (Intan or Axona). The raw voltage traces were filtered off-line in order to

separate the multi-unit activity (bandpass filter 0.46-6 kHz) using a second-order Butterworth filter. Subsequently, for each electrode, a threshold was applied to the high-pass filtered data to isolate multi-units and reject background noise (4.5 times the standard deviation across the recording session, specified per electrode). The number of spikes were counted in 10s windows. As an additional control we lowered the detection threshold which did not change the results, unless it was decreased below the background noise. Recording sessions lasted for 45 min. At 15 min following the start of the recordings (baseline) 30 µg/kg clozapine was injected (intravenously). In order to combine data across mice, the activity at sites with clear multi-unit activity was expressed in percent of the baseline value, i.e., each 10 s bin of MUA activity was divided by the average spike rate during the 15 min pre-injection baseline (100%). All multi-units were then combined from the injected or control region.

MRI setup and animal preparation

Two MRI sessions were performed on a 7T Bruker BioSpec scanner equipped with a Pharmascan magnet, with two coil setups optimized for the two different acquisition sequences i.e., Arterial Spin Labeling (ASL) and resting-state fMRI (rsfMRI). First, the ASL was obtained utilizing a receiver-only surface coil, coupled with a volume resonator for radiofrequency (rf) transmission. For rsfMRI measurements, a high signal-to-noise ratio (SNR) receive-only cryogenic coil (Bruker BioSpin AG, Fällanden, Switzerland) was used in combination with a linearly polarized room temperature volume resonator for rf transmission.

Standardized anesthesia protocols and animal monitoring procedures were utilized for both MRI sessions (Zerbi et al., 2018). Briefly, mice were initially anesthetized with 4% isoflurane in 1:4 O₂ to air mixture for 4 min to allow for endotracheal intubation and tail vein cannulation. Mice were positioned on an MRI-compatible support, equipped with hot water-flowing bed to keep the temperature of the animal constant throughout the entire measurement ($36.6 \pm 0.5^{\circ}\text{C}$). The animals were fixed with ear bars and mechanically ventilated via a small animal ventilator (CWE, Ardmore, USA) at the rate of 80 breaths per minute, with 1.8 ml/min flow with isoflurane at 2%. Subsequently, a bolus containing a mixture of medetomidine (0.05 mg/kg) and pancuronium (0.25 mg/kg) was injected via the cannulated vein and isoflurane lowered at 1%. Five minutes following the bolus injection, a continuous infusion of medetomidine (0.1 mg/kg/h) and pancuronium (0.25 mg/kg/h) was started while isoflurane was further reduced to 0.5%. Animal preparation took on average 15.5 ± 2.7 minutes and all animals fully recovered within 10 min after the measurement.

Arterial Spin Labeling (ASL)

Brain perfusion was measured using an established arterial spin labelling (ASL) method using a flow sensitive alternating inversion recovery (FAIR) sequence (Zerbi et al., 2014a) (Leithner et al., 2008). Briefly, a two-segment Spin-Echo was used with following parameters: echo time

TE=12.47 ms, recovery time TR=13000 ms, image matrix=128 x 96, field of view=20 x 20 mm, slice thickness=1 mm, spatial resolution=0.156 x 0.208 x 1 mm/pixel. Inversion parameters: inversion time=40 ms, inversion slab thickness=4 mm, slice margin = 1.5 mm. Sixteen images at different inversion times (50 ms to 3 s) were obtained for T₁ calculations, resulting in a scan time of 15 min (referred to as 'baseline'). After the first baseline acquisition, clozapine was intravenously injected at 10-30 µg/kg and three more sessions were acquired (i.e., Post 1, Post 2 and Post 3, respectively), resulting in a total scan time of one hour. A total of 26 animals (5 controls, 8 wt-hM3Dq and 13 CAMK-hM3Dq mice) were scanned. Due to a subjective placement of a 1mm thick slice over the cortex prior to scan start, there may be slight differences across subjects in slice position relative to the bregma. However, we made sure that every slice of every subject covers virally transfected SSp.

Cerebral blood flow is a local measurement of glucose metabolism and an indirect marker of neural activity at the cell level (Juepter and Weiller, 1995). Taking this into account, blood flow is expected to increase only at site of DREADD injection, where increased firing of neurons requires more glucose leading to an increase in a blood flow. The blood flow increase/change is not expected at any other anatomically connected regions. We chose our regions of interest based on this analogy and they included: (i) Right primary somatosensory cortex (SSp)– as a DREADD injection site (main region of interest); (ii) Left primary somatosensory cortex – as an anatomically connected region; (iii) Left striatum (dorsomedial part) (CP) – a control region without any anatomical projections to the right primary somatosensory area, according to Allen Mouse Connectivity Atlas (Oh et al., 2014).

Resting-state fMRI (rsfMRI)

Acquisition parameters were the following: repetition time TR=1s, echo time TE=15ms, flip angle= 60°, matrix size = 90x50, in-plane resolution = 0.2x0.2 mm², number of slices = 20, slice thickness = 0.4 mm, 3600 volumes for a total scan of 60 min. Clozapine was intravenously injected 15 min after the scan start at the doses of 10 µg/kg or 30 µg/kg. A total of 40 C57BL/6J animals (13 controls and 14 wt-hM3Dq and 13 CAMK-hM3Dq mice) were scanned. These include 8 C57BL/6J animals that were scanned twice (4 controls and 4 wt-hM3Dq mice), once with 10 µg/kg dose of clozapine and another with a 30 µg/kg dose of clozapine (Table S1).

Data preprocessing

Data was preprocessed using an already established pipeline for removal of artefacts from the time-series (Zerbi et al., 2015, Sethi et al., 2017). Briefly, each 4D dataset was normalized in a study-specific EPI template (Advanced Normalization Tools, ANTs v2.1, picsl.upenn.edu/ANTS) and fed into MELODIC (Multivariate Exploratory Linear Optimized Decomposition of Independent Components) to perform within subject special-ICA with a fixed dimensionality estimation (number of components set to 60). The procedure included motion correction and in-plane smoothing with a 0.3 mm kernel. FSL-FIX study-specific

classifier, obtained from an independent dataset of 15 mice, was used to perform a 'conservative' removal of the variance of the artefactual components (Griffanti et al., 2014). Subsequently, the dataset was despiked, band-pass filtered (0.01-0.25 Hz) and finally normalized into AMBMC template ([www.imaging.org.au /AMBMC](http://www.imaging.org.au/AMBMC)) using ANTs. The choice of our band-pass filter is based on the recent literature where it is stated that the frequency distribution of the fMRI signal yields the maximum amplitude at between 0.1Hz and 0.2Hz under medetomidine anesthesia (Grandjean et al., 2014a) (Pan et al., 2013). Each dataset was split into four parts of 900 data points (equivalent of 15 min of scanning). The difference between the baseline (first 15 min of scan) and the rest of the bins are further referred to as $\Delta 1$, $\Delta 2$ and $\Delta 3$.

Seed to seed analysis

The "somatosensory network" in the mouse was defined anatomically using the tracer-based axonal projection pattern of SSp from the Allen Mouse Brain Connectivity atlas (experiment no. 114290938) and contained contralateral primary SSp, right supplementary somatosensory area (SSs), bilateral somatomotor area (MO), bilateral association cortices (TEa), as well as ipsilateral caudoputamen (CP) and thalamus (TH (Parafascicular nucleus)) (Grandjean et al., 2017b). BOLD time series from these regions, apart from thalamus, were extracted using a voxel cube of 3 mm. Thalamus was excluded because previous study from our lab has shown a rather limited FC of cortico-thalamic pathways (Grandjean et al., 2017b) detected by rsfMRI. Correlation Z-scored matrices were calculated using FSLNets (FMRIB Analysis Group).

Regional Homogeneity (ReHo)

Voxel-wise Regional Homogeneity (ReHo) maps were computed using AFNI. ReHo was calculated for a given voxel and its 19 nearest neighbors and smoothed by Gaussian kernel with Full Width of Half Maximum (FWHM) equal to 10.

Voxel-mirrored homotopic connectivity (VMHC)

VMHC measures the similarity between any pair of symmetric inter-hemispheric voxels by computing the Pearson's correlation coefficient between the time series of each voxel and that of its exact symmetrical inter-hemispheric counterpart. VMHC was computed for all the four timeseries bins and normalized to the baseline for each mouse.

Functional connectome analysis

Whole-brain correlation matrices were obtained from a parcellation scheme of 130 regions using the Allen Mouse Brain ontology (Oh et al., 2014). In total, 65 regions of interest (ROIs) per hemisphere were considered, including regions from isocortex, hippocampal formation, cortical subplate, striato-pallidum, thalamus, midbrain and hindbrain. Cohen's d effect size was calculated, using the time series obtained from these whole-brain correlation matrices.

Statistical analysis

Prior to performing statistical tests, within-subject normalization to the baseline was implemented. FSL General Linear Model (GLM) was used to perform statistical comparison between controls and wt-hM3Dq mice for the rsfMRI data (including seed to seed analysis, ReHo, VMHC, connectome analysis). We performed nonparametric permutation testing with 5000 permutations, using family-wise error correction with threshold-free cluster enhancement (TFCE) (ReHo, VMHC) or FDR correction (seed-to-seed, connectome analysis). Statistical significance was defined as $p < 0.05$. CBF differences were statistically tested using linear mixed models implemented in SPSS24 (IBM, USA). In order to account for possible within-subject variances during scan preparation, all the statistical analysis included 6 covariates: (i) mouse age at the time of surgery; (ii) bodyweight at the time of the scan; (iii) total scan preparation time i.e., time between the first anesthesia induction to the start of the resting-state scan; (iv) bolus time i.e., time from the bolus injection to the start of the continuous anesthetic infusion (isoflurane at 0.5%); (v) the number of ICA components rejected using FSL-FIX and (vi) clozapine dose. These covariates were implemented in all the statistical tests for all types of analysis performed.

Procedures for PVCre (hM4Di) mice study

Transfection procedures for PVCre-hSyn-hM4Di mice

The right primary somatosensory cortex of PVCre mice (mice expressing Cre recombinase in parvalbumin-expressing neurons) was unilaterally targeted with 950 nl of ssAAV8-hSyn1-dlox-hM4Di-mCherry(rev)-dlox-WPRE-hGHP(A) ($n = 19$) of a physical titer $\geq 5.4 \times 10^{12}$ vg/ml (*vector genomes; fluorometric quantification) at the rate of 0.06 μ L/min. The same procedures for animal preparation, anesthesia and coordinates were used as already described for wildtype mice.

In vivo electrophysiology

Four PVCre-hSyn-hM4Di mice underwent in vivo electrophysiological recordings following the same procedures as described for wildtype mice. The only difference was in the location of the control probe (Atlas Neurotechnologies, E32-100-S1-L6NT, 32 sites, 100 μ m spacing, iridium oxide contacts), which was implanted into the right (ipsilateral to the DREADD injection site) striatum.

RsfMRI acquisition

Preparation and anesthesia used for the scanning of the PVCre-hSyn-hM4Di mice was identical to the procedures outlined for wildtype mice. The two acquisitions only differed in the length of the scan. The PVCre-hSyn-hM4Di mice were scanned for 45 min where clozapine was intravenously injected at 15 min at the dose of 30 mg/ml.

Classification of univariate BOLD time series

Note that all code for analysis of univariate BOLD dynamics can be found at https://github.com/benfulcher/hctsa_DREADD.

Data processing and feature computation

We analyzed univariate BOLD time series measured from three brain regions: (i) right SSp (injected region); (ii) left SSp (contralateral region); and (iii) visual cortex (control region). Time-series measurements were split into three 15 min durations and labeled according to four classes of experiments: (i) wt-hSyn-hM3Dq (14 mice); (ii) wt-CAMK-hM3Dq (13 mice); (iii) PVCre-hSyn-hM4Di (19 mice) and (iv) sham controls (13 mice). To understand which time-series properties distinguish different experimental conditions, we converted each univariate time series to a vector of 7873 interpretable properties (or features) using v0.9.6 of the *hctsa* toolbox (Fulcher and Jones, 2017, Fulcher et al., 2013). This toolbox contains implementations of time-series features developed across scientific disciplines, including summaries of the distribution of values in the data, its autocorrelation structure, stationarity, entropy and predictability, parameters and goodness of time-series model fits, and methods from the physical nonlinear time-series analysis literature (see Fulcher and Jones, 2017 for a full list). In each brain region, measured time-series data were then represented as a 108 (experiments) \times 7873 (time-series features) data matrix. Features with well-behaved, real-numbered outputs across the whole dataset and were non-constant within all the three groups were retained for further analysis (7279 features). Each time series was labeled by its experimental condition ('wt-hSyn-hM3Dq', 'wt-CAMK-hM3Dq', 'PVCre-hSyn-hM4Di', or 'sham') and time-point ('baseline', 't2', and 't3').

Classification

We used the feature-based representations of BOLD time-series in each brain area as the basis for classifying the different experimental conditions. We focused our analysis on the $\Delta 1$ time period, first subtracting time-series features computed at baseline, and then normalizing these feature differences using an outlier-robust sigmoidal transformation (Fulcher et al., 2013). A linear support vector machine classification model was learned on the normalized feature matrix for a given brain area, using inverse probability class reweighting to accommodate class imbalance. A measure of discriminability of a pair of classes was quantified as the balanced classification accuracy using 10-fold stratified cross validation. Balanced accuracy was computed as the arithmetic mean of sensitivity and specificity to account for the small class imbalance: 13 sham controls and 14 wt-hSyn-hM3Dq or 13 wt-CAMK-hM3Dq or 19 PVCre-hSyn-hM4Di mice. To reduce variance in the random partition of data into 10 folds, we repeated this procedure 50 times (with each iteration yielding a

balanced accuracy value) and summarized the resulting distribution of balanced accuracies as its mean and standard deviation.

In smaller samples, there is a greater probability that optimistic classification results can be obtained by chance. To quantify this, we evaluated the statistical significance of our classification results relative to random assignments of class labels to data. This was achieved by computing a null distribution of the same performance metric used above (mean across 50 repeats of 10-fold cross-validated balanced accuracy) for 5000 random class label assignments to time series. The statistical significance of a given classification result was then estimated as a permutation test (as the proportion of 5000 null samples with a mean balanced classification rate exceeding that of the true assignment of class labels).

Low-dimensional projections

As explained above, each BOLD signal was represented as a feature vector, or equivalently, as a point in a high-dimensional feature space. To aid visualization of the class structure of data in this space, we projected normalized time series \times feature data matrices into a lower-dimensional space that captures the maximal variance in the full feature space using principal components analysis. In these plots, individual time series are points in the space, providing an intuitive visualization of the structure of the time-series dataset.

Interpreting differences in univariate dynamics

We aimed to determine which properties of the univariate BOLD dynamics in the injected brain area best discriminated: (i) wt-hSyn-hM3Dq from controls; (ii) wt-CAMK-hM3Dq from controls (iii) PVCre-hSyn-hM4Di from controls; and (iv) wt-hSyn-hM3Dq from wt-CAMK-hM3Dq and also from PVCre-hSyn-hM4Di mice. Focusing on the first time period after baseline, we first computed the difference in each feature value between this first time period and the baseline period ($\Delta 1$). We then tested whether these relative feature values differed between groups using a Wilcoxon rank-sum test. Statistical correction for the large number of hypothesis tests was performed as the false discovery rate (Benjamini and Hochberg, 1995), setting a significance threshold of $q = 0.05$.

Predicting *Fmr1*^{Y/-} mice using a classifier trained on PVCre-hSyn-hM4Di

Time series from 46 cortical ROIs (23 in each hemisphere) obtained from *Fmr1*^{Y/-} ($n = 44$) and wildtype littermates ($n = 39$) was obtained from two of our previous studies (Zerbi et al., 2018, Zerbi et al., 2019b). The classification proceeded in two stages. In the training phase, a classification model was trained on normalized features of rsfMRI time series in SSp (right hemisphere) during the $\Delta 1$ time period, as described above. That is, the trained classifier learns features of the BOLD dynamics to accurately predict whether a new time series is PVCre-hSyn-hM4Di or control. In the testing phase, the trained model was used to predict labels of rsfMRI time series in *Fmr1*^{Y/-} dataset. We identified PVCre-hSyn-hM4Di with the

Fmr1^{Y/-} knockout condition, and quantified prediction performance as balanced accuracy (%) as above, evaluated in each brain region independently. P-values were estimated for each brain area using permutation testing with 5×10^6 null samples generated by independent shuffling of labels, and corrected across brain regions (focusing just on the right hemisphere) using the false discovery rate method of Benjamini and Hochberg (Benjamini and Hochberg, 1995).

Histological evaluation of transfection

DREADDs viral expression (for wt-hSyn-hM3Dq, PVCre-hSyn-hM4Di and wt-CAMK-hM3Dq) was confirmed by m-Cherry staining using standard immunohistochemistry protocols. Briefly, after the last MRI session mice were deeply anesthetized using a mixture of Ketamine (100mg/kg; Graeb, Switzerland), Xylazine (10mg/kg; Rompun, Bayer) and Acepromazine (2mg/kg; Fatro S.p.A, Italy) and transcardially perfused with 4% Paraformaldehyde (PFA, pH=7.4). The brains were postfixed in 4% PFA for 1.5 hours at 4°C and then placed overnight in 30% sucrose solution. Brains were frozen in a tissue mounting fluid (Tissue-Tek O.C.T Compound, Sakura Finetek Europe B.V., Netherlands) and sectioned coronally in 40 µm thick slices using a cryostat (MICROM HM 560, histocom AG-Switzerland). Free-floating slices were first permeabilized in 0.2% Triton X-100 for 30 min and then incubated overnight in 0.2% Triton X-100, 2% normal goat serum and rabbit anti-mCherry (1:1000, Ab167453, Abcam) at 4°C under continuous agitation (100rpm/min). The next day sections were incubated for 1h in 0.2% Triton X-100, 2% normal goat serum, goat anti-rabbit Alexa Flour 546 (1:300, A11035, Life Technologies) and Nissl (1:300, NeuroTrace 660, Thermo Molecular Probes) or DAPI (1:300, Sigma-Aldrich) at room temperature under continuous agitation. Afterwards, slices were mounted on the superfrost slides where they were left to airdry and later coverslipped with Dako Fluorescence mounting medium (Agilent Technologies). Confocal laser-scanning microscope (Leica, SP8, Centre for Microscopy and Image Analysis, UZH) and Zeiss Slidescanner (Zeiss Axio scan, Z1, Centre for Microscopy and Image Analysis, UZH) were used to detect the viral expression. Microscopy protocol included a tile scan with a 10x or a 20x objective, pixel size of 1.2µm and image size of 1024x1024 pixels. Images were preprocessed and analyzed using ImageJ-Fiji and Zeiss Zen Blue, respectively.

3.4. Results

The E:I balance, a pathology reported as a putative mechanism in neurodevelopmental diseases, was experimentally increased in the right SSp (Fig. S3.1). Adult mice were transfected with excitatory Designer Receptors Exclusively Activated by Designer Drugs (hM3Dq DREADDs), which were tuned to primarily target pyramidal neurons (wt-CAMK-hM3Dq and wt-hSyn-hM3Dq, $n=13$; $n = 10$). Control mice were sham operated (weight and age-matched littermate controls, $n = 9$; Table S3.1). Three to four weeks after surgery, mice

were lightly anesthetized and electrophysiology or macroscopic brain activity was recorded before and after activating the DREADDs with a low dose of clozapine.

In vivo electrophysiology recordings in wt-hSyn-hM3Dq mice (Fig. S3.1D), used primarily to ensure successful DREADD activation, confirmed that activating the DREADDs increases net excitation within the targeted right SSp but not in a control area, i.e., its homotopic counterpart (left SSp). Multi-unit activity was recorded under isoflurane anesthesia (0.5%) from multi-contact electrode arrays (Fig. 3.1A–D). During the baseline period (15 min) the average basal firing rate was stable in both brain areas. However, upon clozapine injection, the average firing rate in the right SSp increased steadily over time while activity in the left SSp remained virtually unchanged. 30 min after injection, the difference in averaged multi-unit activity between left and right SSp reached 11% (Fig. 3.1A–D). We further investigated the effects of clozapine on neuronal activity in mice that did not express DREADDs. With clozapine injection, the average firing rate in the right SSp as well as in a control region remained unchanged (Fig. S3.2). This suggests that clozapine administered at our concentration have no effect on neuronal activity in the absence of DREADD.

Next, we used non-invasive fMRI to test whether activation of hM3Dq-DREADD in wt-hSyn-hM3Dq would elicit anatomically specific changes in cerebral blood flow (CBF) which reflects glucose metabolism and has been shown to be an indirect marker of neural activity at the cell population level (Chen et al., 2008, Juepter and Weiller, 1995). After administering clozapine, wt-hSyn-hM3Dq mice showed an increase in CBF around the injection site (Fig. 3.1E, H). The increase was significantly higher than in sham-operated mice (controls) scanned with identical procedures for all time points up to 45 min (Linear mixed model: $F_{2,21} = 5.657$, $p = 0.04$, Fig. 3.1F, I). No changes in CBF were observed in other brain regions, i.e., the contralateral somatosensory cortex and ipsilateral striatum (Fig. 3.1J, K). Together our electrophysiological and CBF results show that activating the DREADDs caused microcircuit excitation which was anatomically specific to the injected area.

Activating hM3Dq-DREADD in wt-hSyn-hM3Dq mice decreases short-range connectivity selectively within somatosensory and somatomotor cortex

We next tested whether hM3Dq-DREADD also caused a local disruption of functional connectivity (FC) measured with rsfMRI. To this end, we calculated the regional homogeneity (ReHo) index, a commonly used metric to assess the synchronization of BOLD fluctuations across neighboring voxels. We chose ReHo because it has been shown to reflect alterations occurring in various psychiatric diseases including depression, schizophrenia, and autism (Paakki et al., 2010, Iwabuchi et al., 2015). Activation of hM3Dq-DREADD significantly reduced regional homogeneity only at the injection site when compared to controls (blue cluster in Fig. 3.1L, M; $p < 0.05$, TFCE-corrected). These changes occurred within the first 15 minutes

after clozapine injection and were maintained for the whole scan period (Fig. S3.3A). No other area exhibited similar changes.

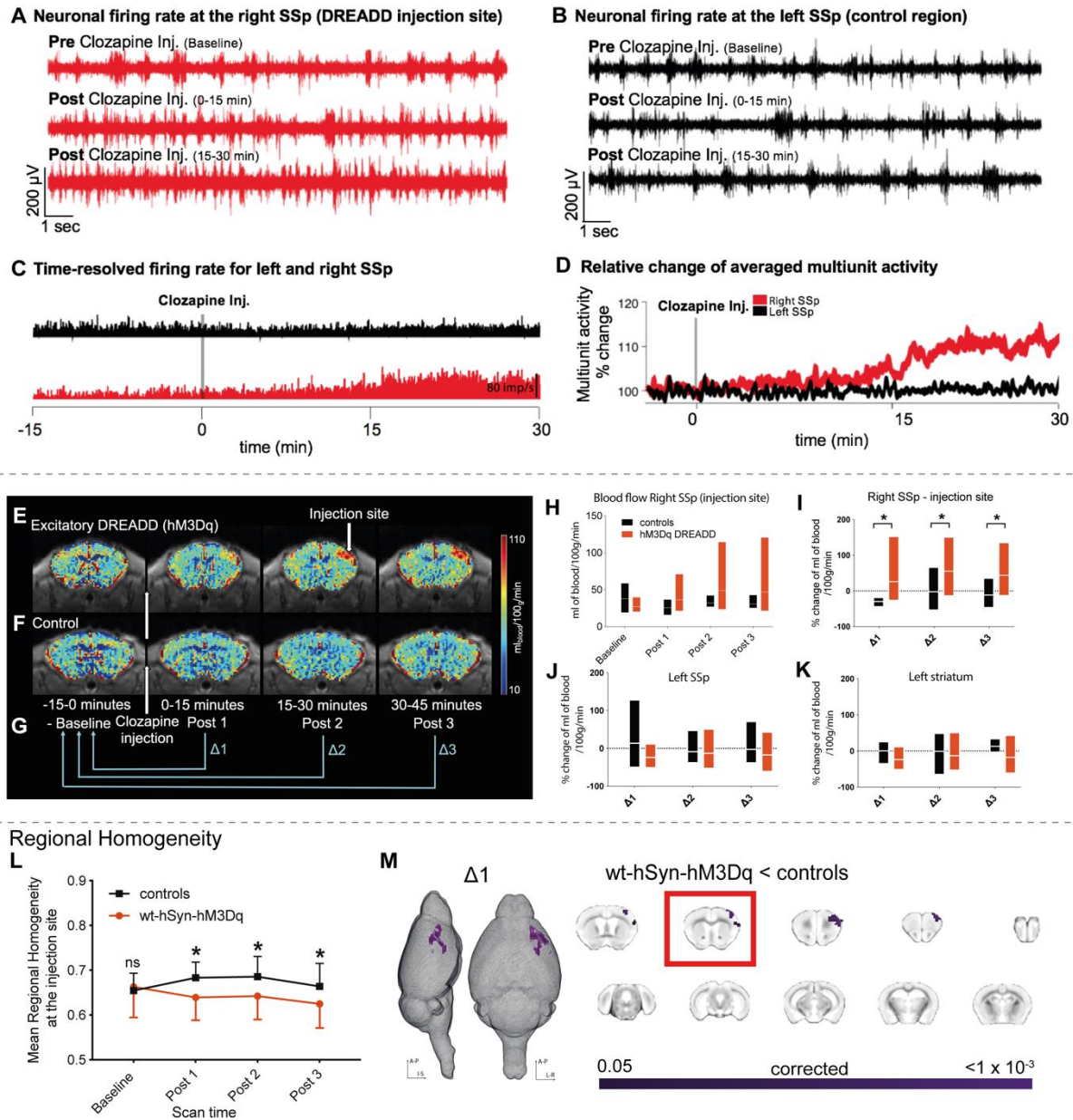


Figure 3.1. Local changes in neural activity induced by activating hSyn-hM3Dq. **A)** Neuronal firing rate before and after clozapine injection in the right SSp, indicating a steady increase in firing rate upon DREADD activation. **B)** As **A** but for the left SSp, (control area) indicating no change in the neuronal firing rate after clozapine injection. **C)** Time-resolved firing rate in millisecond bins for the right (red) and left (black) SSp. A steady increase in firing rate occurs in the right SSp once clozapine is injected, while no change occurs in the left SSp. **D)** Relative change of averaged multiunit activity recorded in the right and left SSp. **E), F)** Cerebral blood flow maps were collected every 15 min wt-hSyn-hM3Dq and control mice, respectively. **G)** Clozapine is injected 15 min after the start of experiment. These 15 minutes are referred as the baseline period (-15-0 min). The rest of the experiment is 45 minutes long and divided into 3 periods i.e., Post 1 (0-15 min), Post 2 (15-30 min), and Post 3 (30-45 min). For all

analyses performed in this experiment (unless otherwise stated), Post data was expressed relative to baseline (Post 1/Post 2/Post 3 – baseline) and is referred to as $\Delta 1$, $\Delta 2$, $\Delta 3$, respectively. **H)** Comparison of blood flow (ml of blood/100g/min) between controls and wt-hSyn-hM3Dq mice over time (measured at the injection site). **I)** Percentage change in blood flow over time between the controls (n=7) and wt-hM3Dq (n=7) mice (measured at the injection site). Linear mixed models indicate a significant main group effect indicating an increase in blood flow in the wt-hSyn-hM3Dq mice ($F_{2,21} = 5.657$; $p=0.04$). **J)** Percentage change in blood flow over time measured in left SSp. **K)** Percentage change in blood flow over time measured in left lateral striatum. **L)** Average regional homogeneity (ReHo) change over time at the injection site. Repeated measures ANOVA (control (n=13); wt-hSyn-hM3Dq (n=14)) showed a significant interaction between scan time and groups ($F_{1,93,75} = 11.8$; $p<0.001$). **M)** Significant decrease in ReHo in wt-hSyn-hM3Dq mice versus controls for $\Delta 1$ depicted as a 3D image and in coronal slices (TFCE-corrected). The slice marked with a red rectangle shows the injection site.

Activated DREADD in wt-hSyn-hM3Dq mice reduces functional connectivity between somatosensory cortex and monosynaptically connected cortical areas

Does an increase in local microcircuit excitation also affect long-range FC as quantified by correlating spontaneous BOLD fluctuations between areas? To address this question, we measured FC between 130 brain regions as identified by the Allen Brain Reference Atlas Common Coordinate Framework (CCFv3) at every one-minute intervals (see Methods). We then extracted the effect size using the standardized difference between the group means (Cohen's d , wt-hSyn-hM3Dq vs control mice) between each pair of regions. During the first 15 minutes (baseline), Cohen's d varied on average between -0.2 and $+0.2$ (null-to-small effect) and did not exhibit an appreciable spatial or temporal pattern. However, immediately after clozapine injection, we noticed a rapid reduction in FC between a number of connections in the somatosensory and somatomotor cortices, which remained hypoconnected for the whole scan session (Fig. 3.2A, B).

We next quantified specific changes in FC within the somatosensory network, i.e. areas which are monosynaptically connected to the chemogenetic target, right SSp according to the Allen Mouse Brain Connectivity Atlas (Oh et al., 2014). This anatomically defined network includes contralateral primary SSp, bilateral somatomotor cortex (MO), ipsilateral supplementary somatosensory cortex (SSs), bilateral association areas (TEa) and ipsilateral caudatum putamen (CP) (Fig. 3.2C). We found high FC between all of these structures at baseline (Fig. 3.2C), and a strong structure–function correspondence (Fig. 3.2D). To increase the power of our analysis, the BOLD time series of the somatosensory network regions were binned into four intervals of 15 minutes each. Pearson's correlations were calculated between regions and are summarized in FC matrices (Figs 3.2E, F, G, and Fig. S3.4A). At baseline, FC did not show differences between groups (Fig. 3.2E). By contrast, after clozapine injection (Fig. 3.2F–H) we observed a reduction in FC between right SSp and nearly all other areas of the network in wt-hSyn-hM3Dq mice, including cortico-striatal circuitry. Significant group differences (permutation testing, $p < 0.05$, FDR corrected) were found between right SSp and left SSp/left MO, as well as between left and right MOp, and were maintained for the duration of the scan session (Fig. 3.2H, Fig. S3.4B). We also performed similar analysis on a small cohort of animals

using 1mg/kg CNO which resulted in FC decrease within MO regions in wt-hSyn-hM3Dq mice (Fig. S3.5).

We further complemented our analysis by assessing the similarity between the BOLD time series of symmetric voxels in the left and right hemisphere. This index has been shown to identify pathological connectivity patterns with high sensitivity as compared to other FC metrics (Hahamy et al., 2015). In line with our previous findings, injecting clozapine caused a significant reduction of symmetric connectivity in wt-hSyn-hM3Dq mice but not in controls which occurred only between the left and right primary SSp, and left and right MO ($p < 0.05$, FDR corrected) (Fig. 3.2I, J). In summary, our analyses demonstrate that increasing local cortical excitation causes a reduction in local connectivity that propagates into long-range FC reduction exclusively within the targeted network.

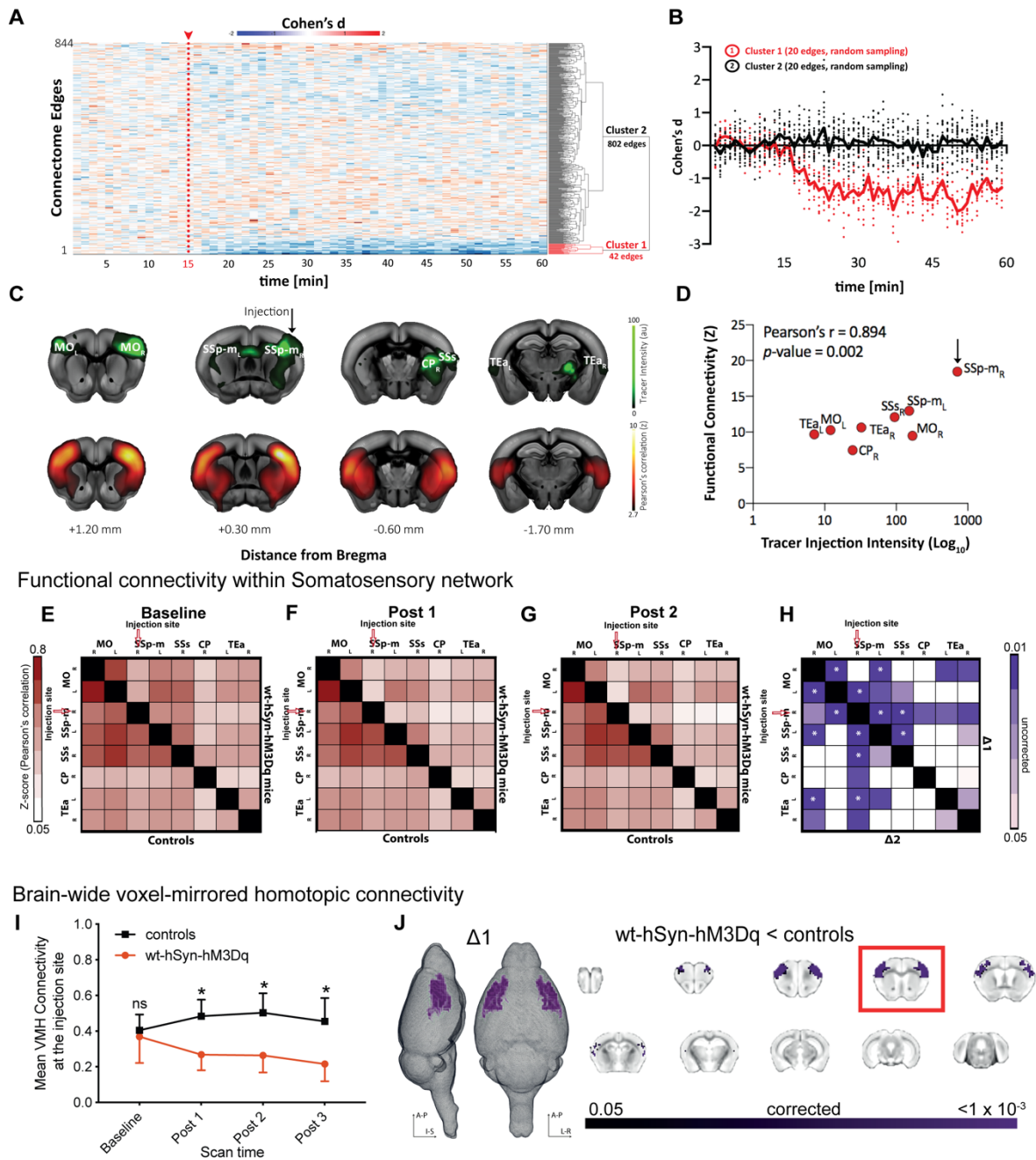


Figure 3.2. Long-range connectivity changes induced by activating hSyn-hM3Dq. **A)** Effect-size analysis (Cohen's d) of functional connectivity is calculated for single-edges ($n=844$). Only cluster 1 shows a decrease in the effect size after Clozapine injection. **B)** Averaged effect-size (Cohen's d) over time for 20 edges of Cluster 1 and 20 randomly selected edges of Cluster 2. **C)** Coronal brain slices depicting tracer data after unilateral injection in SSp (green, obtained from Allen Mouse Brain Connectivity Atlas, Injection ID: 114290938) and averaged voxel-wise Pearson's correlation (Fisher's z -transform) during the baseline period from a seed in the right SSp. **D)** Pearson's correlation between functional connectivity of the target region (right SSp) and tracer injection intensity obtained from images depicted in C. **E) F) G)** Matrices represent averaged and z -transformed Pearson correlation of all control animals (lower triangular matrix) and all wt-hSyn-hM3Dq animals (upper triangular matrix) for the baseline period, Post 1 and Post 2, respectively. **H)** The upper triangle of the matrix shows a reduction in FC in wt-hSyn-hM3Dq ($n=14$) mice compared to controls ($n=13$) during $\Delta 1$ (i.e. Post1-baseline), while the lower triangle shows the same set of comparisons in $\Delta 2$ (i.e., Post2-baseline). Color coding reflects

randomized permutation testing, $p < 0.05$, uncorrected. Asterisks indicate significant differences that survived FDR correction for multiple comparisons. MO – Somatomotor cortex, SSp-m – primary somatosensory cortex (mouth), SSs – supplementary somatosensory cortex, CP –caudoputamen and TEa – temporal association cortex, R – right, L – left. **I**) Change over time of the mean brain-wide VMHC (symmetric connectivity) at the injection site. Repeated measures ANOVA (controls ($n=13$); wt-hSyn-hM3Dq ($n=14$)) showed a significant interaction between the scan time and groups ($F_{1,67,41.9} = 21.18$; $p < 0.001$). **J**) Significant decrease (TFCE-corrected) in symmetric connectivity depicted on 3D images and coronal slices for the $\Delta 1$ time point. The slice marked with a red rectangle is the injection slice.

Activated DREADD in wt-CAMK-hM3Dq mice reduces functional connectivity

The above results were obtained using human Synapsin-1 as the promoter for the viral injection. Human Synapsin-1 promoter is not solely specific towards pyramidal neurons but can also transfect inhibitory interneurons. To ensure specificity for pyramidal neurons, we repeated the above experiments in a separate cohort of wildtype mice ($n=13$) using the CAMKII promoter for AAV hM3Dq-DREADD delivery (Fig. S3.7). Firstly, we measured CBF to confirm reliable DREADD activation at the injection site. After administering clozapine, wt-CAMK-hM3Dq mice showed a significant increase in CBF around the injection site (Fig. 3.3A) as compared with controls (Repeated Measures ANOVA: $F(1.0,20.0) = 7.3$; $p=0.004$). This increase was limited to the injection site and not observed in other brain regions (Fig. 3.3B, C). Regional homogeneity as well as symmetric connectivity metrics both significantly decreased at the injection site after DREADD activation in wt-CAMK-hM3Dq mice versus controls (Repeated Measures ANOVA: $F(1.3, 25.2)=7.74$, $p=0.006$; $F(1.16, 21.98)=8.21$, $p=0.007$, respectively; Fig. 3.3D, E), while under-connectivity was also pronounced within somatosensory network (Fig. 3.3F). Importantly, we replicated our results obtained with human Synapsin-1 promoter and confirmed that increasing E:I by enhancing excitatory synaptic transmission causes a robust reduction of FC within an anatomically connected network.

Chapter 3. Cortical E:I imbalance causes abnormal brain network dynamics as observed in neurodevelopmental disorders

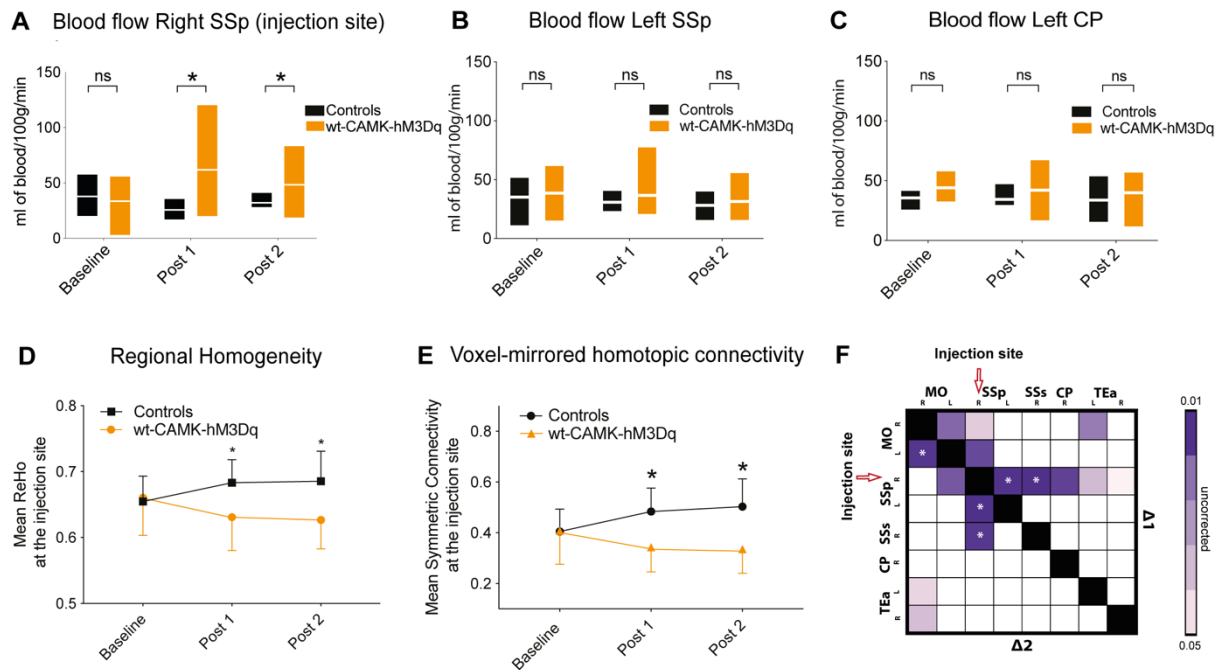


Figure 3.3. Changes induced by activating CAMK-hM3Dq in wildtype mice. **A)** Comparison of blood flow (ml of blood/100g/min) over time between controls and wildtype mice injected with excitatory (hM3Di) DREADD on CAMKII promoter (measured at the injection site). We observe a significant (repeated measures ANOVA indicates a groups*scan time effect: $F(1.0,20.0)=7.3;p=0.004$) increase in blood flow in wt-CAMK-hM3Dq mice ($n=13$) after clozapine injection (similar to wt-hSyn-hM3Dq from Fig. 2H). **B)-C)** Blood flow in the Left SSp and Left CP does not significantly differ between controls and wt-CAMK-hM3Dq mice. **D)** Change over time of mean regional homogeneity at the injection site (right SSp). There is a significant decrease (repeated measures ANOVA shows a groups*scan time effect: $F(1.3, 25.2)=7.74, p=0.006$) in mean connectivity in wt-CAMK-hM3Dq ($n=13$) mice as compared to controls ($n=13$). **E)** Change over time of mean symmetric connectivity at the injection site. There is a significant decrease (repeated measures ANOVA shows a groups*scan time effect: $F(1.16, 21.98)=8.21, p=0.007$) in mean connectivity in wt-CAMK-hM3Dq ($n=13$) mice as compared to controls ($n=13$). **F)** Matrix represents statistically significant differences during $\Delta 1$ and $\Delta 2$ time period among 3 brain regions (MO – Somatomotor cortex, SSp – somatosensory cortex, SSs -supplementary somatosensory cortex, R – right, L - left) between the controls and wt-CAMK-hM3Dq mice. The stars within some ROIs indicate statistically significant differences that survived correction of multiple comparisons.

Changing E:I balance by inhibiting GABAergic parvalbumin neurons

Changes in E:I have been proposed as a principle mechanism that underlies symptoms of neurodevelopmental disorders, irrespective of whether primarily excitatory or inhibitory synapses are affected. Next, we tested whether suppressing the activity of GABAergic PV interneurons — as reported in several mouse models for ASD (Penagarikano et al., 2011, Ajram et al., 2017, Wöhr et al., 2015) — would cause similar macroscopic hypo-connectivity as observed above. Nineteen $Pvalb^{tm1(cre)Arbr}$ (PVCr) were transfected with an inhibitory hM4Di-DREADD. Clozapine activation reduced PV cell activity which resulted in over-excitation of right SSp but not a control region. Accordingly, average firing rate in right SSp went up by 20% following clozapine injection (Fig. 3.4A, B and Fig. S3.6A, B) and local cerebral

blood flow increased moderately (repeated measures ANOVA: $F_{1.4,17.9}=2.45$; $p=0.1$; Fig. 3.4C). Our rsfMRI analysis confirmed the expected reduction in local synchronization around the injection site (Fig. 3.4D) and also marked under-connectivity which was most pronounced between right and left SSp (Fig. 3.4E-H) in PVCre-hSyn-hM4Di mice as compared to controls. In summary, our results reveal that shifting E:I toward excitation by inhibiting PV interneurons leads to a reduction of local and long-range FC, which is qualitatively similar to that observed during direct system excitation.

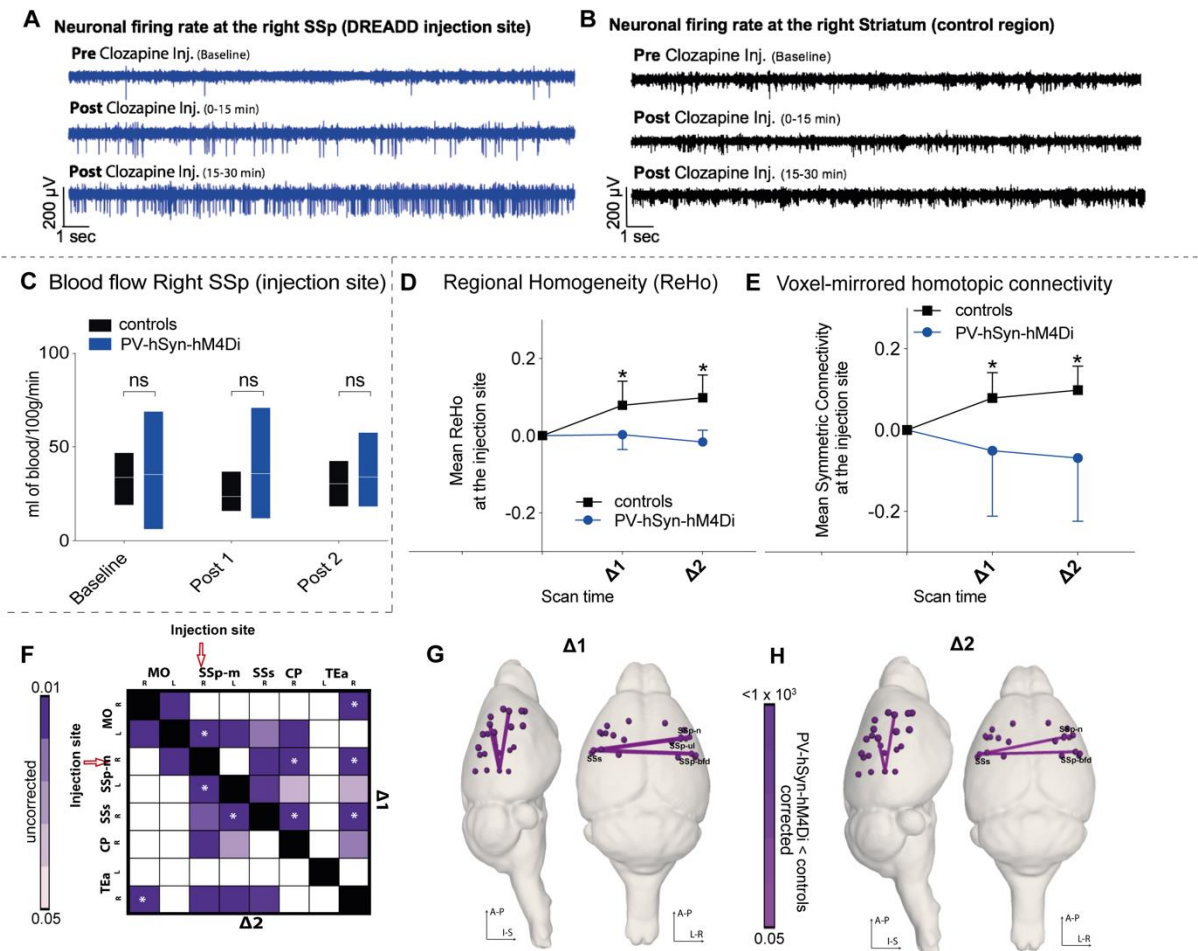


Figure 3.4. Changes induced by activating hSyn-hM4Di in PVCre mice. A) Neuronal firing rate at the right SSp DREADD injection site of the PVCre-hSyn-hM4Di mice before and after clozapine injection, indicating a steady increase in firing rate on DREADD activation. **B)** Similar to figure A but for right caudate putamen, indicating no change in the neuronal firing rate after clozapine injection. **C)** Comparison of blood flow (ml of blood/100g/min) between controls ($n=7$) and PVCre-hSyn-hM4Di ($n=13$) mice over time (measured at the injection site). No significant differences observed between groups (repeated measures ANOVA: $F_{1.4,17.9}=2.45$; $p=0.1$). **D)** Normalized average regional homogeneity (ReHo) change over time at the injection site indicating significant differences between groups (controls: $n=13$; PVCre: $n=19$; repeated measures ANOVA: $F_{1,25}=14.01$; $p=0.001$). Post hoc paired t -test revealed a significant group difference at $\Delta 1$ ($t_{12}=-3.60$; $p=0.004$) and at $\Delta 2$ ($t_{12}=-8.05$; $p < 10^{-4}$). **E)** Normalized averaged symmetric connectivity over time at the injection site. Repeated measures ANOVA (controls ($n=13$); PVCre-hSyn-hM4Di ($n=19$)) showed a significant interaction between scan time and group ($F_{1.2,21.9}=8.21$; $p = 0.007$). Post hoc paired t -test revealed a significant group difference at $\Delta 1$ ($p=0.047$) and

at $\Delta 2$ ($p = 0.004$). **F**) Seed to seed analysis indicates reduced FC (randomized permutation testing, $p < 0.05$, uncorrected) between controls ($n=13$) and *PVCre-hSyn-hM4Di* ($n=19$) mice. **G) H**) Whole-brain connectome analysis shows a significant interhemispheric reduction between somatosensory cortices for $\Delta 1$ and $\Delta 2$ between *PVCre-hSyn-hM4Di* ($n=14$) mice and controls ($n=13$). Regions affected are as follows: *SSp-m*: Primary Somatosensory Area, mouth; *SSp-ul*: Primary Somatosensory Area, upper limb; *SSs*: Supplementary somatosensory area; *SSp-bdf*: Primary Somatosensory Area, barrel field; *SSp-n*: Primary Somatosensory Area, nose.

Altered E:I balance changes local BOLD dynamics

Our previous analyses demonstrated that increasing E:I in right *SSp* affects its FC with other brain regions. We next aimed to understand how microcircuit E:I shapes the fluctuations of spontaneous BOLD regional activity. As depicted in Fig. 3.5A, we focused our analysis on three regions of interest: (i) right *SSp* (the injection site); (ii) left *SSp* (its homotopic counterpart); and (iii) left visual cortex (a control region). The dynamics of BOLD time series were characterized by an interdisciplinary library of over 7000 features (using the software package *hctsa* (Fulcher and Jones, 2017)), which capture distinct properties of the BOLD signal, including spectral power in different frequency bands, temporal entropy, and many more (Fulcher and Jones, 2017, Fulcher et al., 2013, Sethi et al., 2017) (Fig. 3.5B, see Methods for details).

Based on the change of these features from baseline to activated DREADDs, we trained linear Support Vector Machine (SVM) classifiers to distinguish: (i) *wt-hSyn-hM3Dq* versus controls, (ii) *wt-CAMK-hM3Dq* versus control (iii) *PVCre-hM4Di* versus controls, (iv) *wt-hSyn-hM3Dq* versus *wt-CAMK-hM3Dq*, v) *wt-CAMK-hM3Dq* versus *PVCre-hSyn-hM4Di* and vi) *wt-hSyn-hM3Dq* versus *PVCre-hSyn-hM4Di* as shown in Fig. 3.5C.

Our classification results reveal that BOLD dynamics of the injected right *SSp* at $\Delta 1$ are differentiated from control mice in *wt-hSyn-hM3Dq* (Fig. 3.5D), *wt-CAMK-hM3Dq* (Fig. 3.5E) and *PVCre-hSyn-hM4Di* (Fig. 3.5F) with high accuracy ($\geq 84\%$ balanced accuracy after 10-fold cross-validation), significantly exceeding chance levels ($p \leq 1 \times 10^{-3}$, permutation test). Qualitatively similar results were obtained at $\Delta 2$ (see Supplementary Results). DREADD activation had a similarly large effect on the accuracy of classifying BOLD dynamics in the left *SSp* but only for *wt-CAMK-hM3Dq* (81%, $p \leq 1 \times 10^{-3}$), while for the other two groups the effect was much smaller: *wt-hSyn-hM3Dq*, 64% ($p = 0.1$), and *PVCre-hSyn-hM4Di*, 69% ($p = 0.03$), and finally the weakest for the control region, VIS, in all groups *wt-hSyn-hM3Dq*, 43% ($p = 0.7$), *wt-CAMK-hM3Dq*, 45% ($p=0.7$) and *PVCre-hSyn-hM4Di*, 54% ($p = 0.3$).

To aid visualization, we constructed principal component projections of each dataset (including data at $\Delta 2$), shown for *wt-hSyn-hM3Dq* versus control, *wt-CAMK-hM3Dq* versus control, *PVCre-hSyn-hM4Di* versus control in Figs 3.5H, 3.5I, and 3.5J, respectively. These

plots reveal a clear distinction between DREADD-activated and control mice on the basis of their BOLD dynamics in right SSp.

We next sought to investigate the properties of BOLD timeseries between the three DREADD manipulated groups at the right SSp during $\Delta 1$. As shown on Fig. 3.5G, BOLD dynamics at the right SSp between wt-hSyn-hM3Dq versus wt-CAMK-hM3Dq are clearly distinct at 75% ($p=0.01$). BOLD dynamics between wt-hSyn-hM3Dq versus PVCre-hSyn-hM4Di and wt-CAMK-hM3Dq versus PVCre-hSyn-hM4Di at the right SSp are only weakly distinguishable, 63% ($p = 0.09$) and 62% ($p= 0.1$), respectively. Moreover, the clear discrimination of BOLD dynamics in principal components space is starkly absent (Fig. 3.5K, see strongly overlapping distributions). Weak properties of BOLD timeseries were also obtained in left SSp and visual control region during $\Delta 1$ (Fig. S3.9 A, B).

Since wt-hSyn-hM3Dq and PVCre-hSyn-hM4Di increase E:I through different mechanisms, we next sought to further compare the effect of their manipulations on BOLD dynamics, we computed a similarity measure between changes in BOLD time-series properties caused by both manipulations relative to controls (as a Spearman's ρ in right SSp and left SSp relative to the control region across all time-series features, see Fig. S3.10). We found overall agreement between wt-hSyn-hM3Dq and PVCre-hSyn-hM4Di in right SSp ($\rho = 0.59$) and left SSp ($\rho = 0.47$), suggesting that the temporal properties of BOLD dynamics are more sensitive to the net over-excitation common to both DREADD cohorts, than to the underlying synaptic transmission pathway within the cortical microcircuit (see Supplementary Material for an analysis of BOLD time-series features that are individually informative of E:I).

Chapter 3. Cortical E:I imbalance causes abnormal brain network dynamics as observed in neurodevelopmental disorders

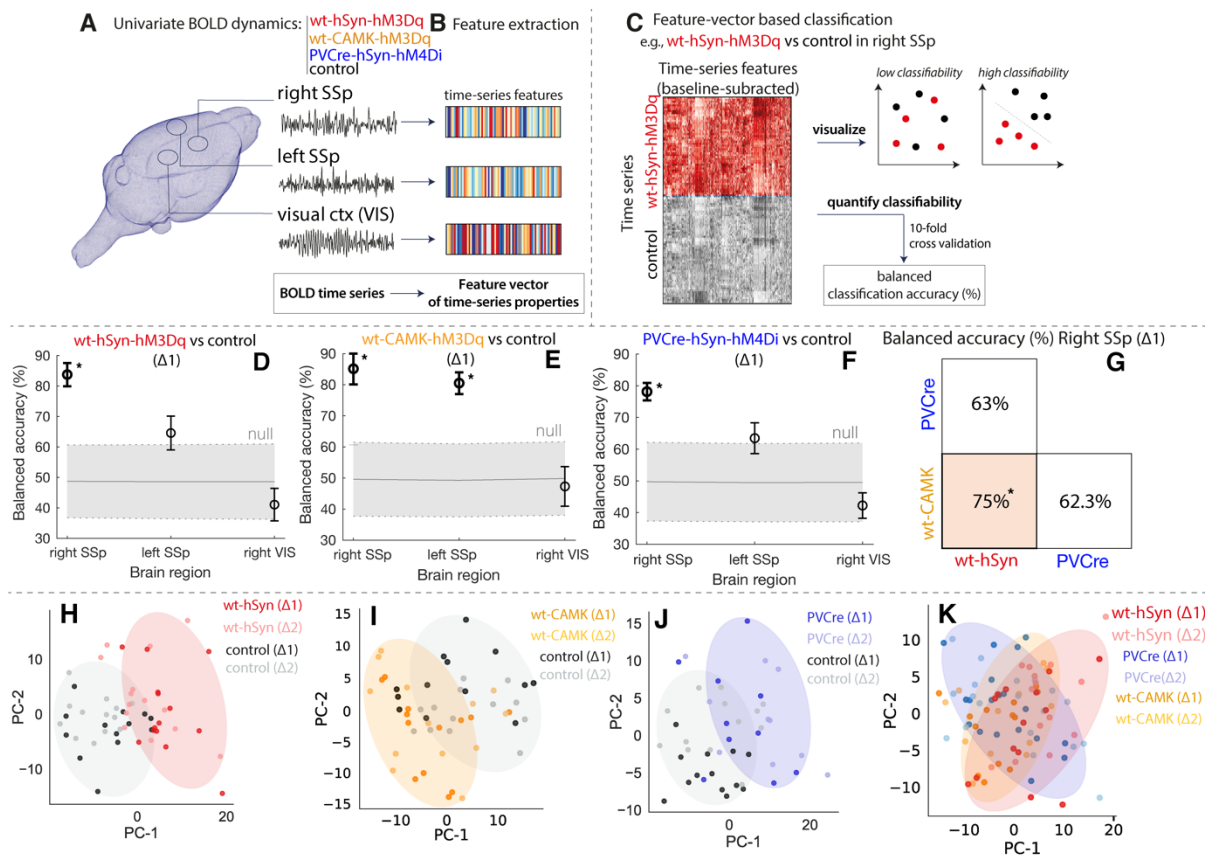


Figure 3.5. DREADD manipulations lead to characteristic changes in univariate BOLD dynamics. Classification of BOLD signal dynamics in three brain regions (the injected right SSp, left SSp, and VIS) across three conditions (*wt-hSyn-hM3Dq*, *PVCre-hSyn-hM4Di*, and control). A schematic of the approach is depicted in **A–C**: **A**) BOLD dynamics are measured from each brain region as a univariate time series (a 15 min time series per time window and experiment), which was **B**) converted to a set of properties (a ‘feature vector’) using *hctsa*. **C**) For a given region and pair of classes, we used the features of each time series (relative to baseline) as the basis for classification, which was visualized using a low-dimensional principal components projection and quantified as the 10-fold cross-validated balanced classification accuracy (%). Classification results in each brain region at $\Delta 1$ are shown for: **D**) *wt-hSyn-hM3Dq* ($n=14$) versus control ($n=13$), **E**) *wt-CAMK-hM3Dq* ($n=13$) versus control ($n=13$) **F**) *PVCre-hSyn-hM4Di* ($n=10$) versus control ($n=13$), revealing significant discriminability in the right SSp for *wt-hSyn-hM3Dq* and *PVCre-hSyn-hM4Di* versus control (permutation test, $p < 0.05$, annotated as ‘*’). There is a consistent trend of high discriminability in the injected region (right SSp), followed by the contralateral region (left SSp), and lowest discriminability in the control region (VIS). **G**) Classification results in the right SSp at $\Delta 1$ are shown for *wt-hSyn-hM3Dq* versus *wt-CAMK-hM4Di*, *wt-hSyn-hM3Dq* versus *PVCre-hSyn-hM4Di* and *wt-CAMK-hM4Di* versus *PVCre-hSyn-hM4Di*. High discriminability is only present for *wt-hSyn-hM3Dq* versus *wt-CAMK-hM4Di* (permutation test, $p < 0.05$, annotated as ‘*’). BOLD time series in right SSp are visualized in two-dimensional principal components spaces in **H)–K**) for the same three pairs of classes as in **D)–G**). Time series with similar properties are close in the space, revealing a visual depiction of the discriminability of *wt-hSyn-hM3Dq*, *wt-CAMK-hM3Dq* and *PVCre-hSyn-hM4Di* relative to control (**H)–J**), but a relative lack of discriminability in (**K**). Shaded ellipses ($\Delta 1$) have been added to guide the eye, and time series from each class are labeled for $\Delta 1$ and $\Delta 2$.

***Fmr1*^{Y/-} exhibit similar local BOLD dynamics to DREADD-manipulated mice**

Our previous analysis yielded a classifier for predicting an acute microcircuit E:I increase from macroscopic BOLD dynamics. Next, we asked whether such a classifier can also detect abnormal BOLD dynamics in a transgenic disease model of ASD. We used rsfMRI data from *Fmr1*^{Y/-} knock-out mice that mimic Fragile X syndrome, a neurodevelopmental disorder characterized by cognitive impairment, epileptic seizures, physical abnormalities and hypersensitivity. Previous studies in *Fmr1*^{Y/-} mice report a reduction in cortical PV cell density, specifically within somatosensory region, followed by cortical hyperexcitability (Wohr et al., 2015, Selby et al., 2007, Gibson et al., 2008, Nomura et al., 2017). These findings indicate that the disease mechanism of *Fmr1*^{Y/-} mice affects the net excitability of cortical microcircuits in a similar manner as chemogenetically suppressing PVCre activity, but it is unknown whether these circuit-level alterations cause analogous alteration of macroscopic rsfMRI dynamics. To test this hypothesis, we trained a classifier for PVCre-hSyn-hM4Di rsfMRI time series in the right SSp during $\Delta 1$ as above (Fig. 3.4E; 3.5A). We then applied this classifier to rsfMRI data from 46 cortical ROIs (23 from each hemisphere) in *Fmr1*^{Y/-} mice ($n = 44$) and wildtype littermates (*Fmr1*^{Y/+}, $n = 39$) and assigned predicted labels to each brain region of *Fmr1*^{Y/-} and *Fmr1*^{Y/+} independently (Fig. 3.6B). As shown in Fig. 3.6C, regional BOLD dynamics of *Fmr1*^{Y/-} versus wildtype controls could be significantly classified in 10 different areas of the right hemisphere (balanced classification accuracy, $p < 0.05$, FDR-corrected) using a classifier trained on PVCre-hSyn-hM4Di data. Corresponding to the brain area in which the DREADDs classifier was trained, regions of the SSp displayed the highest classifiability. Similar results were obtained in the left hemisphere, resulting in a Spearman's $\rho = 0.69$ ($p = 3 \times 10^{-4}$) between the left and right hemispheres (Fig. 3.6E, F). We next tested whether regional variation in classification accuracy was related to differences in PV cell density using data from *qBrain* (Kim et al., 2017a). As shown in Fig. 3.6D, classification accuracy is only weakly correlated with PV cell density, $\rho = 0.33$ ($p = 0.1$), but is highest in SSp regions with the highest PV cell density (dark green in Fig. 3.6D). Interestingly, the classifier identified several prefrontal areas (bright green in Fig. 3.6D) which exhibited abnormal rsfMRI dynamics according to the classifier despite low PV cell density. This finding is in line with former reports of abnormal prefrontal cortex function in *Fmr1*^{Y/-} mice (Paul et al., 2013, Routh et al., 2017). Our results demonstrate that a classifier trained on a controlled chemogenetic manipulation causing an acute shift of the E:I balance is generalizable to *Fmr1*^{Y/-}, indicating a strong degree of similarity between cortical BOLD dynamics resulting from PVCre-hSyn-hM4Di and *Fmr1*^{Y/-} knockout.

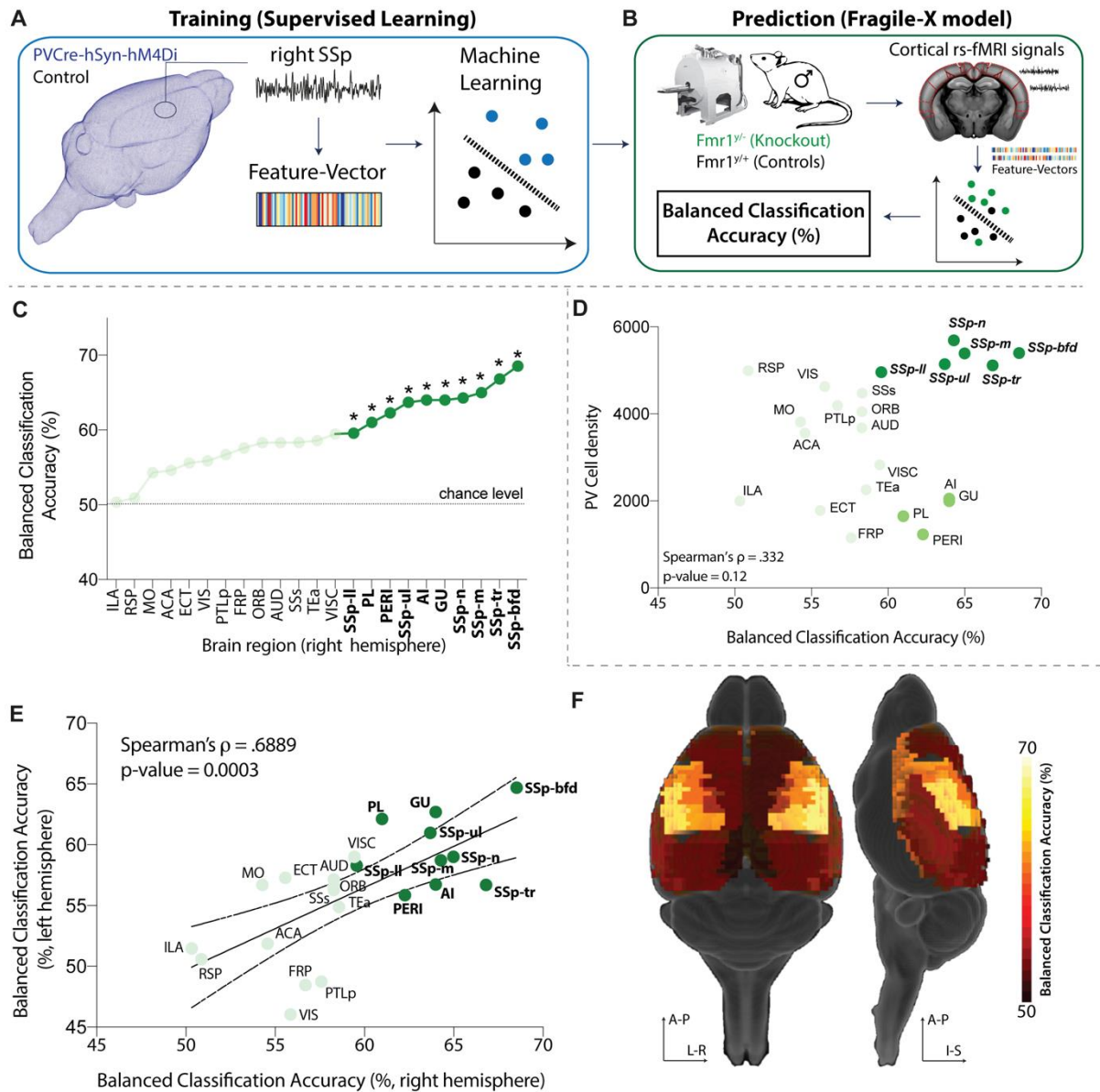


Figure 3.6. *Fmr1*^{-/-} exhibit similar local BOLD dynamics as DREADD-manipulated mice. **A)** The classifier was trained on features of right SSp BOLD time series to distinguish PVCre-hSyn-hM4Di from control mice. **B)** The trained classifier was used to predict the identity of cortical BOLD time series measured from *Fmr1*^{-/-} (knockout) and *Fmr1*^{+/+} (control) mice, identifying predictions of PVCre-hSyn-hM4Di as *Fmr1*^{-/-}. Predictability in each brain region was assessed as balanced classification accuracy (%); p -values were estimated using a permutation test. **C)** Classification results are shown for the right hemisphere, highlighting regions with significant classification accuracy ($p < 0.05$, FDR-corrected) as bold, dark green, and marked with asterisks. **D)** Scatter plot of balanced classification accuracy and PV cell density. **E)** Balanced classification accuracy is plotted for each region in the right and left hemispheres, exhibiting a strong positive correlation, Spearman's $\rho = 0.69$ ($p = 3 \times 10^{-4}$). **F)** Balanced classification accuracy visualized on a 3D brain.

3.5. Discussion

It has been a longstanding question how disease mechanisms at the cellular level map onto abnormal dynamics at the level of macroscopic brain networks. Here we show in three independent cohorts that acutely increasing the microcircuit E:I balance in somatosensory cortex via chemogenetics causes distinct changes of macroscopic brain dynamics and severe functional under-connectivity between the manipulated region of interest (SSp) and monosynaptically connected brain areas. These macroscopic changes were observed irrespective of whether we enhanced excitatory transmission or selectively suppressed inhibitory PV neurons of the same cortical circuits. Our results constitute the first direct evidence that macroscopic BOLD dynamics reflect the state of underlying cortical microcircuits. Furthermore, we show that different cellular mechanisms can cause common pathophysiological abnormalities and converge on highly similar alterations of neural dynamics at the network level. In particular, upon activating the DREADDs there was a marked reduction of FC which was temporally locked to our stimulation paradigm and spatially specific to the injected area and its monosynaptically connected neighbors. Reduced FC has been frequently reported in human fMRI studies of neurodevelopmental disorders, such as autism and schizophrenia (Kraguljac et al., 2016, Minshew and Keller, 2010, Wang et al., 2018b, Gao and Penzes, 2016, Uhlhaas and Singer, 2006), as well as in relevant mouse models of these disorders (*CNTNAP2*, *Fmr1*^{-/-}, *En2*) (Bertero et al., 2018, Zerbi et al., 2018). Many of these mouse models have been shown to exhibit an increased E:I (Contractor et al., 2015, Rubenstein and Merzenich, 2003, Gibson et al., 2008). Additionally, they suffer from reduced PV interneuron expression (Penagarikano et al., 2011, Vogt et al., 2017). Depletion of this specific cell type has been hypothesized to cause aberrant patterns of neural activity and connectivity (Wohr et al., 2015, Penagarikano et al., 2011), as fast-spiking PV interneurons target the proximal regions of pyramidal cells (Hu et al., 2014, Safari et al., 2017) and synchronize firing within pyramidal cell populations (Cardin, 2018, Sohal et al., 2009, Cardin et al., 2009, Bartos et al., 2007, Engel and Singer, 2001, Roux and Buzsaki, 2015). This hypothesis has been recently confirmed by Marissal and colleagues, who found that DREADD-induced suppression of PV activity causes the disinhibition of pyramidal neurons and leads to mass desynchronization of spiking activity (Marissal et al., 2018). Congruent with these previous empirical findings and recent theoretical models (Lee et al., 2018), our data suggest that inhibiting PV neurons reduces the *synchronization* of neuronal ensembles as indicated by the reduction of FC, despite higher net cortical activity.

Interactions among different types of neurons within a microcircuit should be balanced for proper functioning. Lee and colleagues (Lee et al., 2018) have recently built a computational model of the sensory cortex microcircuit and demonstrated the importance of connectivity homeostasis between neuronal types (i.e., inhibitory and excitatory cells) for producing synchronized oscillatory behavior with maximum frequency tuning capacity. Any deviation

from this optimal configuration, such as over-excitation of pyramidal neurons, breaks this synchrony and impairs the communication among neuronal ensembles, which at the macro-scale may be perceived as a reduction in FC. In line with this theoretical framework, we observed a reduction in FC when DREADDs were used to activate pyramidal neurons. We replicated this principle finding across three independent cohorts, using either clozapine or CNO to activate the DREADDs (see supplementary discussion) and using either human Synapsin (hSyn) or CAMKII as a promoter in the AAV constructs. While hSyn promoter is active in both excitatory and inhibitory neurons, CAMKII generates a clear bias towards gene expression in excitatory cortical neurons (up to 85%) even though it might also transfect a small number of inhibitory neurons. Importantly, our electrophysiological results confirmed that activating excitatory DREADDs in the wt-hSyn-hM3Dq mice caused a significant net increase of neuronal firing rate and our CBF measurements confirmed that such an increase was anatomically specific and most pronounced within the targeted SSp. Activating the excitatory DREADDs caused overall a stronger reduction of FC in wt-hSyn-hM3Dq mice than in PVCre-hM4Di mice, which might result from a higher number of transfected neurons: mouse cortex contains 12% GABAergic neurons, of which approximately one quarter are PV (Feldmeyer et al., 2018) resulting in a rather low absolute number of transfected neurons and smaller DREADD induced effects (Grayson et al., 2016).

Our results also characterize a potential role of local E:I balance in shaping the BOLD dynamics of individual brain regions. Specifically, we showed that the chemogenetic manipulation of the cellular excitability causes specific changes of local BOLD features that we could distinguish from neurotypical BOLD dynamics with high accuracy (balanced accuracy >80%) and anatomical specificity, irrespective of whether we increased excitatory transmission (wt-hSyn-hM3Dq and wt-CAMK-hM3Dq cohort) or suppressed inhibition (PVCre-hSyn-hM4Di cohort). In a cohort of wt-CAMK-hM3Dq mice, we detected BOLD dynamics with a high accuracy in the contralateral left SSp, this could be due to DREADD transfected transcallosal excitatory neurons. Moreover, high classification accuracy was also observed in the dynamics of the right SSp between the two excitatory DREADD cohorts (wt-hSyn-hM3Dq and wt-CAMK-hM3Dq). This difference can be attributed to the two promoters and their distinct transfection affinities towards excitatory and inhibitory neurons.

The E:I BOLD signature learned from acutely modulating cell activity, could be detected in two independent cohorts of *Fmr1*^{Y/-} mice, a well-characterized mouse model of ASD. We chose *Fmr1*^{Y/-} mice for external validation because they are known to have deficits in local feedback inhibition due to reduced PV interneuron density (Cea-Del Rio and Huntsman, 2014, Selby et al., 2007). This leads to increased excitability and decreased synchrony of pyramidal cell firing through gamma oscillations (Wohr et al., 2015, Gibson et al., 2008) as well as substantially reduced FC in cortico-cortical and cortico-striatal circuits (Zerbi et al., 2018, Zerbi et al., 2019b). Interestingly, above chance-level detection accuracies of BOLD dynamics

characterizing over-excitation in *Fmr1*^{Y/-} mice were found in regions which normally exhibit high PV cell densities (Selby et al., 2007) providing further indirect evidence that the specific features of abnormal BOLD dynamics are related to the depletion of PV neurons in this mouse model. *Fmr1*^{Y/-} mice exhibit depletion of PV interneurons resulting in chronic overexcitation of the cortex, while PV interneurons in our PVCre-hSyn-hM4Di mice are only acutely manipulated. However, even though these differences between these two models exist, it is only because of their mechanistical similarities that a common dynamical signature with predictive accuracy can be observed. This indicates that the underlying dynamical signature of both acute and chronic overexcitation caused by PV depletion or inhibition is mechanistically similar.

Our findings demonstrate that a chemogenetically inspired and experimentally validated classifier can be used as a “computational sensor” which uses BOLD dynamics to infer whether a specific brain area exhibits increased microcircuit E:I for example, due to abnormal PV neuron activity.

It is unclear whether this discovery is generalizable to the entire cortex since changes in microstructural properties such as cytoarchitecture, E:I, size, density and laminar distribution of distinct cell types vary continuously through mouse cortex (Kim et al., 2017b, Fulcher et al., 2019). These variations in spatial gradients shape functional specialization along the cortex and influence the intrinsic time scale that can be measured in BOLD dynamics in different cortical areas (Sethi et al., 2017). Nevertheless, we show above chance-level detection accuracy in the prefrontal cortex of *Fmr1*^{Y/-} mice that are also attributed to an increased E:I balance from previous studies (Paul et al., 2013). These results provide a new framework for mechanistically linking microscale circuit dynamics to macroscopic fMRI-based brain activity at rest. Thus far, this approach is unique because it uses causal microcircuit alterations to train a classifier that can detect similar alterations from distinct datasets obtained from large-scale imaging techniques. Our framework goes beyond describing long-range connectional aberrations caused by neurodevelopmental disorders and aims at providing deeper insights into how distinct microcircuit dynamics relate to large-scale, non-invasive imaging measurements which can be obtained across different species, including in human patients. Better linking macroscopic alteration to the underlying neurobiology is a pre-requisite for advancing neuroimaging as a tool in the context of clinical decision making.

3.6. Supplementary Figures and Discussion

Figure S3.1. Schematic of the experimental pipeline

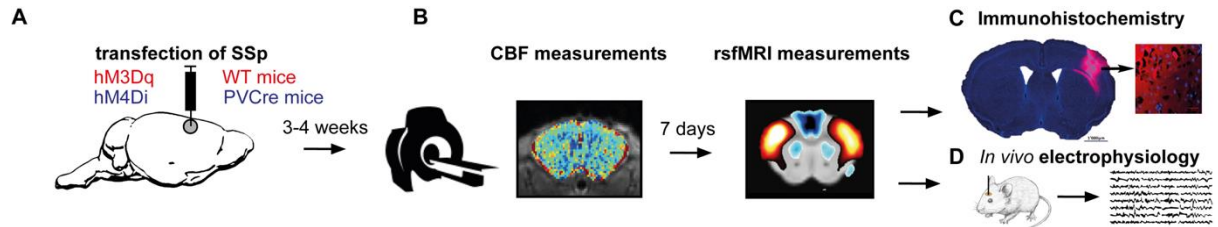


Figure S3.1. A) Administration of excitatory (hM3Dq) or inhibitory (hM4Di) DREADD constructs via viral injection into the right primary somatosensory cortex (SSp) of wildtype and PVCre mice, respectively. **B)** Three to four weeks after surgery, mice underwent multimodal MRI functional imaging for the assessment of cerebral blood flow and resting-state fMRI (rsfMRI). In each session, clozapine was injected iv. (≤ 0.03 mg/kg) to activate the DREADD during the recordings. **C)** After the rsfMRI session, the successful viral transfection was ensured by immunohistochemistry as depicted by the results from a single brain slice. **D)** In some mice, in vivo electrophysiological recordings were taken from the right SSp and from a control region, to confirm that DREADD-transfected neurons are successfully and selectively activated after clozapine injection and cause a net shift towards over-excitation.

Figure S3.2. Low doses of clozapine have no effect on neuronal activity

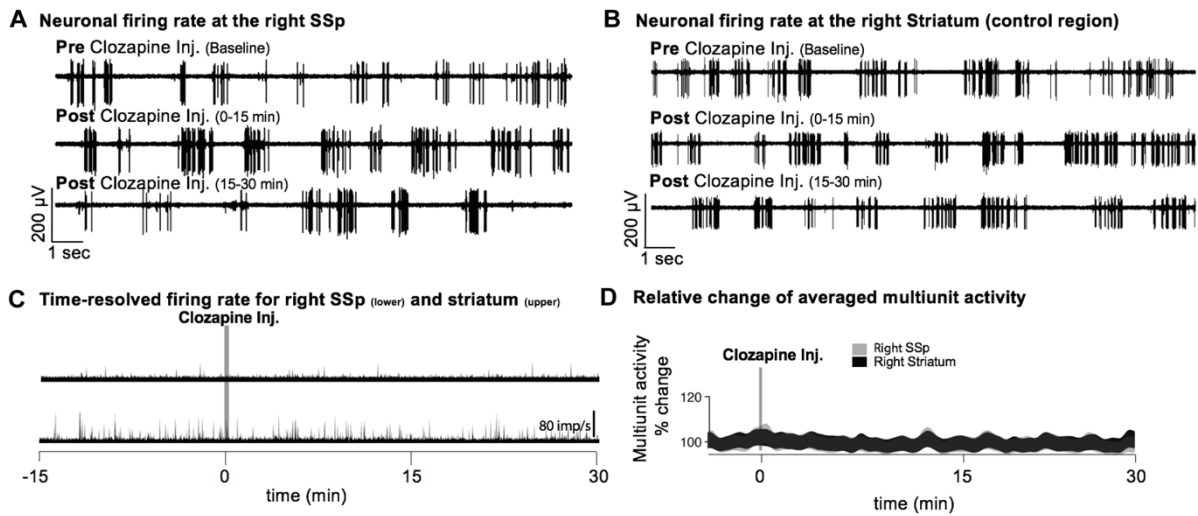
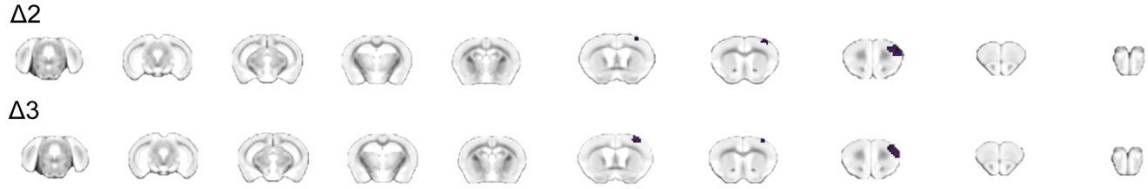


Figure S3.2. A) Neuronal firing rate before and after clozapine injection (30 μ g/kg) within the right SSp of a control animal, indicating unaltered neuronal firing rate. **B)** As **A** but for the right striatum, (control area) indicating no change in the neuronal firing rate after clozapine injection. **C)** Time-resolved firing rate in millisecond bins for the right SSp and right striatum. No change in firing rate after clozapine injection is observed in either of two regions. **D)** Relative change of averaged multiunit activity recorded in the right SSp and right striatum indicating no overall % change upon clozapine injection ($n=2$).

Figure S3.3. Short- and long-range connectivity changes induced by activating hSyn-hM3Dq

Wt-hSyn-hM3Dq mice

A Regional Homogeneity



B Brain-wide voxel-mirrored homotopic connectivity

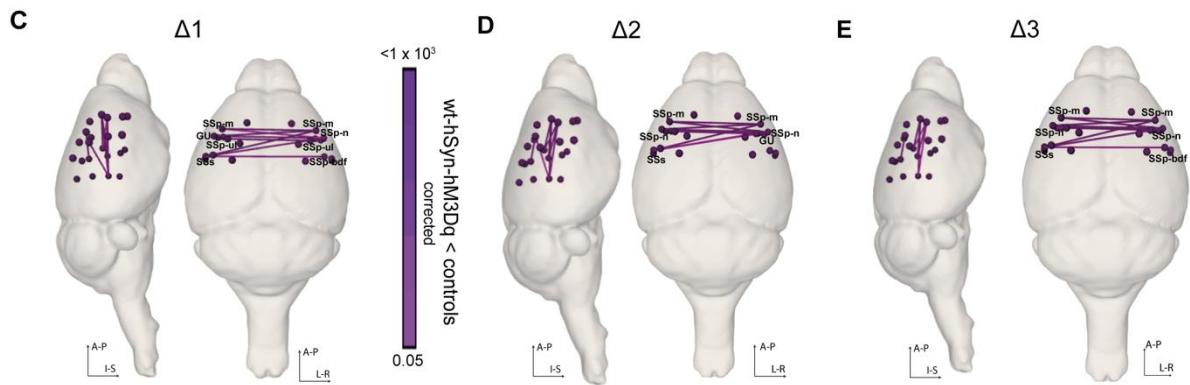


Figure S3.3. A) Significant decrease (corrected) in regional homogeneity shown through coronal slices for $\Delta 2$ and $\Delta 3$ time periods. **B)** Significant (corrected) interhemispheric decrease in VMHC shown through coronal slices for $\Delta 2$ and $\Delta 3$ time periods. **C)** Whole-brain connectome analysis shows a significant interhemispheric reduction between somatosensory cortices for $\Delta 1$, $\Delta 2$ and $\Delta 3$ time periods between wt-hM3Dq ($n=14$) mice and controls ($n=13$). Regions affected are as follows: SSp-m: Primary Somatosensory Area, mouth; GU: Gustatory areas; SSp-ul: Primary Somatosensory Area, upper limb; SSp-bdf: Primary Somatosensory Area, barrel field; SSp-n: Primary Somatosensory Area, nose.

Figure S3.4. Long-range connectivity changes induced by activating hM3Dq

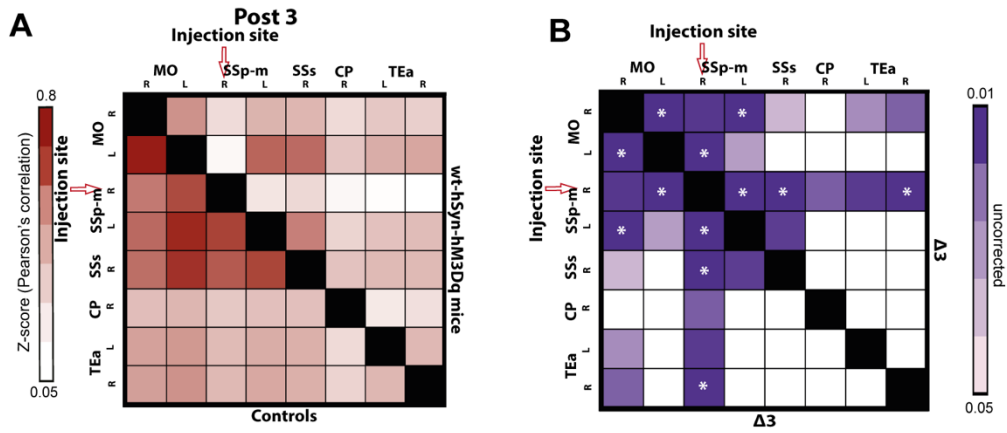


Figure S3.4. A) Averaged and z-scored Pearson's correlation of all control ($n=13$) animals (lower triangle of the matrix) and all wt-hSyn-hM3Dq ($n=14$) animals (upper triangle of the matrix) for Post 3. **B)** Statistically significant differences during $\Delta 3$ time period among 5 brain regions (MO – Somatomotor cortex, SSp – somatosensory cortex, SSs- supplementary somatosensory cortex, CP – caudoputamen and TEa – temporal association cortex, R – right, L - left) between the controls and wt-hM3Dq mice. The stars within some ROIs indicate statistically significant differences that survived correction of multiple comparisons.

Figure S3.5. hM3Dq activated by CNO causes inter-hemispheric connectivity reduction

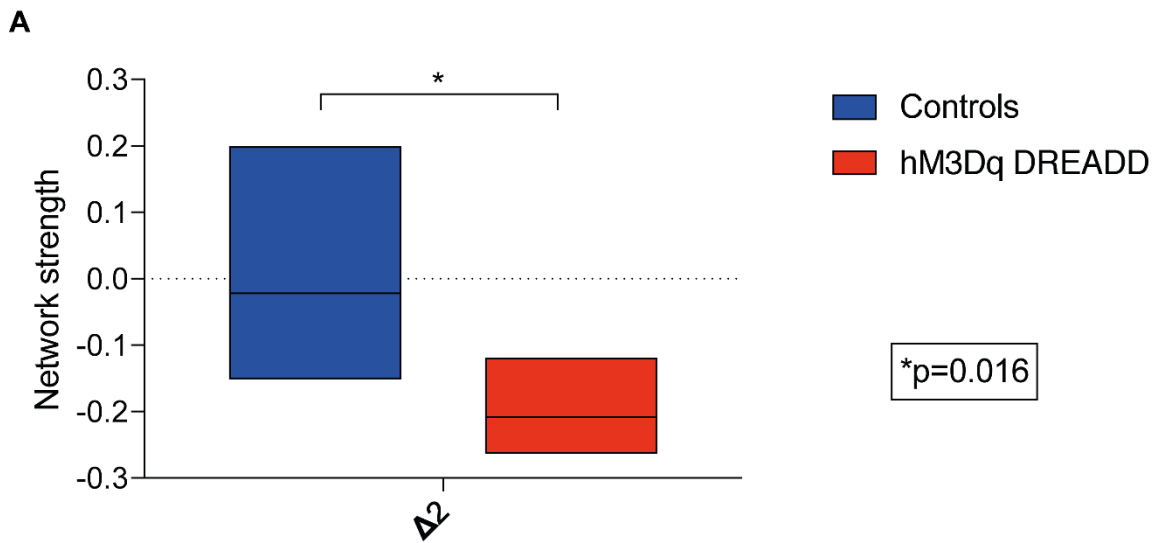


Figure S3.5. Graph represents a decrease in interhemispheric connectivity (z-scored correlation) between the somatomotor regions in wt-hM3Dq mice ($n = 6$) compared to controls ($n = 5$), occurring 15 min after the CNO i.v. injection. The DREADD was activated using 1 mg/kg CNO. Univariate analysis of ANOVA show a significant difference between the groups $F(1,9) = 8.710$, $p = 0.02$.

Figure S3.6. Changes induced by activating hM4Di in PVCre mice.

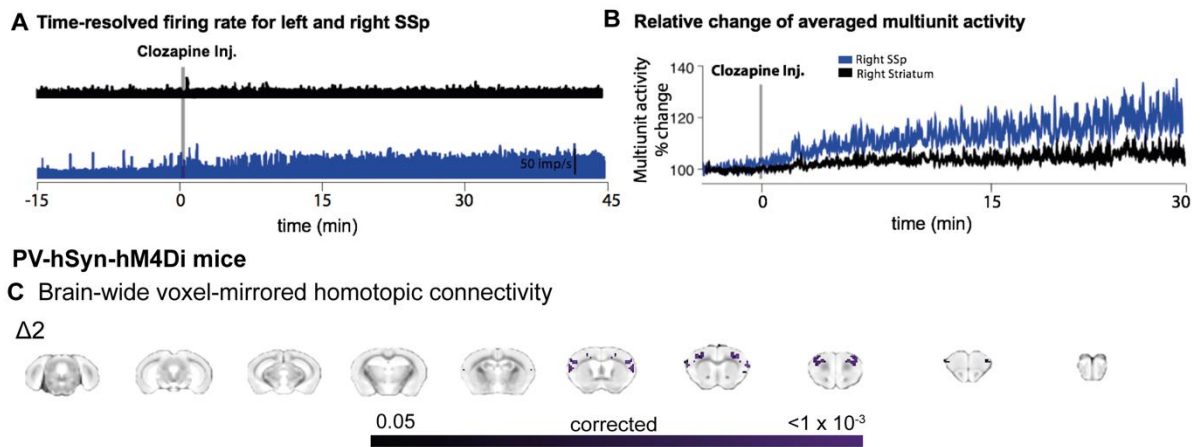


Figure S3.6. A) Time-resolved firing rate in millisecond bins for the right (blue) somatosensory cortex and right striatum (black). A steady increase of firing rate occurs at the right SSp once clozapine is injected, while no change occurs in striatum. **B)** Averaged multiunit activity increase by almost 20% compared to baseline (before clozapine injection) in right SSp and remained similar compared to baseline in the striatum. **C)** Significant decrease (TFCE-corrected) in symmetric connectivity in PVCre-hSyn-hM4Di mice compared to controls depicted on coronal slices for the $\Delta 2$ time point.

Figure S3.7. Viral expressions in the SSp of wt-hSyn-hM3Dq, PVCre-hSyn-hM4Di and wt-CAMKII-hM3Dq mice

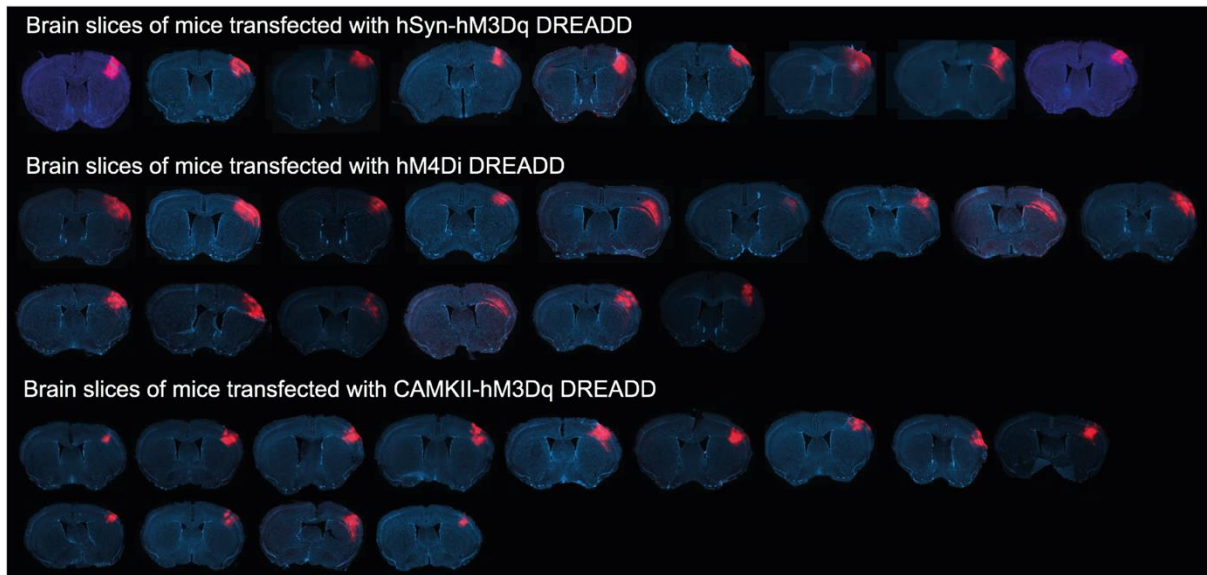


Figure S3.7. Viral expressions at the somatosensory cortex of the wt-hSyn-hM3Dq, PVCre-hSyn-hM4Di and for wt-CAMKII-hM3Dq mice. Each slice represents the expression obtained from a single mouse.

Figure S3.8. Statistical comparison between different doses of clozapine in wt-hSyn-hM3Dq and control mice

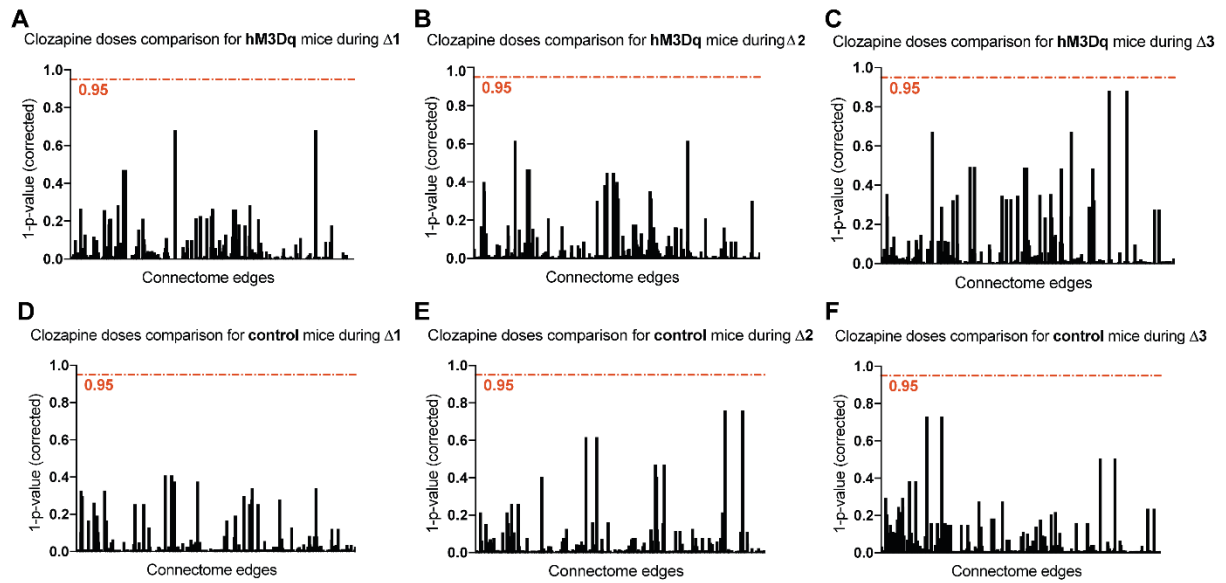


Figure S3.8. A,B,C) Corrected statistical comparison (1-p-value) between the control groups that received 2 different doses of clozapine (10 mg/kg or 30 mg/kg) for the $\Delta 1$, $\Delta 2$ and $\Delta 3$ time periods. Red line represents a start of significance, showing that there are no significant differences between the groups. **D,E,F)** Similar information to the 3 graphs above but only for the mice transfected with hM3Dq DREADD.

Figure S3.9. Univariate BOLD dynamics are weakly distinguishable at the left SSsp and VIS among the three group

A Balanced accuracy (%) Left SSsp ($\Delta 1$) **B** Balanced accuracy (%) VIS (control) ($\Delta 1$)

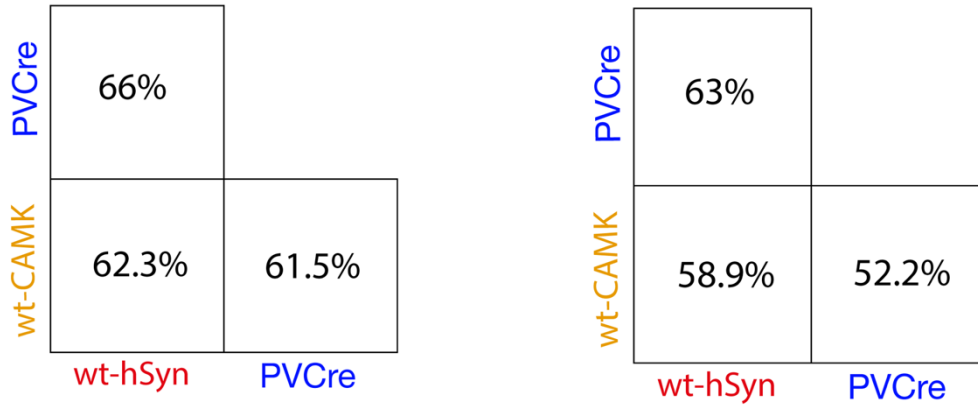


Figure S3.9. For a given region and pair of classes, we used the features of each time series (relative to baseline) as the basis for classification and quantified them as the 10-fold cross-validated balanced classification accuracy (%). Classification results for the Left SSsp (**A**) and VIS control (**B**) region at $\Delta 1$.

Figure S3.10. Univariate BOLD dynamics change in similar ways in wt-hSyn-hM3Dq and PVCre-hSyn-hM4Di

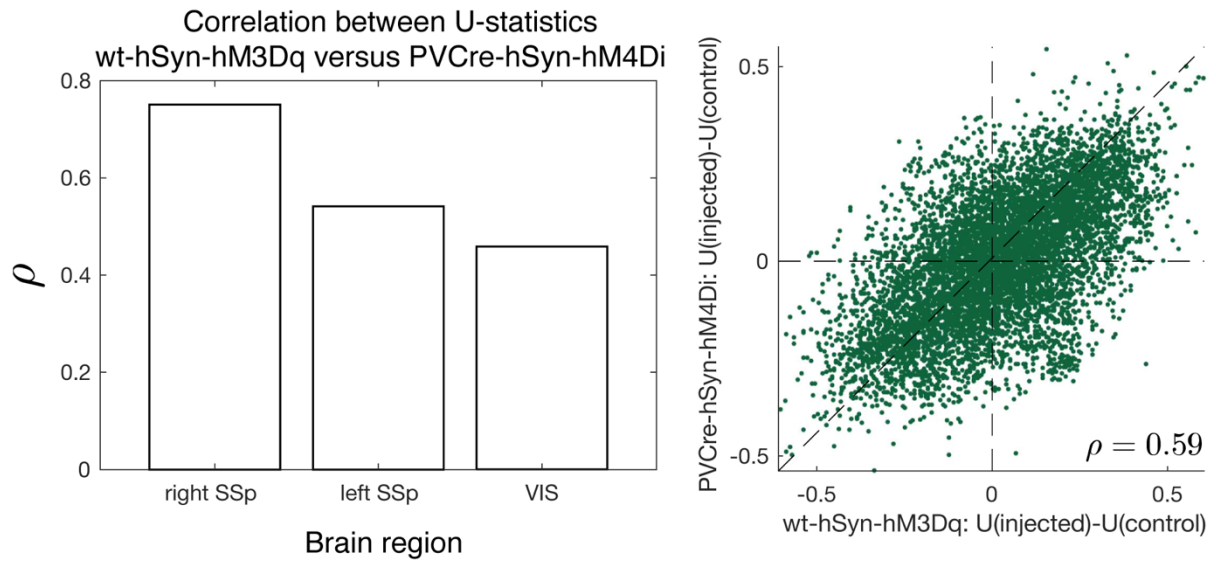


Figure S3.10. A) We measured similarity of dynamical changes in wt-hSyn-hM3Dq and PVCre-hSyn-hM4Di relative to control as the correlation, ρ , of Mann-Whitney U statistics computed for each feature at $\Delta 1$, which are plotted as bars for each brain region. **B)** After subtracting matched test statistics measured in VIS from those measured in right SSp, the residual correlation in the injected region remains strong, shown here as a scatter plot.

Chapter 3. Cortical E:I imbalance causes abnormal brain network dynamics as observed in neurodevelopmental disorders

Table S3.1. Demographics of mice used in the experiment

Mouse ID	Genotype	Age at surgery (days)	Bodyweight at surgery (gr)	Type of DREADD	Gender	Bodyweight on the scan day (gr)	Clozapine Dose ($\mu\text{g}/\text{kg}$)
86	C57BL/6	84	23.4	excitatory	male	25.1	10
89	C57BL/6	84	22.7	excitatory	male	24.3	10
90	C57BL/6	84	22.9	excitatory	male	23.4	10
101	C57BL/6	51	21.9	excitatory	male	25.1	10
102	C57BL/6	51	24.7	excitatory	male	25.6	10
103	C57BL/6	51	24.9	excitatory	male	28.2	10
104	C57BL/6	51	25	excitatory	male	25.5	10
105	C57BL/6	51	27.1	excitatory	male	27.6	10
109	C57BL/6	52	24.4	excitatory	male	25	10
110	C57BL/6	52	25.2	excitatory	male	27	10
101	C57BL/6	51	21.9	excitatory	male	26.2	30
103	C57BL/6	51	24.9	excitatory	male	29.3	30
104	C57BL/6	51	25	excitatory	male	23.3	30
110	C57BL/6	52	25.2	excitatory	male	29.1	30
average		58.29 \pm 13.94	24.23 \pm 1.47			26.05 \pm 1.94	
70	C57BL/6	86	30	sham	male	28.6	10
72	C57BL/6	86	20.8	sham	male	23.6	10
73	C57BL/6	86	21	sham	male	23.3	10
75	C57BL/6	86	22	sham	male	24	10
119	C57BL/6	53	24.9	sham	male	25.5	10
121	C57BL/6	54	26.6	sham	male	27.3	10
123	C57BL/6	54	26.2	sham	male	26.6	10
124	C57BL/6	54	26.7	sham	male	28.6	10
125	C57BL/6	54	25	sham	male	25.9	10
121	C57BL/6	54	26.6	sham	male	29	30
123	C57BL/6	54	26.2	sham	male	29.6	30
124	C57BL/6	54	26.7	sham	male	28.1	30
125	C57BL/6	54	25	sham	male	27.1	30
average		63.77 \pm 15.43	23.21 \pm 2.6			26.71 \pm 2.12	
8	PVCre	89	22	inhibitory	female	26.5	30
9	PVCre	89	20.3	inhibitory	female	20.7	30
10	PVCre	89	21.1	inhibitory	female	22.5	30
11	PVCre	81	28.6	inhibitory	male	29.3	30
12	PVCre	81	30.7	inhibitory	male	33	30
13	PVCre	81	27.3	inhibitory	male	28.1	30
14	PVCre	89	22	inhibitory	female	24.7	30
5	PVCre	89	28.9	inhibitory	male	29.5	30
6	PVCre	90	29.6	inhibitory	male	26.1	30
7	PVCre	89	19.8	inhibitory	female	21.7	30
100	PVCre	61	24.5	inhibitory	male	25.1	30
64	PVCre	98	25.2	inhibitory	male	25.8	30
65	PVCre	98	27.2	inhibitory	male	28	30
71	PVCre	82	30	inhibitory	male	29.3	30
76	PVCre	82	26.9	inhibitory	male	27.8	30
87	PVCre	75	27.9	inhibitory	male	28.2	30
89	PVCre	75	27.5	inhibitory	male	27.9	30
92	PVCre	61	27.5	inhibitory	male	30.1	30
93	PVCre	61	27.7	inhibitory	male	29.7	30
average		82.11 \pm 11.3	26.04 \pm 3.4			27.1 \pm 1.40	
185	C57BL/6	66	23.8	CAMK - excitatory	male	27.3	30
188	C57BL/6	66	24.2	CAMK - excitatory	male	26	30
190	C57BL/6	67	24.5	CAMK - excitatory	male	25.7	30
195	C57BL/6	68	26.7	CAMK - excitatory	male	26	30
199	C57BL/6	67	23.8	CAMK - excitatory	male	27.6	30
192	C57BL/6	67	22.3	CAMK - excitatory	male	25.8	30
193	C57BL/6	67	24.1	CAMK - excitatory	male	26.6	30
194	C57BL/6	67	25.8	CAMK - excitatory	male	28.2	30
200	C57BL/6	76	26.6	CAMK - excitatory	male	29.3	30
201	C57BL/6	76	27	CAMK - excitatory	male	29.2	30
202	C57BL/6	76	25.6	CAMK - excitatory	male	27.2	30
203	C57BL/6	76	23	CAMK - excitatory	male	24.7	30
204	C57BL/6	76	26.1	CAMK - excitatory	male	28.4	30
average		70.4 \pm 4.6	24.9 \pm 1.5			27.1 \pm 1.4	

Table S1. Details about all the mice involved in the experiments with mean + standard deviation calculated for mouse age at surgery, bodyweight at surgery and bodyweight on the scan day.

Supplementary Discussion

Activated DREADDs caused relative over-excitation at the cellular level and within cortical circuits

In our first experiment, we used hM3Dq-DREADD on human Synapsin (hSyn) promoter to achieve a strong shift in E:I balance towards over-excitation in the targeted region. As human Synapsin promoter is active in both excitatory and inhibitory neurons, we decided to repeat the experiment but now using CAMKII promoter to generate clear bias towards gene expression in excitatory cortical neurons (up to 85%). To address this, we injected a cohort of mice with a hM3Dq-DREADD on a CAMKII promoter and confirmed similar results as with hSyn, thus showing that both hM3Dq DREADD on a CAMKII or hSyn promoter generate identical results (Fig. 3.3). While none of the promoters in AAV can restrict its affinity exclusively toward excitatory neurons, our electrophysiological results confirmed that activating DREADDs in the wt-hSyn-hM3Dq mice caused a significant increase of neuronal firing rate in the targeted region, suggesting a general over-excitation. Convergent evidence is also revealed by our CBF measurements in both wt-hSyn-hM3Dq and wt-CAMK-hM3Dq mice. Numerous PET and fMRI studies have demonstrated that CBF reflects glucose metabolism, and it is considered an indirect marker of neural activity at the population level (Chen et al., 2008, Juepter and Weiller, 1995). Here we report an increase in CBF exclusively in the right SSp of DREADD mice, which confirms the anatomical specificity of our intervention in exciting the targeted area.

In the second set of experiments, we used PVCre mice to ensure cell-specificity of the hM4Di DREADD. Analogous to our first experiment, *in vivo* electrophysiology confirmed that inhibiting GABAergic PV neurons via hM4Di significantly increased neuronal population firing and moderately increased blood flow. This finding is consistent with previous literature, which states that suppression of PV interneurons leads to an increased cortical excitation i.e. increase in number of cells spiking at the population level (Moore et al., 2018, Atallah et al., 2012). In summary, even though the two experiments targeted different biological pathways, both manipulations shifted cortical E:I balance in a similar manner by causing a net increase in the firing rate of neuronal populations within the targeted SSp, as shown by convergent evidence from *in vivo* electrophysiology and cerebral blood flow.

In order to activate DREADDs, we used low-doses of clozapine instead of the more commonly used clozapine-N-oxide (CNO). Clozapine is a potent antipsychotic medication used in the treatment of schizophrenia that binds to a number of receptors including serotonin, α 1-adrenergic receptors, muscarinic-1 and histamine (Nucifora et al., 2017). Clozapine is a metabolite of CNO but, unlike CNO, is able to freely pass the blood brain barrier. Because of its high affinity for DREADD receptors, clozapine is thought to be the actual activator of DREADDs in *in vivo* studies (Gomez et al., 2017, Manvich et al., 2018). In our experiments, we used clozapine doses of 0.01–0.03 mg/kg to activate the DREADDs, which are below the

threshold level necessary to elicit a behavioral effect in mice. To further control for any unspecific effect of clozapine, we employed a randomized controlled design injecting identical doses of clozapine in sham-operated mice. We also conducted experiments using two different doses of clozapine (Fig. S3.8) and found no differences in any of the groups, suggesting that the lower dose (0.01 mg/kg) is sufficient to activate DREADDs *in vivo*. Furthermore, we performed analogous experiments in smaller mouse cohorts using CNO, which revealed similar effects, i.e., a significant decrease in interhemispheric connectivity in the targeted somatomotor cortex (Fig. S3.5).

Mildly anesthetized animals were used during the experiment in order to minimize animal movement and potential distress during examination. Increasing body of literature emphasizes that the importance for understanding the effects of anesthesia on functional connectivity is key to correct interpretation of the results (Bukhari et al., 2017, Jonckers et al., 2011, Grandjean et al., 2014a). For optimal results, we used a combination of medetomidine (vasoconstrictor), isoflurane (vasodilator) and pancuronium (muscle relaxant) at very low doses (Zerbi et al., 2015, Grandjean et al., 2014a). Isoflurane is predominantly targeting the GABAergic neurotransmitter system (Lukasik and Gillies, 2003). GABA receptors are widely spread throughout the brain, therefore it is essential to control for percentage of isoflurane used in the anesthesia. Medetomidine predominantly targets $\alpha 2$ adrenergic receptors, whose distribution within the brain varies, being largely located in the brainstem (especially locus coeruleus) (Lukasik and Gillies, 2003). By combining medetomidine with isoflurane we ensured that isoflurane is kept at minimum level (0.5%) and as so does not have a dominant effect on functional connectivity.

Univariate BOLD dynamics change in similar ways in both wt-hSyn-hM3Dq and PVCre-hSyn-hM4Di

We aimed to test whether changes in univariate BOLD dynamics resulting from both DREADDs mechanisms (wt-hSyn-hM3Dq and PVCre-hSyn-hM4Di) relative to controls were similar, focusing on the $\Delta 1$ time period. For each time-series feature, we quantified how the DREADDs condition differed from the sham condition as a Mann-Whitney U statistic, and then compared these statistics between the two different DREADDs. If the properties of BOLD dynamics change similarly due to wt-hSyn-hM3Dq and PVCre-hSyn-hM4Di groups, then we should detect this as an increase in correlation, ρ , between the two sets of Mann-Whitney U statistics. Indeed, we found that this correlation, ρ , is lowest in the control region (VIS, $\rho = 0.46$), increases in the contralateral region (left SSp, $\rho = 0.54$), and is highest in the injected region (right SSp, $\rho = 0.75$), as shown in Fig. S3.6A. The two sets of Mann-Whitney U statistics (wt-hSyn-hM3Dq versus control and PVCre-hSyn-hM4Di versus control) are not independent due to a repeated comparison to the same set of control dynamics, likely accounting for the correlation observed in the VIS. After subtracting matched test statistics between the right

SSp and VIS, correlations between the residuals of this subtraction are strong in both the right SSp ($\rho_{\text{resid}} = 0.59$, shown in Fig. S8B), and left SSp ($\rho_{\text{resid}} = 0.47$).

Discriminatory Time-Series Features

Having demonstrated that wt-hSyn-hM3Dq and PVCre-hSyn-hM4Di manipulations cause distinctive changes to local BOLD dynamics, particularly in the injected region, we aimed to understand the specific properties of BOLD dynamics that drive this discriminability. We first investigated which time-series features most strongly differentiate wt-hSyn-hM3Dq from controls in the right SSp at $\Delta 1$. We scored the discriminability of each feature separately using a rank-sum test, correcting for multiple-hypothesis testing across all individual features by assuming independent tests (Benjamini and Hochberg, 1995) (a conservative correction due to high inter-correlation of many time-series features in *hctsa* (Fulcher et al., 2013)). A total of 924 features of wt-hSyn-hM3Dq BOLD dynamics were significantly different to control ($p_{\text{corr}} < 0.05$), including measures of variance, which were decreased in wt-hSyn-hM3Dq mice (e.g., standard deviation, $p_{\text{corr}} = 2 \times 10^{-3}$), and measures of autocorrelation, which were increased in wt-hSyn-hM3Dq mice (e.g., power in the lowest fifth of frequencies, $p_{\text{corr}} = 3 \times 10^{-3}$). A wide range of other features from diverse literatures also captured a significant difference in BOLD dynamics in wt-hSyn-hM3Dq mice relative to controls, including features of self-affine scaling, linear and nonlinear autocorrelation, local motifs, temporal entropy, model-based fits and forecasting, wavelet decompositions, outliers, and stationarity. Our results indicate a robust time-series signature of wt-hSyn-hM3Dq activation.

Similar analysis was repeated to identify any significant BOLD dynamics between wt-CAMK-hM3Dq relative to sham controls. We identified 189 time-series features that are individually informative of the difference from controls ($p_{\text{corr}} < 0.05$). Significant features are dominated by various measures of autocorrelation in the signal, similar to the characteristics identified above for wt-hSyn-hM3Dq.

We repeated the above analysis to identify whether we can isolate informative changes to BOLD dynamics caused by PVCre-hM4Di. We identified 225 time-series features that are individually informative of the difference from controls ($p_{\text{corr}} < 0.05$). Significant features are dominated by various measures of autocorrelation in the signal, similar to the characteristics identified above for wt-hSyn-hM3Dq.

BOLD time-series classification at $\Delta 2$ and $\Delta 3$

Our main analysis of classifying univariate BOLD dynamics was focused on the $\Delta 1$ time period. Here we demonstrate that the main qualitative results reported hold also for later time periods $\Delta 2$ (and $\Delta 3$, available only for wt-hSyn-hM3Dq and sham). Namely: the control region (VIS) was consistently classified at chance level ($p > 0.05$), the contralateral region (left SSp) mostly displayed a classifiability intermediate between the control and injected regions, while

the injected region (right SSp) consistently displayed the highest classification rates. Individual results are listed here:

- wt-hSyn-hM3Dq versus CONTROL at $\Delta 2$: right SSp: 86% ($p = 2 \times 10^4$), left SSp: 38% ($p = 0.8$), VIS: 53% ($p = 0.4$).
- wt-hSyn-hM3Dq versus CONTROL at $\Delta 3$: right SSp: 75% ($p = 0.01$), left SSp : 49% ($p = 0.5$), VIS: 45% ($p = 0.6$).
- PVCre-hSyn-hM4Di versus CONTROL at $\Delta 2$: right SSp: 66% ($p = 0.05$), left SSp: 72% ($p = 0.01$), VIS: 52% ($p = 0.4$).
- wt-hSyn-hM3Dq versus PVCre-hSyn-hM4Di at $\Delta 2$: right SSp: 68% ($p = 0.03$), left SSp: 52% ($p = 0.4$), VIS: 36% ($p = 0.9$).
- wt-CAMK-hM3Dq versus CONTROL at $\Delta 2$: right SSp: 65% ($p = 0.07$), left SSp: 56% ($p = 0.3$), VIS: 60% ($p = 0.2$).
- wt-CAMK-hM3Dq versus wt-hSyn-hM3Dq at $\Delta 2$: right SSp: 68% ($p = 0.03$), left SSp: 37% ($p = 0.8$), VIS: 48% ($p = 0.6$).
- wt-CAMK-hM3Dq versus PVCre-hSyn-hM4Di at $\Delta 2$: right SSp: 49% ($p = 0.5$), left SSp: 50% ($p = 0.5$), VIS: 38% ($p = 0.8$).

CHAPTER 4

Cell specific neuromodulation in the striatum shapes BOLD fluctuations in multiple thalamic and cortical regions of an anatomically connected circuit

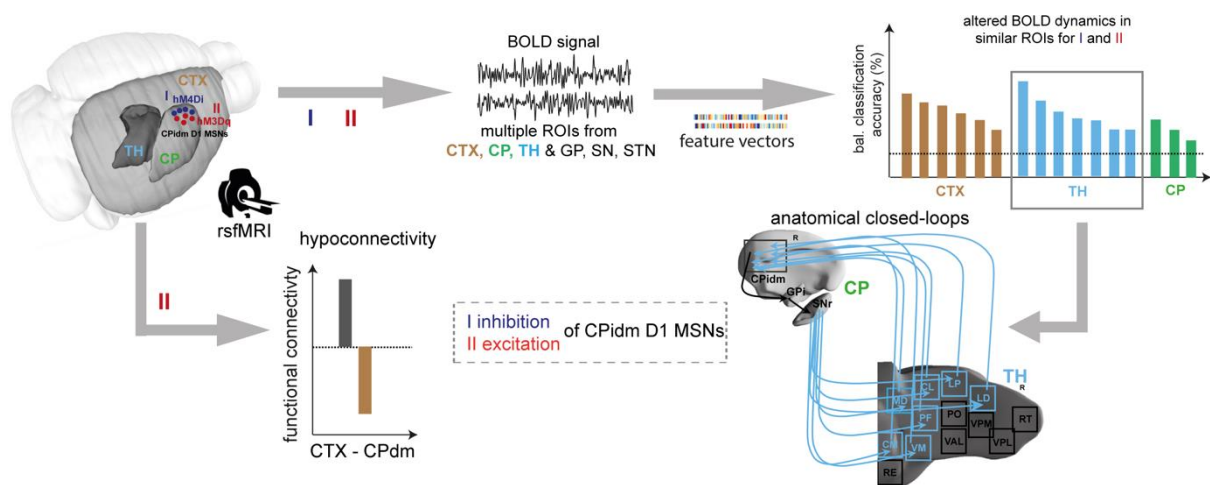
Marija Markicevic, Ben D. Fulcher, Oliver Sturman, Johannes Bohacek, Markus Rudin, Valerio Zerbi* and Nicole Wenderoth*
(*shared last authorship)

Manuscript in preparation

First author contributions

Conceptualization, performed viral injections, behavioral experiments, rsfMRI data acquisition, immunohistochemistry, all data analysis (except behavioural parameter extraction from the behavioural videos) and wrote the manuscript.

Graphical abstract



4.1. Abstract

Resting-state functional magnetic resonance imaging (rsfMRI) is a unique tool for detecting macroscale patterns of neuronal interactions across the whole brain at rest. Yet understanding how cellular level mechanisms map onto the macroscopic brain networks remains incompletely understood. While previous research has shown that regional cell-specific neuromodulation affects local BOLD dynamics, whether this neuromodulation also alters the BOLD dynamics of remote but anatomically connected regions, remains an open question. Here, we chemogenetically excited or inhibited D1 MSNs of right dorsomedial striatum and found that alterations of D1 MSN activity in the striatum propagate through anatomically connected networks, thereby shaping the dynamics of multiple thalamic and cortical regions within an anatomically defined circuit. Cortico-striatal functional connectivity

was reduced during excitation, while a trend towards an increase of functional connectivity was observed during inhibition. Our approach to analyze the BOLD dynamics within a region of interest can be readily applied to a large body of resting-state fMRI data obtained in humans. Such an analysis would provide region-specific information on altered neural activity which is complementary to conventional functional connectivity analyses.

4.2. Introduction

The brain is a complex network of anatomically connected and perpetually interacting neural populations. It has been shown that functional magnetic resonance imaging during the resting state is a unique tool for detecting macroscale patterns of neural interactions across the whole brain which emerge without performing a specific task. A large body of work has used rsfMRI for identifying interregional communication streams by estimating functional connectivity (FC) between pairs of brain areas. High FC is inferred when the spontaneous fluctuations of the blood oxygen level dependent (BOLD) signal are temporally correlated.

While FC analyses focus on statistical interdependencies between two brain areas, they do not directly consider the BOLD signal fluctuations themselves. However, we and others have shown recently that the dynamics of the spontaneous BOLD signal measured within a given brain area at rest, carry information regarding the underlying activity at the cell level (Roelofs et al., 2017, Peeters et al., 2020, Nakamura et al., 2020, Markicevic et al., 2020). In our previous work we combined rodent rsfMRI with chemogenetic neuromodulation of the somatosensory cortex and machine learning to show that manipulating neurons of the cortical microcircuit in a cell-type specific manner causes systematic alterations which can be detected by analyzing the BOLD timeseries dynamics measured with rsfMRI (Markicevic et al., 2020). This is a non-trivial and highly intriguing finding since the BOLD signal, which fluctuates in the range of 0.01 to 0.1 Hz, is several magnitudes slower than the dynamics of neural activity recorded at the cell level. Importantly, this result opens up new opportunities for using non-invasive neuroimaging to detect cell level alterations within a specific brain area, an analysis which provides complementary information to more conventional FC approaches that focus on interregional communication streams.

Here, we investigated whether modulating the cell-specific activity within one area also changes the BOLD signal dynamics of remote yet anatomically connected areas. To explore this, we chemogenetically excited or inhibited (Roth, 2016) the activity of D1 medium spiny neurons (MSNs) in the intermediate portion of the right dorsomedial caudate putamen (CPidm, i.e., the input area of the striatum) while acquiring rsfMRI data across the whole brain. We chose CPidm because it is part of an anatomically well-defined and broadly studied striato-thalamic-cortical circuit (Wall et al., 2013, Runegaard et al., 2019, Lee et al., 2016). We hypothesized that the chemogenetic manipulation would modulate neural activity within the

target area CPidm as well as in anatomically connected sub-areas of thalamus and cortex (Grandjean et al., 2017b). To test this hypothesis, the Allen Mouse Brain Connectivity Atlas (Oh et al., 2014) and Mouse Cortico-Striatal Projectome (Hintiryan et al., 2016) were used to identify the strongest monosynaptic projections among basal ganglia, thalamus and cortex and to identify anatomically connected regions of interest. We applied two different analytical approaches: first, we investigated whether either exciting or inhibiting D1 MSNs modulates BOLD timeseries fluctuations within regions of interest. These concerns (i) the modulated CPidm region but also (ii) anatomically connected regions along the striato-thalamic-cortical circuit. Spontaneous BOLD signal fluctuations were identified via a set of general features which are used across multiple scientific fields for timeseries analysis of various signals. Each feature captures a different type of interpretable property of the univariate timeseries, enabling an unbiased assessment of regional BOLD fluctuations (Fulcher et al., 2013, Fulcher and Jones, 2017). Second, we also tested whether the chemogenetic manipulation of CPidm alters FC. According to our anatomical hypothesis, we focused on connections between the targeted area CPidm and all other thalamic and cortical regions-of-interest (ROIs).

These assessments of regional BOLD dynamics within this anatomically defined circuit provides new insights into how the effect of cell specific manipulations propagates through anatomically connected networks.

4.3. Materials and Methods

All experiments and procedures were conducted following the Swiss federal Ordinance for animal experimentation and approved by Zurich cantonal Veterinary Office (ZH238/15 and ZH062/18). House inbred BAC-mediated transgenic mouse line from GENSAT (BAC-Cre *Drd1a*-262 – D1Cre) (Gong et al., 2003) was used in this study, while the first generation was obtained from the lab of Prof. Jin Hyung Lee at Stanford University (Lee et al., 2016). All D1Cre mice were kept in standard housing under 12h light/dark cycle with food and water provided *ad libitum* throughout the whole experiment. A total of 38 mice were used in the experiment, aged 16.2 ± 2.8 weeks and weighing 24.9 ± 3.3 gr at the day of the surgery.

Stereotactic transfection procedure

Each mouse was initially anesthetized using a mixture of midazolam (5mg/ml; Sintetica, Switzerland), fentanyl (50mcg/ml; Actavis AG, Switzerland) and medetomidine (1mg/ml; Orion Pharma, Finland). Upon anesthesia induction, mice were placed on a heating pad and the temperature was kept at 35°C (Harvard Apparatus, USA). Following shaving and cleaning, an incision along the midline of scalp was made. The intermediate portion of the right dorsomedial caudate-putamen (CPidm) was targeted at the coordinates of +0.5mm AP (anterior posterior), -1.5mm ML (medio-lateral) and -3.0mm DV (dorso-ventral) relative to

the Bregma using a drill and microinjection robot (Neurostar, Germany) with a 10 ul NanoFil syringe and 34Ga bevelled needle (World Precision Instruments, Germany). 950 nl of double-floxed inverted (DIO) recombinant AAV8 virus was used to express either hM3Dq-mCherry (excitatory DREADD, n=13, 8 female) or hM4Di-mCherry (inhibitory DREADD, n=15, 7 female) or mCherry (control, n=10, 6 female). The virus was injected at the rate of 0.06 ul/min and provided by Viral Vector Core Facility of the Neuroscience Centre Zurich (<http://www.vvf.uzh.ch/en.html>). Upon the injection, the needle was left in place for 10 min and then slowly withdrawn. Subsequently, mice were given an anesthesia antidote consisting of tegmestic (0.3mg/ml; Reckitt Benckiser AG, Switzerland), annexate (0.1mg/ml; Swissmedic, Switzerland) and antisedan (0.1mg/ml; Orion Pharma, Finland) and left to fully recover. Following the surgery, ketoprofen (10mg/kg; Richter Pharma AG, Austria) was subcutaneously injected daily for at least 3 days to reduce any post-operative pain. Animals were given 3-4 weeks to fully recover from the surgery and to allow for expression of the transgene prior to the scanning session. The viral expression map showing the viral expression of all mice included in this study is shown in Fig. 4.1C.

Behavioral open field test

A custom-made box (50 x 50 x 50 cm) consisting of light grey walls and a floor was designed and placed in a room with homogeneously spread light source. Each mouse spent 5 min exploring the box before the start of the experiment. To activate the DREADD, clozapine was intraperitoneally injected at the dose of 30 µg/kg, 10min before the start of recording. A total of 32 mice underwent an open field behavioral test and each recording lasted 25 min. Data was analyzed using EthoVision XT14 (Noldus, the Netherlands) software for total distance travelled, a number of clockwise and anticlockwise rotations for each mouse. Statistical analysis was performed using multivariate ANOVA implemented in SPSS24 (IBM, USA). To account for possible gender differences, age and weight were used as covariates.

MRI setup and animal preparation

Resting-state fMRI (rsfMRI) measurements were obtained at the 7T Bruker BioSpec scanner equipped with a Pharmascan magnet and a high signal-to-noise ratio (SNR) receive-only cryogenic coil (Bruker BioSpin AG, Fällanden, Switzerland) in combination with a linearly polarized room temperature volume resonator for rf transmission.

Standardized anesthesia protocols and animal monitoring procedures were utilized for performing rsfMRI scans (Markicevic et al., 2020). Briefly, mice were initially anesthetized with 3% isoflurane in 1:4 O₂ to air mixture for 3 min to allow for endotracheal intubation and tail vein cannulation. Mice were positioned on an MRI-compatible support, equipped with hot water-flowing bed to keep the temperature of the animal constant throughout the entire measurement (36.6 ± 0.5°C). The animals were fixed with ear bars and mechanically ventilated via a small animal ventilator (CWE, Ardmore, USA) at the rate of 80 breaths per

minute, with 1.8 ml/min flow of isoflurane at 2%. Subsequently, a bolus containing a mixture of medetomidine (0.05 mg/kg) and pancuronium (0.25 mg/kg) was injected via the cannulated vein and isoflurane lowered at 1%. Five minutes following the bolus injection, a continuous infusion of medetomidine (0.1 mg/kg/h) and pancuronium (0.25 mg/kg/h) was started while isoflurane was further reduced to 0.5%. Animal preparation took on average 16.1 ± 2.7 minutes and all animals fully recovered within 10 min after the measurement.

Resting-state fMRI acquisition and data preprocessing

Acquisition parameters were the following: repetition time TR=1s, echo time TE=15ms, flip angle= 60°, matrix size = 90x50, in-plane resolution = 0.2x0.2 mm², number of slices = 20, slice thickness = 0.4 mm, 2280 volumes for a total scan of 38 min. Clozapine, the DREADD activator, was intravenously injected 15 min after the scan start at the dose of 30 µg/kg and a total of 38 D1Cre animals (10 controls and 13 D1 excitatory and 15 D1 inhibitory mice) were scanned. Data was preprocessed using an already established pipeline for removal of artefacts from the time-series (Zerbi et al., 2015, Markicevic et al., 2020). Briefly, each 4D dataset was normalized in a study-specific EPI template (Advanced Normalization Tools, ANTs v2.1, picsl.upenn.edu/ANTS) and fed into MELODIC (Multivariate Exploratory Linear Optimized Decomposition of Independent Components) to perform within subject special-ICA with a fixed dimensionality estimation (number of components set to 60). The procedure included motion correction and in-plane smoothing with a 0.3 mm kernel. FSL-FIX study-specific classifier, obtained from an independent dataset of 15 mice, was used to perform a 'conservative' removal of the variance of the artefactual components (Griffanti et al., 2014). Subsequently, the dataset was despiked, band-pass filtered (0.01-0.25 Hz) based on the frequency distribution of the fMRI signal under medetomidine anesthesia (Grandjean et al., 2014a) (Pan et al., 2013) and finally normalized into AMBMC template (www.imaging.org.au/AMBMC) using ANTs. Each dataset was split into two 900 data points (equivalent of 15 min of scanning), first of the baseline and second after the clozapine injection (post clozapine). Four minutes or 240 data points between the baseline and post clozapine were discarded, as it is the time required for the DREADD to become fully activated. The difference between the baseline (first 15 min of scan) and post clozapine is further referred to as $\Delta 1$.

Defining Regions of Interests (ROI) based on structural connectivity within striato-thalamic-cortical circuits

The Allen Mouse Brain Connectivity Atlas (Oh et al., 2014) was used to map out the mesoscale structural connectome of the striato-thalamic-cortical circuit containing our striatal target area CPidm. The Allen Mouse Brain Connectivity Atlas defines 213 brain regions, and the connectivity data was summarized in a form of normalized connectivity strength represented by a p-value for each edge in the connectome of 213 by 213 brain regions. These connectivity strengths between ontological brain regions were constructed via a computational model, where normalized tracer volumes between each source and target were used to define the

connection strengths. A monosynaptic projection from one region to another was inferred if the edge's p-value was smaller than 0.05.

Based on these structural connectome data, we re-constructed which regions of interest (ROIs) form the striato-thalamic-cortical loop including CPidm using a step-wise approach. First, starting from the caudate putamen (CP) as our "seed area" (since the Allen Mouse Brain Connectivity Atlas contains no more detailed sub-divisions), we identified globus pallidus external (GPe)/ internal (GPi) and substantia nigra par compacta (SNc)/pars reticulata (SNr) as monosynaptically connected brain areas. Second, GPe/i and SNc/SNr were used as seed areas to identify STN as well as several thalamic ROIs (RT, PP, LH, VM, PF, VAL, IMD, SPA, SPFp, VPMpc and POL, see Fig. 4.2A-D for more detailed explanations) as being monosynaptically connected.

Third, using the identified thalamic regions as a seed we found direct projections to other thalamic subregions (MD, CM, AM, VPM, VPL, PO, CL, SPFm, LP, RH, RE, LD; see Fig.4.2D for explanations of the abbreviations). Forth, using all thalamic ROIs which were identified in the 2nd or 3rd step, we identified all connected cortical ROIs but only maintained those with a significant monosynaptic projection to CP, thereby closing the loop. These cortical regions were ACA, AI, MOp/s, SSp, GU, VISC, PL or RSP, ORB, PERI, VIS, PTLp (see Fig.4.2 for explanations of the abbreviations). Figure 4.2A-E graphically summarizes these steps.

Since some of the extracted thalamic and cortical ROIs consisted only of a few voxels they were merged with neighboring ROIs to improve the signal-to-noise ratio for the BOLD time series analysis. The following thalamic ROIs were merged together: 1) RE|LH|RH, 2) SPF|SPA|PP, 3) PO|POL, 4) VAL|VPM|VPMpc, 5) VM|CM; and the following cortical ROIs were merged together 6) VISC|GU and 7) ECT|PERI (full names of abbreviated ROIs are summarized in Fig. 4.2). Note that these specific ROIs were merged because they were (i) located next to each other and (ii) had similar anatomical connectivity patterns derived from Allen Mouse Brain Connectivity atlas. This resulted in total of 14 thalamic (TH) ROIs and 13 cortical (CTX) ROIs.

Note that the Allen Mouse Brain Connectivity Atlas contains caudate-putamen (CP) only as one large area. However, recent research has shown that the CP consists of functionally segregated parts (Hintiryan et al., 2016) which can be distinguished along a rostral-intermediate-caudal gradient, a dorsal-ventral gradient and a medial-lateral gradient. Therefore, we aimed to further refine the above selection of ROIs using more specific anatomical information. To do so we used the Mouse Cortico-Striatal Projectome consisting of 29 distinct regions within the CP (Hintiryan et al., 2016). We had a very specific a-priori hypothesis that activating the DREADDs with clozapine would modulate BOLD activity within the targeted CPidm subarea. Additionally, we used the fine-grained CP parcellation consisting

of 29 ROIs for an exploratory analysis, to check whether also other CP subareas might have been affected by our experimental manipulation.

Finally, we used information from the literature (Wall et al., 2013, Guo et al., 2015, Parker et al., 2016, Hunnicutt et al., 2016, Alloway et al., 2017, Collins et al., 2018, Evangelio et al., 2018, Diaz-Hernandez et al., 2018, Perry and Mitchell, 2019, Mandelbaum et al., 2019, Lee et al., 2020) to identify which of the thalamic nuclei identified above from the Allen Mouse Brain Connectivity Atlas, were specifically connected to CPidm (i.e. our targeted subarea of the caudate-putamen). Based on this information we refined our selection of thalamic ROIs to VM/CM, LD, MD, PF, LP and CL which are all reciprocally connected to CPidm, i.e., these thalamic nuclei receive projection from CPidm via the GP/SN and project back to the CPidm.

These 3 approaches to define ROIs that are a part of striato-thalamic-cortical circuit resulted in a total of 27 ROIs, 13 part of CTX, 7 part of TH, 3 part of CP and GPI, GPe, SNc, SNr and STN. These regions were utilized to analyze effects of CPidm neuromodulation displayed in figures 4.4 and 4.5.

Resting-state fMRI data analysis: Classification of univariate BOLD time series

Data processing and feature computation

Univariate BOLD timeseries were extracted for the ROIs described above (i.e., averaged across all voxels within the ROI), the timeseries were separated into 15 min during baseline and 15 min following clozapine injection (post clozapine) and labelled according to the three experimental groups they belonged to; i) D1 excitation (n=13) ii) D1 inhibition (n=15) and iii) D1 control (n=10).

Univariate timeseries properties were characterized using the *hctsa* toolbox (Fulcher and Jones, 2017, Fulcher et al., 2013) which extracts 7702 interpretable features per time series. For a detailed description of the *hctsa* toolbox see Fulcher and Jones, 2017. For each of the ROIs, 7702 timeseries features data were determined for 2 time points (baseline vs post clozapine injection) x 38 individual subjects (n=13 D1 excitation, n=15 D1 inhibition, n=10 controls). Features which were non-constant, fell within the pre-defined range of values and with real-numbered outputs within all three groups were used for further analysis. Each timeseries was labelled by the experimental group (D1 excitation, D1 inhibition, D1 control) and time point (baseline, t1 and post clozapine injection, t2).

Classification

The feature-based representations of BOLD timeseries in each brain area was used as the basis for classifying the different experimental conditions. The analysis focused on *changes*

of the timeseries features caused by activating the DREADDs by injecting clozapine. Therefore, timeseries features computed at baseline were subtracted from timeseries features obtained for post clozapine period, and the resulting feature differences were normalized using an outlier-robust sigmoidal transformation (Fulcher et al., 2013). A linear support vector machine classification model was trained on the normalized feature matrix for a given brain area, using inverse probability class reweighting to account for imbalances between experimental groups. A measure of discriminability of a pair of experimental groups was quantified as the balanced classification accuracy using 10-fold stratified cross validation, ensuring that each fold is an appropriate representative of the original data in terms of class imbalance, class distribution, mean and variance. Balanced accuracy was computed as the arithmetic mean of sensitivity and specificity. To reduce variance caused by the random partition of data into 10 folds, the procedure was repeated 50 times (with each iteration yielding a balanced accuracy value) and the resulting distribution of balanced accuracies was summarized as its mean and standard deviation.

In small samples, there is a greater probability that optimistic classification results can be obtained by chance. To account for this effect, statistical significance of the classification results obtained via a permutation tests whereby the group labels were randomly permuted. The null distribution of the classification accuracy metric used above (mean across 50 repeats of 10-fold cross-validated balanced accuracy) was obtained for 5000 random group label assignments. The statistical significance of a given classification result was then estimated as a permutation test (i.e., as the proportion of the 5000 null samples with a mean balanced classification rate exceeding the balanced accuracy obtained for the true group labels). Note that we reported uncorrected p-values (p_{uncor}) for exploratory control analysis for 29 CP subregions. As all the ROIs are statistically dependent, the FDR (False Discovery Rate) method of Benjamini and Hochberg was applied to correct for multiple comparisons (Benjamini and Hochberg, 1995).

Resting-state fMRI data analysis: functional connectivity analysis

BOLD timeseries were extracted from each of the ROIs that are part of the striato-thalamic-cortical circuit of interest. Functional connectivity between CPidm and all other ROIs was measured using regularized Pearson's correlation coefficient implemented in FSLnets (Figure 4.5B, C) on the normalized (post clozapine – baseline) data ($\Delta 1$). FSL General Linear Model (GLM) was used to perform statistical comparison among the 3 groups (D1 excitation, D1 inhibition and D1 control). The connectivity matrices were fed into a nonparametric permutation testing with 5000 permutations to detect whether activating the DREADDs caused functional connectivity changes between groups. Correction for multiple comparisons was applied using the FDR (False Discovery Rate) method with statistical significance defined at $p < 0.05$. To account for possible gender differences, age and weight were used as covariates.

Histological evaluation of transfection

Viral expression of the DREADDs (for DIO-hM3Dq-mCherry, DIO-hM4Di-mCherry and DIO-mCherry) was confirmed by mCherry staining using standard immunohistochemistry protocols, while qualitative transfection of D1 MSNs was confirmed using antibodies against D1 marker prodynorphin. Briefly, after the last MRI session, mice were deeply anesthetized using a mixture of Ketamine (100mg/kg; Graeb, Switzerland), Xylazine (10mg/kg; Rompun, Bayer) and Acepromazine (2mg/kg; Fatro S.p.A, Italy) and transcidentally perfused with 4% Paraformaldehyde (PFA, pH=7.4). The brains were postfixed in 4% PFA for 1.5 hours at 4°C and then placed overnight in 30% sucrose solution. Brains were frozen in a tissue mounting fluid (Tissue-Tek O.C.T Compound, Sakura Finetek Europe B.V., Netherlands) and sectioned coronally in 40 µm thick slices using a cryostat (MICROM HM 560, histocom AG-Switzerland). Free-floating slices were first permeabilized in 0.2% Triton X-100 for 30 min and then incubated overnight in 0.2% Triton X-100, 2% normal goat serum, guinea pig anti-prodynorphin (1:500, Ab10280, Abcam) and rabbit anti-mCherry (1:1000, Ab167453, Abcam) or rabbit anti-cfos (1:5000, AB2231974, Synaptic systems) at 4°C under continuous agitation (100rpm/min). The next day, sections were incubated for 1h in 0.2% Triton X-100, 2% normal goat serum, goat anti-rabbit Alexa Flour 546 (1:300, A11035, Life Technologies), goat anti-guinea pig Alexa Flour 647 (1:200, cat #A-21450, ThermoFisher Scientific) and DAPI (1:300, Sigma-Aldrich) at room temperature under continuous agitation. Afterwards, slices were mounted on the superfrost slides where they were left to air-dry and later coverslipped with Dako Fluorescence mounting medium (Agilent Technologies). Confocal laser-scanning microscope (CLSM 880, Carl Zeiss AG, Germany) and Zeiss Brightfield microscope (Carl Zeiss, AG Germany) were used to detect the viral expression. Microscopy protocol included a tile scan with a 10x or a 20x objective, pixel size of 1.2µm and image size of 1024x1024 pixels. Images were analyzed using ImageJ-Fiji.

4.4. Results

Chemogenetic manipulation of D1 MSNs of CPidm affects rotational behavior

Four weeks after surgery, mice underwent a behavioural open field test upon activating the DREADDs with a low dose of clozapine (Fig. 4.1B). The behavioral open field test was performed as a manipulation check, to test whether activating the DREADDs in CPidm caused behavioral changes as predicted by previous work. Exciting D1 MSNs with clozapine increased the frequency of contraversive rotations and decreased the frequency of ipsiversive rotations compared to controls who also received clozapine (MANOVA, $p_{\text{contra}}=0.01$, $p_{\text{ipsi}}=0.028$; Fig. 4.1E-F). Exciting D1 MSNs caused the mice also to cover a larger total distance when compared to control mice (MANOVA, $p=0.03$; Fig. 4.1D). By contrast, inhibiting D1 MSNs of CPidm with clozapine, decreased the frequency of contraversive rotations, while increasing the frequency of ipsiversive rotations when compared to control mice or to excitatory D1

MSN mice (MANOVA, $p_{\text{contra}}=0.001$, $p_{\text{ipsi}}=1.3 \times 10^{-5}$; Fig. 4.1E-F). These results replicate the behavior which is typically observed for unilateral excitation versus inhibition of D1 MSNs (Tecuapetla et al., 2014, Lee et al., 2016, Bay Konig et al., 2019, Runegaard et al., 2019).

We also qualitatively assessed the viral transfection in the CPidm by immunostaining. Figure 4.1C shows the superimposed viral expression maps of all mice which clearly cover CPidm. Together these results indicate that our approach allowed us to successfully modulate D1 MSNs in CPidm.

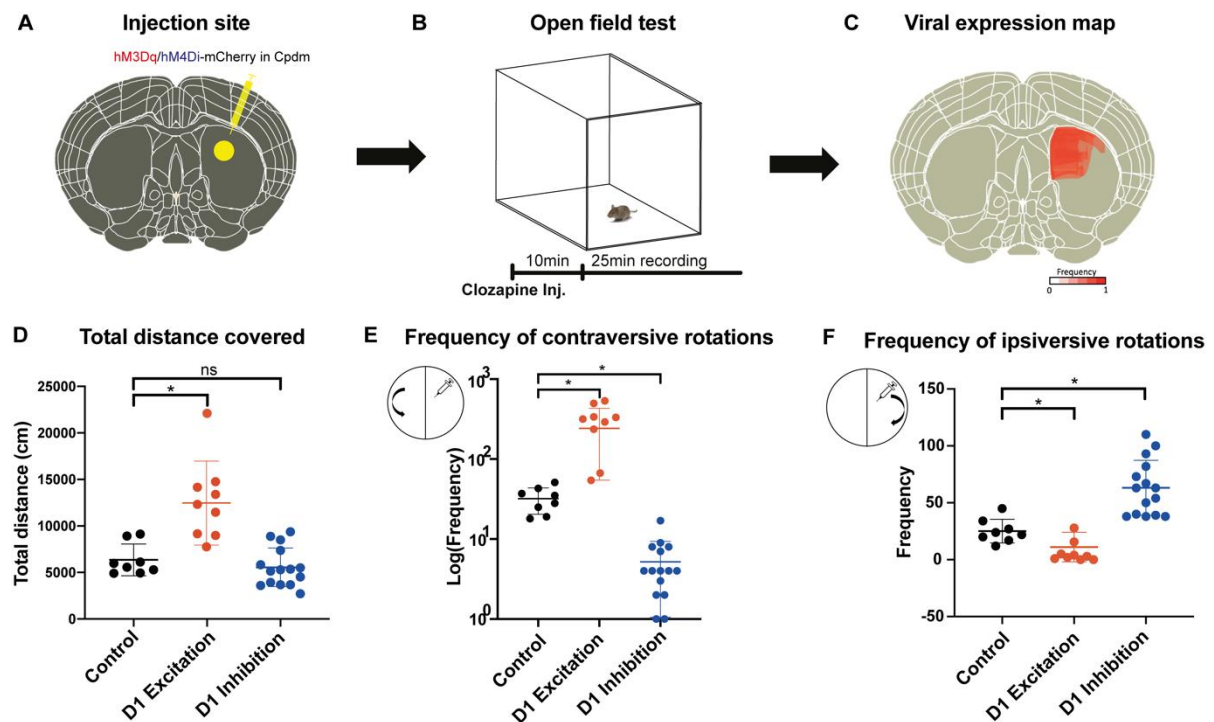


Figure 4.1. Chemogenetic targeting of D1 MSNs induces behavioral effects. **A)** Either DIO-hM3Di-mCherry, DIO-hM4Dq-mCherry or DIO-mCherry (control) virus was injected in the right dorsomedial striatum (CPidm) of D1Cre mice. **B)** Four weeks upon viral injection, open field test was performed. **C)** Qualitative viral expression map for every mouse included in the experiment. **D)** Only mice whose D1 MSNs of CPidm were excited, and not inhibited, covered significantly more distance when compared to controls (MANOVA, $p=0.03$). **E)** Exciting D1 MSNs of the right CPidm increased the frequency of contraversive rotations (turning in the direction opposite from the injection site as illustrated within the small circle, $p=0.01$), when compared to controls. On the contrary, inhibiting D1 MSNs of the right CPidm decreased contraversive rotations ($p=0.001$). **F)** Compared to controls, the frequency of ipsiversive rotations (turning in the same direction as the injection site, as illustrated within the small circle) significantly decreased when D1 MSNs of the CPidm were excited ($p=0.028$), while rotations significantly increased when D1 MSNs were inhibited ($p=1.3 \times 10^{-5}$).

Altered dynamics of neuromodulated CP subregion and its anatomically adjacent regions

A week later, mice were lightly anesthetized and macroscopic brain activity was measured via rsfMRI before and after activating the DREADDs with clozapine. Since we cell-specifically neuromodulated the intermediate portion of the dorsomedial part of CP (CPidm), we were

specifically interested whether this target area or other striatal subregions would be affected. To do so, we trained separate classifiers for each of the 29 CP subregions to determine whether changes in the BOLD time series dynamics were caused either by (i) D1 excitation versus no modulation in the control mice; or by (ii) D1 inhibition versus no modulation in the control mice. The balanced classification accuracy and the significance level for each of the 29 subregions is reported and displayed in Figure 4.2F-G and in Table S4.1. According to the Mouse Cortico-Striatal Projectome atlas, the DREADD was injected into the subarea labelled “CPi,dm,cd” (Fig. 4.2F). We first tested our anatomical a priori-hypothesis and found that the BOLD dynamics within the injection site CPi,dm,cd were significantly modulated during both excitation and inhibition of D1 MSNs when compared to control mice ($p \leq 0.029$). Next, we performed exploratory classification analyses on all other 28 CP subareas to test for DREADD effects outside of our injection site. We found that in addition to the injection site, also anatomically adjacent CP subareas in the intermediate-ventral portion or the rostral-dorsomedial portion of the CP_r were significantly modulated ($p_{\text{uncor}} < 0.05$). Based on the anatomical pattern of the classification results and viral expression map of our study (Fig. S4.1A), we added not only CPi_{dm} but also an adjacent rostral ROI (CP_rdm) and an adjacent ventral ROI (CPi_v) to the striato-thalamic-cortical circuit analysis. The detailed anatomical definition of these specific CP ROIs can be found in suppl. Fig. S4.1A.

Chapter 4. Cell specific neuromodulation in the striatum shapes BOLD fluctuations in multiple thalamic and cortical regions of an anatomically connected circuit

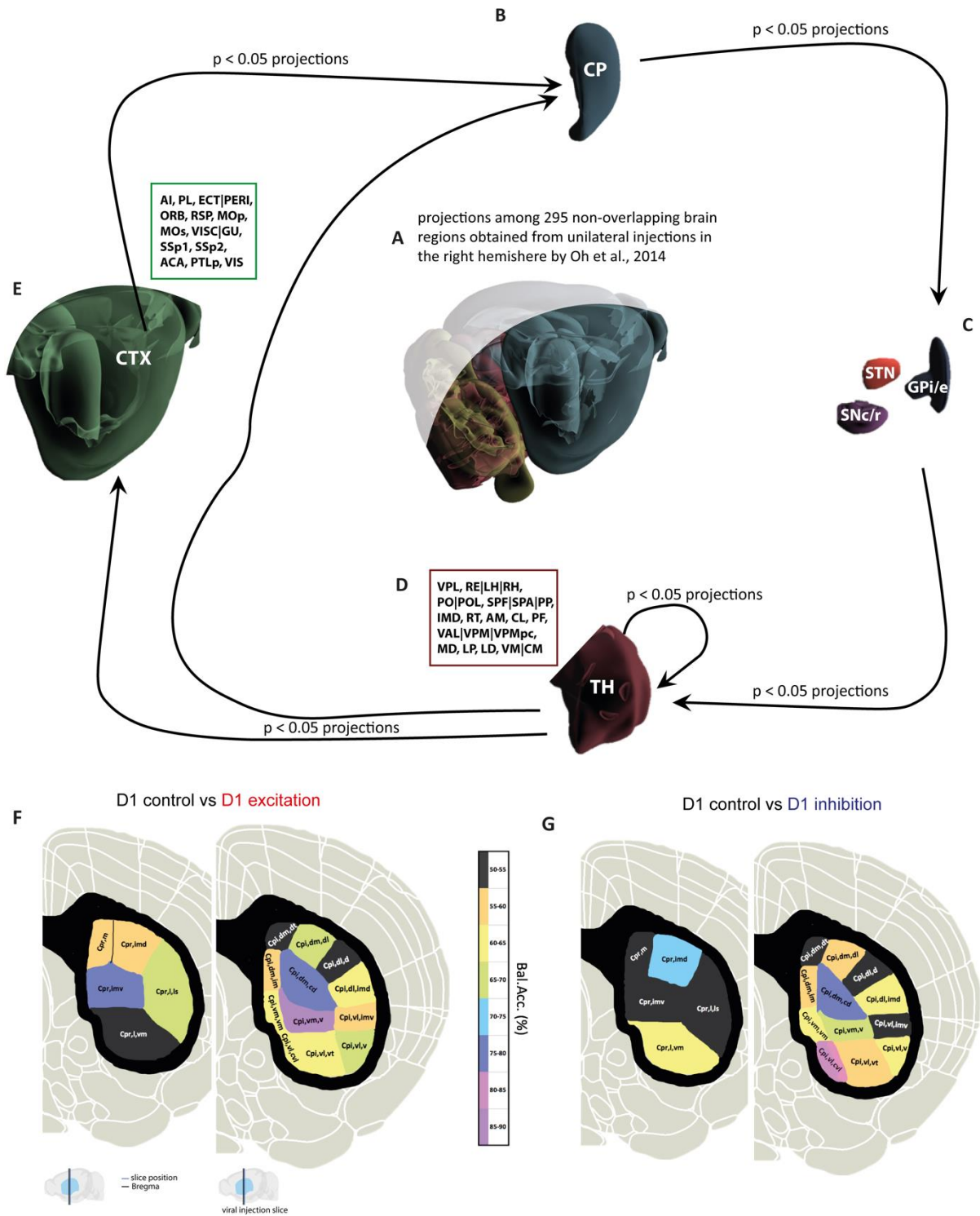


Figure 4.2. Simplified illustration of the procedure for striato-thalamic-cortical region selection. **A)** The Allen Mouse Brain Connectivity atlas (Oh et al., 2014) was used to obtain significant monosynaptic projections ($p < 0.05$) among regions (cortex (CTX), caudate putamen (CP), thalamus (TH), GPi, GPe, STN, SNc and SNr) constituting striato-thalamo-cortical circuit. **B)** Significant projections that caudate putamen projects to were extracted (GPi/e, SNc/r and STN). **C)** GPi/e and SNc/r significantly project to a number of thalamic regions, while these selected regions **(D)** further project to either other new thalamic regions, cortex or CP. **E)** The circuit was completed by extracting all the cortical regions (obtained from significant thalamic projections) that either

directly or indirectly (via another cortical region) have a significant projection to CP. **F) – G)** Coronal slices of the mouse brain with colour-coded balanced classification accuracy results for CP subregions obtained from Mouse Cortico-Striatal Projectome (Hintiryan et al., 2016) for D1 control vs D1 excitation groups (F) and D1 control vs D1 inhibition (G), respectively. CP subregions with classification accuracy above 70% are significant (permutation test, uncorrected), more detailed information available in Suppl. Fig 4.1/ Suppl. Table 4.1.

Full names of abbreviated ROIs: CPr – caudate putamen rostral; CPv - caudate putamen ventral; CPidm- caudate putamen dorsomedial; STN -subthalamic nucleus; SNC/r – substantia nigra compact/reticular part; GPi/e – globus pallidus internal/external; VPL - ventral posterolateral nucleus of thalamus; RE|LH|RH - nucleus of reuniens|lateral habenula|rhomboid nucleus; PO|POL – posterior complex and posterior limiting nucleus of thalamus; SPF|SPA|PP - subparafascicular nucleus subparafascicular area with peripeduncular nucleus of thalamus; IMD -intermediodorsal nucleus of thalamus ; RT - reticular nucleus of thalamus; AM – anteromedial nucleus; CL -central lateral nucleus of thalamus; PF -parafascicular nucleus; VAL|VPM| VPMpc - ventral anterior-lateral complex of the thalamus with ventral posteromedial nucleus of the thalamus and its parvicellular part; MD – mediodorsal nucleus of thalamus; LD - lateral dorsal nucleus of thalamus; LP – lateral posterior nucleus of thalamus; VM|CM – ventral and central medial nuclei of thalamus; AI - agranular insular area ; PL – prelimbic area; ECT|PERI -ectorhinal and perirhinal area; VISC|GU – visceral and gustatory areas; ORB – orbital area; RSP - retrosplenial area; MOp/s - primary and secondary motor cortex; SSp1/2 - primary somatosensory cortex; ACA - anterior cingulate area; PTLp - posterior parietal association area; VIS – visual area.

Thalamic regions with significant changes in BOLD dynamics form anatomically closed loops with CPidm

Next, we sought to understand whether activating the DREADDs in CPidm affects the BOLD dynamics of anatomically connected thalamic nuclei. Therefore, we applied a classification analysis to the MSN D1 excitation versus control group and the MSN D1 inhibition versus control group and found classification accuracies above chance for most of the thalamic ROIs. Interestingly, the largest effects were observed for those thalamic ROIs that have a specific reciprocal anatomical connection with CPidm (Fig. 4.3), i.e., they receive projections from CPidm via GP/SN and project back to CPidm. Statistics confirmed this observation for both D1 excitation vs D1 control (Mann-Whitney U test, $p=7*10^{-4}$, Fig. 4.3A) and D1 inhibition vs D1 control (Mann-Whitney U test, $p=0.038$, Fig. 4.3B).

Our results indicate that cell-specific neuromodulation of D1 MSNs alters the dynamics of the BOLD signal in downstream thalamic regions, that form strong closed loop anatomical connections with the neuromodulated CPidm. These thalamic regions were maintained as ROIs forming the specific striato-thalamic-cortical loop including CPidm.

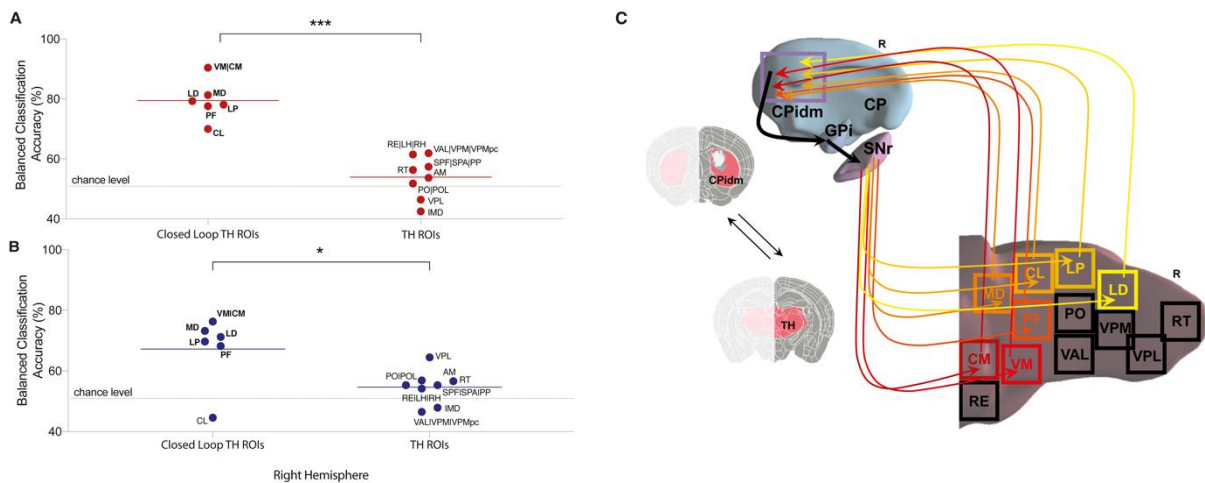


Figure 4.3. Altered dynamics in thalamic regions forming anatomically closed loops with dorsomedial caudate putamen. **A)** High balanced accuracy detected only in thalamic regions reciprocally connected to our modulated site i.e. dorsomedial striatum for D1 control vs D1 excitation group comparison (two tailed Mann-Whitney test; $p=7*10^{-4}$) **B)** Similar to B but for D1 control vs D1 inhibitory group comparison (two tailed Mann-Whitney test; $p=0.038$). **C)** Figure illustrating thalamic regions (brightly coloured) that form anatomically closed loop connections with dorsomedial striatum.

BOLD dynamics significantly altered in regions part of striato-thalamic-cortical circuit

Next, we asked whether neuromodulation of D1 MSNs in the CPidm affects the BOLD dynamics of monosynaptically connected regions which form the CPidm – thalamic-cortical loop. We applied again our classification approach (Fig. 4.4A-C) and asked whether regional BOLD timeseries dynamics can be significantly distinguished between D1 excitation versus no modulation in the control mice. As depicted in Fig. 4.4D, balanced classification accuracy was determined for each of the 27 ROIs constituting the striato-thalamic-cortical circuit of interest. Significant alterations in BOLD dynamics were obtained for all the CP subregions CPidm, CP_r and CP_v (Fig. 4.4D light green opaque bars with asterisk), all thalamic nuclei (i.e., parafascicular nucleus (PF), central-lateral (CL), lateral-dorsal (LD), lateral-posterior (LP), mediodorsal (MD), as well as ventral/central-medial (VM|CM) thalamic nuclei; Fig. 4.4D green opaque bars with asterisk)) as well as the primary somatosensory cortex (SSp1), visual area (VIS), the posterior parietal association area (PTLp), primary and secondary motor cortex (MOp/s) and anterior cingulate area (ACA) (Fig. 4.4D brown opaque bars with asterisk). Somewhat surprisingly we found no significant alterations of the globus pallidus, substantia nigra or STN, not even at the trend level.

An analogous classification approach was applied to distinguish between D1 inhibition versus no modulation in the control mice. We identified less areas to exhibit significant changes of their BOLD timeseries dynamics and only the MD and VM/CM thalamic nuclei (Fig. 4.4E green opaque bars with asterisk) as well as the cortical areas SSp1 and PTLp (Fig. 4.4E brown opaque bars with asterisk) reached significance (FDR corrected). Note that all of these areas were also identified when D1 MSNs were excited. Finally, we tested whether we could distinguish between D1 MSNs excitation versus inhibition. Our statistics revealed significant classification

results only for the CL and LD thalamic nuclei (Fig. 4.4F green opaque bars) but only at uncorrected levels.

Our results reveal that cell-specific neuromodulation of D1 MSNs of CPidm leads to characteristic alterations in BOLD dynamics in the specific neuromodulated region and also in remote yet anatomically connected cortical and thalamic regions. Excitation and inhibition of D1 MSNs seems to alter the BOLD dynamics in similar ways in most striato-thalamic-cortical regions and only a pair of thalamic regions were differentially affected as indicated by the significant classification results, albeit at uncorrected levels (Fig. 4.4F).

Chapter 4. Cell specific neuromodulation in the striatum shapes BOLD fluctuations in multiple thalamic and cortical regions of an anatomically connected circuit

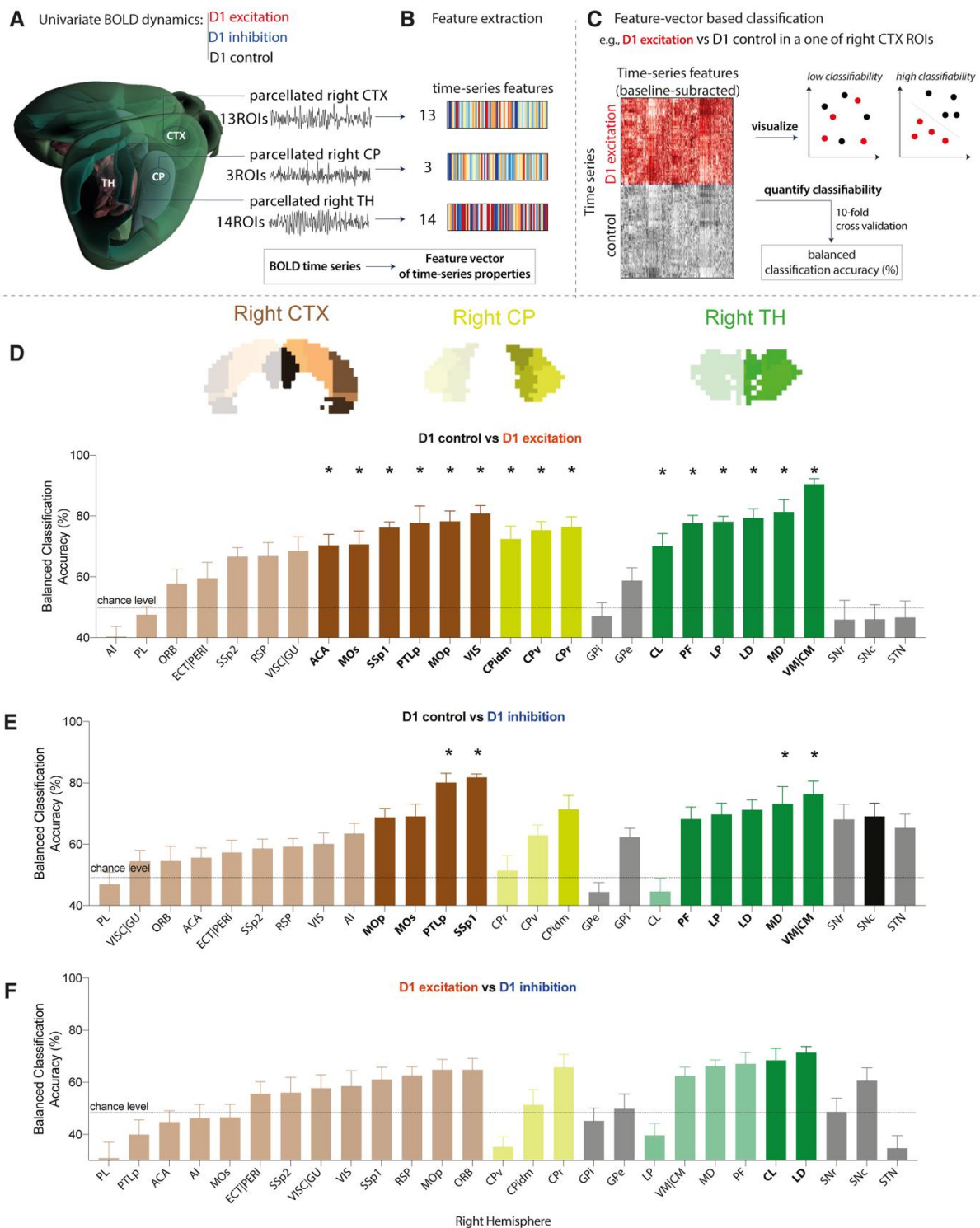


Figure 4.4. Characteristic changes observed in BOLD dynamics of region part of the striato-thalamic-cortical circuit. Classification of BOLD dynamics in 27 regions across three groups (D1 control, D1 excitation and D1 inhibition). The schematic of the approach is depicted in A-C: **A)** BOLD dynamics were measured from each brain region as a univariate time series (a 15 min time series per time window and experiment), which was **B)** converted to a set of properties (a 'feature vector') using hctsa. **C)** For a given region and groups, we used the features of each time series (relative to baseline) as the basis for classification, which was quantified as the 10-fold cross-validated balanced classification accuracy (%). Classification results in each brain region at $\Delta 1$ are shown for: **D)** D1 control versus D1 excitation; **E)** D1 control versus D1 inhibition; **F)** D1 excitation vs D1 inhibition. Each region

is colour coded depending on whether it is a part of CTX, CP or TH. Transparent bars indicate that BOLD dynamics in those ROIs were not significantly different between groups ($p > 0.05$ uncorrected). Significant difference in BOLD dynamics between the two groups ($p < 0.05$) was depicted with solid colour bars, where * indicates that statistical significance was reached after FDR correction for multiple comparisons.

Functional connectivity changes induced by chemogenetic neuromodulation

Since excitation and inhibition of D1 MSNs of CPidm significantly alters the dynamics of remote regions which constitute striato-thalamic-cortical circuit, we next aimed to examine the functional connectivity between CPidm and these ROIs (Fig. 4.5A). We assessed how injecting clozapine changes FC between CPidm and each of the anatomically connected ROIs. Analyzing the difference in FC between the 15min baseline period and 15min following clozapine injection, we compared the D1 excitatory group to the D1 control group for all 27 ROIs of interest. While a number of regions displayed significant reduction in FC with CPidm when D1 MSNs were excited as compared to controls ($p_{\text{uncor}} < 0.05$, solid color bars Fig. 4.5B), only anterior cingulate area (ACA) survived the correction for multiple comparisons ($p < 0.05$, FDR-corrected). An analogous analysis was performed to identify whether inhibiting D1 MSNs influences FC between CPidm and the ROIs in comparison to control animals, however no significant effects were observed (data not shown). Finally, we directly compared whether exciting versus inhibiting D1 MSNs differentially affects CPidm connectivity. Figure 4.5C shows that excitation typically reduced FC, while there was a trend towards FC increase during inhibition, resulting in an effect that reached significance in some cortical and thalamic ROIs (Fig 4.5C, solid color bars). However, only FC changes between CPidm - ACA and CPidm - RSP and CPidm - MOs survived correction for multiple comparisons ($p < 0.05$, FDR-corrected). Full FC analysis among all 27 ROIs was performed but no connection reached significance after correction for multiple comparisons (data not shown).

Overall, our FC results indicate a significant decrease in FC between CPidm and three cortical nodes, when D1 MSNs were excited and compared to D1 MSNs inhibition.

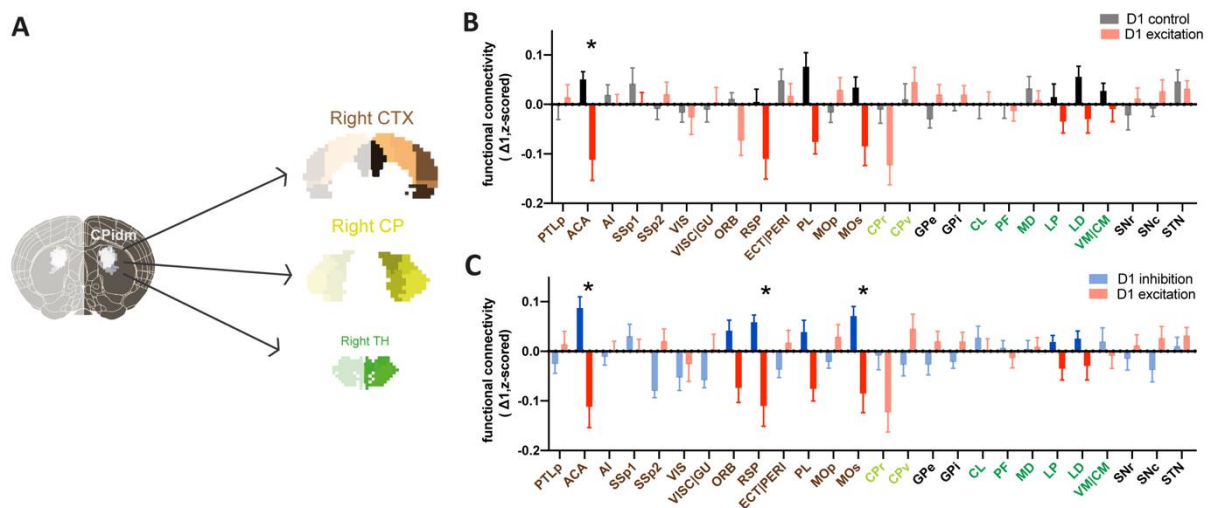


Figure 4.5. Functional connectivity changes induced by chemogenetic neuromodulation. **A)** Illustration of the analysis presented in this figure i.e. functional connectivity between CPidm and the rest of ROIs from striato-thalamo-cortical circuit. **B) – C)** Baseline corrected functional connectivity changes between CPidm and the rest of ROIs, colour coded based on whether they are a part of cortex (CTX, brown), thalamus (TH, green), caudate putamen (CP, yellow) or GPi/e, SNc/r, STN (black). The graphs show z-scored FC between CPidm and each individual ROI for **(B)** D1 controls (black bars) vs D1 excitation group (red bars) or **(C)** D1 excitation (red bars) vs D1 inhibition group (blue bars). Transparent bars depict insignificant FC changes. Significant FC changes (uncorrected, $p < 0.05$), depicted by solid colour bars, are observed between CPidm and anterior cingulate (ACA), retrosplenial area (RSP), prelimbic area (PL), secondary motor cortex (MOs), orbital area (ORB, only in Fig. 4.5C), lateral posterior (LP), lateral dorsal (LD) and ventral/central medial (VM|CM, only in Fig. 4.5B) nuclei of thalamus. * indicates FDR-corrected significance.

4.5. Discussion

Previous research has shown that regional cell-specific neuromodulation affects local BOLD dynamics. However, whether regional cell-specific activity also changes the BOLD dynamics of remote but anatomically connected regions, remains an open question. Here, we chemogenetically excited or inhibited D1 MSNs of right dorsomedial striatum (more specifically CPidm) and found that anatomically connected subareas of thalamus and cortex display significantly altered BOLD dynamics. Interestingly, results were most robust when D1 MSNs were excited while the effect was much weaker when D1 MSNs were inhibited. We also assessed functional connectivity between the neuromodulated dorsomedial striatum and areas of the connected striato-thalamic-cortical circuit but only found a robust reduction in functional connectivity between CPidm and the anterior cingulate cortex in the chemogenetically excited group while a trend towards an increase of functional connectivity was observed during inhibition.

Altered BOLD dynamics of a targeted CPidm and its anatomically adjacent CP subareas

Our results confirmed that BOLD dynamics changed in CPidm, the targeted striatal subarea, upon activating the DREADDs. Additionally, we observed substantial modulation of the BOLD dynamics in anatomically adjacent CP subregions, located either ventrally or rostrally to the injection area CPidm (Fig. 4.2F). Even though we cannot exclude that the injected virus spread to neighboring CP subareas, it is unlikely that virus spread alone explains the robust neuromodulator effects which we observed at the whole group level. An alternative explanation is that our results reflect intra-striatal communication between the identified CP subareas. The striatum is the main input structure of the basal ganglia and receives glutamatergic inputs from cortical, thalamic and limbic regions combined with dopaminergic input from the midbrain, thus acting as an integrative hub that assists in the selection of appropriate behaviors through its output to downstream basal ganglia nuclei (Reig and Silberberg, 2014). This integrative function of the striatum is thought to happen at the level of the local intra-striatal circuitry (Burke et al., 2017). Intra-striatal connectivity involves synaptic connections between MSNs and striatal interneurons. However, there is also

evidence of functional neuronal ensembles, which are formed by widely distributed MSNs throughout the striatum, not necessarily in close proximity to each other (Burke et al., 2017). Specifically, *in vivo* electrophysiological recordings across a large fraction of striatum along the CPidm and CPv axis, revealed that ensembles of MSN which fired in a highly correlated manner were formed throughout the recorded striatal subdivisions (Bakhurin et al., 2016). Activity in these MSN ensembles was not only highly correlated when the animal executed a task but also during the resting-state period (Bakhurin et al., 2016). Moreover, cortico-striatal projections that project to distinct intermediate parts of CP (CPi) were found to extend to rostral part of CP, indicating another possible way of intra-striatal communication mediated by cortical inputs (Hintiryan et al., 2016). Based on these findings it is tempting to speculate that chemogenetically exciting D1 MSNs altered not only the BOLD dynamics of the target area CPidm but also of intra-striatally connected subareas CPr and CPv. Inhibiting D1 MSNs (Fig. 4.4E) also resulted in significant change in CPidm dynamics, however, these effects were statistically less robust and did not survive correction for multiple comparisons. When we directly contrasted exciting versus inhibiting D1 MSN via a classifier approach, classification accuracy for CPidm was above chance level but did not reach significance. It is likely that a larger sample size is required to detect changes in the macroscale BOLD dynamics induced by cellular inhibition and for dissociating inhibitory from excitatory DREADD effects.

Altered BOLD dynamics in thalamic regions mediated by direct anatomical projections with CPidm

Next, we focused on thalamic regions and trained a classifier to distinguish altered BOLD dynamics when D1 MSNs excitation and D1 MSNs inhibition were compared to controls. Thalamus is a highly heterogeneous structure, forming bidirectional connections with visual, limbic, associative, sensory and motor regions of the cortex as well as striatum. Extensive amount of research has focused on anatomically mapping the striathalamic and thalamostriatal projections (Mandelbaum et al., 2019, Wall et al., 2013, Guo et al., 2015, Lee et al., 2020, Perry and Mitchell, 2019, Parker et al., 2016, Hunnicutt et al., 2016, Diaz-Hernandez et al., 2018, Alloway et al., 2017, Vertes et al., 2015, Namboodiri et al., 2016, El-Boustani et al., 2020, Kamishina et al., 2008, Smith et al., 2004, Bubb et al., 2017, Antal et al., 2014, Elena Erro et al., 2002, Linke et al., 2000, Wang et al., 2006, Van der Werf et al., 2002), which enabled us to further distinguish thalamic ROIs based on their projections to/from the neuromodulated CPidm. We show that upon D1 MSNs excitation and inhibition only those thalamic ROIs that form anatomically closed loops with CPidm display altered dynamics, indicating that experimentally induced changes in BOLD fluctuations propagate across areas in accordance to direct anatomical projections. Interestingly, two thalamic subareas CL and LD, were the only regions where excitation versus inhibition of D1 MSNs could be classified with accuracies which differed significantly from chance.

Altered BOLD dynamics in cortical regions part of striato-thalamic-cortical circuit

A number of cortical ROIs exhibited significantly altered BOLD dynamics upon D1 MSN excitation and upon D1 MSN inhibition, though a smaller number of regions reached significance in the inhibitory DREADD group. This is remarkable as it provides further evidence that modulating D1 MSN activity in the CP seems to cause changes in BOLD dynamics which propagate through poly-synaptically connected circuits. There was substantial variation in how strongly the BOLD dynamics of cortical regions changed in response to neuromodulating striatal D1 MSN cells. Even though this result pattern might have been modulated by anatomical determinant, these were not obvious from our data. There might be a number of reasons for this heterogeneity of the cortical response. First, neuronal cell density could play a part in cortical response. Keller and colleagues reviewed neuronal cell densities across mouse cortex and strikingly, the cortical regions with the highest classification accuracy also displayed highest neuronal cell density (VIS, SSp, PTLp, ACA) (Keller et al., 2018). Second, from an anatomical perspective a cortical region receive inputs from and project to multiple cortical and subcortical regions (Froudarakis et al., 2019). For example, the visual area (VIS), receives afferent projections from numerous cortical (ORB, SSp, RSP, ACA, AUD) and thalamic ROIs (LP, LD) which are part of the anatomically defined striato-thalamic-cortical circuit. This type of dense and diverse cortico-cortical, cortio-thalamo-cortical and cortio-striatal communication is also applicable to other cortical ROIs (Oh et al., 2014, Hintiryan et al., 2016, Hunnicutt et al., 2016). Understanding of these anatomically diverse projections is important because regional BOLD dynamics are shaped by the strength of integrated incoming projections (Sethi et al., 2017), thus reflecting integration of multiple networks of which a region is a part of. Consequently, a model consisting of weighted anatomical inputs and outputs for all cortical regions, which are part of striato-thalamic-cortical circuit, could better elucidate on reasons behind cortical BOLD fluctuations displayed in our data.

Functional connectivity changes between CPidm and striato-thalamic-cortical regions

We also assessed functional connectivity between CPidm and the rest of the anatomically identified striato-thalamic-cortical regions using a conventional correlational approach. We observed differential modulation of functional connectivity for exciting versus inhibiting D1 MSN cells between CPidm and ACA, RSP and MOs. For these areas, FC decreased when D1 MSNs were excited, an effect which was particularly strong with ACA which has dense monosynaptic projections to CPidm (Hintiryan et al., 2016). By contrast, a trend towards an increase of FC between CPidm and these cortical areas was observed during D1 MSNs inhibition. Cell-specific excitation leading to a decrease in functional connectivity has been illustrated before. Namely, we have shown that chemogenetic activation of somatosensory cortex led to an increase in neural firing at the neuromodulated site, resulting in functional connectivity decrease with monosynaptically connected regions (Markicevic et al., 2020), indicating possible localized neuronal desynchronization. Nakamura and colleagues have recorded increased neural activity upon D1 MSNs excitation of the dorsal striatum (Nakamura

et al., 2020), while our results indicate that D1 MSNs activation of CPidm leads to decreased FC with monosynaptically connected regions. Taken together, this increase in neuronal firing followed by an FC decrease could indicate possible localized neuronal desynchronization, regardless of the brain region targeted. Furthermore, they performed electrophysiological recordings in both dorsal striatum and motor cortex. Results indicate increased delta power in dorsal striatum but no change in delta power in motor cortex, upon D1 excitation (Nakamura et al., 2020). Slow oscillations of delta band fluctuations contribute to functional connectivity (Wang et al., 2012) and are characterized by brain wide synchrony (Uhlhaas et al., 2010, Pan et al., 2013). Accordingly, we speculate that a change in delta power localized to neuromodulated region, might disrupt synchrony to brain regions with no change in delta power leading to reduced functional connectivity.

Limitations and interpretational issues

Changes in BOLD dynamics were obtained by extracting a large set of features describing timeseries fluctuations for a given region-of-interest. These features were subsequently analyzed by a classification approach to answer the question whether changes in BOLD dynamics caused by chemogenetics can be distinguished from changes in BOLD dynamics observed in control mice. This approach makes few a-priori assumptions since it is strongly data-driven, however, it is limited in providing insights into which timeseries features do actually change by activating the DREADDs or which biological substrates might drive the observed effects. The former question could be answered by more detailed analysis, but our present study is most likely under-powered for such endeavor. Thus, while we provided convincing evidence that modulating D1 MSNs causes changes in both BOLD dynamics and functional connectivity of areas structurally connected with CPidm, we provide no detailed mechanistic insights into how changes in cellular activity drive BOLD signal changes.

Furthermore, we observed that BOLD dynamics seem to be more strongly modulated by exciting rather than inhibiting D1 MSNs, but a direct comparison between these experimental groups revealed only subtle differences. This suggests that exciting versus inhibiting D1 MSN might cause far less pronounced differences in BOLD activity when tested in a resting state, than observed during a task. Finally, dynamics of the basal ganglia structures downstream from CP, namely GPi/e, SNr/c, and STN are affected neither by exciting nor inhibiting D1 MSNs. While this is at odds with conventional models of the basal ganglia, some studies indicate that upon D1 excitation or D1 inhibition within the dorsal striatum, the firing rates of these downstream structures change in a non-uniform manner i.e. partially displaying firing rate increases and partially decreases within a single structure (Kravitz et al., 2010, Freeze et al., 2013, Tecuapetla et al., 2014, Lee et al., 2016). The resolution to delineate these changes from a BOLD signal are insufficient, as BOLD signal picks up only the net effect from a single structure. Consequently, it is not surprising that the dynamics of basal ganglia downstream regions are affected by neither D1 MSNs excitation nor inhibition. Moreover, recent tracer

study illustrated that projections from CP to the output nuclei GPi and SNr are topographically segregated so that CPidm projects only to a specific anatomically defined section of GPi/SNr (Lee et al., 2020). If only a small fraction of an already small nucleus is affected by CPidm neuromodulation, it is likely that this effect cannot be reliably measured because the spatial resolution of our approach is too low.

Mildly anesthetized animals were used during the experiment in order to minimize animal movement and potential distress during examination. We used a combination of medetomidine (vasoconstrictor), isoflurane (vasodilator) and pancuronium (muscle relaxant) at very low doses (Grandjean et al., 2014a). Isoflurane is predominantly targeting the widespread GABAergic neurotransmitter system, while medetomidine targets α_2 adrenergic receptors, localized in the brainstem (Lukasik and Gillies, 2003). In order to minimize the percentage of isoflurane used in the anesthesia and its dominant effect on BOLD fluctuations, isoflurane is combined with medetomidine and kept at 0.5%.

Note that changes in functional connectivity are believed to reflect neural interactions *between* two brain areas while changes in BOLD response dynamics reflect the modulation of oscillatory activity *within* a single brain region. Accordingly, changes in FC and changes in BOLD dynamics provide complementary information.

4.6. Conclusions

Studies using rsfMRI to assess FC have provided extensive insights into network connectivity in health and disease, and in different species. Yet understanding how cellular level mechanisms map onto the interaction of macroscopic brain networks remains incompletely understood and an area of active research. Here, we show that the chemogenetic modulation of specific cell types cause alterations of BOLD timeseries dynamics within the target region of interest. Importantly, we show that alterations of D1 MSN activity in the striatum propagate through anatomically connected networks, thereby shaping the dynamics of multiple thalamic and cortical regions within an anatomically defined circuit.

Our approach to analyse the BOLD dynamics within a region of interest is not limited to animal models but can be readily applied to a large body of resting-state fMRI data obtained in human patients and controls. Such an analysis would provide region-specific information on altered neural activity which is complementary to conventional functional connectivity analyses.

4.7. Supplementary Figures and Tables

Figure S4.1. Illustration on steps used to create three main CP subregions

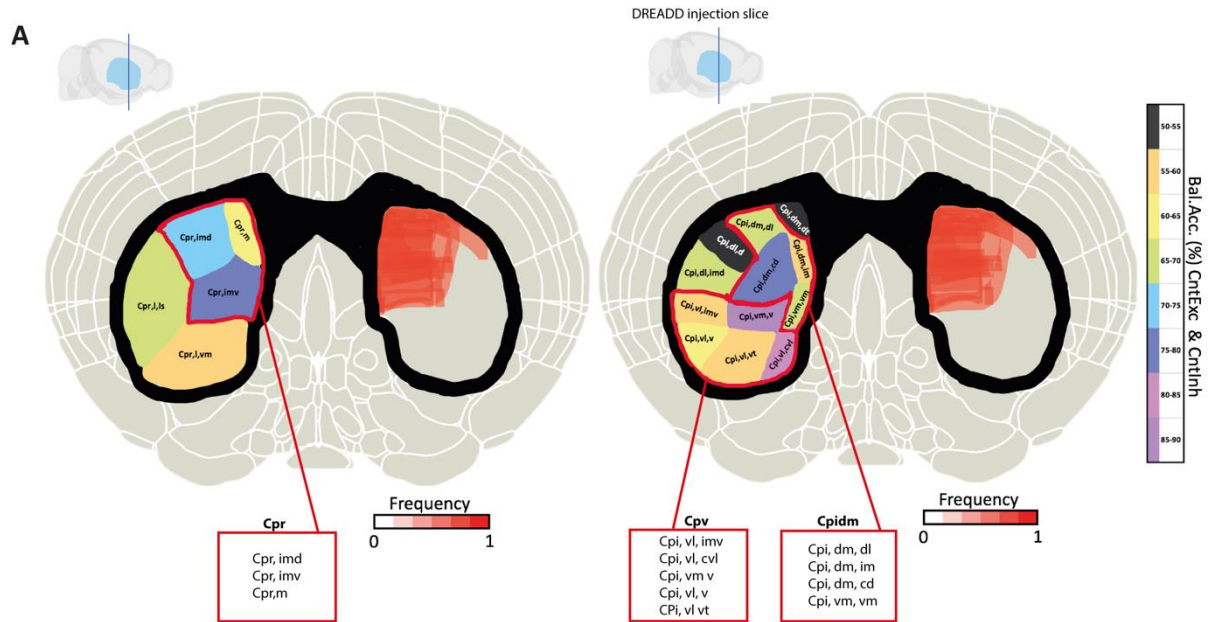


Figure S4.1. A) Coronal slices of the mouse brain with colour-coded balanced classification accuracy results for CP subregions obtained from Mouse Cortico-Striatal Projectome (Hintiryan et al., 2016) (on the left) with viral expression map (on the right). Based on high classification accuracy results (above chance level) for both groups (D1 control vs D1 excitation; D1 control vs D1 inhibition, higher value taken to color code the depicted slices) and their overlap with the viral expression map, three main CP subregions (consisting of the regions depicted in the red box) were created, CPr, CPv, and CPidm. Cpi,dm,dt subregion (colour coded black on the right slice) was not included in the defining the CPidm region because of its below chance level classification accuracy result. This ROI had a small number of voxels ($n=48$) of which some have been found outside of CP region, therefore the entire ROI was excluded. Cpi,dl,imd was excluded because of its below chance level classification accuracy results and because most of it was not transfected by the virus. All other ROIs depicted on the two slices were excluded because their spatial location indicated no viral transfection. Frequency 0 means no mouse displayed transfection in that spatial location, while frequency 1 means all mice had a viral expression in that location.

Table S4.1. Balanced Accuracies for 29 subregions of CP obtained from Mouse-Striatal Projectome

A	CntExc	5000nulls	
	ROI	Bal. accuracy	p-perm
	CPidld	44.20%	0.67
	CPcv	48.20%	0.54
	CPce-right	50.20%	0.48
	CPidmdt	52.60%	0.41
	CPcivm	52.60%	0.39
	CPrlvm	54.10%	0.37
	CPivlt	56.20%	0.26
	CPrimd	57.00%	0.27
	CPidmim	58.80%	0.23
	CPivlimv	59.20%	0.22
	CPrm	59.50%	0.23
	CPcivl	59.60%	0.23
	CPci	59.90%	0.18
	CPcid	61.50%	0.17
	CPcddl	61.70%	0.17
	CPivmvm	62.10%	0.16
	CPivlcvl	62.80%	0.15
	CPcdvm	64.00%	0.1
	CPidlimd	64.30%	0.12
	CPcd	64.70%	0.093
	CPivlv	66.30%	0.098
	CPrls	67.30%	0.076
	CPidmdl	67.90%	0.074
	CPcddm	69.90%	0.05
	CPivmvm	70.80%	0.048
	CPidmcd	72.40%	0.029
	CPrimv	75.90%	0.017
	Cpre	87.50%	0.0002
	CPivmv	88.70%	0.0002

B	CntInh	5000nulls	
	ROI	Bal. accuracy	p-perm
	CPrm	42.90%	0.73
	CPcddl	44.90%	0.69
	CPrls	45.60%	0.63
	CPcdvm	48.50%	0.51
	CPcv	49.00%	0.52
	CPci	49.80%	0.53
	CPidmdt	50.30%	0.47
	CPrimv	53.30%	0.39
	CPivlimv	53.70%	0.34
	CPidld	54.00%	0.33
	CPcivm	56.40%	0.3
	CPivmvm	56.50%	0.29
	CPivlt	56.60%	0.29
	CPcivl	58.60%	0.2
	CPidmdl	58.80%	0.2
	Cpce	58.90%	0.2
	CPidmim	59.50%	0.21
	CPivlv	60.10%	0.15
	CPrlvm	60.50%	0.16
	CPcd	60.90%	0.15
	CPivmvm	62.60%	0.12
	CPidlimd	64.40%	0.097
	CPcid	65.00%	0.073
	CPivmv	65.90%	0.076
	CPcddm	69.80%	0.04
	CPrimd	73.80%	0.013
	Cpre	76.00%	0.014
	CPidmcd	78.40%	0.0058
	CPivlcvl	79.80%	0.0056

Table S4.1. A) Balanced classification accuracy results for a pair of groups i.e., D1 control vs D1 excitation together with permutation test p-values calculated using 5000 nulls. All p-values are uncorrected for multiple comparisons B) Identical to A but for D1 control vs D1 inhibition. The exact location of ROIs with balanced accuracies are illustrated in Fig. 4.2F-G, respectively.

Chapter 4. Cell specific neuromodulation in the striatum shapes BOLD fluctuations in multiple thalamic and cortical regions of an anatomically connected circuit

Table S4.2. List of thalamic ROIs and their anatomical projections from/to dorsomedial CP with references to the literature where the information was obtained

Thalamic nuclei	Projections FROM CPidm (via Gpi/SNr)	Projections TO CPidm	Reference(s)
CL	yes	yes	Parker et al., 2016; Wall et al., 2013; Guo et al., 2015; Kamishina et al., 2008
CM	yes	yes	Wall et al., 2013; Parker et al., 2016;
PF	yes	yes	Mandelbaum et al., 2019; Lee et al., 2020; Wall et al., 2013
MD	yes	yes	Hunnicuttt et al., 2016; Collins et al., 2018; Wall et al., 2013
LP	yes	yes	Guo et al., 2015; Evangelio et al., 2018; Kamishina et al., 2008; Alloway et al., 2017;
LD	yes	yes	Hunnicuttt et al., 2016; Perry & Mitchell, 2019;
VM	yes	yes	Lee et al., 2020; Wall et al., 2013; Collins et al., 2018
RE	no	no	Vertes et al., 2016;
LH	no	no	Namboodiri et al., 2016
RH	no	yes (to dorsal CP but scarce)	Parker et al., 2016; Vertes et al., 2016
PO	no	no	El-Boustani et al., 2020; Kamishina et al., 2008; Alloway et al., 2017;
POL	no	no	El-Boustani et al., 2020; Alloway et al., 2017
IMD	no	no	Van der Werf et al., 2002; Smith et al., 2004
RT	no	no	Antal et al., 2014; Hunnicutt et al., 2016;
AM	no	yes (to dorsal CP but scarce)	Perry & Mitchell, 2019; Wall et al., 2013; Bubb et al., 2017
VPL	no	no/scarce	Antal et al., 2014; Diaz-Hernandes et al., 2018; Erro et al., 2002
VPM/VPMpc	no/scarce	no	Hunnicuttt et al., 2016; Diaz-Hernandes et al., 2018
VAL	no	no	Alloyway et al., 2017; Smith et al., 2004;
SPF	no	no	Palkovits et al., 2006; Oh et al., 2014
SPA	no	no	Palkovits et al., 2006; Oh et al., 2014
PP	no	no	Linke et al., 2000; Oh et al., 2014

CHAPTER 5

General discussion and outlook

The work presented in this thesis investigated the causal effects of cell specific neuromodulation on resting-state fMRI fluctuations. The overarching aim of this work was to establish how microscopic cell alterations propagate through scales and are reflected at the level of brain networks. Resting-state fMRI studies have provided compelling evidence of functional brain organization in health and disease, although the mechanistic insights into the neuronal basis of this functional organization remain unclear. Using rodent rsfMRI, a compelling translational tool, together with chemogenetics, a powerful tool for targeted and controlled neuromodulation of neuronal signaling, we provide causal evidence on how distinct cellular mechanisms alter functional connectivity and neuronal dynamics at the network level.

The sections that follow outline some general implications of the major findings, including the outlook for future work. This is followed by a discussion of the main limitations of the work presented here, and final conclusions.

5.1. Hypoconnectivity following cell-specific DREADD-induced neuromodulation

In the first set of experiments presented in chapter 3, we locally perturbed the excitation-inhibition (E:I) balance within the right somatosensory cortex of a mouse by either i) exciting pyramidal neurons or ii) inhibiting inhibitory PV interneurons. We observed reduced local and long-range functional connectivity (FC) between somatosensory cortex and its anatomically connected ROIs. We hypothesized that a local desynchronization of neuronal assemblies could lead to the observed FC reduction. Our hypothesis comes from an extensive body of literature reporting on the function of parvalbumin (PV) neurons in synchronizing the firing of pyramidal neurons (Cardin et al., 2009, Sohal et al., 2009, Cardin, 2018, Marissal et al., 2018). This hypothesis could be extended to include brain oscillations. Gamma band oscillations (30-80 Hz) rely on fast inhibitory synaptic transmission of GABAergic interneurons, and PV interneurons are shown to be essential in the generation of these gamma oscillations (Sohal et al., 2009, Cardin, 2016, Cardin, 2018). Optogenetic activation of PV interneurons in the sensory cortex evokes robust gamma oscillations, while inhibition of PV suppresses them (Sohal et al., 2009, Liu et al., 2020a). However, optogenetic activation of pyramidal neurons in the sensory cortex induces gamma oscillations (Adesnik and Scanziani, 2010). This points towards a complex relationship between inhibitory and excitatory synaptic transmission, whose temporally correlated activity is necessary for the generation of cortical gamma rhythms (Cardin, 2018). Intuitively, perturbation of the E:I balance in this case would lead to impaired intrinsic gamma oscillations (Yizhar et al., 2011).

Synchronized neural oscillations are fundamental for enabling coordinated activity of a healthy brain. Studies in humans, primates and rodents have shown that spontaneous BOLD fluctuations are coupled to spontaneous neural activity, particularly in the gamma band of local field potentials (LFP) (He et al., 2008, Nir et al., 2008, Shmuel and Leopold, 2008, Pan et al., 2013, Keilholz, 2014, Drew et al., 2020). This indicates that any local disruptions of gamma oscillations, such as perturbation of E:I, could be reflected in the spontaneous BOLD signals. Since functional connectivity is assumed to reflect interregional coherence of fluctuations of underlying neuronal activity, local perturbation of gamma oscillations may lead to disruption of interregional coherence and a reduction in FC. It has been demonstrated before that changes in gamma oscillations affect functional connectivity (Tagliazucchi et al., 2012, Keilholz, 2014). Consequently, our chemogenetically increased E:I ratio might have perturbed gamma oscillations within the somatosensory area leading to decreased functional connectivity between the neuromodulated area and its anatomically connected regions.

Gamma rhythms are not the only rhythms involved in interregional coherence and neuronal synchrony. A number of studies have demonstrated the contribution of low-frequency (delta, theta, alpha) LFP signals to resting-state BOLD fluctuations (Keilholz, 2014, Pan et al., 2013, Shi et al., 2019, Wang et al., 2012, Jaime et al., 2019). Shi and colleagues (Shi et al., 2019) recorded electrocorticographic signals simultaneously with rsfMRI from the primary somatosensory cortex of monkeys, demonstrating that BOLD connectivity reflects more the variations within low frequency LFPs than gamma LFP signals. Similar results were also obtained within the monkey visual networks (Wang et al., 2012). Two independent studies where electrophysiology and rsfMRI were recorded in separate sessions, reported strong synchrony in the low frequency LFP signal in the somatosensory cortex, where strong FC is normally detected (Lu et al., 2007, He et al., 2008). Using interventional approaches, Canella and colleagues (Canella et al., 2020) acutely inhibited prefrontal cortex of a mouse and recorded increased functional connectivity between the targeted region and its anatomically connected cortico-cortical and thalamo-cortical regions. They also independently measured LFPs and noted an increased delta band neural coherence between overconnected regions and decreased gamma power within each cortical and thalamic region. Their interpretative model suggests that cortical silencing leads to a decreased direct gamma frequency axonal communication with its targets and a concomitant increase in low delta frequency neural coherence between overconnected regions. Consequently, the observed increase in FC reflects the relative contribution of delta frequency interactions with respect to gamma frequency rhythms. Moreover, Nakamura and colleagues (Nakamura et al., 2020) acutely excited D1 medium spiny neurons (MSNs) of the dorsal striatum and recorded LFPs from the targeted site and motor cortex. Results illustrate an increase in delta power in the striatum but not in the motor cortex, and an increase in gamma power in both regions. Following the logic of Canella and colleagues (2020) on the results from Nakamura and colleagues (2020): exciting a region leads to an increased direct gamma frequency axonal communication and a

concomitant decrease in delta neural coherence. Taken together, this would result in reduced functional connectivity between striatum and motor cortex. Reduced FC between striatum and motor cortex is exactly what we observed in the study described in chapter 4, where D1 MSNs of dorsomedial striatum were excited.

Taken together, these hypothetical interpretations of mechanistic insights behind functional connectivity reduction suggest a complex picture regarding the relationship between cell-specific modulation and spontaneous BOLD fluctuations. Mechanistic understanding could potentially be provided by changes in LFP signals. Although simultaneous assessment of the broad spectrum of LFP frequency bands and the interactions of oscillations at different frequency bands (i.e., cross-frequency coupling) could provide a deeper understanding of the mechanism, compared to focusing solely on changes within a single LFP band.

5.1.1 Outlook

In order to better decipher these mechanistic insights following DREADD neuromodulation the simultaneous measurement of electrophysiology and rsfMRI in mouse is necessary. This would allow direct mechanistic insights into the effects of DREADD-induced LFP changes on the BOLD signal. Alternatively, cell-type specific population activity following DREADD modulation and their influence on FC could be assessed by combining fiber photometry and rsfMRI. Calcium and BOLD signals have already been acquired simultaneously and their coupling investigated (Schlegel et al., 2018, Tong et al., 2019), although not under cell-specific neuromodulation. This approach could yield an understanding of the DREADD-induced population activity patterns, such as synchronous vs asynchronous firing, and their effect on FC alterations. Understanding the mechanism behind the causal effects of cell-specific neuromodulation on functional connectivity could ultimately lead to better mechanistic interpretations of altered macroscopic functional connectivity observed in various brain disorders.

5.2. Using machine learning to assess DREADD-induced alterations in brain

dynamics

Resting-state BOLD signals not only comprise information regarding the functional connectivity between two regions, but also reflect the dynamics within these regions. In the context of regional timeseries, dynamical characteristics of each timeseries can be extracted in terms of features, comprised of an interpretable set of real numbers obtained from interdisciplinary timeseries analysis algorithms (Fulcher et al., 2013). As detailed in chapter 3, features extracted from the neuromodulated somatosensory area were used to train SVM classifiers to distinguish BOLD dynamics altered during the acute perturbation of E:I ratio. E:I imbalance is the putative mechanism thought to be responsible for many neurodevelopmental disorders, often linked to a lack of inhibitory feedback caused by

depletion of PV interneurons (Sohal and Rubenstein, 2019). Our classifier trained on rsfMRI timeseries data obtained during DREADD-induced PV inhibition, was cross-validated in an independent cohort of *Fmr1*^{-/-} knockout mice, known for their loss of PV neurons and chronic alterations in E:I. This classifier was able to identify a number of cortical regions which are most affected by the depletion of PV neurons. In chapter 4, the same set of features was used to assess the effects of a DREADD-induced perturbation of D1 MSNs on BOLD dynamics within each region of the striato-thalamic-cortical circuit. These classifiers (D1 inhibition and D1 excitation classifiers) were able to identify all thalamic regions which form anatomically closed-loop projections with the neuromodulated part of striatum. This result is striking because functional connectivity analysis was not sensitive enough to pick up such anatomically accurate details, indicating the sensitivity of this rich macroscopic feature set to controlled cellular neuromodulation. Distinct macroscopic changes in brain dynamics observed in the neuromodulated areas, as well as within anatomically defined circuitry, provide the first direct evidence that macroscopic brain dynamics reflect the state of cortical and subcortical microcircuits. Our approach could be leveraged to explore rsfMRI data in human patients and healthy controls by using classifiers trained on the data obtained from causal neuromodulatory experiments. We refer to these classifiers as ‘computational sensors’, in chapter 3.

5.2.1 Translational potential of ‘computational sensors’

Resting-state fMRI is a commonly used modality to derive imaging-based biomarkers for obtaining diagnostic predictions and to guide treatments of multiple brain disorders. Machine learning has been extensively deployed to investigate the diagnostic value of rsfMRI data (Khosla et al., 2019). Supervised machine learning algorithms, such as SVMs, rely on resting-state functional connections obtained for a specific brain disorder (biomarkers), as discriminative features in a classifier (Du et al., 2018, Demirtaş and Deco, 2018, Khosla et al., 2019). Because the underlying biological basis of psychiatric and neurodevelopmental disorders remains elusive, functional connectivity biomarkers display an overlap between the regions with observed significant differences among different clinical populations (Demirtaş and Deco, 2018), consequently impeding the differentiation of disorders. Using machine learning algorithms trained on data obtained following microcircuit or cellular modulations, which are hypothesized as a potential biological basis of a disorder, could help differentiate disorders based on their biological underpinnings and ultimately provide some mechanistic insight useful for guiding treatment.

Our high classification accuracy in a number of cortical regions of a mouse disease model known for its PV depletion, obtained with a classifier trained on data with controlled acute inhibition of PV interneurons within somatosensory cortex, is a first indication of a potential of such an approach. Correspondence of PV gene distribution between human and mouse cortex was recently demonstrated (Anderson et al., 2020, Fulcher et al., 2019). A noninvasive

MRI contrast map was used as a common spatial reference for interspecies comparison, indicating that PV gene distribution exhibits strong interspecies correspondence across the mouse and human cortex (Fulcher et al., 2019). Anderson and colleagues show that interneuron gene distribution is consistent across species and further demonstrate that cortical PV gene distribution is associated with genetic risk for schizophrenia in the general population (Anderson et al., 2020). It is therefore tempting to speculate that our classifier may be leveraged to distinguish altered cortical dynamics of rsfMRI data obtained from schizophrenic patients, who, similarly to ASD patients, display perturbed cortical E:I balance. However, this translational approach may be hampered by other distinctive microstructural properties across the two species, such as cytoarchitecture (Vogt and Paxinos, 2014) and future work should elucidate more on generalizability of these ‘computational sensors’. The development and cross-validation of such classifiers could provide a platform to significantly increase the explanatory power, in the context of biological underpinnings, of the vast amount of publicly available rsfMRI datasets of various brain disorders.

5.2.2 Outlook

Timeseries fluctuations for each region of interest (analyzed in chapters 3 and 4 of this thesis) were represented by a massive set of features, significantly complicating interpretations of underlying dynamical mechanisms upon cell-specific neuromodulation. In the context of regional BOLD dynamics presented in chapter 4, I will outline a couple of possible approaches that could help in assessing which specific features contribute the most to significant alterations in brain dynamics of regions that constitute the striato-thalamic-cortical circuit. By applying further analyses, it would be of interest to identify whether these features are identical or belong to a similar category of features (e.g., autocorrelation properties, entropy, stationarity, etc.) across thalamus, cortex and striatum. This could provide mechanistic insights into how striatal cell-specific neuromodulation affects BOLD signal changes across different regions and reveal whether there is a circuit specific signature to D1 MSNs modulation.

A first approach could involve applying principal component analysis (PCA). PCA allows dimensionality reduction of our massive feature datasets, while the first two PCA components consist of the highest percentage of explained variances in the data. Correlating each principal component to the timeseries feature vectors of each individual region would provide a list of features, which could further be assessed for their similarity. Another approach could be to reduce the initial number of features by applying a pre-selected subset of features such as *catch22* (Lubba et al., 2019) or other pre-selected features based on rodent rsfMRI data, followed by their assessment of similarity.

Since each feature is obtained through a timeseries signal processing algorithm, understanding which features shape BOLD dynamics could provide the basis for further

characterization of the DREADD-induced changes of the BOLD signal. This could lead to insights about the exact generative processes underlying the timeseries signal and how they are shaped by DREADD-induced neuromodulation.

5.3. DREADD-rsfMRI approach; potential benefits for computational models

Biophysical computational models are used to provide a mechanistic understanding of how cell-level disturbances propagate through scales, impact system level neural activity and network dynamics, and bring about complex behavior (Murray et al., 2018). These models use mathematical equations to describe properties of neurons, neuronal circuits and dynamic brain networks based on a biophysical foundation obtained from empirical experiments. Further advancement of the sophisticated models requires invasive animal experiments to causally confirm generated simulations (Demirtaş and Deco, 2018, Kringelbach and Deco, 2020). The cell-specific perturbations of macroscopic functional connectivity and brain dynamics presented in this thesis, are the type of *in vivo* experiments that can provide confirmation of *in silico* predictions. The rich set of informative features obtained for numerous individual brain regions could inform biophysical computational models, thus guiding the attempt to perturb neuronal activity with the empirically confirmed effects on spatiotemporal dynamics of each region.

In silico brain models are also applied to study circuit mechanisms underlying neuroimaging biomarkers of brain disorders (Maki-Marttunen et al., 2019). Perturbations of specific neuronal parameters can simulate hypothesized disease mechanism and predicted simulations can be further confirmed in experimental settings (Murray et al., 2018, Deco et al., 2018, Deco and Kringelbach, 2014). This can then be further leveraged to form hypotheses of human psychiatric and neurodevelopmental disorders. Recently, Trakoshis and colleagues used an *in silico* model of local neuronal microcircuitry to predict changes in LFP and BOLD signal following E:I perturbations, by assessing spectral properties of neuronal timeseries data. Simulated timeseries spectral property changes, considered as neuroimaging markers of E:I balance, were confirmed by *in vivo* experiments in mice, where resting-state BOLD signal was measured following cortical E:I perturbations. By assessing these neuroimaging markers in rsfMRI of autistic human patients, they illustrated a dysfunctional E:I balance in social brain networks of autistic males (Trakoshis et al., 2020). This study illustrates the potential of combining chemogenetic neuromodulation with rsfMRI to confirm simulated neuroimaging markers of E:I balance and directly assess these markers in the rsfMRI data of human patients. Experiments similar to the ones presented in this thesis could offer guidance for the development of functional models of cortical and subcortical circuits, which could be leveraged to explore novel biomarkers of brain disorders.

5.4. Limitations

5.4.1 Anesthetics

The widespread use of anesthetics for animal imaging studies presents one of the caveats for investigating the relationship between animal behavior and rsfMRI results or for direct across species comparisons. While acquiring rsfMRI data in humans is a straightforward process, mouse rsfMRI has its challenges. As animals are mildly anesthetized during scanning, procedures such as endotracheal intubation and intravenous cannulation are required to ensure that the animal's physiological processes are maintained at a constant rate, such as respiration rate, body temperature and also depth of anesthesia. Any deviation from optimally set parameters has an influence on the BOLD signal acquired, including the choice of anesthetics. Using anesthetics during functional imaging of rodents minimizes animal movements and eliminates the effects of animal stress on its basic physiology and ultimately quality of signal acquired. Anesthetics exert their dose-dependent sedatory effects by acting on specific target receptors, including γ -aminobutyric acid subtype A ($GABA_A$), α_2 adrenoreceptor (α_2AR) and N-methyl-d-aspartate (NMDA) receptors (Reimann and Niendorf, 2020). A choice in anesthetics could potentially be guided by the region of interest investigated during rsfMRI in order to ensure minimal interference with processes to be studied. This was recently demonstrated in our work aimed at exploring brain wide effects of locus coeruleus (LC) activation. Specifically, the use of medetomidine, an α_2AR agonist known to suppress LC firing, prevented DREADD-induced LC activation, while brain-wide effects of LC activation were observed with the use of isoflurane anesthetic (Zerbi et al., 2019a).

For the studies presented in this thesis, anesthetics used included a combination of medetomidine, pancuronium (muscle relaxant) and $GABA_A$ agonist isoflurane at very low doses (Grandjean et al., 2014a). $GABA$ receptors are widely distributed throughout the brain, thus isoflurane was kept at minimal doses (Lukasik and Gillies, 2003). Isoflurane is a vasodilator, medetomidine a vasoconstrictor, while the former decreases cerebral blood flow the latter increases it, and both can contribute to the impairment of BOLD signal in mice. Nonetheless, recent studies indicate that the combination of the two anesthetics seems to 'balance out' each of their specific effects, yielding functional connectivity results with good correspondence to awake animals, and with anatomical connectivity of the mouse brain (Bukhari et al., 2017, Grandjean et al., 2020, Steiner et al., 2021, Grandjean et al., 2017b). Cortico-cortical and striato-cortical connectivity results illustrated in this thesis also demonstrate good correspondence between functional and structural connectivity of the mouse brain.

An alternative to using anesthesia is to perform awake animal imaging. Awake animals are stressed and prone to unexpected movements which affect the BOLD signal. The acclimation protocols may reduce motion artefacts, but the repeated stress of acclimation may have its

own effects on the BOLD signal (Henckens et al., 2015, Steiner et al., 2021). Researchers have reported increased cortical somatosensory functional connectivity in rats after undergoing immobilization protocols for ten days in a row (Henckens et al., 2015). Maintaining consistent and constant physiological processes in awake animals may present a challenge, introducing variability into the acquired data. The choice of anesthetized vs awake animal imaging may be guided by the research question of interest, particularly if it involves direct comparisons between rsfMRI and behavior. For the purpose of this thesis, a well-designed balanced anesthesia protocol tailored to our experimental conditions with careful monitoring of basic animal physiology allowed us to produce interpretable, reproducible and reliable rsfMRI results.

5.4.2 Translational insights

Given that there is continuously growing interest in the translational potential of animal research, it is important to take into account the similarities and differences of rodent and human neuroanatomy and brain function. Human and rodent rsfMRI share identical sequences for signal generation and (pre)processing techniques, making rsfMRI a valuable tool for determining the scope and limits of rodent translational potential. The mouse brain is three orders of magnitude smaller than the human brain, yet astonishing similarities between the brains of the two species have been observed. Many robust and evolutionary conserved networks across humans and mice have already been demonstrated, albeit differences have also been noted, such as in default mode network (Sforazzini et al., 2014, Zerbi et al., 2015, Grandjean et al., 2017b). Similarities in limbic and sensorimotor cortico-striatal circuits between humans and mice were demonstrated, while anterior portion of the putamen and caudate circuits displayed notable differences between the two species (Balsters et al., 2020). Using a common MRI based spatial reference map across species, correspondence of large-scale cortical gradients of cytoarchitecture between mice and humans has been demonstrated (Fulcher et al., 2019). Assessment of homology in network connectivity between mice and humans demonstrated similar overall connective distribution, albeit with unique differences between the species. This indicates that while some specific connections within the rodent and human brains may not correspond directly, many of the network properties do (Stafford et al., 2014).

While this thesis does not directly compare rsfMRI data across the two species, its work has been motivated by the lack of biological underpinnings of alterations in macroscopic FC detected in human brains. In this type of research, the ultimate goal is to provide further insight into functions of the human brain, of which some possible directions have been discussed in this chapter. However, it remains crucial to acknowledge the neuroanatomical and functional differences between the brains of the two species, in order to correctly assess the feasibility of translational approaches.

5.5. Chemogenetic neuromodulation combined with resting-state fMRI

This PhD thesis was motivated by the lack of biological insights underlying macroscopic resting-state functional connectivity observed in healthy and diseased brains of humans, as well as mouse models of brain disorders. Our results provide causal evidence of network alterations upon cell-specific neuromodulation, which could be leveraged to understand aberrant macroscopic brain connectivity observed in various brain disorders. This work contributes towards a rapidly expanding field directed towards assessing the biological underpinnings of macroscopic altered connectivity. The overarching goal of such a research effort is to generate essential mechanistic insight that can be used to back-translate clinical evidence of aberrant connectivity into interpretable neurophysiological markers or models that can help understand, diagnose and guide treatment of brain disorders (Liska and Gozzi, 2016).

Combining DREADD neuromodulation with fMRI in rodents is an approach in its infancy and only a handful of research groups have combined the two modalities in rodents. Initial studies focused on the pharmacological assessment of the BOLD signal, reporting no significant alterations observed in resting-state functional connectivity (Roelofs et al., 2017, Nakamura et al., 2020). We were the first to show robust changes in functional connectivity upon DREADD-induced stimulation (Zerbi et al., 2019a, Markicevic et al., 2020), the changes now observed by a couple of other research groups (Peeters et al., 2020, Canella et al., 2020). Work presented in this thesis is the first to offer an insight into how DREADD neuromodulation could be applied to study macroscopic effects of apparent putative disease mechanisms by applying advanced machine learning approaches. We used a rich feature set obtained from a diverse range of interdisciplinary applications and completely data-driven machine learning approaches, to provide the first direct evidence that macroscopic dynamics of the BOLD signal reflect the state of underlying microcircuits. We extended this analysis to a well-defined anatomical circuit to show that cell-specific neuromodulation shapes the BOLD dynamics not only in the neuromodulated area but in anatomically connected networks.

Chemogenetics were chosen for cell-specific neuromodulation because of their effectiveness, ease of use, specificity, acute reversible effects and their growing possibility to be used as a therapeutic intervention (English and Roth, 2015, Magnus et al., 2019). Unlike optogenetics, chemogenetics can be combined with rsfMRI, a method extensively applied to study functional connectivity alterations associated with disease and derive imaging-based biomarkers for diagnostic predictions of brain disorders. Consequently, linking neuronal changes across scales via chemogenetics and rsfMRI holds potentially major implications for translational work.

Our aim was to bridge the gap between microscopic and macroscopic brain levels via chemogenetics and rsfMRI. We have successfully illustrated causal effects of micro-

modulation on macro-connectivity, albeit leaving much work for future research. Research that will focus on elucidating exact mechanistic details that bring about macroscale connectivity alterations and research that will further tackle the translational potential of insights obtained by combining chemogenetic neuromodulation with rsfMRI in either slightly anesthetized or even awake rodents. The hope and ultimate goal of this scientific endeavor would be to provide a deeper understanding of brain function across scales, ultimately leading to more specific and effective therapeutics for treatment of brain disorders.

“Look at me, still talking when there’s Science to do.” - Glados

References

- Abe, Y., Tsurugizawa, T. & Le Bihan, D. 2017a. Water diffusion closely reveals neural activity status in rat brain loci affected by anesthesia. *PLoS Biology*, 15, e2001494.
- Abe, Y., Van Nguyen, K., Tsurugizawa, T., Ciobanu, L. & Le Bihan, D. 2017b. Modulation of water diffusion by activation-induced neural cell swelling in *Aplysia Californica*. *Scientific Reports*, 7, 6178.
- Adesnik, H. & Scanziani, M. 2010. Lateral competition for cortical space by layer-specific horizontal circuits. *Nature*, 464, 1155-60.
- Ajram, L. A., Horder, J., Mendez, M. A., Galanopoulos, A., Brennan, L. P., Wichers, R. H., Robertson, D. M., Murphy, C. M., Zinkstok, J., Ivin, G., Heasman, M., Meek, D., Tricklebank, M. D., Barker, G. J., Lythgoe, D. J., Edden, R. a. E., Williams, S. C., Murphy, D. G. M. & Mcalonan, G. M. 2017. Shifting brain inhibitory balance and connectivity of the prefrontal cortex of adults with autism spectrum disorder. *Transl Psychiatry*, 7, e1137.
- Albin, R. L., Young, A. B. & Penney, J. B. 1989. The functional anatomy of basal ganglia disorders. *Trends Neurosci*, 12, 366-75.
- Alexander, G. M., Rogan, S. C., Abbas, A. I., Armbruster, B. N., Pei, Y., Allen, J. A., Nonneman, R. J., Hartmann, J., Moy, S. S., Nicoletis, M. A., Mcnamara, J. O. & Roth, B. L. 2009. Remote control of neuronal activity in transgenic mice expressing evolved G protein-coupled receptors. *Neuron*, 63, 27-39.
- Allen, J. A. & Roth, B. L. 2011. Strategies to Discover Unexpected Targets for Drugs Active at G Protein-Coupled Receptors. *Annual Review of Pharmacology and Toxicology*, 51, 117-144.
- Alloway, K. D., Smith, J. B., Mowery, T. M. & Watson, G. D. R. 2017. Sensory Processing in the Dorsolateral Striatum: The Contribution of Thalamostriatal Pathways. *Front Syst Neurosci*, 11, 53.
- Alves, P. N., Foulon, C., Karolis, V., Bzdok, D., Margulies, D. S., Volle, E. & Thiebaut De Schotten, M. 2019. An improved neuroanatomical model of the default-mode network reconciles previous neuroimaging and neuropathological findings. *Commun Biol*, 2, 370.
- Anderson, K. M., Collins, M. A., Chin, R., Ge, T., Rosenberg, M. D. & Holmes, A. J. 2020. Transcriptional and imaging-genetic association of cortical interneurons, brain function, and schizophrenia risk. *Nat Commun*, 11, 2889.
- Andrew, R. D., Jarvis, C. R. & Obeidat, A. S. 1999. Potential Sources of Intrinsic Optical Signals Imaged in Live Brain Slices. *Methods*, 18, 185-196.
- Andrew, R. D. & Macvicar, B. A. 1994. Imaging cell volume changes and neuronal excitation in the hippocampal slice. *Neuroscience*, 62, 371-83.
- Anenberg, E., Chan, A. W., Xie, Y., Ledue, J. M. & Murphy, T. H. 2015. Optogenetic stimulation of GABA neurons can decrease local neuronal activity while increasing cortical blood flow. *J Cereb Blood Flow Metab*, 35, 1579-86.
- Antal, M., Beneduce, B. M. & Regehr, W. G. 2014. The substantia nigra conveys target-dependent excitatory and inhibitory outputs from the basal ganglia to the thalamus. *J Neurosci*, 34, 8032-42.

- Antoine, M. W., Langberg, T., Schnepel, P. & Feldman, D. E. 2019. Increased Excitation-Inhibition Ratio Stabilizes Synapse and Circuit Excitability in Four Autism Mouse Models. *Neuron*, 101, 648-661 e4.
- Armbruster, B. N., Li, X., Pausch, M. H., Herlitze, S. & Roth, B. L. 2007. Evolving the lock to fit the key to create a family of G protein-coupled receptors potentially activated by an inert ligand. *PNAS*, 104, 5163–5168.
- Aso, T., Urayama, S.-I., Fukuyama, H. & Le Bihan, D. 2013. Comparison of diffusion-weighted fMRI and BOLD fMRI responses in a verbal working memory task. *NeuroImage*, 67, 25-32.
- Atallah, B. V., Bruns, W., Carandini, M. & Scanziani, M. 2012. Parvalbumin-expressing interneurons linearly transform cortical responses to visual stimuli. *Neuron*, 73, 159-70.
- Atasoy, D. & Sternson, S. M. 2018. Chemogenetic Tools for Causal Cellular and Neuronal Biology. *Physiol Rev*, 98, 391-418.
- Avanaki, M. R. N., Xia, J. & Wang, L. V. High resolution functional photoacoustic computed tomography of the mouse brain during electrical stimulation. *Proc.SPIE*, 2013.
- Bakhurin, K. I., Mac, V., Golshani, P. & Masmanidis, S. C. 2016. Temporal correlations among functionally specialized striatal neural ensembles in reward-conditioned mice. *J Neurophysiol*, 115, 1521-32.
- Balsters, J. H., Zerbi, V., Sallet, J., Wenderoth, N. & Mars, R. B. 2020. Primate homologs of mouse cortico-striatal circuits. *eLife*, 9, e53680.
- Baltes, C., Radzwill, N., Bosshard, S., Marek, D. & Rudin, M. 2009. Micro MRI of the mouse brain using a novel 400 MHz cryogenic quadrature RF probe. *NMR Biomed*, 22, 834-42.
- Bando, Y., Grimm, C., Cornejo, V. H. & Yuste, R. 2019. Genetic voltage indicators. *BMC Biol*, 17, 71.
- Barbier, E. L., Lamalle, L. & Decorps, M. 2001. Methodology of Brain Perfusion Imaging *Journal of Magnetic Resonance Imaging* 13, 496-520.
- Barch, D. M., Burgess, G. C., Harms, M. P., Petersen, S. E., Schlaggar, B. L., Corbetta, M., Glasser, M. F., Curtiss, S., Dixit, S., Feldt, C., Nolan, D., Bryant, E., Hartley, T., Footer, O., Bjork, J. M., Poldrack, R., Smith, S., Johansen-Berg, H., Snyder, A. Z., Van Essen, D. C. & Consortium, W. U.-M. H. 2013. Function in the human connectome: task-fMRI and individual differences in behavior. *NeuroImage*, 80, 169-189.
- Bartelle, B. B., Barandov, A. & Jasanoff, A. 2016. Molecular fMRI. *J Neurosci*, 36, 4139-48.
- Bartos, M., Vida, I. & Jonas, P. 2007. Synaptic mechanisms of synchronized gamma oscillations in inhibitory interneuron networks. *Nat Rev Neurosci*, 8, 45-56.
- Bay Konig, A., Ciriachi, C., Gether, U. & Rickhag, M. 2019. Chemogenetic Targeting of Dorsomedial Direct-pathway Striatal Projection Neurons Selectively Elicits Rotational Behavior in Mice. *Neuroscience*, 401, 106-116.
- Belloy, M. E., Naeyaert, M., Abbas, A., Shah, D., Vanreusel, V., Van Audekerke, J., Keilholz, S. D., Keliris, G. A., Van Der Linden, A. & Verhoye, M. 2018. Dynamic resting state fMRI analysis in mice reveals a set of Quasi-Periodic Patterns and illustrates their relationship with the global signal. *Neuroimage*, 180, 463-484.
- Benjamini, Y. & Hochberg, Y. 1995. Controlling the False Discovery Rate: A Practical and Powerful Approach to Multile Testing. *Journal of Royal Statistical Society: Series B (Methodological)*, 57(1), 289-300.

- Bertero, A., Liska, A., Pagani, M., Parolisi, R., Masferrer, M. E., Gritti, M., Pedrazzoli, M., Galbusera, A., Sarica, A., Cerasa, A., Buffelli, A., Tonini, R., Buffo, A., Gross, C., Pasqualetti, M. & Gozzi, A. 2018. Autism-associated 16p11.2 microdeletion impairs prefrontal functional connectivity in mouse and human. *Brain*, 141, 2055-2065.
- Biswal, B., Yetkin, F. Z., Haughton, V. M. & Hyde, J. H. 1995. Functional Connectivity in the Motor Cortex of Resting Human Brain Using Echo-Planar MRI. *Magn Reson Med* 34, 537-541.
- Bonaventura, J., Eldridge, M. a. G., Hu, F., Gomez, J. L., Sanchez-Soto, M., Abramyan, A. M., Lam, S., Boehm, M. A., Ruiz, C., Farrell, M. R., Moreno, A., Galal Faress, I. M., Andersen, N., Lin, J. Y., Moaddel, R., Morris, P. J., Shi, L., Sibley, D. R., Mahler, S. V., Nabavi, S., Pomper, M. G., Bonci, A., Horti, A. G., Richmond, B. J. & Michaelides, M. 2019. High-potency ligands for DREADD imaging and activation in rodents and monkeys. *Nature Communications*, 10, 4627.
- Bonnavion, P., Fernandez, E. P., Varin, C. & De Kerchove D'exaerde, A. 2019. It takes two to tango: Dorsal direct and indirect pathways orchestration of motor learning and behavioral flexibility. *Neurochem Int*, 124, 200-214.
- Bouchard, M. B., Voleti, V., Mendes, C. S., Lacefield, C., Grueber, W. B., Mann, R. S., Bruno, R. M. & Hillman, E. M. C. 2015. Swept confocally-aligned planar excitation (SCAPE) microscopy for high-speed volumetric imaging of behaving organisms. *Nature Photonics*.
- Boxerman, J. L., Hamberg, L. M., Rosen, B. R. & Weisskoff, R. M. 1995. MR contrast due to intravascular magnetic susceptibility perturbations. *Magn Reson Med*, 34, 555-66.
- Boyden, E. S., Zhang, F., Bamberg, E., Nagel, G. & Deisseroth, K. 2005. Millisecond-timescale, genetically targeted optical control of neural activity. *Nat Neurosci*, 8, 1263-8.
- Brookes, M. J., Woolrich, M., Luckhoo, H., Price, D., Hale, J. R., Stephenson, M. C., Barnes, G. R., Smith, S. M. & Morris, P. G. 2011. Investigating the electrophysiological basis of resting state networks using magnetoencephalography. *Proceedings of the National Academy of Sciences*, 108, 16783.
- Bubb, E. J., Kinnavane, L. & Aggleton, J. P. 2017. Hippocampal - diencephalic - cingulate networks for memory and emotion: An anatomical guide. *Brain Neurosci Adv*, 1.
- Buehlmann, D., Grandjean, J., Xandry, J. & Rudin, M. 2018. Longitudinal resting-state functional magnetic resonance imaging in a mouse model of metastatic bone cancer reveals distinct functional reorganizations along a developing chronic pain state. *PAIN*, 159, 719-727.
- Bukhari, Q., Schroeter, A., Cole, D. M. & Rudin, M. 2017. Resting State fMRI in Mice Reveals Anesthesia Specific Signatures of Brain Functional Networks and Their Interactions. *Front Neural Circuits*, 11, 5.
- Bulow, P., Murphy, T. J., Bassell, G. J. & Wenner, P. 2019. Homeostatic Intrinsic Plasticity Is Functionally Altered in Fmr1 KO Cortical Neurons. *Cell Rep*, 26, 1378-1388 e3.
- Burke, D. A., Rotstein, H. G. & Alvarez, V. A. 2017. Striatal Local Circuitry: A New Framework for Lateral Inhibition. *Neuron*, 96, 267-284.
- Buxton, R. B. 2013. The physics of functional magnetic resonance imaging (fMRI). *Rep Prog Phys*, 76, 096601.
- Buxton, R. B., Griffeth, V. E. M., Simon, A. B. & Moradi, F. 2014. Variability of the coupling of blood flow and oxygen metabolism responses in the brain: a problem for interpreting BOLD studies but potentially a new window on the underlying neural activity. *Frontiers in Neuroscience*, 8.

- Calabresi, P., Picconi, B., Tozzi, A., Ghiglieri, V. & Di Filippo, M. 2014. Direct and indirect pathways of basal ganglia: a critical reappraisal. *Nat Neurosci*, 17, 1022-30.
- Canella, C., Rocchi, F., Noei, S., Gutierrez-Barragan, D., Coletta, L., Galbusera, A., Vassanelli, S., Pasqualetti, M., Iurilli, G., Panzeri, S. & Gozzi, A. 2020. Cortical silencing results in paradoxical fMRI overconnectivity. *BioRxiv*.
- Cardin, J. A. 2016. Snapshots of the Brain in Action: Local Circuit Operations through the Lens of γ Oscillations. *The Journal of Neuroscience*, 36, 10496.
- Cardin, J. A. 2018. Inhibitory Interneurons Regulate Temporal Precision and Correlations in Cortical Circuits. *Trends Neurosci*, 41, 689-700.
- Cardin, J. A., Carlen, M., Meletis, K., Knoblich, U., Zhang, F., Deisseroth, K., Tsai, L. H. & Moore, C. I. 2009. Driving fast-spiking cells induces gamma rhythm and controls sensory responses. *Nature*, 459, 663-7.
- Cassataro, D., Bergfeldt, D., Malekian, C., Van Snellenberg, J. X., Thanos, P. K., Fishell, G. & Sjulson, L. 2014. Reverse pharmacogenetic modulation of the nucleus accumbens reduces ethanol consumption in a limited access paradigm. *Neuropsychopharmacology*, 39, 283-90.
- Cassataro, D. & Sjulson, L. 2015. The Use of DREADDs (Designer Receptors Exclusively Activated by Designer Receptors) in Transgenic Mouse Behavioral Models. 108, 95-108.
- Cauli, B. & Hamel, E. 2010. Revisiting the role of neurons in neurovascular coupling. *Frontiers in Neuroenergetics*, 2.
- Cea-Del Rio, C. A. & Huntsman, M. M. 2014. The contribution of inhibitory interneurons to circuit dysfunction in Fragile X Syndrome. *Frontiers in Cellular Neuroscience*, 8.
- Chavhan, G. B., Babyn, P. S., Thomas, B., Shroff, M. M. & Haacke, E. M. 2009. Principles, techniques, and applications of T2*-based MR imaging and its special applications. *Radiographics : a review publication of the Radiological Society of North America, Inc*, 29, 1433-1449.
- Chelini, G., Zerbi, V., Cimino, L., Grigoli, A., Markicevic, M., Libera, F., Robbiati, S., Gadler, M., Bronzoni, S., Miorelli, S., Galbusera, A., Gozzi, A., Casarosa, S., Provenzano, G. & Bozzi, Y. 2019. Aberrant Somatosensory Processing and Connectivity in Mice Lacking Engrailed-2. *J Neurosci*, 39, 1525-1538.
- Chen, J. J., Wieckowska, M., Meyer, E. & Pike, G. B. 2008. Cerebral blood flow measurement using fMRI and PET: a cross-validation study. *Int J Biomed Imaging*, 2008, 516359.
- Chen, K., Azeez, A., Chen, D. Y. & Biswal, B. B. 2020a. Resting-State Functional Connectivity: Signal Origins and Analytic Methods. *Neuroimaging Clin N Am*, 30, 15-23.
- Chen, T. W., Wardill, T. J., Sun, Y., Pulver, S. R., Renninger, S. L., Baohan, A., Schreiter, E. R., Kerr, R. A., Orger, M. B., Jayaraman, V., Looger, L. L., Svoboda, K. & Kim, D. S. 2013. Ultrasensitive fluorescent proteins for imaging neuronal activity. *Nature*, 499, 295-300.
- Chen, Z., Özbek, A., Rebling, J., Zhou, Q., Deán-Ben, X. L. & Razansky, D. 2020b. Multifocal structured illumination optoacoustic microscopy. *Light: Science & Applications*, 9, 1-9.
- Cheng, L. C., Chang, C. Y., Lin, C. Y., Cho, K. C., Yen, W. C., Chang, N. S., Xu, C., Dong, C. Y. & Chen, S. J. 2012. Spatiotemporal focusing-based widefield multiphoton microscopy for fast optical sectioning. *Opt Express*, 20, 8939-48.
- Choi, M., Kwok, S. J. & Yun, S. H. 2015. In vivo fluorescence microscopy: lessons from observing cell behavior in their native environment. *Physiology (Bethesda)*, 30, 40-9.

- Chuang, K. H. & Nasrallah, F. A. 2017. Functional networks and network perturbations in rodents. *Neuroimage*, 163, 419-436.
- Chudakov, D. M., Matz, M. V., Lukyanov, S. & Lukyanov, K. A. 2010. Fluorescent proteins and their applications in imaging living cells and tissues. *Physiol Rev*, 90, 1103-63.
- Collins, D. P., Anastasiades, P. G., Marlin, J. J. & Carter, A. G. 2018. Reciprocal Circuits Linking the Prefrontal Cortex with Dorsal and Ventral Thalamic Nuclei. *Neuron*, 98, 366-379.e4.
- Contractor, A., Klyachko, V. A. & Portera-Cailliau, C. 2015. Altered Neuronal and Circuit Excitability in Fragile X Syndrome. *Neuron*, 87, 699-715.
- Corbetta, M., Patel, G. & Shulman, G. L. 2008. The reorienting system of the human brain: from environment to theory of mind. *Neuron*, 58, 306-324.
- Dana, H., Sun, Y., Mohar, B., Hulse, B. K., Kerlin, A. M., Hasseman, J. P., Tsegaye, G., Tsang, A., Wong, A., Patel, R., Macklin, J. J., Chen, Y., Konnerth, A., Jayaraman, V., Looger, L. L., Schreiter, E. R., Svoboda, K. & Kim, D. S. 2019. High-performance calcium sensors for imaging activity in neuronal populations and microcompartments. *Nat Methods*, 16, 649-657.
- De Groot, A., Van Den Boom, B. J., Van Genderen, R. M., Coppens, J., Van Veldhuijzen, J., Bos, J., Hoedemaker, H., Negrello, M., Willuhn, I., De Zeeuw, C. I. & Hoogland, T. M. 2020. NINscope, a versatile miniscope for multi-region circuit investigations. *Elife*, 9.
- De Luca, A., Schlaffke, L., Siero, J. C. W., Froeling, M. & Leemans, A. 2019. On the sensitivity of the diffusion MRI signal to brain activity in response to a motor cortex paradigm. *Human Brain Mapping*, 40, 5069-5082.
- Deán-Ben, X. L., Gottschalk, S., Mc Larney, B., Shoham, S. & Razansky, D. 2017. Advanced optoacoustic methods for multiscale imaging of in vivo dynamics. *Chem Soc Rev*, 46, 2158-2198.
- Deco, G., Cruzat, J., Cabral, J., Knudsen, G. M., Carhart-Harris, R. L., Whybrow, P. C., Logothetis, N. K. & Kringelbach, M. L. 2018. Whole-Brain Multimodal Neuroimaging Model Using Serotonin Receptor Maps Explains Non-linear Functional Effects of LSD. *Current Biology*, 28, 3065-3074.e6.
- Deco, G. & Kringelbach, M. L. 2014. Great expectations: using whole-brain computational connectomics for understanding neuropsychiatric disorders. *Neuron*, 84, 892-905.
- Deffieux, T., Demene, C., Pernot, M. & Tanter, M. 2018. Functional ultrasound neuroimaging: a review of the preclinical and clinical state of the art. *Current Opinion in Neurobiology*, 50, 128-135.
- Dehghani, N., Peyrache, A., Telenczuk, B., Le Van Quyen, M., Halgren, E., Cash, S. S., Hatsopoulos, N. G. & Destexhe, A. 2016. Dynamic Balance of Excitation and Inhibition in Human and Monkey Neocortex. *Sci Rep*, 6, 23176.
- Demirtaş, M. & Deco, G. 2018. Computational Models of Dysconnectivity in Large-Scale Resting-State Networks. *Computational Psychiatry*.
- Denk, W., Strickler, J. H. & Webb, W. W. 1990. Two-photon laser scanning fluorescence microscopy. *Science*, 248, 73-6.
- Desjardins, M., Kiliç, K., Thunemann, M., Mateo, C., Holland, D., Ferri, C. G. L., Cremonesi, J. A., Li, B., Cheng, Q., Weldy, K. L., Saisan, P. A., Kleinfeld, D., Komiyama, T., Liu, T. T., Bussell, R., Wong, E. C., Scadeng, M., Dunn, A. K., Boas, D. A., Sakadžić, S., Mandeville, J. B., Buxton, R. B., Dale, A. M. & Devor, A. 2019. Awake Mouse Imaging: From Two-Photon Microscopy to Blood Oxygen Level-Dependent Functional

- Magnetic Resonance Imaging. *Biological Psychiatry: Cognitive Neuroscience and Neuroimaging*, 4, 533-542.
- Devor, A. & Boas, D. 2012. Neurovascular Imaging. *Frontiers in Neuroenergetics*, 4.
- Devor, A., Tian, P., Nishimura, N., Teng, I. C., Hillman, E. M. C., Narayanan, S. N., Ulbert, I., Boas, D. A., Kleinfeld, D. & Dale, A. M. 2007. Suppressed Neuronal Activity and Concurrent Arteriolar Vasoconstriction May Explain Negative Blood Oxygenation Level-Dependent Signal. *The Journal of Neuroscience*, 27, 4452.
- Diaz-Hernandez, E., Contreras-Lopez, R., Sanchez-Fuentes, A., Rodriguez-Sibrian, L., Ramirez-Jarquín, J. O. & Tecuapetla, F. 2018. The Thalamostriatal Projections Contribute to the Initiation and Execution of a Sequence of Movements. *Neuron*, 100, 739-752 e5.
- Drew, P. J., Mateo, C., Turner, K. L., Yu, X. & Kleinfeld, D. 2020. Ultra-slow Oscillations in fMRI and Resting-State Connectivity: Neuronal and Vascular Contributions and Technical Confounds. *Neuron*, 107, 782-804.
- Du, Y., Fu, Z. & Calhoun, V. D. 2018. Classification and Prediction of Brain Disorders Using Functional Connectivity: Promising but Challenging. *Front Neurosci*, 12, 525.
- Dunn, A. K., Bolay, H., Moskowitz, M. A. & Boas, D. A. 2001. Dynamic imaging of cerebral blood flow using laser speckle. *J Cereb Blood Flow Metab*, 21, 195-201.
- Dussaux, C., Szabo, V., Chastagnier, Y., Fodor, J., Léger, J. F., Bourdieu, L., Perroy, J. & Ventalon, C. 2018. Fast confocal fluorescence imaging in freely behaving mice. *Sci Rep*, 8, 16262.
- El-Boustani, S., Sermet, B. S., Foustoukos, G., Oram, T. B., Yizhar, O. & Petersen, C. C. H. 2020. Anatomically and functionally distinct thalamocortical inputs to primary and secondary mouse whisker somatosensory cortices. *Nature Communications*, 11, 3342.
- Elena Erro, M., Lanciego, J. L. & Giménez-Amaya, J. M. 2002. Re-examination of the thalamostriatal projections in the rat with retrograde tracers. *Neuroscience Research*, 42, 45-55.
- Elsayed, G. F. & Cunningham, J. P. 2017. Structure in neural population recordings: an expected byproduct of simpler phenomena? *Nat Neurosci*, 20, 1310-1318.
- Engel, A. K. & Singer, W. 2001. Temporal binding and the neural correlates of sensory awareness. *TRENDS in Cognitive Sciences*, 5.
- English, J. G. & Roth, B. L. 2015. Chemogenetics—A Transformational and Translational Platform. *JAMA Neurology*, 72, 1361-1366.
- Errico, C., Osmanski, B. F., Pezet, S., Couture, O., Lenkei, Z. & Tanter, M. 2016. Transcranial functional ultrasound imaging of the brain using microbubble-enhanced ultrasensitive Doppler. *Neuroimage*, 124, 752-761.
- Errico, C., Pierre, J., Pezet, S., Desailly, Y., Lenkei, Z., Couture, O. & Tanter, M. 2015a. Ultrafast ultrasound localization microscopy for deep super-resolution vascular imaging. *Nature*, 527, 499-502.
- Errico, F., D'argenio, V., Sforazzini, F., Iasevoli, F., Squillace, M., Guerri, G., Napolitano, F., Angrisano, T., Di Maio, A., Keller, S., Vitucci, D., Galbusera, A., Chiariotti, L., Bertolino, A., De Bartolomeis, A., Salvatore, F., Gozzi, A. & Usiello, A. 2015b. A role for D-aspartate oxidase in schizophrenia and in schizophrenia-related symptoms induced by phencyclidine in mice. *Translational Psychiatry*, 5, e512-e512.
- Evangelio, M., García-Amado, M. & Clascá, F. 2018. Thalamocortical Projection Neuron and Interneuron Numbers in the Visual Thalamic Nuclei of the Adult C57BL/6 Mouse. *Frontiers in neuroanatomy*, 12, 27-27.

- Evans, H. D. & McDicken, W. N. 2000. *Doppler Ultrasound: Physics, Instrumentation and Signal Processing*, Wiley.
- Farrell, M. S., Pei, Y., Wan, Y., Yadav, P. N., Daigle, T. L., Urban, D. J., Lee, H. M., Sciaky, N., Simmons, A., Nonneman, R. J., Huang, X. P., Hufeisen, S. J., Guettier, J. M., Moy, S. S., Wess, J., Caron, M. G., Calakos, N. & Roth, B. L. 2013. A Galphas DREADD mouse for selective modulation of cAMP production in striatopallidal neurons. *Neuropsychopharmacology*, 38, 854-62.
- Feldmeyer, D., Qi, G., Emmenegger, V. & Staiger, J. F. 2018. Inhibitory interneurons and their circuit motifs in the many layers of the barrel cortex. *Neuroscience*, 368, 132-151.
- Fercher, A. F. & Briers, J. D. 1981. Flow Visualization by Means of Single-Exposure Speckle Photography. *Optics Communications*, 37, 326-330.
- Fox, M. D. & Greicius, M. 2010. Clinical applications of resting state functional connectivity. *Front Syst Neurosci*, 4, 19.
- Fox, M. D. & Raichle, M. E. 2007. Spontaneous fluctuations in brain activity observed with functional magnetic resonance imaging. *Nat Rev Neurosci*, 8, 700-11.
- Fox, P. T. & Raichle, M. E. 1986. Focal physiological uncoupling of cerebral blood flow and oxidative metabolism during somatosensory stimulation in human subjects. *Proceedings of the National Academy of Sciences of the United States of America*, 83, 1140-1144.
- Freeze, B. S., Kravitz, A. V., Hammack, N., Berke, J. D. & Kreitzer, A. C. 2013. Control of basal ganglia output by direct and indirect pathway projection neurons. *The Journal of neuroscience : the official journal of the Society for Neuroscience*, 33, 18531-18539.
- Froudarakis, E., Fahey, P. G., Reimer, J., Smirnakis, S. M., Tehovnik, E. J. & Tolia, A. S. 2019. The Visual Cortex in Context. *Annu Rev Vis Sci*, 5, 317-339.
- Fulcher, B. D. & Jones, N. S. 2017. hctsa: A Computational Framework for Automated Time-Series Phenotyping Using Massive Feature Extraction. *Cell Syst*, 5, 527-531 e3.
- Fulcher, B. D., Little, M. A. & Jones, N. S. 2013. Highly comparative time-series analysis: the empirical structure of time series and their methods. *Journal of the Royal Society Interface*, 10(83).
- Fulcher, B. D., Murray, J. D., Zerbi, V. & Wang, X. J. 2019. Multimodal gradients across mouse cortex. *Proc Natl Acad Sci U S A*, 116 (10).
- Gallego, J. A., Perich, M. G., Naufel, S. N., Ethier, C., Solla, S. A. & Miller, L. E. 2018. Cortical population activity within a preserved neural manifold underlies multiple motor behaviors. *Nature Communications*, 9, 4233.
- Gao, P. & Ganguli, S. 2015. On simplicity and complexity in the brave new world of large-scale neuroscience. *Curr Opin Neurobiol*, 32, 148-55.
- Gao, R. & Penzes, P. 2016. Common Mechanisms of Excitatory and Inhibitory Imbalance in Schizophrenia and Autism Spectrum Disorders. *Curr Mol Med*, 15(2): 146-167.
- Ghosh, S., Harvey, P., Simon, J. C. & Jasanoff, A. 2018. Probing the brain with molecular fMRI. *Curr Opin Neurobiol*, 50, 201-210.
- Gibson, J. R., Bartley, A. F., Hays, S. A. & Huber, K. M. 2008. Imbalance of neocortical excitation and inhibition and altered UP states reflect network hyperexcitability in the mouse model of fragile X syndrome. *J Neurophysiol*, 100, 2615-26.
- Giepmans, B. N., Adams, S. R., Ellisman, M. H. & Tsien, R. Y. 2006. The fluorescent toolbox for assessing protein location and function. *Science*, 312, 217-24.

- Giorgi, A., Migliarini, S., Galbusera, A., Maddaloni, G., Mereu, M., Margiani, G., Gritti, M., Landi, S., Trovato, F., Bertozzi, S. M., Armirotti, A., Ratto, G. M., De Luca, M. A., Tonini, R., Gozzi, A. & Pasqualetti, M. 2017. Brain-wide Mapping of Endogenous Serotonergic Transmission via Chemogenetic fMRI. *Cell Rep*, 21, 910-918.
- Gomez, J. L., Bonaventura, J., Lesniak, W., Mathews, W. B., Sysa-Shah, P., Rodriguez, L. A., Ellis, R. J., Richie, C. T., Harvey, B. K., Dannals, R. F., Pomper, M. G., Bonci, A. & Michaelides, M. 2017. Chemogenetics revealed: DREADD occupancy and activation via converted clozapine. *Science*, 357, 503-507.
- Gomez-Ramirez, J. & Wu, J. 2014. Network-based biomarkers in Alzheimer's disease: review and future directions. *Front Aging Neurosci*, 6, 12.
- Gong, S., Zheng, C., Doughty, M. L., Losos, K., Didkovsky, N., Schambra, U. B., Nowak, N. J., Joyner, A., Leblanc, G., Hatten, M. E. & Heintz, N. 2003. A gene expression atlas of the central nervous system based on bacterial artificial chromosomes. *Nature*, 425, 917-25.
- Gonzalez, W. G., Zhang, H., Harutyunyan, A. & Lois, C. 2019. Persistence of neuronal representations through time and damage in the hippocampus. *Science*, 365, 821-825.
- Gore, J. C. 2003. Principles and practice of functional MRI of the human brain. *Journal of Clinical Investigation*, 112, 4-9.
- Gottschalk, S., Fehm, T. F., Deán-Ben, X. L., Tsytsarev, V. & Razansky, D. 2017. Correlation between volumetric oxygenation responses and electrophysiology identifies deep thalamocortical activity during epileptic seizures. *Neurophotonics*, 4, 011007.
- Goutaudier, R., Coizet, V., Carcenac, C. & Carnicella, S. 2019. DREADDs: The Power of the Lock, the Weakness of the Key. Favoring the Pursuit of Specific Conditions Rather than Specific Ligands. *eneuro*, 6, ENEURO.0171-19.2019.
- Gozzi, A. & Schwarz, A. J. 2016. Large-scale functional connectivity networks in the rodent brain. *NeuroImage*, 127, 496-509.
- Grandjean, J., Canella, C., Anckaerts, C., Ayranci, G., Bougacha, S., Bienert, T., Buehlmann, D., Coletta, L., Gallino, D., Gass, N., Garin, C. M., Nadkarni, N. A., Hubner, N. S., Karatas, M., Komaki, Y., Kreitz, S., Mandino, F., Mechling, A. E., Sato, C., Sauer, K., Shah, D., Strobel, S., Takata, N., Wank, I., Wu, T., Yahata, N., Yeow, L. Y., Yee, Y., Aoki, I., Chakravarty, M. M., Chang, W. T., Dhenain, M., Von Elverfeldt, D., Harsan, L. A., Hess, A., Jiang, T., Keliris, G. A., Lerch, J. P., Meyer-Lindenberg, A., Okano, H., Rudin, M., Sartorius, A., Van Der Linden, A., Verhoye, M., Weber-Fahr, W., Wenderoth, N., Zerbi, V. & Gozzi, A. 2020. Common functional networks in the mouse brain revealed by multi-centre resting-state fMRI analysis. *Neuroimage*, 205, 116278.
- Grandjean, J., Corcoba, A., Kahn, M. C., Upton, A. L., Deneris, E. S., Seifritz, E., Helmchen, F., Mann, E. O., Rudin, M. & Saab, B. J. 2019. A brain-wide functional map of the serotonergic responses to acute stress and fluoxetine. *Nat Commun*, 10, 350.
- Grandjean, J., Derungs, R., Kulic, L., Welt, T., Henkelman, M., Nitsch, R. M. & Rudin, M. 2016. Complex interplay between brain function and structure during cerebral amyloidosis in APP transgenic mouse strains revealed by multi-parametric MRI comparison. *NeuroImage*, 134, 1-11.
- Grandjean, J., Preti, M. G., Bolton, T. a. W., Buerge, M., Seifritz, E., Pryce, C. R., Van De Ville, D. & Rudin, M. 2017a. Dynamic reorganization of intrinsic functional networks in the mouse brain. *Neuroimage*, 152, 497-508.

- Grandjean, J., Schroeter, A., Batata, I. & Rudin, M. 2014a. Optimization of anesthesia protocol for resting-state fMRI in mice based on differential effects of anesthetics on functional connectivity patterns. *Neuroimage*, 102 Pt 2, 838-47.
- Grandjean, J., Schroeter, A., He, P., Tanadini, M., Keist, R., Krstic, D., Konietzko, U., Klohs, J., Nitsch, R. M. & Rudin, M. 2014b. Early Alterations in Functional Connectivity and White Matter Structure in a Transgenic Mouse Model of Cerebral Amyloidosis. *The Journal of Neuroscience*, 34, 13780.
- Grandjean, J., Zerbi, V., Balsters, J. H., Wenderoth, N. & Rudin, M. 2017b. Structural Basis of Large-Scale Functional Connectivity in the Mouse. *J Neurosci*, 37, 8092-8101.
- Grayson, D. S., Bliss-Moreau, E., Machado, C. J., Bennett, J., Shen, K., Grant, K. A., Fair, D. A. & Amaral, D. G. 2016. The Rhesus Monkey Connectome Predicts Disrupted Functional Networks Resulting from Pharmacogenetic Inactivation of the Amygdala. *Neuron*, 91, 453-66.
- Greicius, M. D., Krasnow, B., Reiss, A. L. & Menon, V. 2003. Functional connectivity in the resting brain: A network analysis of the default mode hypothesis. *Proceedings of the National Academy of Sciences*, 100, 253.
- Griffanti, L., Salimi-Khorshidi, G., Beckmann, C. F., Auerbach, E. J., Douaud, G., Sexton, C. E., Zsoldos, E., Ebmeier, K. P., Filippini, N., Mackay, C. E., Moeller, S., Xu, J., Yacoub, E., Baselli, G., Ugurbil, K., Miller, K. L. & Smith, S. M. 2014. ICA-based artefact removal and accelerated fMRI acquisition for improved resting state network imaging. *Neuroimage*, 95, 232-47.
- Grinvald, A., Lieke, E., Frostig, R. D., Gilbert, C. D. & Wiesel, T. N. 1986. Functional architecture of cortex revealed by optical imaging of intrinsic signals. *Nature*, 324, 361-4.
- Guo, Q., Wang, D., He, X., Feng, Q., Lin, R., Xu, F., Fu, L. & Luo, M. 2015. Whole-brain mapping of inputs to projection neurons and cholinergic interneurons in the dorsal striatum. *PLoS One*, 10, e0123381.
- Haberl M. G., Zerbi V., Veltien A., Ginger M., Heerschap A. & A., F. 2015. Structural-functional connectivity deficits of neocortical circuits in the Fmr1-/- mouse model of autism. *Science Advances*, 1500775.
- Hahamy, A., Behrmann, M. & Malach, R. 2015. The idiosyncratic brain: distortion of spontaneous connectivity patterns in autism spectrum disorder. *Nat Neurosci*, 18, 302-9.
- Haider, B., Duque, A., Hasenstaub, A. R. & McCormick, D. A. 2006. Neocortical Network Activity & In Vivo Is Generated through a Dynamic Balance of Excitation and Inhibition. *The Journal of Neuroscience*, 26, 4535.
- Hamel, E. J., Grewe, B. F., Parker, J. G. & Schnitzer, M. J. 2015. Cellular level brain imaging in behaving mammals: an engineering approach. *Neuron*, 86, 140-59.
- Hariri, A., Bely, N., Chen, C. & Nasirivanaki, M. Towards ultrahigh resting-state functional connectivity in the mouse brain using photoacoustic microscopy. *Proc.SPIE*, 2016.
- He, B. J., Snyder, A. Z., Zempel, J. M., Smyth, M. D. & Raichle, M. E. 2008. Electrophysiological correlates of the brain's intrinsic large-scale functional architecture. *Proc Natl Acad Sci U S A*, 105, 16039-44.
- He, H. Y., Shen, W., Zheng, L., Guo, X. & Cline, H. T. 2018. Excitatory synaptic dysfunction cell-autonomously decreases inhibitory inputs and disrupts structural and functional plasticity. *Nat Commun*, 9, 2893.

- Heine, L., Soddu, A., Gomez, F., Vanhaudenhuyse, A., Tshibanda, L., Thonnard, M., Charland-Verville, V., Kirsch, M., Laureys, S. & Demertzi, A. 2012. Resting state networks and consciousness: alterations of multiple resting state network connectivity in physiological, pharmacological, and pathological consciousness States. *Front Psychol*, 3, 295.
- Helmchen, F., Denk, W. & Kerr, J. N. 2013. Miniaturization of two-photon microscopy for imaging in freely moving animals. *Cold Spring Harb Protoc*, 2013, 904-13.
- Helmchen, F., Fee, M. S., Tank, D. W. & Denk, W. 2001. A miniature head-mounted two-photon microscope. high-resolution brain imaging in freely moving animals. *Neuron*, 31, 903-12.
- Henckens, M. J., Van Der Marel, K., Van Der Toorn, A., Pillai, A. G., Fernández, G., Dijkhuizen, R. M. & Joëls, M. 2015. Stress-induced alterations in large-scale functional networks of the rodent brain. *Neuroimage*, 105, 312-22.
- Hillman, E. M. 2007. Optical brain imaging in vivo: techniques and applications from animal to man. *J Biomed Opt*, 12, 051402.
- Hillman, E. M. C., Voleti, V., Li, W. & Yu, H. 2019. Light-Sheet Microscopy in Neuroscience. *Annu Rev Neurosci*, 42, 295-313.
- Hintiryan, H., Foster, N. N., Bowman, I., Bay, M., Song, M. Y., Gou, L., Yamashita, S., Bienkowski, M. S., Zingg, B., Zhu, M., Yang, X. W., Shih, J. C., Toga, A. W. & Dong, H. W. 2016. The mouse cortico-striatal projectome. *Nat Neurosci*, 19(8), 1100-14.
- Hohenfeld, C., Werner, C. J. & Reetz, K. 2018. Resting-state connectivity in neurodegenerative disorders: Is there potential for an imaging biomarker? *Neuroimage Clin*, 18, 849-870.
- Horien, C., Noble, S., Greene, A. S., Lee, K., Barron, D. S., Gao, S., O'connor, D., Salehi, M., Dadashkarimi, J., Shen, X., Lake, E. M. R., Constable, R. T. & Scheinost, D. 2021. A hitchhiker's guide to working with large, open-source neuroimaging datasets. *Nat Hum Behav*, 5, 185-193.
- Houweling, A. R. & Brecht, M. 2008. Behavioural report of single neuron stimulation in somatosensory cortex. *Nature*, 451, 65-8.
- Hsieh, V. & Jasanoff, A. 2012. Bioengineered probes for molecular magnetic resonance imaging in the nervous system. *ACS chemical neuroscience*, 3, 593-602.
- Hu, H., Gan, J. & Jonas, P. 2014. Interneurons. Fast-spiking, parvalbumin(+) GABAergic interneurons: from cellular design to microcircuit function. *Science*, 345, 1255263.
- Hu, S., Maslov, K., Tsytsarev, V. & Wang, L. V. 2009. Functional transcranial brain imaging by optical-resolution photoacoustic microscopy. *J Biomed Opt*, 14, 040503.
- Hull, J. V., Jacokes, Z. J., Torgerson, C. M., Irimia, A. & Van Horn, J. D. 2016. Resting-State Functional Connectivity in Autism Spectrum Disorders: A Review. *Front Psychiatry*, 7, 205.
- Hunnicutt, B. J., Jongbloets, B. C., Birdsong, W. T., Gertz, K. J., Zhong, H. & Mao, T. 2016. A comprehensive excitatory input map of the striatum reveals novel functional organization. *Elife*, 5.
- Hutchison, R. M., Mirsattari, S. M., Jones, C. K., Gati, J. S. & Leung, L. S. 2010. Functional networks in the anesthetized rat brain revealed by independent component analysis of resting-state fMRI. *J Neurophysiol*, 103, 3398-406.
- Iwabuchi, S. J., Krishnadas, R., Li, C., Auer, D. P., Radua, J. & Palaniyappan, L. 2015. Localized connectivity in depression: a meta-analysis of resting state functional imaging studies. *Neurosci Biobehav Rev*, 51, 77-86.

- Jack, A. 2018. Neuroimaging in neurodevelopmental disorders: focus on resting-state fMRI analysis of intrinsic functional brain connectivity. *Curr Opin Neurol*, 31, 140-148.
- Jaime, S., Gu, H., Sadacca, B. F., Stein, E. A., Cavazos, J. E., Yang, Y. & Lu, H. 2019. Delta Rhythm Orchestrates the Neural Activity Underlying the Resting State BOLD Signal via Phase-amplitude Coupling. *Cereb Cortex*, 29, 119-133.
- Jalilianhasanpour, R., Beheshtian, E., Sherbaf, G., Sahraian, S. & Sair, H. I. 2019. Functional Connectivity in Neurodegenerative Disorders: Alzheimer's Disease and Frontotemporal Dementia. *Top Magn Reson Imaging*, 28, 317-324.
- Jasanoff, A. 2007. Bloodless fMRI. *Trends Neurosci*, 30, 603-10.
- Jonckers, E., Delgado Y Palacios, R., Shah, D., Guglielmetti, C., Verhoye, M. & Van Der Linden, A. 2014. Different anesthesia regimes modulate the functional connectivity outcome in mice. *Magnetic Resonance in Medicine*, 72, 1103-1112.
- Jonckers, E., Van Audekerke, J., De Visscher, G., Van Der Linden, A. & Verhoye, M. 2011. Functional connectivity fMRI of the rodent brain: comparison of functional connectivity networks in rat and mouse. *PLoS One*, 6, e18876.
- Juepter, M. & Weiller, C. 1995. Review: Does Measurement of Regional Cerebral Blood Flow Reflect Synaptic Activity? - Implications for PET and fMRI *Neuroimage*, 2, 148-156.
- Jung, W. B., Im, G. H., Jiang, H. & Kim, S. G. 2021. Early fMRI responses to somatosensory and optogenetic stimulation reflect neural information flow. *Proc Natl Acad Sci U S A*, 118.
- Just, N. 2021. Proton functional magnetic resonance spectroscopy in rodents. *NMR Biomed*, 34, e4254.
- Kamishina, H., Yurcisin, G. H., Corwin, J. V. & Reep, R. L. 2008. Striatal projections from the rat lateral posterior thalamic nucleus. *Brain Research*, 1204, 24-39.
- Kang, J., Zhang, H. K., Kadam, S. D., Fedorko, J., Valentine, H., Malla, A. P., Yan, P., Harraz, M. M., Kang, J. U., Rahmim, A., Gjedde, A., Loew, L. M., Wong, D. F. & Boctor, E. M. 2019. Transcranial Recording of Electrophysiological Neural Activity in the Rodent Brain in vivo Using Functional Photoacoustic Imaging of Near-Infrared Voltage-Sensitive Dye. *Front Neurosci*, 13, 579.
- Karim, H. T., Andreescu, C., Tudorascu, D., Smagula, S. F., Butters, M. A., Karp, J. F., Reynolds, C. & Aizenstein, H. J. 2017. Intrinsic functional connectivity in late-life depression: trajectories over the course of pharmacotherapy in remitters and non-remitters. *Mol Psychiatry*, 22, 450-457.
- Katona, G., Szalay, G., Maák, P., Kaszás, A., Veress, M., Hillier, D., Chiovini, B., Vizi, E. S., Roska, B. & Rózsa, B. 2012. Fast two-photon in vivo imaging with three-dimensional random-access scanning in large tissue volumes. *Nat Methods*, 9, 201-8.
- Kazdoba, T. M., Leach, P. T., Silverman, J. L. & Crawley, J. N. 2014. Modeling fragile X syndrome in the Fmr1 knockout mouse. *Intractable Rare Dis Res*, 3, 118-33.
- Kazeminejad, A. & Sotero, R. C. 2019. Topological Properties of Resting-State fMRI Functional Networks Improve Machine Learning-Based Autism Classification. *Frontiers in Neuroscience*, 12.
- Keilholz, S. D. 2014. The neural basis of time-varying resting-state functional connectivity. *Brain Connect*, 4, 769-79.
- Keilholz, S. D., Silva, A. C., Raman, M., Merkle, H. & Koretsky, A. P. 2006. BOLD and CBV-weighted functional magnetic resonance imaging of the rat somatosensory system. *Magn Reson Med*, 55, 316-24.

- Keller, D., Ero, C. & Markram, H. 2018. Cell Densities in the Mouse Brain: A Systematic Review. *Front Neuroanat*, 12, 83.
- Kernbach, J. M., Yeo, B. T. T., Smallwood, J., Margulies, D. S., Thiebaut De Schotten, M., Walter, H., Sabuncu, M. R., Holmes, A. J., Gramfort, A., Varoquaux, G., Thirion, B. & Bzdok, D. 2018. Subspecialization within default mode nodes characterized in 10,000 UK Biobank participants. *Proceedings of the National Academy of Sciences*, 115, 12295.
- Khosla, M., Jamison, K., Ngo, G. H., Kuceyeski, A. & Sabuncu, M. R. 2019. Machine learning in resting-state fMRI analysis. *Magn Reson Imaging*, 64, 101-121.
- Kim, C. K., Ye, L., Jennings, J. H., Pichamoorthy, N., Tang, D. D., Yoo, A. W., Ramakrishnan, C. & Deisseroth, K. 2017a. Molecular and Circuit-Dynamical Identification of Top-Down Neural Mechanisms for Restraint of Reward Seeking. *Cell*, 170, 1013-1027 e14.
- Kim, S.-G., Harel, N., Jin, T., Kim, T., Lee, P. & Zhao, F. 2013. Cerebral blood volume MRI with intravascular superparamagnetic iron oxide nanoparticles. *NMR in biomedicine*, 26, 949-962.
- Kim, S.-G. & Ogawa, S. 2012. Biophysical and Physiological Origins of Blood Oxygenation Level-Dependent fMRI Signals. *Journal of Cerebral Blood Flow & Metabolism*, 32, 1188-1206.
- Kim, T. H., Zhang, Y., Lecoq, J., Jung, J. C., Li, J., Zeng, H., Niell, C. M. & Schnitzer, M. J. 2016. Long-Term Optical Access to an Estimated One Million Neurons in the Live Mouse Cortex. *Cell Rep*, 17, 3385-3394.
- Kim, Y., Yang, G. R., Pradhan, K., Venkataraju, K. U., Bota, M., Garcia Del Molino, L. C., Fitzgerald, G., Ram, K., He, M., Levine, J. M., Mitra, P., Huang, Z. J., Wang, X. J. & Osten, P. 2017b. Brain-wide Maps Reveal Stereotyped Cell-Type-Based Cortical Architecture and Subcortical Sexual Dimorphism. *Cell*, 171, 456-469 e22.
- Kleinfeld, D., Blinder, P., Drew, P., Driscoll, J., Muller, A., Tsai, P. & Shih, A. 2011. A Guide to Delineate the Logic of Neurovascular Signaling in the Brain. *Frontiers in Neuroenergetics*, 3.
- Klioutchnikov, A., Wallace, D. J., Frosz, M. H., Zeltner, R., Sawinski, J., Pawlak, V., Voit, K. M., Russell, P. S. J. & Kerr, J. N. D. 2020. Three-photon head-mounted microscope for imaging deep cortical layers in freely moving rats. *Nat Methods*, 17, 509-513.
- Kraguljac, N. V., White, D. M., Hadley, N., Hadley, J. A., Ver Hoef, L., Davis, E. & Lahti, A. C. 2016. Aberrant Hippocampal Connectivity in Unmedicated Patients With Schizophrenia and Effects of Antipsychotic Medication: A Longitudinal Resting State Functional MRI Study. *Schizophr Bull*, 42, 1046-55.
- Kravitz, A. V., Freeze, B. S., Parker, P. R., Kay, K., Thwin, M. T., Deisseroth, K. & Kreitzer, A. C. 2010. Regulation of parkinsonian motor behaviours by optogenetic control of basal ganglia circuitry. *Nature*, 466, 622-6.
- Kringelbach, M. L. & Deco, G. 2020. Brain States and Transitions: Insights from Computational Neuroscience. *Cell Rep*, 32, 108128.
- Ku, G. & Wang, L. V. 2005. Deeply penetrating photoacoustic tomography in biological tissues enhanced with an optical contrast agent. *Opt Lett*, 30, 507-9.
- Kuhn, B. & Roome, C. J. 2019. Primer to Voltage Imaging With ANNINE Dyes and Two-Photon Microscopy. *Front Cell Neurosci*, 13, 321.
- Kura, S., Xie, H., Fu, B., Ayata, C., Boas, D. A. & Sakadžić, S. 2018. Intrinsic optical signal imaging of the blood volume changes is sufficient for mapping the resting state functional connectivity in the rodent cortex. *J Neural Eng*, 15, 035003.

- Kwong, K. K., Belliveau, J. W., Chesler, D. A., Goldberg, I. E., Weisskopf, R. M., Poncelet, B. P., Kennedy, D. N., Hoppel, B. E., S.Cohen, M., Turner, R., Cheng, H.-M., J.Brady, T. & Rosen, B. R. 1992. Dynamic magnetic resonance imaging of human brain activity during primary sensory stimulation. *Proceedings of the National Academy of Sciences of the United States of America*, 89, 5675-5679.
- Lakatos, P., Gross, J. & Thut, G. 2019. A New Unifying Account of the Roles of Neuronal Entrainment. *Current Biology*, 29, R890-R905.
- Lake, E. M. R., Ge, X., Shen, X., Herman, P., Hyder, F., Cardin, J. A., Higley, M. J., Scheinost, D., Papademetris, X., Crair, M. C. & Constable, R. T. 2020. Simultaneous cortex-wide fluorescence Ca(2+) imaging and whole-brain fMRI. *Nat Methods*, 17, 1262-1271.
- Larovere, K. L. 2015. Transcranial Doppler ultrasound in children with stroke and cerebrovascular disorders. *Curr Opin Pediatr*, 27, 712-8.
- Laufer, J., Johnson, P., Zhang, E., Treeby, B., Cox, B., Pedley, B. & Beard, P. 2012. In vivo preclinical photoacoustic imaging of tumor vasculature development and therapy. *J Biomed Opt*, 17, 056016.
- Le Bihan, D., Urayama, S.-I., Aso, T., Hanakawa, T. & Fukuyama, H. 2006. Direct and fast detection of neuronal activation in the human brain with diffusion MRI. *Proceedings of the National Academy of Sciences*, 103, 8263.
- Lee, B., Shin, D., Gross, S. P. & Cho, K. H. 2018. Combined Positive and Negative Feedback Allows Modulation of Neuronal Oscillation Frequency during Sensory Processing. *Cell Rep*, 25, 1548-1560 e3.
- Lee, E., Lee, J. & Kim, E. 2017. Excitation/Inhibition Imbalance in Animal Models of Autism Spectrum Disorders. *Biol Psychiatry*, 81, 838-847.
- Lee, H.-L., Li, Z., Coulson, E. J. & Chuang, K.-H. 2019. Ultrafast fMRI of the rodent brain using simultaneous multi-slice EPI. *NeuroImage*, 195, 48-58.
- Lee, H. J., Weitz, A. J., Bernal-Casas, D., Duffy, B. A., Choy, M., Kravitz, A. V., Kreitzer, A. C. & Lee, J. H. 2016. Activation of Direct and Indirect Pathway Medium Spiny Neurons Drives Distinct Brain-wide Responses. *Neuron*, 91, 412-24.
- Lee, J., Wang, W. & Sabatini, B. L. 2020. Anatomically segregated basal ganglia pathways allow parallel behavioral modulation. *Nat Neurosci*, 23, 1388-1398.
- Lee, T., Cai, L. X., Lelyveld, V. S., Hai, A. & Jasanoff, A. 2014. Molecular-Level Functional Magnetic Resonance Imaging of Dopaminergic Signaling. *Science*, 344, 533.
- Leithner, C., Gertz, K., Schrock, H., Priller, J., Prass, K., Steinbrink, J., Villringer, A., Endres, M., Lindauer, U., Dirnagl, U. & Royl, G. 2008. A flow sensitive alternating inversion recovery (FAIR)-MRI protocol to measure hemispheric cerebral blood flow in a mouse stroke model. *Exp Neurol*, 210, 118-27.
- Levi, J., Kothapalli, S. R., Bohndiek, S., Yoon, J. K., Dragulescu-Andrasi, A., Nielsen, C., Tisma, A., Bodapati, S., Gowrishankar, G., Yan, X., Chan, C., Starcevic, D. & Gambhir, S. S. 2013. Molecular photoacoustic imaging of follicular thyroid carcinoma. *Clin Cancer Res*, 19, 1494-502.
- Li, L., Xia, J., Li, G., Garcia-Urbe, A., Sheng, Q., Anastasio, M. A. & Wang, L. V. 2016. Label-free photoacoustic tomography of whole mouse brain structures. *NeuroPhotonics*, 3, 035001.
- Li, N. & Jasanoff, A. 2020. Local and global consequences of reward-evoked striatal dopamine release. *Nature*, 580, 239-244.
- Liang, Z., Liu, X. & Zhang, N. 2015. Dynamic resting state functional connectivity in awake and anesthetized rodents. *NeuroImage*, 104, 89-99.

- Liao, L. D., Lin, C. T., Shih, Y. Y., Duong, T. Q., Lai, H. Y., Wang, P. H., Wu, R., Tsang, S., Chang, J. Y., Li, M. L. & Chen, Y. Y. 2012. Transcranial imaging of functional cerebral hemodynamic changes in single blood vessels using in vivo photoacoustic microscopy. *J Cereb Blood Flow Metab*, 32, 938-51.
- Linke, R., Braune, G. & Schwegler, H. 2000. Differential projection of the posterior paralamina thalamic nuclei to the amygdaloid complex in the rat. *Experimental Brain Research*, 134, 520-532.
- Liska, A., Bertero, A., Gomolka, R., Sabbioni, M., Galbusera, A., Barsotti, N., Panzeri, S., Scattoni, M. L., Pasqualetti, M. & Gozzi, A. 2018. Homozygous Loss of Autism-Risk Gene CNTNAP2 Results in Reduced Local and Long-Range Prefrontal Functional Connectivity. *Cereb Cortex*, 28, 1141-1153.
- Liska, A., Galbusera, A., Schwarz, A. J. & Gozzi, A. 2015. Functional connectivity hubs of the mouse brain. *Neuroimage*, 115, 281-91.
- Liska, A. & Gozzi, A. 2016. Can Mouse Imaging Studies Bring Order to Autism Connectivity Chaos? *Frontiers in Neuroscience*, 10.
- Liu, L., Xu, H., Wang, J., Li, J., Tian, Y., Zheng, J., He, M., Xu, T.-L., Wu, Z.-Y., Li, X.-M., Duan, S.-M. & Xu, H. 2020a. Cell type–differential modulation of prefrontal cortical GABAergic interneurons on low gamma rhythm and social interaction. *Science Advances*, 6, eaay4073.
- Liu, Y., Liu, H., Yan, H., Liu, Y., Zhang, J., Shan, W., Lai, P., Li, H., Ren, L., Li, Z. & Nie, L. 2019. Aggregation-Induced Absorption Enhancement for Deep Near-Infrared II Photoacoustic Imaging of Brain Gliomas In Vivo. *Adv Sci (Weinh)*, 6, 1801615.
- Liu, Y., Perez, P. D., Ma, Z., Ma, Z., Dopfel, D., Cramer, S., Tu, W. & Zhang, N. 2020b. An open database of resting-state fMRI in awake rats. *NeuroImage*, 220, 117094.
- Lu, H., Zou, Q., Gu, H., Raichle, M. E., Stein, E. A. & Yang, Y. 2012. Rat brains also have a default mode network. *Proceedings of the National Academy of Sciences*, 109, 3979-3984.
- Lu, H., Zuo, Y., Gu, H., Waltz, J. A., Zhan, W., Scholl, C. A., Rea, W., Yang, Y. & Stein, E. A. 2007. Synchronized delta oscillations correlate with the resting-state functional MRI signal. *Proc Natl Acad Sci U S A*, 104, 18265-9.
- Lubba, C. H., Sethi, S. S., Knaute, P., Schultz, S. R., Fulcher, B. D. & Jones, N. S. 2019. catch22: CAnonical Time-series CHaracteristics. *Data Mining and Knowledge Discovery*, 33, 1821-1852.
- Lukasik, V. M. & Gillies, R. J. 2003. Animal anaesthesia for in vivo magnetic resonance. *NMR Biomed*, 16, 459-67.
- Ma, Y., Shaik, M. A., Kim, S. H., Kozberg, M. G., Thibodeaux, D. N., Zhao, H. T., Yu, H. & Hillman, E. M. 2016. Wide-field optical mapping of neural activity and brain haemodynamics: considerations and novel approaches. *Philos Trans R Soc Lond B Biol Sci*, 371.
- Macé, E., Montaldo, G., Cohen, I., Baulac, M., Fink, M. & Tanter, M. 2011. Functional ultrasound imaging of the brain. *Nat Methods*, 8, 662-4.
- Mace, E., Montaldo, G., Osmanski, B. F., Cohen, I., Fink, M. & Tanter, M. 2013. Functional ultrasound imaging of the brain: theory and basic principles. *IEEE Trans Ultrason Ferroelectr Freq Control*, 60, 492-506.
- Macé, É., Montaldo, G., Trenholm, S., Cowan, C., Brignall, A., Urban, A. & Roska, B. 2018. Whole-Brain Functional Ultrasound Imaging Reveals Brain Modules for Visuomotor Integration. *Neuron*, 100, 1241-1251.e7.

- Mackinnon, M. J., Song, S., H., L-M., Lee, S-H., Johnson G. A., Shih, I. Y-Y., 2020. iZTE-fMRI. *Proceedings of the International Society for Magnetic Resonance in Medicine (ISMRM)*. Wiley.
- Macvicar, B. A. & Hochman, D. 1991. Imaging of synaptically evoked intrinsic optical signals in hippocampal slices. *J Neurosci*, 11, 1458-69.
- Magnus, C. J., Lee, P. H., Bonaventura, J., Zemla, R., Gomez, J. L., Ramirez, M. H., Hu, X., Galvan, A., Basu, J., Michaelides, M. & Sternson, S. M. 2019. Ultrapotent chemogenetics for research and potential clinical applications. *Science*, 364.
- Maioli, V., Boniface, A., Mahou, P., Ortas, J. F., Abdeladim, L., Beaurepaire, E. & Supatto, W. 2020. Fast in vivo multiphoton light-sheet microscopy with optimal pulse frequency. *Biomedical Optics Express*.
- Maki-Marttunen, T., Kaufmann, T., Elvsashagen, T., Devor, A., Djurovic, S., Westlye, L. T., Linne, M. L., Rietschel, M., Schubert, D., Borgwardt, S., Efrim-Budisteanu, M., Bettella, F., Halnes, G., Hagen, E., Naess, S., Ness, T. V., Moberget, T., Metzner, C., Edwards, A. G., Fyhn, M., Dale, A. M., Einevoll, G. T. & Andreassen, O. A. 2019. Biophysical Psychiatry-How Computational Neuroscience Can Help to Understand the Complex Mechanisms of Mental Disorders. *Front Psychiatry*, 10, 534.
- Malvaut, S., Constantinescu, V. S., Dehez, H., Doric, S. & Saghatelian, A. 2020. Deciphering Brain Function by Miniaturized Fluorescence Microscopy in Freely Behaving Animals. *Front Neurosci*, 14, 819.
- Mandelbaum, G., Taranda, J., Haynes, T. M., Hochbaum, D. R., Huang, K. W., Hyun, M., Umadevi Venkataraju, K., Straub, C., Wang, W., Robertson, K., Osten, P. & Sabatini, B. L. 2019. Distinct Cortical-Thalamic-Striatal Circuits through the Parafascicular Nucleus. *Neuron*, 102, 636-652 e7.
- Mandino, F., Cerri, D. H., Garin, C. M., Straathof, M., Van Tilborg, G. a. F., Chakravarty, M. M., Dhenain, M., Dijkhuizen, R. M., Gozzi, A., Hess, A., Keilholz, S. D., Lerch, J. P., Shih, Y.-Y. I. & Grandjean, J. 2020. Animal Functional Magnetic Resonance Imaging: Trends and Path Toward Standardization. *Frontiers in Neuroinformatics*, 13.
- Manvich, D. F., Webster, K. A., Foster, S. L., Farrell, M. S., Ritchie, J. C., Porter, J. H. & Weinschenker, D. 2018. The DREADD agonist clozapine N-oxide (CNO) is reverse-metabolized to clozapine and produces clozapine-like interoceptive stimulus effects in rats and mice. *Sci Rep*, 8, 3840.
- Marissal, T., Salazar, R. F., Bertollini, C., Mutel, S., De Roo, M., Rodriguez, I., Muller, D. & Carleton, A. 2018. Restoring wild-type-like CA1 network dynamics and behavior during adulthood in a mouse model of schizophrenia. *Nat Neurosci*, 21, 1412-1420.
- Markicevic, M., Fulcher, B. D., Lewis, C., Helmchen, F., Rudin, M., Zerbi, V. & Wenderoth, N. 2020. Cortical Excitation:Inhibition Imbalance Causes Abnormal Brain Network Dynamics as Observed in Neurodevelopmental Disorders. *Cerebral Cortex*, 30, 4922-4937.
- Markl, M. & Leupold, J. 2012. Gradient echo imaging. *Journal of Magnetic Resonance Imaging*, 35, 1274-1289.
- Maslov, K., Zhang, H. F., Hu, S. & Wang, L. V. 2008. Optical-resolution photoacoustic microscopy for in vivo imaging of single capillaries. *Opt Lett*, 33, 929-31.
- Mateo, C., Knutsen, P. M., Tsai, P. S., Shih, A. Y. & Kleinfeld, D. 2017. Entrainment of Arteriole Vasomotor Fluctuations by Neural Activity Is a Basis of Blood-Oxygenation-Level-Dependent "Resting-State" Connectivity. *Neuron*, 96, 936-948 e3.
- Michaelides, M. & Hurd, Y. L. 2016. Chemogenetics: DREADDs. 2847-2856.

- Miller, K. L., Alfaro-Almagro, F., Bangerter, N. K., Thomas, D. L., Yacoub, E., Xu, J., Bartsch, A. J., Jbabdi, S., Sotiropoulos, S. N., Andersson, J. L. R., Griffanti, L., Douaud, G., Okell, T. W., Weale, P., Dragonu, I., Garratt, S., Hudson, S., Collins, R., Jenkinson, M., Matthews, P. M. & Smith, S. M. 2016. Multimodal population brain imaging in the UK Biobank prospective epidemiological study. *Nature Neuroscience*, 19, 1523-1536.
- Mills, B. D., Grayson, D. S., Shunmugavel, A., Miranda-Dominguez, O., Feczko, E., Earl, E., Neve, K. A. & Fair, D. A. 2018. Correlated Gene Expression and Anatomical Communication Support Synchronized Brain Activity in the Mouse Functional Connectome. *J Neurosci*, 38, 5774-5787.
- Minschew, N. J. & Keller, T. A. 2010. The nature of brain dysfunction in autism: functional brain imaging studies. *Curr Opin Neurol*, 23, 124-30.
- Miyawaki, A., Llopis, J., Heim, R., Mccaffery, J. M., Adams, J. A., Ikura, M. & Tsien, R. Y. 1997. Fluorescent indicators for Ca²⁺ based on green fluorescent proteins and calmodulin. *Nature*, 388, 882-7.
- Moore, A. K., Weible, A. P., Balmer, T. S., Trussell, L. O. & Wehr, M. 2018. Rapid Rebalancing of Excitation and Inhibition by Cortical Circuitry. *Neuron*, 97, 1341-1355 e6.
- Murray, J. D., Demirtas, M. & Anticevic, A. 2018. Biophysical Modeling of Large-Scale Brain Dynamics and Applications for Computational Psychiatry. *Biol Psychiatry Cogn Neurosci Neuroimaging*, 3, 777-787.
- Nakamura, Y., Nakamura, Y., Pelosi, A., Djemai, B., Debacker, C., Herve, D., Girault, J. A. & Tsurugizawa, T. 2020. fMRI detects bilateral brain network activation following unilateral chemogenetic activation of direct striatal projection neurons. *Neuroimage*, 220, 117079.
- Namboodiri, V. M., Rodriguez-Romaguera, J. & Stuber, G. D. 2016. The habenula. *Curr Biol*, 26, R873-R877.
- Nasirivanaki, M., Xia, J., Wan, H., Bauer, A. Q., Culver, J. P. & Wang, L. V. 2014. High-resolution photoacoustic tomography of resting-state functional connectivity in the mouse brain. *Proc Natl Acad Sci U S A*, 111, 21-6.
- Nasrallah, F. A., Tay, H. C. & Chuang, K. H. 2014. Detection of functional connectivity in the resting mouse brain. *Neuroimage*, 86, 417-24.
- Nelson, A. B. & Kreitzer, A. C. 2014. Reassessing models of basal ganglia function and dysfunction. *Annu Rev Neurosci*, 37, 117-35.
- Nir, Y., Mukamel, R., Dinstein, I., Privman, E., Harel, M., Fisch, L., Gelbard-Sagiv, H., Kipervasser, S., Andelman, F., Neufeld, M. Y., Kramer, U., Arieli, A., Fried, I. & Malach, R. 2008. Interhemispheric correlations of slow spontaneous neuronal fluctuations revealed in human sensory cortex. *Nature Neuroscience*, 11, 1100-1108.
- Nomura, T., Musial, T. F., Marshall, J. J., Zhu, Y., Remmers, C. L., Xu, J., Nicholson, D. A. & Contractor, A. 2017. Delayed Maturation of Fast-Spiking Interneurons Is Rectified by Activation of the TrkB Receptor in the Mouse Model of Fragile X Syndrome. *J Neurosci*, 37, 11298-11310.
- Ntziachristos, V. 2010. Going deeper than microscopy: the optical imaging frontier in biology. *Nat Methods*, 7, 603-14.
- Nucifora, F. C., Jr., Mihaljevic, M., Lee, B. J. & Sawa, A. 2017. Clozapine as a Model for Antipsychotic Development. *Neurotherapeutics*, 14, 750-761.
- Nunes, D., Gil, R. & Shemesh, N. 2021. A rapid-onset diffusion functional MRI signal reflects neuromorphological coupling dynamics. *Neuroimage*, 231, 117862.

- Nunes, D., Ianus, A. & Shemesh, N. 2019. Layer-specific connectivity revealed by diffusion-weighted functional MRI in the rat thalamocortical pathway. *Neuroimage*, 184, 646-657.
- Ogawa, S., Lee, T.-M., Nayak, A. S. & Glynn, P. 1990a. Oxygenation-sensitive contrast in magnetic resonance image of rodent brain at high magnetic fields. *Magnetic Resonance in Medicine*, 14, 68-78.
- Ogawa, S., Lee, T. M., Kay, A. R. & Tank, D. W. 1990b. Brain magnetic resonance imaging with contrast dependent on blood oxygenation. *Proceedings of the National Academy of Sciences of the United States of America*, 87, 9868-9872.
- Oh, J., Lee, C. & Kaang, B. K. 2019. Imaging and analysis of genetically encoded calcium indicators linking neural circuits and behaviors. *Korean J Physiol Pharmacol*, 23, 237-249.
- Oh, S. W., Harris, J. A., Ng, L., Winslow, B., Cain, N., Mihalas, S., Wang, Q., Lau, C., Kuan, L., Henry, A. M., Mortrud, M. T., Ouellette, B., Nguyen, T. N., Sorensen, S. A., Slaughterbeck, C. R., Wakeman, W., Li, Y., Feng, D., Ho, A., Nicholas, E., Hirokawa, K. E., Bohn, P., Joines, K. M., Peng, H., Hawrylycz, M. J., Phillips, J. W., Hohmann, J. G., Wahnoutka, P., Gerfen, C. R., Koch, C., Bernard, A., Dang, C., Jones, A. R. & Zeng, H. 2014. A mesoscale connectome of the mouse brain. *Nature*, 508, 207-14.
- Osmanski, B.-F., Pezet, S., Ricobaraza, A., Lenkei, Z. & Tanter, M. 2014. Functional ultrasound imaging of intrinsic connectivity in the living rat brain with high spatiotemporal resolution. *Nature Communications*, 5, 5023.
- Ovsepian, S. V., Olefir, I., Westmeyer, G., Razansky, D. & Ntziachristos, V. 2017. Pushing the Boundaries of Neuroimaging with Optoacoustics. *Neuron*, 96, 966-988.
- Paakki, J. J., Rahko, J., Long, X., Moilanen, I., Tervonen, O., Nikkinen, J., Starck, T., Remes, J., Hurtig, T., Haapsamo, H., Jussila, K., Kuusikko-Gauffin, S., Mattila, M. L., Zang, Y. & Kiviniemi, V. 2010. Alterations in regional homogeneity of resting-state brain activity in autism spectrum disorders. *Brain Res*, 1321, 169-79.
- Paasonen, J., Stenroos, P., Salo, R. A., Kiviniemi, V. & Grohn, O. 2018. Functional connectivity under six anesthesia protocols and the awake condition in rat brain. *Neuroimage*, 172, 9-20.
- Pagani, M., Bertero, A., Liska, A., Galbusera, A., Sabbioni, M., Scattoni, M. L., Pasqualetti, M. & Gozzi, A. 2018. Deletion of autism risk gene Shank3 disrupts prefrontal connectivity. *bioArchive*.
- Pan, W. J., Lee, S. Y., Billings, J., Nezafati, M., Majeed, W., Buckley, E. & Keilholz, S. 2018. Detection of neural light-scattering activity in vivo: optical transmittance studies in the rat brain. *Neuroimage*, 179, 207-214.
- Pan, W. J., Thompson, G. J., Magnuson, M. E., Jaeger, D. & Keilholz, S. 2013. Infralow LFP correlates to resting-state fMRI BOLD signals. *Neuroimage*, 74, 288-97.
- Paredes, R. M., Etzler, J. C., Watts, L. T., Zheng, W. & Lechleiter, J. D. 2008. Chemical calcium indicators. *Methods*, 46, 143-51.
- Parker, P. R. L., Lalive, A. L. & Kreitzer, A. C. 2016. Pathway-Specific Remodeling of Thalamostriatal Synapses in Parkinsonian Mice. *Neuron*, 89, 734-740.
- Paul, K., Venkitaramani, D. V. & Cox, C. L. 2013. Dampened dopamine-mediated neuromodulation in prefrontal cortex of fragile X mice. *J Physiol*, 591, 1133-43.
- Pawela, C. P., Biswal, B. B., Cho, Y. R., Kao, D. S., Li, R., Jones, S. R., Schulte, M. L., Matloub, H. S., Hudetz, A. G. & Hyde, J. S. 2008. Resting-state functional connectivity of the rat brain. *Magnetic resonance in medicine*, 59, 1021-1029.

- Peeters, L. M., Hinz, R., Detrez, J. R., Missault, S., De Vos, W. H., Verhoye, M., Van Der Linden, A. & Keliris, G. A. 2020. Chemogenetic silencing of neurons in the mouse anterior cingulate area modulates neuronal activity and functional connectivity. *NeuroImage*, 220, 117088.
- Penagarikano, O., Abrahams, B. S., Herman, E. I., Winden, K. D., Gdalyahu, A., Dong, H., Sonnenblick, L. I., Gruver, R., Almajano, J., Bragin, A., Golshani, P., Trachtenberg, J. T., Peles, E. & Geschwind, D. H. 2011. Absence of CNTNAP2 leads to epilepsy, neuronal migration abnormalities, and core autism-related deficits. *Cell*, 147, 235-46.
- Peñagarikano, O., Lázaro, M. T., Lu, X. H., Gordon, A., Dong, H., Lam, H. A., Peles, E., Maidment, N. T., Murphy, N. P., Yang, X. W., Golshani, P. & Geschwind, D. H. 2015. Exogenous and evoked oxytocin restores social behavior in the Cntnap2 mouse model of autism. *Sci Transl Med*, 7, 271ra8.
- Perry, B. a. L. & Mitchell, A. S. 2019. Considering the Evidence for Anterior and Laterodorsal Thalamic Nuclei as Higher Order Relays to Cortex. *Frontiers in Molecular Neuroscience*, 12, 167.
- Peters, A. J., Fabre, J. M. J., Steinmetz, N. A., Harris, K. D. & Carandini, M. 2021. Striatal activity topographically reflects cortical activity. *Nature*, 591, 420-425.
- Piatkevich, K. D., Bensussen, S., Tseng, H. A., Shroff, S. N., Lopez-Huerta, V. G., Park, D., Jung, E. E., Shemesh, O. A., Straub, C., Gritton, H. J., Romano, M. F., Costa, E., Sabatini, B. L., Fu, Z., Boyden, E. S. & Han, X. 2019. Population imaging of neural activity in awake behaving mice. *Nature*, 574, 413-417.
- Postnov, D. D., Tang, J., Erdener, S. E., Kilic, K. & Boas, D. A. 2020. Dynamic light scattering imaging. *Sci Adv*, 6.
- Raichle, M. E. & Mintun, M. A. 2006. Brain work and brain imaging. *Annu Rev Neurosci*, 29, 449-76.
- Rector, D. M., Carter, K. M., Volegov, P. L. & George, J. S. 2005. Spatio-temporal mapping of rat whisker barrels with fast scattered light signals. *Neuroimage*, 26, 619-27.
- Rector, D. M., Rogers, R. F. & George, J. S. 1999. A focusing image probe for assessing neural activity in vivo. *J Neurosci Methods*, 91, 135-45.
- Reig, R. & Silberberg, G. 2014. Multisensory integration in the mouse striatum. *Neuron*, 83, 1200-12.
- Reimann, H. M. & Niendorf, T. 2020. The (Un)Conscious Mouse as a Model for Human Brain Functions: Key Principles of Anesthesia and Their Impact on Translational Neuroimaging. *Front Syst Neurosci*, 14, 8.
- Rhodes, C. J. 2017. Magnetic resonance spectroscopy. *Sci Prog*, 100, 241-292.
- Richards, L. M., Kazmi, S. S., Olin, K. E., Waldron, J. S., Fox, D. J., Jr. & Dunn, A. K. 2017. Intraoperative multi-exposure speckle imaging of cerebral blood flow. *J Cereb Blood Flow Metab*, 37, 3097-3109.
- Rideau, A. B. N., Pham, H., Van De Looij, Y., Bernal, M., Mairesse, J., Zana-Taieb, E., Colella, M., Jarreau, P. H., Pansiot, J., Dumont, F., Sizonenko, S., Gressens, P., Charriaut-Marlangue, C., Tanter, M., Demene, C., Vaiman, D. & Baud, O. 2016. Transcriptomic regulations in oligodendroglial and microglial cells related to brain damage following fetal growth restriction. *Glia*, 64, 2306-2320.
- Roelofs, T. J. M., Verharen, J. P. H., Van Tilborg, G. a. F., Boekhoudt, L., Van Der Toorn, A., De Jong, J. W., Luijendijk, M. C. M., Otte, W. M., Adan, R. a. H. & Dijkhuizen, R. M. 2017. A novel approach to map induced activation of neuronal networks using

- chemogenetics and functional neuroimaging in rats: A proof-of-concept study on the mesocorticolimbic system. *Neuroimage*, 156, 109-118.
- Rogan, S. C. & Roth, B. L. 2011. Remote control of neuronal signaling. *Pharmacol Rev*, 63, 291-315.
- Rossi, L. F., Wykes, R. C., Kullmann, D. M. & Carandini, M. 2017. Focal cortical seizures start as standing waves and propagate respecting homotopic connectivity. *Nat Commun*, 8, 217.
- Roth, B. L. 2016. DREADDs for Neuroscientists. *Neuron*, 89, 683-94.
- Routh, B. N., Rathour, R. K., Baumgardner, M. E., Kalmbach, B. E., Johnston, D. & Brager, D. H. 2017. Increased transient Na(+) conductance and action potential output in layer 2/3 prefrontal cortex neurons of the *fmr1(-/y)* mouse. *J Physiol*, 595, 4431-4448.
- Roux, L. & Buzsaki, G. 2015. Tasks for inhibitory interneurons in intact brain circuits. *Neuropharmacology*, 88, 10-23.
- Rubenstein, J. L. R. & Merzenich, M. M. 2003. Model of autism: increased ratio of excitation/inhibition in key neural systems. *Genes, Brain and Behavior*, 255-267.
- Runegaard, A. H., Fitzpatrick, C. M., Woldbye, D. P. D., Andreasen, J. T., Sorensen, A. T. & Gether, U. 2019. Modulating Dopamine Signaling and Behavior with Chemogenetics: Concepts, Progress, and Challenges. *Pharmacol Rev*, 71, 123-156.
- Russell, J. T. 2011. Imaging calcium signals in vivo: A powerful tool in physiology and pharmacology. *British Journal of Pharmacology*.
- Safari, M. S., Mirnajafi-Zadeh, J., Hioki, H. & Tsumoto, T. 2017. Parvalbumin-expressing interneurons can act solo while somatostatin-expressing interneurons act in chorus in most cases on cortical pyramidal cells. *Sci Rep*, 7, 12764.
- Schlegel, F., Sych, Y., Schroeter, A., Stobart, J., Weber, B., Helmchen, F. & Rudin, M. 2018. Fiber-optic implant for simultaneous fluorescence-based calcium recordings and BOLD fMRI in mice. *Nat Protoc*, 13, 840-855.
- Schrödel, T., Prevedel, R., Aumayr, K., Zimmer, M. & Vaziri, A. 2013. Brain-wide 3D imaging of neuronal activity in *Caenorhabditis elegans* with sculpted light. *Nature Methods*.
- Schulz, K., Sydekum, E., Krueppel, R., Engelbrecht, C. J., Schlegel, F., Schroter, A., Rudin, M. & Helmchen, F. 2012. Simultaneous BOLD fMRI and fiber-optic calcium recording in rat neocortex. *Nat Methods*, 9, 597-602.
- Selby, L., Zhang, C. & Sun, Q. Q. 2007. Major defects in neocortical GABAergic inhibitory circuits in mice lacking the fragile X mental retardation protein. *Neurosci Lett*, 412, 227-32.
- Selten, M., Van Bokhoven, H. & Nadif Kasri, N. 2018. Inhibitory control of the excitatory/inhibitory balance in psychiatric disorders. *F1000Res*, 7, 23.
- Sethi, S. S., Zerbi, V., Wenderoth, N., Fornito, A. & Fulcher, B. D. 2017. Structural connectome topology relates to regional BOLD signal dynamics in the mouse brain. *Chaos*, 27, 047405.
- Seung, S. 2012. *Connectome: How the brain's wiring makes us who we are*, Houghton Mifflin Harcourt.
- Sforazzini, F., Bertero, A., Doderio, L., David, G., Galbusera, A., Scattoni, M. L., Pasqualetti, M. & Gozzi, A. 2016. Altered functional connectivity networks in acallosal and socially impaired BTBR mice. *Brain Struct Funct*, 221, 941-54.
- Sforazzini, F., Schwarz, A. J., Galbusera, A., Bifone, A. & Gozzi, A. 2014. Distributed BOLD and CBV-weighted resting-state networks in the mouse brain. *Neuroimage*, 87, 403-15.

- Shemetov, A. A., Monakhov, M. V., Zhang, Q., Canton-Josh, J. E., Kumar, M., Chen, M., Matlashov, M. E., Li, X., Yang, W., Nie, L., Shcherbakova, D. M., Kozorovitskiy, Y., Yao, J., Ji, N. & Verkhusa, V. V. 2020. A near-infrared genetically encoded calcium indicator for in vivo imaging. *Nature Biotechnology*, 1-10.
- Shi, Z., Wilkes, D. M., Yang, P. F., Wang, F., Wu, R., Wu, T. L., Chen, L. M. & Gore, J. C. 2019. On the Relationship between MRI and Local Field Potential Measurements of Spatial and Temporal Variations in Functional Connectivity. *Sci Rep*, 9, 8871.
- Shmuel, A. & Leopold, D. A. 2008. Neuronal correlates of spontaneous fluctuations in fMRI signals in monkey visual cortex: Implications for functional connectivity at rest. *Hum Brain Mapp*, 29, 751-61.
- Shofty, B., Bergmann, E., Zur, G., Asleh, J., Bosak, N., Kavushansky, A., Castellanos, F. X., Ben-Sira, L., Packer, R. J., Vezina, G. L., Constantini, S., Acosta, M. T. & Kahn, I. 2019. Autism-associated Nf1 deficiency disrupts corticocortical and corticostriatal functional connectivity in human and mouse. *Neurobiol Dis*, 130, 104479.
- Silverman, J. L., Yang, M., Lord, C. & Crawley, J. N. 2010. Behavioural phenotyping assays for mouse models of autism. *Nat Rev Neurosci*, 11, 490-502.
- Smith, K. S., Bucci, D. J., Luikart, B. W. & Mahler, S. V. 2016. DREADDs: Use and application in behavioral neuroscience. *Behav Neurosci*, 130, 137-55.
- Smith, S. M., Fox, P. T., Miller, K. L., Glahn, D. C., Fox, P. M., Mackay, C. E., Filippini, N., Watkins, K. E., Toro, R., Laird, A. R. & Beckmann, C. F. 2009. Correspondence of the brain's functional architecture during activation and rest. *Proc Natl Acad Sci U S A*, 106, 13040-5.
- Smith, S. M. & Nichols, T. E. 2018. Statistical Challenges in "Big Data" Human Neuroimaging. *Neuron*, 97, 263-268.
- Smith, Y., Raju, D. V., Pare, J. F. & Sidibe, M. 2004. The thalamostriatal system: a highly specific network of the basal ganglia circuitry. *Trends Neurosci*, 27, 520-7.
- Smucny, J., Wylie, K. P. & Tregellas, J. R. 2014. Functional magnetic resonance imaging of intrinsic brain networks for translational drug discovery. *Trends Pharmacol Sci*, 35, 397-403.
- Sofroniew, N. J., Flickinger, D., King, J. & Svoboda, K. 2016. A large field of view two-photon mesoscope with subcellular resolution for in vivo imaging. *Elife*, 5.
- Sohal, V. S. & Rubenstein, J. L. R. 2019. Excitation-inhibition balance as a framework for investigating mechanisms in neuropsychiatric disorders. *Mol Psychiatry*, 24, 1248-1257.
- Sohal, V. S., Zhang, F., Yizhar, O. & Deisseroth, K. 2009. Parvalbumin neurons and gamma rhythms enhance cortical circuit performance. *Nature*, 459, 698-702.
- Sporns, O. 2011. *Networks of the brain*, The MIT Press.
- Sporns, O., Tononi, G. & Kötter, R. 2005. The human connectome: A structural description of the human brain. *PLoS Comput Biol*, 1, e42.
- Stafford, J. M., Jarrett, B. R., Miranda-Dominguez, O., Mills, B. D., Cain, N., Mihalas, S., Lahvis, G. P., Lattal, K. M., Mitchell, S. H., David, S. V., Fryer, J. D., Nigg, J. T. & Fair, D. A. 2014. Large-scale topology and the default mode network in the mouse connectome. *Proceedings of the National Academy of Sciences of the United States of America*, 111, 18745-18750.
- Stein, E. W., Maslov, K. & Wang, L. V. 2009. Noninvasive, in vivo imaging of blood-oxygenation dynamics within the mouse brain using photoacoustic microscopy. *Journal of biomedical optics*, 14, 020502-020502.

- Steiner, A. R., Rousseau-Blass, F., Schroeter, A., Hartnack, S. & Bettschart-Wolfensberger, R. 2021. Systematic Review: Anesthetic Protocols and Management as Confounders in Rodent Blood Oxygen Level Dependent Functional Magnetic Resonance Imaging (BOLD fMRI)-Part B: Effects of Anesthetic Agents, Doses and Timing. *Animals (Basel)*, 11.
- Stenroos, P., Paasonen, J., Salo, R. A., Jokivarsi, K., Shatillo, A., Tanila, H. & Gröhn, O. 2018. Awake Rat Brain Functional Magnetic Resonance Imaging Using Standard Radio Frequency Coils and a 3D Printed Restraint Kit. *Frontiers in Neuroscience*, 12.
- Strand, A. D., Aragaki, A. K., Baquet, Z. C., Hodges, A., Cunningham, P., Holmans, P., Jones, K. R., Jones, L., Kooperberg, C. & Olson, J. M. 2007. Conservation of regional gene expression in mouse and human brain. *PLoS Genet*, 3, e59.
- Tagliazucchi, E., Von Wegner, F., Morzelewski, A., Brodbeck, V. & Laufs, H. 2012. Dynamic BOLD functional connectivity in humans and its electrophysiological correlates. *Frontiers in human neuroscience*, 6, 339-339.
- Tang, J., Coleman, J. E., Dai, X. & Jiang, H. 2016a. Wearable 3-D Photoacoustic Tomography for Functional Brain Imaging in Behaving Rats. *Sci Rep*, 6, 25470.
- Tang, J., Dai, X. & Jiang, H. 2016b. Wearable scanning photoacoustic brain imaging in behaving rats. *J Biophotonics*, 9, 570-5.
- Tasaki, I., Iwasa, K. & Gibbons, R. C. 1980. Mechanical changes in crab nerve fibers during action potentials. *Jpn J Physiol*, 30, 897-905.
- Tecuapetla, F., Matias, S., Dugue, G. P., Mainen, Z. F. & Costa, R. M. 2014. Balanced activity in basal ganglia projection pathways is critical for contraversive movements. *Nat Commun*, 5, 4315.
- Thompson, K. J., Khajehali, E., Bradley, S. J., Navarrete, J. S., Huang, X. P., Slocum, S., Jin, J., Liu, J., Xiong, Y., Olsen, R. H. J., Diberto, J. F., Boyt, K. M., Pina, M. M., Pati, D., Molloy, C., Bundgaard, C., Sexton, P. M., Kash, T. L., Krashes, M. J., Christopoulos, A., Roth, B. L. & Tobin, A. B. 2018. DREADD Agonist 21 Is an Effective Agonist for Muscarinic-Based DREADDs in Vitro and in Vivo. *ACS Pharmacology & Translational Science*, 1, 61-72.
- Tiran, E., Ferrier, J., Deffieux, T., Gennisson, J. L., Pezet, S., Lenkei, Z. & Tanter, M. 2017. Transcranial Functional Ultrasound Imaging in Freely Moving Awake Mice and Anesthetized Young Rats without Contrast Agent. *Ultrasound Med Biol*, 43, 1679-1689.
- Tong, C., Dai, J. K., Chen, Y., Zhang, K., Feng, Y. & Liang, Z. 2019. Differential coupling between subcortical calcium and BOLD signals during evoked and resting state through simultaneous calcium fiber photometry and fMRI. *Neuroimage*, 200, 405-413.
- Trakoshis, S., Martínez-Cañada, P., Rocchi, F., Canella, C., You, W., Chakrabarti, B., Ruigrok, A. N. V., Bullmore, E. T., Suckling, J., Markicevic, M., Zerbi, V., Consortium, M. A., Baron-Cohen, S., Gozzi, A., Lai, M.-C., Panzeri, S. & Lombardo, M. V. 2020. Intrinsic excitation-inhibition imbalance affects medial prefrontal cortex differently in autistic men versus women. *eLife*, 9, e55684.
- Truong, T. V., Supatto, W., Koos, D. S., Choi, J. M. & Fraser, S. E. 2011. Deep and fast live imaging with two-photon scanned light-sheet microscopy. *Nat Methods*, 8, 757-60.
- Uhlhaas, P. J., Roux, F., Rodriguez, E., Rotarska-Jagiela, A. & Singer, W. 2010. Neural synchrony and the development of cortical networks. *Trends in Cognitive Sciences*, 14, 72-80.

- Uhlhaas, P. J. & Singer, W. 2006. Neural synchrony in brain disorders: relevance for cognitive dysfunctions and pathophysiology. *Neuron*, 52, 155-68.
- Uhlirva, H., Kilic, K., Tian, P., Thunemann, M., Desjardins, M., Saisan, P. A., Sakadzic, S., Ness, T. V., Mateo, C., Cheng, Q., Weldy, K. L., Razoux, F., Vandenberghe, M., Cremonesi, J. A., Ferri, C. G., Nizar, K., Sridhar, V. B., Steed, T. C., Abashin, M., Fainman, Y., Masliah, E., Djurovic, S., Andreassen, O. A., Silva, G. A., Boas, D. A., Kleinfeld, D., Buxton, R. B., Einevoll, G. T., Dale, A. M. & Devor, A. 2016. Cell type specificity of neurovascular coupling in cerebral cortex. *Elife*, 5.
- Urban, A., Mace, E., Brunner, C., Heidmann, M., Rossier, J. & Montaldo, G. 2014. Chronic assessment of cerebral hemodynamics during rat forepaw electrical stimulation using functional ultrasound imaging. *Neuroimage*, 101, 138-49.
- Urban, D. J. & Roth, B. L. 2015. DREADDs (designer receptors exclusively activated by designer drugs): chemogenetic tools with therapeutic utility. *Annu Rev Pharmacol Toxicol*, 55, 399-417.
- Van Den Heuvel, M. P. & Hulshoff Pol, H. E. 2010. Exploring the brain network: A review on resting-state fMRI functional connectivity. *European Neuropsychopharmacology*, 20, 519-534.
- Van Der Werf, Y. D., Witter, M. P. & Groenewegen, H. J. 2002. The intralaminar and midline nuclei of the thalamus. Anatomical and functional evidence for participation in processes of arousal and awareness. *Brain Res Brain Res Rev*, 39, 107-40.
- Van Essen, D. C., Smith, S. M., Barch, D. M., Behrens, T. E. J., Yacoub, E. & Ugurbil, K. 2013. The WU-Minn Human Connectome Project: An overview. *NeuroImage*, 80, 62-79.
- Van Vreeswijk, C. & Sompolinsky, H. 1996. Chaos in Neuronal Networks with Balanced Excitatory and Inhibitory Activity. *Science*, 274, 1724.
- Vardy, E., Robinson, J. E., Li, C., Olsen, R. H., Diberto, J. F., Giguere, P. M., Sassano, F. M., Huang, X. P., Zhu, H., Urban, D. J., White, K. L., Rittiner, J. E., Crowley, N. A., Pleil, K. E., Mazzone, C. M., Mosier, P. D., Song, J., Kash, T. L., Malanga, C. J., Krashes, M. J. & Roth, B. L. 2015. A New DREADD Facilitates the Multiplexed Chemogenetic Interrogation of Behavior. *Neuron*, 86, 936-46.
- Vertes, R. P., Linley, S. B. & Hoover, W. B. 2015. Limbic circuitry of the midline thalamus. *Neurosci Biobehav Rev*, 54, 89-107.
- Vicente, A. M., Galvao-Ferreira, P., Tecuapetla, F. & Costa, R. M. 2016. Direct and indirect dorsolateral striatum pathways reinforce different action strategies. *Curr Biol*, 26, R267-9.
- Villringer, A. & Chance, B. 1997. Non-invasive optical spectroscopy and imaging of human brain function. *Trends Neurosci*, 20, 435-42.
- Vlasov, K., Van Dort, C. J. & Solt, K. 2018. Optogenetics and Chemogenetics. *Methods Enzymol.*, 603.
- Vogt, B. A. & Paxinos, G. 2014. Cytoarchitecture of mouse and rat cingulate cortex with human homologies. *Brain Struct Funct*, 219, 185-92.
- Vogt, D., Cho, K. K. A., Shelton, S. M., Paul, A., Huang, Z. J., Sohal, V. S. & Rubenstein, J. L. R. 2017. Mouse Cntnap2 and Human CNTNAP2 ASD Alleles Cell Autonomously Regulate PV+ Cortical Interneurons. *Cereb Cortex*, 1-12.
- Wager, T. D. & Woo, C.-W. 2017. Imaging biomarkers and biotypes for depression. *Nature Medicine*, 23, 16-17.

- Wagner, M. J., Kim, T. H., Kadmon, J., Nguyen, N. D., Ganguli, S., Schnitzer, M. J. & Luo, L. 2019. Shared Cortex-Cerebellum Dynamics in the Execution and Learning of a Motor Task. *Cell*, 177, 669-682.e24.
- Wall, N. R., De La Parra, M., Callaway, E. M. & Kreitzer, A. C. 2013. Differential innervation of direct- and indirect-pathway striatal projection neurons. *Neuron*, 79, 347-60.
- Wang, J., Palkovits, M., Usdin, T. B. & Dobolyi, A. 2006. Afferent connections of the subparafascicular area in rat. *Neuroscience*, 138, 197-220.
- Wang, L., Saalman, Y. B., Pinski, M. A., Arcaro, M. J. & Kastner, S. 2012. Electrophysiological low-frequency coherence and cross-frequency coupling contribute to BOLD connectivity. *Neuron*, 76, 1010-1020.
- Wang, L. V. & Gao, L. 2014. Photoacoustic microscopy and computed tomography: from bench to bedside. *Annu Rev Biomed Eng*, 16, 155-85.
- Wang, L. V. & Yao, J. 2016. A practical guide to photoacoustic tomography in the life sciences. *Nat Methods*, 13, 627-38.
- Wang, M., He, Y., Sejnowski, T. J. & Yu, X. 2018a. Brain-state dependent astrocytic Ca(2+) signals are coupled to both positive and negative BOLD-fMRI signals. *Proc Natl Acad Sci U S A*, 115, E1647-e1656.
- Wang, S., Zhan, Y., Zhang, Y., Lyu, L., Lyu, H., Wang, G., Wu, R., Zhao, J. & Guo, W. 2018b. Abnormal long- and short-range functional connectivity in adolescent-onset schizophrenia patients: A resting-state fMRI study. *Prog Neuropsychopharmacol Biol Psychiatry*, 81, 445-451.
- Wang, X., Pang, Y., Ku, G., Xie, X., Stoica, G. & Wang, L. V. 2003. Noninvasive laser-induced photoacoustic tomography for structural and functional in vivo imaging of the brain. *Nat Biotechnol*, 21, 803-6.
- Webb, R. H., Hughes, G. W. & Delori, F. C. 1987. Confocal scanning laser ophthalmoscope. *Appl Opt*, 26, 1492-9.
- Wess, J., Nakajima, K. & Jain, S. 2013. Novel designer receptors to probe GPCR signaling and physiology. *Trends Pharmacol Sci*, 34, 385-92.
- Whissell, P. D., Tohyama, S. & Martin, L. J. 2016. The Use of DREADDs to Deconstruct Behavior. *Front Genet*, 7, 70.
- White, B. R., Bauer, A. Q., Snyder, A. Z., Schlaggar, B. L., Lee, J. M. & Culver, J. P. 2011. Imaging of functional connectivity in the mouse brain. *PLoS ONE*.
- Wirestam, R. 2012. Using contrast agents to obtain maps of regional perfusion and capillary wall permeability. *Imaging in Medicine*, 4, 423-442.
- Wohr, M., Orduz, D., Gregory, P., Moreno, H., Khan, U., Vorckel, K. J., Wolfer, D. P., Welzl, H., Gall, D., Schiffmann, S. N. & Schwaller, B. 2015. Lack of parvalbumin in mice leads to behavioral deficits relevant to all human autism core symptoms and related neural morphofunctional abnormalities. *Transl Psychiatry*, 5, e525.
- Wolters, A. F., Van De Weijer, S. C. F., Leentjens, A. F. G., Duits, A. A., Jacobs, H. I. L. & Kuijf, M. L. 2019. Resting-state fMRI in Parkinson's disease patients with cognitive impairment: A meta-analysis. *Parkinsonism Relat Disord*, 62, 16-27.
- Yang, M., Zhou, Z., Zhang, J., Jia, S., Li, T., Guan, J., Liao, X., Leng, B., Lyu, J., Zhang, K., Li, M., Gong, Y., Zhu, Z., Yan, J., Zhou, Y., Liu, J. K., Varga, Z., Konnerth, A., Tang, Y., Gao, J., Chen, X. & Jia, H. 2019. Matriex imaging: multiarea two-photon real-time in vivo explorer. *Light Sci Appl*, 8, 109.
- Yang, W. & Yuste, R. 2017. In vivo imaging of neural activity. *Nature Methods*.

- Yao, J., Wang, L., Yang, J.-M., Maslov, K. I., Wong, T. T. W., Li, L., Huang, C.-H., Zou, J. & Wang, L. V. 2015. High-speed label-free functional photoacoustic microscopy of mouse brain in action. *Nature Methods*, 12, 407-410.
- Yao, J., Xia, J., Maslov, K. I., Nasirivanaki, M., Tsytsarev, V., Demchenko, A. V. & Wang, L. V. 2013. Noninvasive photoacoustic computed tomography of mouse brain metabolism in vivo. *Neuroimage*, 64, 257-66.
- Yizhar, O., Fenno, L. E., Prigge, M., Schneider, F., Davidson, T. J., O'shea, D. J., Sohal, V. S., Goshen, I., Finkelstein, J., Paz, J. T., Stehfest, K., Fudim, R., Ramakrishnan, C., Huguenard, J. R., Hegemann, P. & Deisseroth, K. 2011. Neocortical excitation/inhibition balance in information processing and social dysfunction. *Nature*, 477, 171-8.
- Yoshida, E., Terada, S. I., Tanaka, Y. H., Kobayashi, K., Ohkura, M., Nakai, J. & Matsuzaki, M. 2018. In vivo wide-field calcium imaging of mouse thalamocortical synapses with an 8 K ultra-high-definition camera. *Sci Rep*, 8, 8324.
- Zackrisson, S., Van De Ven, S. M. W. Y. & Gambhir, S. S. 2014. Light in and sound out: emerging translational strategies for photoacoustic imaging. *Cancer Res*, 74, 979-1004.
- Zerbi, V., Floriou-Servou, A., Markicevic, M., Vermeiren, Y., Sturman, O., Privitera, M., Von Ziegler, L., Ferrari, K. D., Weber, B., De Deyn, P. P., Wenderoth, N. & Bohacek, J. 2019a. Rapid Reconfiguration of the Functional Connectome after Chemogenetic Locus Coeruleus Activation. *Neuron*, 103, 702-718 e5.
- Zerbi, V., Grandjean, J., Rudin, M. & Wenderoth, N. 2015. Mapping the mouse brain with rs-fMRI: An optimized pipeline for functional network identification. *Neuroimage*, 123, 11-21.
- Zerbi, V., Ielacqua, G. D., Markicevic, M., Haberl, M. G., Ellisman, M. H., A, A. B., Frick, A., Rudin, M. & Wenderoth, N. 2018. Dysfunctional Autism Risk Genes Cause Circuit-Specific Connectivity Deficits With Distinct Developmental Trajectories. *Cereb Cortex*, 28, 2495-2506.
- Zerbi, V., Jansen, D., Wiesmann, M., Fang, X., Broersen, L. M., Veltien, A., Heerschap, A. & Kiliaan, A. J. 2014a. Multinutrient diets improve cerebral perfusion and neuroprotection in a murine model of Alzheimer's disease. *Neurobiol Aging*, 35, 600-13.
- Zerbi, V., Markicevic, M., Gasparini, F., Schroeter, A., Rudin, M. & Wenderoth, N. 2019b. Inhibiting mGluR5 activity by AFQ056/Mavoglurant rescues circuit-specific functional connectivity in Fmr1 knockout mice. *Neuroimage*, 191, 392-402.
- Zerbi, V., Wiesmann, M., Emmerzaal, T. L., Jansen, D., Van Beek, M., Mutsaers, M. P. C., Beckmann, C. F., Heerschap, A. & Kiliaan, A. J. 2014b. Resting-State Functional Connectivity Changes in Aging apoE4 and apoE-KO Mice. *The Journal of Neuroscience*, 34, 13963.
- Zhang, F., Gradinaru, V., Adamantidis, A. R., Durand, R., Airan, R. D., De Lecea, L. & Deisseroth, K. 2010. Optogenetic interrogation of neural circuits: technology for probing mammalian brain structures. *Nat Protoc*, 5, 439-56.
- Zhang, P., Li, L., Lin, L., Hu, P., Shi, J., He, Y., Zhu, L., Zhou, Y. & Wang, L. V. 2018. High-resolution deep functional imaging of the whole mouse brain by photoacoustic computed tomography in vivo. *J Biophotonics*, 11.
- Zhao, F., Wang, P. & Kim, S. G. 2004. Cortical depth-dependent gradient-echo and spin-echo BOLD fMRI at 9.4T. *Magn Reson Med*, 51, 518-24.

- Zhao, F., Zhao, T., Zhou, L., Wu, Q. & Hu, X. 2008. BOLD study of stimulation-induced neural activity and resting-state connectivity in medetomidine-sedated rat. *NeuroImage*, 39, 248-260.
- Zhu, H. & Roth, B. L. 2015. DREADD: a chemogenetic GPCR signaling platform. *Int J Neuropsychopharmacol*, 18.
- Ziv, Y. & Ghosh, K. K. 2015. Miniature microscopes for large-scale imaging of neuronal activity in freely behaving rodents. *Curr Opin Neurobiol*, 32, 141-7.
- Zong, W., Wu, R., Li, M., Hu, Y., Li, Y., Li, J., Rong, H., Wu, H., Xu, Y., Lu, Y., Jia, H., Fan, M., Zhou, Z., Zhang, Y., Wang, A., Chen, L. & Cheng, H. 2017. Fast high-resolution miniature two-photon microscopy for brain imaging in freely behaving mice. *Nat Methods*, 14, 713-719.

CURRICULUM VITAE



PERSONAL INFORMATION

Full Name Marija Markicevic
Nationality Serbian
Date of Birth April 02, 1990

EDUCATION

Oct. 2015 – present **PhD Researcher at the Neural Control of Movement Lab**
Department of Health Sciences and Technology, ETH Zurich,
Switzerland

2014 – 2015 **Master of Science, Neural Engineering (Bioengineering)**
Second year of the joint CEMACUBE program
Trinity College Dublin, the University of Dublin, Dublin, Ireland

2013 – 2014 **Master of Science in Biomedical Engineering**
First year of the joint CEMACUBE program
University of Groningen, Groningen, the Netherlands

2009 – 2013 **Bachelor of Science in Biochemical Engineering and Biotechnology**
University of Belgrade, Faculty of Technology and Metallurgy
Department of Biochemical Engineering and Biotechnology, Serbia

2011 – 2012 **Department of Chemical and Biological Engineering**
University of Maine, Orono, Maine, the United States of America
“Forecast Exchange” scholarship from US State Department (USAID)

INTERNSHIP AND TEACHING EXPERIENCE

January – April 2020 **Visiting PhD researcher at University of Sydney, Australia**
School of Physics, Faculty of Science; Computational Neuroscience

2016 – 2018 **Lecturer in Methods and Concepts of human systems neuroscience
and motor control** for a practical part of the course focused on tACS
and EEG for two winter semesters

April – July 2014 **Internship at Delft University of Technology**
Biomechanical Engineering Department, Delft Prosthetics,
Netherlands

2008 – 2009 **Newcastle for English Courses, OCSMA**
Tripoli, Libya; English teacher (levels A1-B2) at the private school

SCHOLARSHIPS & GRANTS

2020 Educational stipend to attend **ISMRM 2020**, Sydney, Australia

2019 **Blue Brain Project** award to attend NM2 in Champéry, Switzerland

2018 **ZNZ PhD Travel Grant** to attend SFN 2018 in San Diego, USA

2013 – 2015 **Erasmus Mundus Master Course Programme** Scholarship
(CEMACUBE)

	1 of 7 recipients of a 2-year joint masters at 2/5 European Universities.
2012 – 2013	Monthly scholarship from the Municipality of Mladenovac, Serbia
2009 – 2013	University tuition fee and monthly scholarship from Ministry of Education of Serbia
2011 – 2012	“Forecast Exchange” Scholarship from the US State Department (USAID)

PUBLICATIONS

Publications from my main PhD project and collaborative projects during my PhD

M Markicevic, B D Fulcher, O Sturman, J Bohacek, M Rudin, V Zerbi, N Wenderoth. Cell Specific neuromodulation in the striatum shapes BOLD fluctuations in multiple thalamic and cortical regions of anatomically connected circuit. *In preparation* (2021)

M Markicevic, I Savvateev, C Grimm, V Zerbi. Emerging imaging methods to study whole-brain function in rodent models. *Under Review* (2021)

M Markicevic, B D Fulcher, C Lewis, F Helmchen, M Rudin, V Zerbi, N Wenderoth. Cortical excitation: inhibition imbalance causes abnormal brain network dynamics as observed in neurodevelopmental disorders. *Cerebral Cortex* (2020)

F Mirabella, G Desiato, S Mancinelli, G Fossati, M Rasile, R Morini, **M Markicevic**, C Grimm, A Termanini, C Peano, P Kunderfranco, G DiCristo, V Zerbi, S Lodato, E Menna, M Matteoli, D Pozzi. Transient Maternal IL-6 boosts glutamatergic synapses and disrupts hippocampal connectivity in the offspring. *BioRxiv* (2020)

V Zerbi, M Pagani, **M Markicevic**, M Matteoli, D Pozzi, M Fagiolini, Y Bozzi, A Galbusera, ML Scattoni, G Provenzano, A Banerjee, F Helmchen, M Albert Basson, J Ellegood, J P Lerch, M Rudin, A Gozzi, N Wenderoth. Brain mapping across 16 autism mouse models reveals a spectrum of functional connectivity subtypes. *BioRxiv* (2020)

S Trakoshis, P Martinez-Canada, F Rocchi, C Canella, W You, B Chakrabarti, A NV Ruigrok, E T Bullmore, J Suckling, **M Markicevic**, V Zerbi, MRC AIMS Consortium, S Baron-Cohen. A Gozzi, M-C Lai, S Panzeri, M V Lombardo. Intrinsic excitation-inhibition imbalance affects medial prefrontal cortex differently in autistic men versus women. *eLife* (2020)

V Zerbi*, A Floriou-Servou*, **M Markicevic**, Y Vermeiren, O Sturman, M Privitera, L von Ziegler, K D Ferrari, B Weber, P P De Deyn, N Wenderoth, J Bohacek. Rapid Reconfiguration of the Functional Connectome after Chemogenetic Locus Coeruleus Activation. *Neuron* (2019)

F Filipello, R Morini, I Corradini, V Zerbi, A Canzi, B Michalski, M Erreni, **M Markicevic**, C Starvaggi-Cucuzza, K Otero, L Piccio, F Cignarella, F Perrucci, M Tamborini, M Genua, L Rajendran, E Menna, S Vetrano, M Fahnstock, R C Paolicelli, M Matteoli. The microglial innate immune receptor TREM2 is required for synapse elimination and normal brain connectivity. *Immunity* (2019)

V Zerbi, **M Markicevic**, F Gasparini, A Schroeter, M Rudin, N Wenderoth. Inhibiting mGluR5 activity by AFQ056/Mavoglurant rescues circuit-specific functional connectivity in Fmr1 knockout mice. *Neuroimage* (2019)

G Chelini, V Zerbi, L Cimino, A Grigoli, **M Markicevic**, F Libera, S Robbiati, M Gadler, S Bronzoni, S Miorelli, A Galbusera, A Gozzi, S Casarosa, G Provenzano, Y Bozzi. Aberrant somatosensory processing and connectivity in mice lacking Engrailed-2. *Journal of Neuroscience* (2019)

V Zerbi, G D Ielacqua, **M Markicevic**, M G Haberl, MH Ellisman, AA-Bhaskaran, A Frick, M Rudin, N Wenderoth. Dysfunctional autism risk genes cause circuit-specific connectivity deficits with distinct developmental trajectories. *Cerebral Cortex* (2018)

Other publications

B O'Connor, **M Markicevic**, L Newman, RK Poduval, E Tiernan, E Hanrahan, S Cuffe, RB Reilly, D Walsh. Clinical utility of portable electrophysiology to measure fatigue in treatment-naive non-small cell lung cancer. *Supportive Care in Cancer* (2019)

INTERESTS & ACTIVITIES

January 2021 **ETH Zurich** representative to the **Singapore Global Young Scientist Summit** (GYSS), held virtually

Selected volunteer work

2016 – Present Member of the **Association of Scientific Staff at ETH**, Switzerland

February 2020 Volunteer at **Serbian Festival Sydney**, Australia

2016-2018 Member of **Association of Serbian Students** in Zurich, Switzerland

October 2016 Volunteer at **Cyathlon** in Zurich, Switzerland

2009-2016 **World Assembly of Youth (WAY)**, Melaka, Malaysia

Volunteer for Europe

2013-2014 Member of **BMT (Biomedical Technologies Committee)**

University of Groningen, the Netherlands

Selected Certificates

August 2018 **“Successful Leadership in Academia”**

Organized by D-HEST Scientific Staff Association (HAS)

October 2017 **“Connectomics: from micro- to meso- and macro-scales”**

The CAJAL Advanced Neuroscience Training Program at Bordeaux Neurocampus, France

August 2017 **“Extended DISC Communication and Leadership Training”**

Organized by D-HEST Scientific Staff Association (HAS)

February 2016 **FELASA Category B** Certificate

Introductory Course in Laboratory Animal Science, Zurich, Switzerland

August 2010 **5th World Youth Congress** in Istanbul, Turkey

Sustainability and global warming

Languages

Serbian

Native

English

Fluent

Polish

Fluent

Arabic

Intermediate (B1)

German

Intermediate (B1)